DANIEL LÓPEZ MENDOZA

SCOPING PREDICTION OF GROUND AND BUILDING VIBRATIONS INDUCED BY RAILWAY TRAFFIC

SCOPING PREDICTION OF GROUND AND BUILDING VIBRATIONS INDUCED BY RAILWAY TRAFFIC

DANIEL LÓPEZ MENDOZA

UNIVERSIDAD D SEVILLA

THESIS FOR THE DEGREE OF DOCTOR OF PHILOSOPHY WITH INTERNATIONAL MENTION FOR THE UNIVERSIDAD DE SEVILLA

ADVISORS
PROF. DR. PEDRO GALVÍN BARRERA
ASSOC. PROF. DR. ANTONIO ROMERO ORDÓÑEZ
UNIVERSIDAD DE SEVILLA

Daniel López Mendoza: *Scoping prediction of ground and building vibrations induced by railway traffic*. Thesis for the Degree of Doctor of Philosophy with International Mention for the Universidad de Sevilla. Civil Engineer.

Department of Continuum Mechanics and Structural Analysis. School of Engineering. Universidad de Sevilla.

Advisor: Prof. Dr. Pedro Galvín Barrera.

Co-advisor: Assoc. Prof. Dr. Antonio Romero Ordóñez.

Seville, May 2019.

A Zora
A mis hijos Darío y Estrella
A mi familia
A mis amigos

ABSTRACT

The research proposed in this Thesis approaches induced vibrations by railway traffic at the soil surface and buildings close to the track. It is proposed a scoping model to predict the vibration levels in the free-field and nearby buildings in minimal time, using metrics compatible with international standards. The methodology considers soil stiffness, the combination of both the dynamic and static forces generated due to train passage and the Soil-Structure Interaction (SSI). The proposed model assumes the train-track-soil interaction (source-propagation problem) is decoupled from the soil-structure interaction (immission problem), then it is divided into two sub-models. The sub-model to assess free-field vibrations (train-track-soil system), uses the direct stiffness method to compute the soil Green's function, and a novel two-and-a-half dimensional (2.5D) finite element strategy for the train-track interaction. The soil Green's function is modulated using a Neural Network (NN) procedure to save the time consuming computation of track-soil coupling. On the other hand, two SSI sub-models to estimate building vibrations by railway traffic are proposed. The first SSI sub-model computes structural vibration levels using modal superposition, whereas an alternative SSI sub-model based on soil-structure transfer functions, is also presented.

The sub-model to assess soil vibrations is validated by comparing track receptance, free-field mobility and free-field vibration with both measurements and a more comprehensive 2.5D coupled Finite Element Method (FEM)-Boundary Element Method (BEM) model. Moreover, both SSI sub-models are validated by comparing results against a more complex 3D FEM-BEM model.

The results show that the scoping model provides a powerful tool to use during the early design stages of a railway system when multiple scenarios require analysis.

RESUMEN

La investigación propuesta en esta Tesis Doctoral aborda las vibraciones inducidas por el tráfico ferroviario en el suelo y en las edificaciones cercanas a la vía. Se propone un modelo de alcance que permita predecir niveles de vibraciones en el suelo y edificios anexos en un tiempo mínimo, usando medidas compatibles con normativas internacionales. La metodología considera la rigidez del suelo, la combinación de las excitaciones dinámicas y estáticas generadas por el paso del tren y la interacción suelo-estructura (SSI). El modelo propuesto asume que la interacción tren-vía-suelo (problema de generación-propagación) está desacoplada respecto a la interacción suelo-estructura (problema de inmisión), por lo tanto el modelo se divide en dos submodelos. El submodelo para estimar las vibraciones en la superficie libre (sistema tren-vía-suelo) usa el método directo de la rigidez para calcular la función de Green del suelo y un novedoso modelo en elementos finitos en dos dimensiones y media (2.5D) para representar la interacción tren-vía. La función de Green se estima mediante un procedimiento basado en redes neuronales para ahorrar el tiempo de cálculo computacional que implica el acoplamiento vía-suelo. Por otro lado, se proponen dos submodelos para estimar las vibraciones en edificaciones debido al tráfico ferroviario. El primer submodelo para la interacción suelo-estructura calcula los niveles de vibración de la estructura usando superposición modal, y, así mismo, también se presenta un submodelo alternativo para la interacción suelo-estructura basado en las funciones de transferencia suelo-estructura.

El submodelo para estimar las vibraciones en el suelo se valida comparando la receptancia de la vía, la movilidad y la vibración en la superficie libre con medidas experimentales, y también se verifica con un modelo 2.5D acoplado de Método de los Elementos Finitos (MEF)-Método de los Elementos de Contorno (MEC). Además los dos submodelos usados para la interacción suelo-estructura se validan comparando resultados con un modelo tridimensional (3D) MEF-MEC.

Los resultados muestran que el modelo de predicción propuesto supone una herramienta valiosa para usar en una etapa de un diseño preeliminar de un trazado ferroviario en el que se requiera el análisis de múltiples alternativas.

PUBLICATIONS

This Thesis is presented as a compilation of four publications to obtain the Degree of Doctor for the Universidad de Sevilla, according to Article 9, Agreement 9.1/CG12/04/19 of the Universidad de Sevilla, that fix the requirement for PhD Thesis. This specifies that the Thesis has to include an introduction, a description of objectives, a discussion of the overall results and the conclusions obtained.

This Thesis consists of an extended summary of the research proposed and the following appended publications:

- **Paper A** D. López-Mendoza, A. Romero, D.P. Connolly and P. Galvín. Scoping assessment of building vibration induced by railway traffic, *Soil Dynamics and Earthquake Engineering*, 2017, 93, 147-161.
- **Paper B** P. Galvín, D. López-Mendoza, D.P. Connolly, G. Degrande, G. Lombaert and A. Romero. Scoping assessment of free-field vibrations due to railway traffic, *Soil Dynamics and Earthquake Engineering*, 2018, 114, 598-614.
- **Paper C** D. López-Mendoza, D.P. Connolly, A. Romero, G. Kouroussis and P. Galvín. A transfer function method to predict building vibration and its application to railway defects, *Construction and Building Materials*, (*Submitted, April 2019*).
- **Book chapter** P. Galvín, D. López-Mendoza, D.P. Connolly and A. Romero. Chapter 10: Scoping assessment of ground and building vibrations due to railway traffic, *Ground Vibrations from High-Speed Railways: Prediction and mitigation.*, Institution of Civil Engineering ICE. ISBN: 9780727763792.

The appended publications were prepared in collaboration with co-authors. The author of this Thesis is responsible for the major progress of work in these publications, including the development/deduction of the solution and numerical methods, performing the numerical simulations and writing the main parts of the papers.

No matter how you travel, how 'successful' your tour, or foreshortened, you always learn something and learn to change your thoughts.

— Jack Kerouac

ACKNOWLEDGMENTS

I would like to express my gratitude for those who have contributed to the development of the research carried out by the author of this Thesis.

To my advisors, Prof. Dr. Pedro Galvín Barrera and Assoc. Prof. Dr. Antonio Romero Ordóñez, for trusting, encouraging and supporting me to develop this work.

To Assoc. Prof. Dr. David P. Connolly, who provided a nice workplace during my research stay at the *Institute for Infrastructure and Environment, Heriot-Watt University (Edinburgh, UK)*, making sure I had everything I needed to continue with my research.

To my colleagues of the Department of Continuum Mechanics and Structural Analysis.

To the support given by the Andalusian Scientific Computing Centre (CICA) and the Spanish Ministry of Economy and Competitiveness (Ministerio de Economía y Competitividad).

Daniel López Mendoza
Seville, May 2019.

CONTENTS

LIST OF FIGURES

LIST OF TABLES

ACRONYMS

The plural form will be constructed by adding an *s* at the end of the acronym.

CICA Andalusian Scientific Computing Centre

MEC Método de los Elementos de Contorno

MEF Método de los Elementos Finitos

RMS Root-Mean-Square

SSI Soil-Structure Interaction

EIA Environmental Impact Assesment

HSR High-Speed Rail

HST High Speed Train

BEM Boundary Element Method

FEM Finite Element Method

FRA Federal Railroad Administration

FTA Federal Transit Administration

GSSSS Generalized Single Solved

VdB Velocity Decibel

RSA Response Spectrum Analysis

SPR Single Point Response

NN Neural Network

MLP Multilayer Perceptron

MTVV Maximum Transient Vibration Value

PSD Power Spectral Density

PML Perfectly Matched Layers

NIST National Institute of Standards and Technology

PPV Peak Particle Value

VdB Vibration decibels

1 INTRODUCTION

Globally, the number of High-Speed Rail (HSR) lines both operational and under construction is growing rapidly. This has led to an increase in real estate located close to lines, and thus the number of properties affected by ground-borne vibrations [10, 48, 77, 78, 87]. Ground-borne vibrations are vibrational waves generated within the track structure that propagate to nearby structures, causing shaking and in-door noise. These effects are undesirable and post-construction mitigation measures are expensive. Therefore, vibration levels require prediction during the early stages of planning/development, typically in the form of a desktop study.

International standard ISO 2631 [34, 35] addresses these negative effects and evaluates the whole-body human exposure to vibration. In addition, ISO 14837 [36] is railway focused and describes the emission-propagation-immission mechanisms of waves from the train-track system (source) to the building (receiver). It provides a guide on the measurement of experimental data, vibration evaluation, and mitigation.

ISO 14837 [36] also outlines suggested numerical approaches for predicting vibrations arising from the railway. Comprehensive and detailed design models are often used at locations of sensitive receptors (e.g. theatres, hospital, education centres, among others) or where vibration has identified to be a problem. These kind of models are computationally expensive. At the earlier stage, simplified scoping models are used to identify the track locations where nearby buildings can be affected by railway traffic. These models allow engineers to assess long lengths of the track quickly in the absence of detailed design information. Typically, scoping models consider the generation and the propagation mechanisms decoupled from the immission in building and other structures close to the track. Coulier et. al [11] studied the validity of this approach in a ballasted track, concluding that can be neglected for distances to the track longer than six times the Rayleigh wavelength, thus validating this assumption.

1.1 RESEARCH BACKGROUND

The research developed in this thesis studies the formulation of scoping models to predict the vibrations produced by railway traffic in in the context previously defined. Following, the research background is defined to provide a comprehensive theoretical basis and a survey of published works in this regards.

The most accurate prediction model should consider the three-dimensional (3D) nature of the coupled problem that defines the wave propagation from the track to the immission receiver, including the train-track interaction and the Soil-Structure Interaction (SSI).

Vibrations induced by a train passage are rigorously analysed using models based on the Boundary Element Method (BEM) [17] and the Finite Element Method (FEM) [88].

The SSI represents an important issue for predicting the response of structures due to ground-borne vibrations [42, 82]. The BEM is very suitable to properly describe the soil wave propagation due to the Sommerfeld radiation condition [22] is satisfied when the Green's function of the half-space is used as the fundamental solution. On the other hand, the FEM is especially useful to represent the dynamic behaviour of structures. Therefore, coupled formulations based on the BEM and the FEM allow accurate solutions for SSI problem.

Many authors have proposed different BEM-FEM models to assess railway vibrations in different conditions. Xia et al. [83] have presented a coupled train-track-soil model formulated in the frequency domain to adequately characterise the ground-borne vibration using the layered half-space Green's functions [85]. Moreover, Galvín and Romero [5, 28, 30, 66] developed a 3D BEM-FEM model formulated in the time domain representing the behaviour of the train–track–soil-structure system. These works included a detailed analysis of the High Speed Train (HST) passage effects on a concrete underpass, the importance of rigorously modelling the transition track zone, and the SSI influence in resonant behaviour of railway bridges. The last case represents another sensitive structure that requires be studying by comprehensive models [6, 16, 66]. Fiala et al. [25] studied different mitigation systems to reduce ground-borne noise and vibration in buildings, that included floating-floors, isolated rooms, and base-isolation. These authors found that the best reduction is obtained when the structure is isolated from the foundation through a spring-damper system.

Alternatively, in certain cases, two-and-a-half-dimensional (2.5D) approaches have been developed in the frequency-wavenumber domain to reduce the computational effort of 3D models. The 2.5D formulations assume the problem is homogeneous in the track direction. The contributions of Lombaert et al. [51, 52] have had an important impact on the development of this type of models. They studied the influence of the coupling vehicle-track on the prediction of ground-borne vibrations. The work presented by Auersch [1] was also noticeable. This author described the parametric excitation due to the sleeper passage using a method in which the vehicle was modelled by a multi-body approach and the soil is represented with the Green's function for layered half-space proposed by Kausel and Roësset [43]. The influence of both vehicle and track irregularities on free-field response was well described. Moreover, Sheng et al. [73] have used an infinite layered beam coupled to a layered half-space to represent the track-soil interaction in the estimation of ground-borne vibrations. This method considered both the quasi-static and the dynamic excitations, and it was concluded that the dynamic contribution is dominant when the train speed is lower than the Rayleigh wave speed of the soil. Regarding the performance of these methods, Galvín et al. used a 2.5D BEM-FEM model [27, 31] to compare two approaches for modelling ballasted tracks on an embankment. In the first approach, the ballast and the embankment were modelled using solid finite elements, whereas the second approach consisted of a simplified beam representation. This methodology was used to analyse the

influence of the stratification on tunnel behaviour. They concluded that the refracted waves affect the tunnel–soil interaction problem when the distance between the tunnel and the surface of the halfspace is smaller than the wavelength in the soil. Recently, Romero et al. [67, 68] have rigorously computed the radiated noise and vibration from underground structures using a 2.5D method that used the Green's function for a fluid-solid formation to represent the soil and the air above the ground surface [74].

Although the previously cited works were useful for predicting ground-borne vibrations, cannot be considered strictly valid to predict vibrations in a building located close to the track, because it violates the assumptions in the formulation of 2.5D models. Therefore, it is very common for predicting building vibrations develop uncoupled methods combining a 2.5D train-track-soil method with a 3D soil-structure model. In this way, the ground-borne vibration computed from a 2.5D model is the input of the 3D model used to evaluate building response. Lopes et al. [54, 55, 65] developed a methodology to evaluate building vibrations induced by railway traffic in tunnels. Kuo et al. [50] analysed how railway induced vibrations change as they propagate through the foundations and floors of nearby buildings. Kouroussis et al. [44] developed a scoping method to predict railway vibration in buildings using only the finite element method. This model was based on a decoupled approach for representing a building nearby to a tramway network. The building was triggered by an important rail unevenness as a local defect. Also, Connolly et al. [21] presented a decoupled procedure to analyse soil-building vibrations due to railway defects. In this case, a 2.5D FEM time-frequency domain model was used to compute soil vibrations and later was combined with a 3D FEM procedure to obtain building vibrations. The track-soil interaction was modelled by a spring-damper element described in Reference [32].

These works showed that comprehensive models are able to accurately compute vibrations levels in buildings during the planning and construction of new railway lines. They are well suited to a planning and environmental assessment stage [36]. However, in preliminary design stages, the practical application of the comprehensive model is unusual due to the high computational cost to study long stretches of the track [36]. Simplified procedures commonly consists of uncoupled methodologies where the interaction between the source (train-track-soil system) and the receiver (building-soil system) is discarded. Regarding the scoping models focused on free-field predictions, Rossi and Nicolini [69] presented an approach to predict maximum Root-Mean-Square (RMS) velocity considering different train types, train speeds, track properties and distances to the track. The analytical expressions of the model were calibrated by experimental data. With et al. [81] proposed an empirical scoping model to compute running RMS values of velocity based on the wheel force, the train speed and the distance to the track. Recently, Connolly et al. [18] presented a simplified method to instantly compute ground vibrations due to train passages, predicting two vibration descriptors: the Peak Particle Value (PPV) [15] and the $KB_{F,\max}$ [14]. A machine learning approach was developed to obtain free-field vibrations using numerical predictions for a wide range of train speeds and soil types. The main drawback of existing scoping models is related to the computation time history of the free-field response.

Alternatively, some researches proposed simplified methods to predict the time history of induced ground vibrations railway traffic. Triepaischajonsak and Thompson [75] presented a hybrid model that combines a detailed vehicle-track model formulated in the time domain with a model based on the the solution proposed by Kausel and Roësset [43] for layered soils in the frequency domain. Thus, the force transmitted to the soil was obtained from the train-track model and was used later to obtain the free-field vibration. Moreover, Kuo et al. [49] developed a hybrid model where the source and propagation mechanisms were also decoupled. This model combined experimental tests and numerical predictions considering the definitions proposed by the Federal Railroad Administration (FRA) and the Federal Transit Administration (FTA) of the U.S. Department of Transportation [7, 8]. Kouroussis et al. [46, 47] developed a hybrid experimental-numerical model to predict ground vibrations from urban railway traffic. The vibration levels were computed by combining the force density obtained from a numerical train-track model with the soil mobility function measured through an experimental approach.

Scoping methodologies have also been applied to investigate the dynamic behaviour of buildings. Although the scoping methods must be simpler than comprehensive models, its application should accurately consider the SSI to predict building vibrations. Attending this idea, Auersch [2, 3] proposed a simplify correlation for layered soils to include the SSI effects in buildings for different foundation systems. Also, Auersch [4] examined the building response using a simple soil-wall-floor model based on an empirical transfer function obtained from the behaviour of the structure. In this case, the soil was modelled using a spring and a viscous damper that represented the SSI. Alternatively, the National Institute of Standards and Technology (NIST) [61] suggests recommendations to consider the SSI for several types of building foundations. François et al. [26] developed simplified methods to assess building vibrations ignoring SSI, but take into account the relative stiffness between the building and the soil. Similar procedures than those related above are commonly used to include the SSI in the scoping models focused on the prediction of building vibrations due to railway traffic.

Some empirical researches have been carried out to assess ground-borne vibration in buildings. Nelson and Sauernmann [40] presented a prediction procedure for railway noise and vibration assessment. They estimated low-frequency ground-borne noise and vibration between 6.3 and 200 Hz in residential and commercial structures near at-grade and subway track using an impact-testing procedure to characterize the propagation of vibrations in soils. Similarly, Wilson [79] and Wilson et al. [80] proposed a semi-empirical procedure to assess building vibration and interior noise. This method combined ground vibrations with empirical corrections to add the effects of the SSI. The authors recommended adding a safety factor about 5 to 10 dB to the predictions. Madshus et al. [59] developed a semi-empirical model for structures founded in soft soils, that was based on the statistical analysis of experimental measurements in Norway and Sweden. This method allowed the computation of the one-third octave RMS values of the building response in the frequency range from 1 to 80 Hz according to ISO standards 2631 [34] and 8041 [37]. The empirical

approaches proposed by the FRA and the FTA [7, 8] are widely used to predict Vibration decibels (VdB) values of the ground and building responses. The simplifications assumed in the FRA and FTA procedures were verified by Verbraken et al. [76] using a comprehensive numerical model, concluding that the prediction ability is especially good at higher frequencies. More recently, Connolly et al. [18, 19] presented the scoping toolbox Scoperail to predict in-door noise and the structural VdB value due to high-speed trains. This prediction combined ground-borne vibrations with empirical correction factors.

The aforementioned empirical approaches did not allow to predict the time history of the building response. The human exposition and the effects on structures are better evaluated when the time history of the response is known because of different existing standards can be used. However, the empirical approaches are commonly based on a statistical analysis and the time history of the building estimation would involve large number of data with an inadmissible computational cost. Some approaches have been proposed to overcome this drawback on the empirical prediction. Rücker et al. [70] developed a simplified prediction tool that allows evaluating the immission of vibration in a building due to a train passage with the soil-wall-floor model presented in Reference [4]. The simple building model consisted of one wall representing all supporting structures (walls and columns) and one floor for each storey. Later, Hussein et al. [33] studied the vibrations generated by underground railway traffic in a building on a piled foundation. They used a sub-modelling method that combines a 3D train-track-soil model with a simple 2D frame building. Although these methods allowed the full computation of building response, there is some uncertainty in the simplifications adopted in the soil-wall-floor model [70] and 2D frame building [33] that should be taken into account.

The analysis of the research background reveals that simplified models could give very conservative estimations with higher related project costs in planning new railway lines. This thesis contributes to the development of accurate prediction scoping tools.

1.2 OBJECTIVES AND CONTRIBUTIONS

This Thesis builds upon the previous approaches developed by Galvín et al. [28, 29, 30, 31], who presented comprehensive BEM-FEM methodologies to rigorously analyse the railway vibration problem. Also, Romero et al. [67, 68] complemented their research proposing a complex 2.5D BEM-FEM formulation to compute radiated noise and vibrations in structures. Although these methodologies present high computational requirements, and they are useful in detailed studies, a simplified method is needed to extend the ideas of these previous works to desktop studies, assessing long stretches of the track quickly, in the absence of detailed design information. Then, the main objective of this Thesis is to develop a train-track-soil-building scoping methodology to predict the vibration levels in the free-field and nearby buildings, using metrics compatible with international standards. These predictions need a fraction of the time typically required to analyse a complex SSI problem, and thus provides a practical tool to rapidly analyse the vibration response of several struc-

tures near railway lines. Also, the proposed model assumes the train-track-soil interaction (source-propagation problem) can be decoupled from the soil-structure interaction (immission problem).

The proposed train-track-soil model to evaluate the free-field vibrations is aimed at aiding vibration assessments undertaken during the planning stages of a new railway line. It is able to model the effect of a large variety of input variables using a minimal computational effort. Free-field predictions are assessed by combining a track-soil model with a train-track model. The proposed method allows for the estimation of the track receptance, free-field mobility and soil response in the time and frequency domains, with low computational effort.

The excitation of the building foundation corresponds with the soil response due to railway traffic.

The main novelties proposed in this Thesis are related below:

- Representation of track-soil interaction to define the vibration transmission by modulating the soil Green's function [41, 43, 72] with a correction factor obtained from a Neural Network (NN) approach. The evaluation of the coupled track-soil response takes only the time of the soils Green's function computation.

- Development of a 2.5D finite element strategy for the train-track interaction. The train-track forces are calculated using a simplified FEM track model where the underlying soil is modelled using a spring-damper element with properties depending on the Green's function of a homogeneous or layered half-space.

- Two approaches are proposed to solve the immission problem in buildings considering SSI. The first approach predicts structural vibration levels using modal superposition avoiding intensive computations. This approach involves a powerful tool easily implementable in a general purpose FEM code. It allows obtaining the overall RMS value of the building response and the contribution of the dominant frequencies, giving conservative predictions well suited in preliminary designs (e.g. master planning and route selection stage) [36]. However, the time domain history of the response cannot be calculated using this approach. On the other hand, the second proposal is based on soil-structure transfer functions. The computational requirements are slightly higher, but it allows to compute the building response in the time and frequency domains with better accuracy. It is useful to be used in environmental assessment stages [36].

1.3 CONTENTS

Following, the proposed train-track-soil-building scoping methodology is presented. Some of the main results of this Thesis are shown, including the validation of the proposed

methodology and a study on the influence of soil properties and local irregularities on vibration levels. The main conclusions and future developments are exposed. These topics are more elaborated in the appended publications. In **Paper A** [56] the dynamic analysis of the building due to railway traffic is computed from the 3D FEM methodology based on a modal superposition analysis. This procedure allows assessing an overall value of the response and the contribution of the modes to this response. The train-track-soil model used to evaluate the free-field vibrations is presented in **Paper B** [32]. The train-track-soil system is divided into two sub-models. The train-track sub-model proposed is based on a simplified FEM track approach, where the underlying soil is modelled using a spring-damper element. Moreover, the track-soil interaction is approximated from the soil Green's function modulated by a correction factor estimated from a neural network procedure. The soil-structure transfer function proposed for the evaluation of structural vibrations is described in **Paper C**. The time history of the building response is obtained using this approach. Applications of the complete train-track-soil-building model (available as a `MATLAB` toolbox on the website `http://personal.us.es/pedrogalvin/scoping.en.html`) are related in the **Book Chapter**, that includes a sensitivity analysis of track type, soil stiffness, building height and train speed effects on predictions. It is also studied the simplification of using equivalent homogeneous soils to predict vibration levels in layered soils.

2

NUMERICAL MODEL

A wide variety of modelling approaches can be used to predict ground and building vibrations due to railway traffic. Typically, due to the large size of the modelling domain, the train-track-soil-building problem is divided into different sub-models (Figure 2.1). These sub-models typically use simplified strategies, that can achieve similar accuracy, but in much reduced time.

The proposed model assumes that the train-track-soil interaction (source-propagation problem, Figure 2.1, step 2.3) can be decoupled from the soil-structure interaction (immission problem, Figure 2.1, step 2.4). The simplified methodology presented in **Paper B** is followed for the computation of the free-field response (Figure 2.1, step 2.3). The train-track-soil system is divided into two sub-models: a train-track sub-model (Figure 2.1, step 2.1) and a track-soil sub-model (Figure 2.1, step 2.2). These sub-models are described below.

After obtaining the free-field response, it is used to compute the vibrations in buildings close to the line (Figure 2.1, step 2.4). To do so, the free-field response is the input of the SSI problem. In this Thesis, two methodologies are described in **Paper A** and **Paper C** to evaluate building vibrations.

To minimise the required computational cost, the following strategies are used:

- The train-track forces $\mathbf{g}$ are calculated using a simplified FEM track model. The underlying soil is modelled using a spring-damper element, that approximates the underlying soil response (step 2.1).
- The track-soil transfer function $\tilde{\mathbf{u}}_{ff}$ (step 2.2) is approximated from the soil Green's function $\tilde{\mathbf{u}}_g$ using a correction factor $\tilde{A}_g$, that is estimated using a neural network procedure.
- For the building response $\mathbf{u}_t$, the scoping model uses two different FEM approaches considering the SSI through a set of spring-damper elements at the foundation (step 2.4). The procedure presented in **Paper A** is based on a modal superposition analysis, whereas a simple method is described in **Paper C** using the soil-structure transfer function that does not depend on the free-field response.

2.1 SOURCE-PROPAGATION PROBLEM

Next, the main steps of the proposed methodology are presented. A more detailed description can be found in **Paper B**.

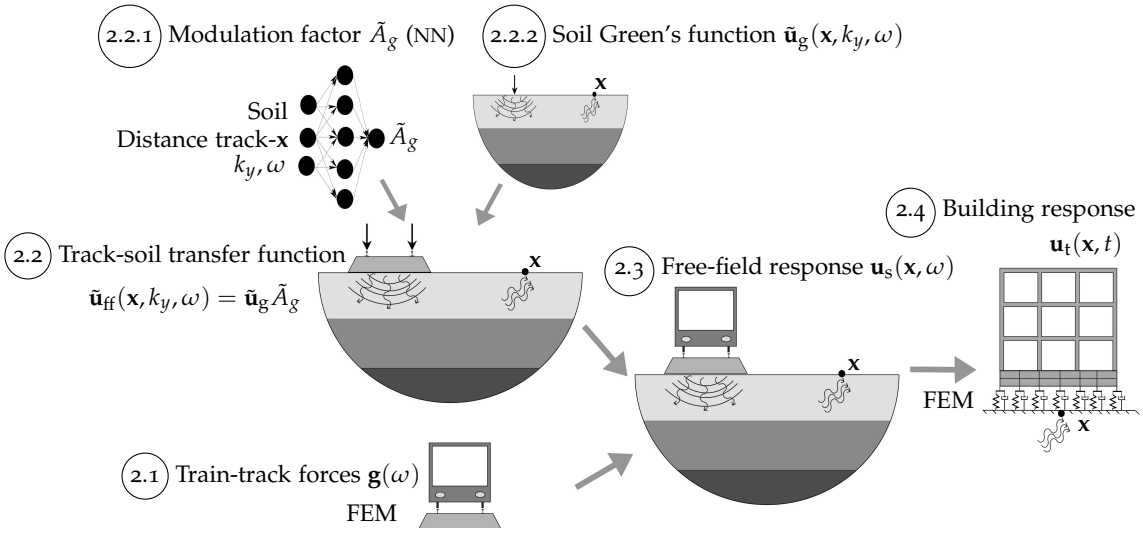

Figure 2.1: Scheme of the scoping model.

2.1.1 *Train-track forces*

2.1.1.1 *Track model*

The train-track forces (Figure 2.1, step 2.1) are calculated using a simplified 2.5D FEM model (Figure 2.2). The model allows both linear hysteretic or viscous damping models for the ballasted and slab track structures.

For the ballasted track model, the rails are represented using Euler-Bernoulli beams with bending stiffness $E_r I_r$ and mass $\rho_r A_r$ per unit length. The rail displacements are denoted as $u_{r1}(x_1, t)$ and $u_{r2}(x_2, t)$. The position of the rails is determined by the track gauge w_r. The internal energy dissipation in the rail is modelled as a loss factor η_r.

The rail pads are modelled with continuous spring-damper connections. The rail pad stiffness k_{rp} and damping coefficient c_{rp} are used to calculate the equivalent stiffness $\overline{k}_{rp} = k_{rp}/d_{sl}$ and damping $\overline{c}_{rp} = c_{rp}/d_{sl}$, where d_{sl} is the sleeper spacing. Alternatively, a loss factor η_{rp} can be used to describe rail pad behaviour as, $\overline{k}_{rp} = \overline{k}_{rp}(1 + i\eta_{rp})$.

The concrete sleepers are assumed to be rigid, therefore the vertical sleeper displacements along the track are determined by the vertical displacement $u_{sl}(x, t)$ and rotation $\theta_{sl}(x, t)$ at the centre of gravity of the sleeper. The sleepers are modelled as a uniformly distributed mass $\overline{m}_{sl} = m_{sl}/d_{sl}$, where m_{sl} is the mass of the sleeper. The rotational inertia of the sleeper is estimated as $\rho_{sl}\overline{I}_{sl} = \rho_{sl} I_{sl}/d_{sl}$, where the inertia I_{sl} is calculated as $I_{sl} = 1/6 l_{sl} h_{sl} b_{sl}(h_{sl}^2 + l_{sl}^2)$, and l_{sl}, h_{sl} and b_{sl} are the sleeper length, height and width, respectively.

The ballast bed is represented by a set of distributed linear spring-damper elements. The equivalent ballast stiffness is computed from the vertical spring stiffness k_b for each sleeper as $\overline{k}_b = k_b/d_{sl}$. The viscous damping in the ballast bed is accounted using a

complex impedance $\overline{k}_\mathrm{b} + i\omega\overline{c}_\mathrm{b}$. Alternatively, a loss factor η_b can be used to describe ballast behaviour as $\overline{k}_\mathrm{b} = \overline{k}_\mathrm{b}(1 + i\eta_\mathrm{b})$. The equivalent ballast mass under each sleeper is estimated as $m_\mathrm{b}/d_\mathrm{sl}$. The ballast mass m_b is estimated from the height h_b of the ballast layer and lengths $l_\mathrm{b1} = l_\mathrm{sl}$ and l_b2 at the top and the bottom of the ballast layer, respectively, as $m_\mathrm{b} = 0.5\rho_\mathrm{b}h_\mathrm{b}(l_\mathrm{b1} + l_\mathrm{b2})b_\mathrm{sl}$.

The embankment is represented using a Euler-Bernoulli beam with a bending stiffness $E_\mathrm{e}I_\mathrm{e}$, a torsional stiffness $G_\mathrm{e}J_\mathrm{e}$, a loss factor η_e, a rotational inertia $\rho_\mathrm{e}I_{pe}$, and a mass $\rho_\mathrm{e}A_\mathrm{e}$ per unit length, where E_e, I_e, G_e, J_e, I_{pe}, ρ_e and A_e are the Young's modulus, the bending moment of inertia, the shear modulus, the torsion constant, the polar moment of inertia, the density and the area, respectively. The embankment properties are approximated to be equal to the uppermost soil layer.

A ballast mat can be simulated using spring-damper elements between the embankment and the ballast with equivalent stiffness and damping (or loss factor) $\overline{k}_\mathrm{m}$ and $\overline{c}_\mathrm{m}$ (or η_m), respectively.

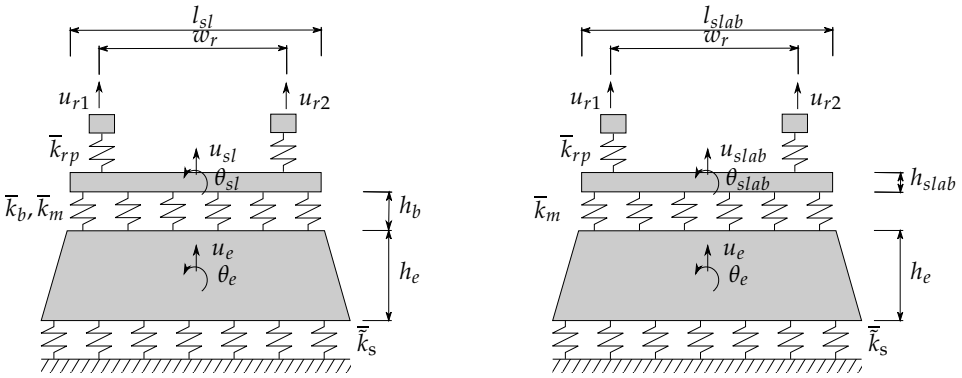

Figure 2.2: Cross section of (left) ballasted and (right) slab track models.

For the slab track model, the rails, rail pads and embankment are modelled following the same procedure for the ballasted track model. The slab is represented as a Euler-Bernoulli beam with a bending stiffness $E_\mathrm{slab}I_\mathrm{slab}$, a torsional stiffness $G_\mathrm{slab}J_\mathrm{slab}$, a rotational inertia $\rho_\mathrm{slab}I_{p\mathrm{slab}}$, a loss factor η_slab and a mass per unit length $\rho_\mathrm{slab}A_\mathrm{slab}$, where E_slab, I_slab, G_slab, J_slab, $I_{p\mathrm{slab}}$, ρ_slab and A_slab are analogous to the embankment definition.

The underlying soil is represented using a spring-damper element with stiffness $\overline{\overline{k}}_\mathrm{s}(k_y, \omega)$. A tilde above a variable denotes its representation in the frequency-wavenumber domain. The soil equivalent stiffness and damping are estimated by the vertical soil response computed from the Green's function for a homogeneous or layered half-space due to a unit vertical load applied at a distance $w_\mathrm{r}/2$ from the track axis. Note that because the spring-damper element does not consider the effect of a moving load, the model ignores the dynamic effects that may be induced when approaching critical velocity [71]. The continuity of displacement is ensured between the soil and the track.

The 2.5D FEM formulation follows that outlined by Galvín et al. [31]:

$$\left[-\omega^2\mathbf{M}_{\mathrm{bb}} + \mathbf{K}^0_{\mathrm{bb}} - ik_y\mathbf{K}^1_{\mathrm{bb}} - k_y^2\mathbf{K}^2_{\mathrm{bb}} + ik_y^3\mathbf{K}^3_{\mathrm{bb}} + k_y^4\mathbf{K}^4_{\mathrm{bb}} + \tilde{\mathbf{K}}^{\mathrm{s}}_{\mathrm{bb}}(k_y,\omega)\right]\tilde{\mathbf{u}}_{\mathrm{b}}(k_y,\omega) = \tilde{\mathbf{f}}_{\mathrm{b}}(k_y,\omega) \tag{1}$$

where $\mathbf{K}^0_{\mathrm{bb}}$, $\mathbf{K}^1_{\mathrm{bb}}$, $\mathbf{K}^2_{\mathrm{bb}}$, $\mathbf{K}^3_{\mathrm{bb}}$ and $\mathbf{K}^4_{\mathrm{bb}}$ are the stiffness matrices, $\mathbf{M}_{\mathrm{bb}}$ is the mass matrix, $\tilde{\mathbf{f}}_{\mathrm{b}}(k_y,\omega)$ is the external load vector, $\tilde{\mathbf{u}}_{\mathrm{b}}$ are the finite element degrees of freedom and $\mathbf{K}^{\mathrm{s}}_{\mathrm{bb}}(k_y,\omega)$ represents the dynamic soil stiffness matrix. For simplicity, matrices $\mathbf{K}^1_{\mathrm{bb}}$, $\mathbf{K}^2_{\mathrm{bb}}$ and $\mathbf{K}^3_{\mathrm{bb}}$ are discarded so that the proposed model does not contain any volume or shell elements. The finite element matrices $\mathbf{M}_{\mathrm{bb}}$, $\mathbf{K}^0_{\mathrm{bb}}$ and $\mathbf{K}^4_{\mathrm{bb}}$ in Equation (1) are independent of wavenumber k_y and frequency ω, and are only assembled once. The dynamic soil stiffness matrix $\tilde{\mathbf{K}}^{\mathrm{s}}_{\mathrm{bb}}(k_y,\omega)$ is calculated from the stiffness $\overline{\tilde{k}}_{\mathrm{s}}(k_y,\omega)$, obtained by means of the Green's function [43] (Figure 2.1 step 2.2.2).

2.1.1.2 *Train forces*

The train forces $\mathbf{g}(\omega)$ (Figure 2.1, step 2.1) are computed by the superposition of the dynamic $\mathbf{g}_d$ and quasi-static $\mathbf{g}_q$ excitations [53].

The quasi-static load is computed as:

$$\mathbf{g}_q(\omega) = \sum_{k=1}^{n_a} w_k \exp\left(i\frac{\omega}{v}y_k\right) \tag{2}$$

where w_k and y_k are the weight and the position of the k-th axle, v is the train speed and n_a is the number of axles.

Additionally, the dynamic forces $\mathbf{g}_d(\omega)$ are computed from the track and vehicle compliances assuming a perfect contact between both [52]:

$$\left[\mathbf{C}^t(\omega) + \mathbf{C}^v(\omega)\right]\mathbf{g}_d(\omega) = -\mathbf{u}_{w/r}(\omega) \tag{3}$$

where $\mathbf{C}^v(\omega)$ is the vehicle compliance, $\mathbf{C}^t(\omega)$ is the track compliance and $\mathbf{u}_{w/r}(\omega)$ is the rail unevenness. The track compliance $\mathbf{C}^t(\omega)$ depends upon the rail impulse response $\tilde{\mathrm{u}}_{\mathrm{r}}(k_y,\omega)$ included within the degrees of freedom $\tilde{\mathbf{u}}_{\mathrm{b}}$ (Equation (1)). The procedure to compute the vehicle and track compliances and the rail unevenness can be found in **Paper B**.

2.1.2 *Track-soil transfer function*

Many vibration prediction models consider the track-soil interaction using comprehensive methodologies, which imply a high computational cost. In order to reduce the computational effort, the proposed model estimates the track-soil transfer function $\tilde{\mathbf{u}}_{\mathrm{ff}}(\mathbf{x},k_y,\omega)$

(Figure 2.1, step 2.2) by combining the Green's functions $\tilde{\mathbf{u}}_{\mathrm{g}}(\mathbf{x}, k_y, \omega)$ [43] (Figure 2.1, step 2.2.2) with a correction factor $\tilde{A}_g$ obtained from a neural network (Figure 2.1, step 2.2.1). Note that the sub-indexes ff and g indicate free-field response and Green's functions, respectively. The track-soil transfer function $\tilde{\mathbf{u}}_{\mathrm{ff}}(\mathbf{x}, k_y, \omega)$ represents the response at a point $\mathbf{x} = \{d, y, 0\}$ located at the soil surface due to an impulsive vertical load at the rail, where d is the distance between the evaluated point $\mathbf{x}$ and the track. The correction factor $\tilde{A}_g$ depends on the track type and the soil properties, that is evaluated for a point $\mathbf{x}$, in the frequency-wavenumber domain. Therefore the track-soil transfer function at a point $\mathbf{x}$ can be obtained as:

$$\tilde{\mathbf{u}}_{\mathrm{ff}}(\mathbf{x}, k_y, \omega) = \tilde{A}_g(d, k_y, \omega)\tilde{\mathbf{u}}_{\mathrm{g}}(\mathbf{x}, k_y, \omega) \tag{4}$$

In order to estimate the correction factor a Multilayer Perceptron (MLP) neural network architecture based on a back-propagation training algorithm [12] is used. One, two and three hidden layers are tested. A NN framework with four layers (Figure 2.3: one input, two hidden and one output) is chosen to construct the proposed model.

The input layer (Figure 2.3) contains six inputs parameter: soil parameters c_{s_1}, h_1, V_{s30}, the distance d, frequency ω and wavenumber, that is represented by the non-dimensional wavenumber $k_{dy} = k_y c_{s_1}/\omega$. h_1 and c_{s_1} are the depth and the shear wave velocity of the upper layer respectively. Whereas, V_{s30} is the average shear wave velocity defined in Eurocode 8 [23]. The shear wave velocity of the upper layer matches with the V_{s30} parameter $c_{s_1} = V_{s30}$, with $h_1 = 30\,\mathrm{m}$ for a homogeneous soil.

The output layer has two parameters because the correction factor $\tilde{A}_g$ is a complex number. Therefore it is defined using its modulus $\left|\tilde{A}_g\right|$ (transformed to a logarithmic scale $K_g = 20\log_{10}\left|\tilde{A}_g\right|$) and the argument $arg\left(\tilde{A}_g\right)$ wrapped to 2π rad.

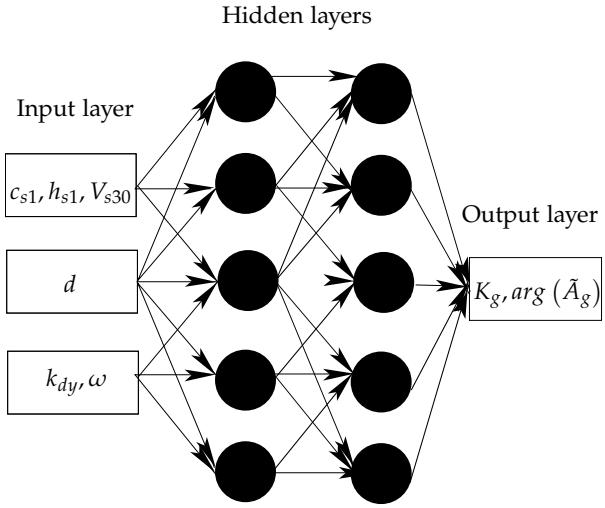

Figure 2.3: Neural network model schematic.

The aim of the NN procedure is to map the weighted inputs (e.g. distance) to outputs (i.e. vibration). First, weighted inputs are assumed and the resulting predicted outputs are compared against the known output targets to quantify the error. This error is fed back through the network using a back-propagation training algorithm. The input weightings are then modified and the process is repeated until convergence.

The NN approach is developed using the `Matlab Neural Network Toolbox` [57]. A tangent hyperbolic function is used as the activation function in the hidden layer due to its faster convergence compared to nonsymmetric functions [84]. The NN architecture is trained using the Levenberg-Marqurdt algorithm that has been shown to be one of the faster methods for training NN [58]. Also, to evaluate the performance of the NN model and select the best framework, mean squared error (MSE) and determination coefficient (R^2) are used [60, 63, 86].

Next expressions are used to build the output targets:

$$\arg\left(\tilde{A}_g\right) = \arg\left(\tilde{\mathbf{u}}^r_{\mathrm{ff}}\right) - \arg\left(\tilde{\mathbf{u}}_{\mathrm{g}}\right) \tag{5}$$

$$K_g = 20\log_{10}\left(\frac{\left|\tilde{\mathbf{u}}^r_{\mathrm{ff}}\right|}{\left|\tilde{\mathbf{u}}_{\mathrm{g}}\right|}\right) \tag{6}$$

where $\tilde{\mathbf{u}}^r_{\mathrm{ff}}$ is the track-soil transfer function computed by using a comprehensive 2.5D BEM-FEM model [31, 52] (super-index r) and $\tilde{\mathbf{u}}_{\mathrm{g}}$ the Green's functions.

A large number of data output targets are used to train and evaluate the NN. Ballasted and slab tracks located on top of an embankment are considered (Figure 2.2). The material properties of the embankment are chosen equal to those of the top layer of the soil.

A description of the NN database construction and performance is given in **Paper B**.

2.1.3 *Free-field response*

Once the track-soil transfer function $\tilde{\mathbf{u}}_{\mathrm{ff}}$ (Equation (4)), dynamic $\mathbf{g}_d$ (Equation (3)), and quasi-static $\mathbf{g}_q$ (Equation (2)) excitations are obtained, soil response $\mathbf{u}_{\mathrm{s}}(\mathbf{x},\omega)$ due a train passage at speed v is determined by following the 2.5D formulation in the frequency-wavenumber domain described in Reference [52]. The free-field response $\mathbf{u}_{\mathrm{s}}(\mathbf{x},\omega)$ is decomposed into its quasi-static $\mathbf{u}_{\mathrm{qs}}$ and dynamic $\mathbf{u}_{\mathrm{ds}}$ components as $\mathbf{u}_{\mathrm{s}}(\mathbf{x},\omega) = \mathbf{u}_{\mathrm{qs}}(\mathbf{x},\omega) + \mathbf{u}_{\mathrm{ds}}(\mathbf{x},\omega)$. The quasi-static u_{qsi} and dynamic u_{dsi} contributions in the i-th direction at a point $\mathbf{x}$ is evaluated as:

$$u_{\mathrm{qsi}}(\mathbf{x},\omega) = \sum_{k=1}^{n_a} w_k \tilde{h}_{\mathrm{ffi}}(y - y_k, \omega, 0) \tag{7}$$

$$u_{\mathrm{dsi}}(\mathbf{x},\omega) = \frac{1}{2\pi}\sum_{k=1}^{n_a}\int_{-\infty}^{+\infty} \tilde{h}_{\mathrm{ffi}}(y - y_k, \omega, \tilde{\omega}) g_{\mathrm{d}_k}(\tilde{\omega})\mathrm{d}\tilde{\omega} \tag{8}$$

where n_a is the number of axles and w_k, y_k and g_{d_k} referred to weight, position and dynamic load of the k-th axle, respectively. A change of variables $\tilde{\omega} = \omega - k_y v$ is considered, and the relation used to express Equations (7) and (8) in compact forms is:

$$\tilde{h}_{\text{ffi}}(y - y_k, \omega, \tilde{\omega}) = \frac{1}{v}\tilde{u}_{\text{ffi}}(\mathbf{x}, \frac{\omega - \tilde{\omega}}{v}, \omega) \exp\left[-i\frac{\omega - \tilde{\omega}}{v}(y - y_k)\right] \tag{9}$$

2.2 IMMISSION PROBLEM

Next, the building foundation is excited by a ground motion that corresponds with the free-field response $\mathbf{u}_s$ calculated previously (Equations (7) and (8)).

The dynamic equilibrium equation of a structure subjected to support excitation can be written as:

$$\mathbf{M}\ddot{\mathbf{u}}_t(t) + \mathbf{C}\dot{\mathbf{u}}_t(t) + \mathbf{K}\mathbf{u}_t(t) = \mathbf{F} \tag{10}$$

where $\mathbf{M}$, $\mathbf{C}$ and $\mathbf{K}$ are the mass, damping and stiffness matrices, respectively. $\mathbf{u}_t(t)$, $\dot{\mathbf{u}}_t(t)$ and $\ddot{\mathbf{u}}_t(t)$ are the building displacement, velocity and acceleration, respectively, while $\mathbf{F}$ represents the external force.

Two simplified 3D FEM methods are proposed to solve Equation (10). The first method based on modal superposition analysis is described in **Paper A**, whereas the second method in **Paper C** proposes soil-structure transfer functions to solve the immission problem. In spite of better computational efficiency, the modal superposition approach does not allow to obtain the time domain history of the building response. On the other hand, although this Thesis is focused on the assessment of building vibrations by railway traffic, both methods can be used to predict building vibration due to diverse sources (e.g. construction, earthquake, road traffic, blast) where the free-field vibration is known. These methods are described below.

Both methods consider the soil-structure interaction by adding spring-damper elements to the foundation of the building model. In this Thesis, two procedures are used to calculate spring-damper elements for slab foundations. The correlations proposed by Auersch [4] are followed in **Paper A** and **Book Chapter**, whereas the recommendation from the NIST [61] is used in **Paper C**. Several tests are performed comparing both procedures.

2.2.1 *Soil-structure transfer functions*

ISO 14837-1 standard [36] defines the magnitude of building vibration $A(\omega)$ in the frequency domain as a function of the source $S(\omega)$, the propagation $P(\omega)$ and the receiver $R(\omega)$. In this Thesis, it is assumed that all the three terms are uncoupled (Figure 2.4), and the magnitude of the building vibration $A(\omega)$ can be expressed as:

$$A(\omega) = S(\omega)P(\omega)R(\omega) \tag{11}$$

The procedure developed by the FRA [24] to estimate building response due to railway

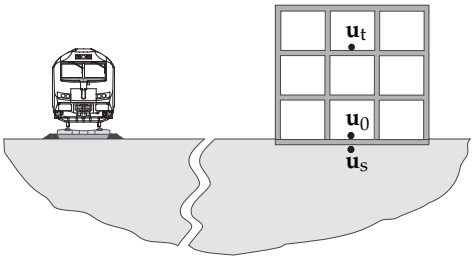

Figure 2.4: Scheme of decoupled model.

traffic proposes two factors influencing the receiver: 1) the floor-to-floor attenuation, and, 2) the amplification due to the resonance of floors, walls, and ceilings. This Thesis includes these factors defining the floor amplification F_a as the increment in the building response $\mathbf{u}_t$ with respect to the foundation response $\mathbf{u}_0$ (Figure 2.4). The floor amplification is computed as:

$$F_a(\omega) = \mathbf{u}_t(\omega)/\mathbf{u}_0(\omega) \tag{12}$$

Also, the effect of the building foundation should be considered using the coupling loss C_l [24]. The coupling loss is related to the soil-foundation interaction. Therefore it is the ratio between the building foundation response $\mathbf{u}_0$ and the free-field vibration $\mathbf{u}_s$. In this Thesis, the coupling is evaluated as:

$$C_l(\omega) = \mathbf{u}_0(\omega)/\mathbf{u}_s(\omega) \tag{13}$$

The following expression to calculate the building response $\mathbf{u}_t$ can be obtained by combining Equations (12) and (13):

$$\mathbf{u}_t(\omega) = F_a(\omega)C_l(\omega)\mathbf{u}_s(\omega) \tag{14}$$

Comparing Equations (11) and (14), it can be seen that the source $S(\omega)$ and the propagation $P(\omega)$ terms are included in the free-field vibration $\mathbf{u}_s$, whereas the receiver term $R(\omega)$ is obtained from the floor amplification F_a and the coupling loss C_l.

The novelty of this Thesis to predict building vibration by railway traffic is applying the soil-structure transfer functions $\mathbf{u}_t/\mathbf{u}_s = F_a(\omega)\ C_l(\omega)$ depending only on the receiver. The soil-structure transfer function represents the building response due to a displacement impulse $\breve{\mathbf{u}}_s = \delta(t)$ applied at the building foundation, where δ is the Dirac delta function. Therefore, the displacement impulse in the frequency domain represents a constant value.

The impulse building response function is calculated in the time domain. The FEM Equation (10) is solved at each time step following an implicit time integration GN22 Newmark method [62, 88]. Structural damping is considered following a Rayleigh model [9], where the damping matrix $\mathbf{C}$ is proportional to the mass $\mathbf{M}$ and stiffness $\mathbf{K}$ matrices as $\mathbf{C} = d_m\mathbf{M} + d_k\mathbf{K}$. Constants d_m and d_k are chosen depending on the modal damping of the structure. Later, the frequency response $\mathbf{u}_t(\omega)/\mathbf{u}_s(\omega)$ is evaluated from a Fourier transform of time domain responses. Finally, the soil-structure transfer function is combined with an arbitrary soil excitation to assess the building response.

The key advantage of this approach is the computational efficiency arising because of the soil-structure transfer function $\mathbf{u}_t/\mathbf{u}_s$ is computed only once for a soil-building subsystem and later it is combined with a wide range of free-field vibration data $\mathbf{u}_s$ to analyse multiple scenarios.

2.2.2 *Modal superposition*

The dynamic analysis of the building due to railway traffic is computed from the 3D FEM methodology presented in **Paper A**. This methodology is based on a modal superposition analysis [9], to assess an overall value of the response and the contribution of the modes to this response. However, the time domain history of the building response cannot be obtained from the proposed model. Below, this methodology is briefly summarised.

The total building response $\mathbf{u}_t$ (Figure 2.1, step 2.4) is defined as the superposition of the ground motion $\mathbf{u}_s$ and structure deformation $\mathbf{u}_b$:

$$\mathbf{u}_t(t) = \mathbf{u}_b(t) + \mathbf{r}\mathbf{u}_s(t) \tag{15}$$

where $\mathbf{u}_s$ is the free-field response in the time domain and the influence matrix $\mathbf{r}$ defines the incident wave on the structure. The structure deformation $\mathbf{u}_b$ is obtained by modal superposition as:

$$\mathbf{u}_b(t) = \sum_{i=1}^{N}\sum_{j=1}^{3} \boldsymbol{\phi}_i \Gamma_i^j \xi_i^j(t) \tag{16}$$

where $\boldsymbol{\phi}_i$ is the i-th mode shape, N the number of modes, and Γ_i^j and ξ_i^j the modal participation factor and the amplitude for the i-th mode at direction j, respectively.

The vibration level of the structure is evaluated using the overall RMS value of the acceleration [34]:

$$a_{RMS} = \sqrt{\frac{1}{T}\int_0^T \ddot{\mathbf{u}}_t^2(t)dt} \tag{17}$$

where T is the characteristic period defined by the DIN 45672 standard [13] in which the structural response is assumed to be stationary. Substituting the building response (Equation (15)) and the structure deformation (Equation (16)) in Equation (17), and considering

some assumptions in the methodology [56], leads to the next simplified expression to estimate the overall RMS:

$$a_{RMS} = \sqrt{H_s + H'_b} \tag{18}$$

where $\sqrt{H_s}$ and $\sqrt{H'_b}$ are related to the contributions to the RMS value of the ground motion and the structural response respectively. H_s is calculated as:

$$H_s = \frac{1}{M^2} \sum_{n=1}^{M} \sum_{j=1}^{3} r^{j^2} \left| \ddot{U}_s^j(f_n) \right|^2 \tag{19}$$

where $M = \frac{T}{\Delta t}$, $\ddot{U}_s^j(f_n)$ is the Discrete Fourier transform of $\ddot{u}_s^j(t_n)$, t_n is the time sampling and f_n is the frequency sampling. On the other hand, H'_b is computed from superposition of the modes as $H'_b = \sum_{i=1}^{N} H'_{bi}$, where the participation H'_{bi} of the i-th mode is evaluated by:

$$H'_{bi} = \boldsymbol{\phi}_i^2 \sum_{j=1}^{3} \left(\Gamma_i^j \Lambda_i^j \right)^2 \tag{20}$$

where Λ_i^j is the ground-borne response spectra defined for the natural frequency f_i at direction j. The ground-borne response spectra Λ_i^j is obtained as:

$$\Lambda_i^j = \frac{1}{M} \sqrt{\sum_{n=1}^{M} \left| \ddot{\Xi}_i^j(f_n) \right|^2} \tag{21}$$

where $\ddot{\Xi}_i^j(f_n)$ represents the Discrete Fourier transform of the amplitude $\ddot{\xi}_i^j(t_n)$ computed by solving the Duhamel's integral as [9]:

$$\ddot{\xi}_i^j(t) = \frac{1}{f_{di}} \int_0^t -\ddot{u}_s^j(\tau)\, e^{-2\pi\zeta_i f_i (t-\tau)} \sin\left(2\pi f_{di}\,(t-\tau)\right) d\tau \tag{22}$$

where ζ_i is the damping ratio and $f_{di} = f_i\sqrt{1-\zeta_i^2}$ the damped natural frequency.

The contribution of the i-th mode to the overall RMS value of the acceleration is estimated from Equations (18) and (20) as:

$$C_i = \sqrt{H'_{bi}} \tag{23}$$

2.3 METHODOLOGY SUMMARY

Finally, Table 2.1 summarises the main steps to compute track vibration generation and its propagation into buildings (Figure 2.1):

Table 2.1: Scoping model implementation.

1. Compute rail displacement $\tilde{u}_r(k_y, \omega)$ (step 2.1) using 2.5D FEM method (Equation (1))
2. Compute dynamic $\mathbf{g}_d(\omega)$ and quasi-static $\mathbf{g}_q(\omega)$ train excitations (step 2.1) using Equations (3) and (2).
3. Estimate correction factor $\tilde{A}_g(d, k_y, \omega)$ via NN (step 2.2.1).
4. Evaluate soil Green's function $\tilde{\mathbf{u}}_g(\mathbf{x}, k_y, \omega)$ (step 2.2.2).
5. Compute track-soil transfer function $\tilde{\mathbf{u}}_{ff}(\mathbf{x}, k_y, \omega)$ (step 2.2) using Equation (4).
6. Compute soil response due to a train passage $\mathbf{u}_s(\mathbf{x}, \omega)$ (Equations (7) and (8)) (step 2.3).
7. Compute the spring-damper system supporting the building foundation [4, 61] and assemble it with the building model (matrices **M**, **C** and **K**) (step 2.4).
8. Solve the immission problem of waves in building (step 2.4):
   a) Modal superposition analysis (Equations (18) and (23)).
   b) Compute soil-structure transfer function $\mathbf{u}_t/\mathbf{u}_s = F_a(\omega)C_l(\omega)$ (Equation (10)) and combine with the free-field vibration $\mathbf{u}_s(\mathbf{x}, \omega)$ (Equation (14)).

3

OVERALL RESULTS

This section presents a summary of the results obtained in this Thesis. This includes the validation of uncoupled proposed methodology to evaluate free-field and building response by railway traffic. Also, a brief analysis of the effects of soil properties and local track defects on vibration levels are shown.

3.1 FREE-FIELD RESPONSE

This section shows results about the experimental and numerical validation of the proposed model to assess free-field vibration. A detailed description of this validation can be found in **Paper B**.

Experimental data are taken from Reference [52], that describes the field test undertaken on the HST line between Brussels and Köln. The report presents rail and sleeper receptances, the free-field mobility and the free-field vibrations generated during the passage of Thalys HST at a speed of $v = 294\,\mathrm{km/h}$. A ballasted track supported by a layered subgrade was studied. A detailed description of the field work campaign is given in [52].

Figure 3.1 shows a comparison between rail receptances, free-field mobility and free-field response due to a train passage calculated using the scoping model and those measured experimentally. The results presented in reference [52] are also presented. It is seen from the results that the scoping model slightly overestimates experimental rail receptance up to 27 Hz (Figure 3.1. (a)). On the other hand, the prediction from the scoping model is under the experimental response at mid and high frequencies. The agreement with the experimental result is less good than in those presented in reference [52], however, this is expected due to the underlying simplifications and is considered acceptable for a scoping prediction (Figure 3.1. (a)). The free-field mobility (Figure 3.1. (b)) is overestimated, but the agreement is good and the computed results exhibit a similar frequency content as in the experimental data. Differences between the scoping model and Reference [52] are because of the NN approach was trained for a ballasted track over an embankment, while the HST line between Brussels and Köln is an at-grade track. The effect of the embankment is significant at the locations closer to the track [31, 64]. Regarding the free-field response due to a Thalys HST passage at $v = 294$ km/h (Figure 3.1. (c)), the frequency content is concentrated at frequencies below 100 Hz, for both the scoping model and experimental results. In general, the computed response from the scoping model underestimates the experimental results. The discrepancies between both results computed using the scoping model and presented in [52] are in accordance with those observed in free-field mobilities (Figure 3.1. (b)).

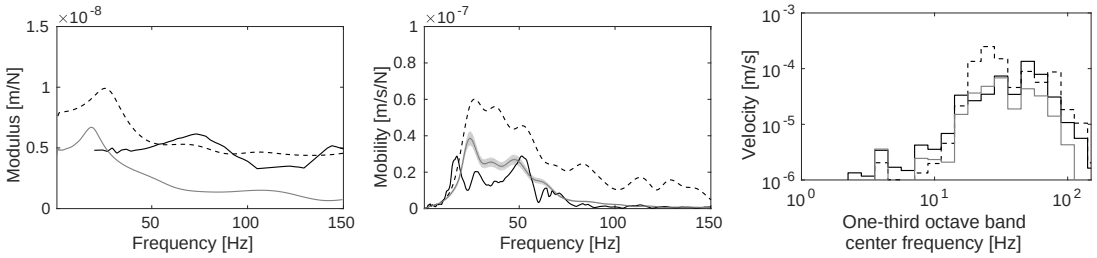

Figure 3.1: (Black line) the experimental and (grey line) computed with the scoping model (a) rail receptance, (b) free-field vertical mobility and (c) one-third octave band center frequency of the vertical velocity at the free field at a distance of 16 m from the track centreline. The effect on mobility predictions of a $\pm 10\%$ variation in $|\tilde{A}_g|$-values is represented by the grey area. Superimposed (dashed black line) the solution presented in reference [52]. **Paper B**.

A numerical validation is developed to further validate the scoping model, where its predictions are compared against a more comprehensive model. The reference model is based upon a 2.5D BEM-FEM methodology in the frequency-wavenumber domain [31, 52]. A variety of scenarios are analysed. The passages of a Renfe S-100 train travelling at speeds $\{100,\ 150\,,200\}$ km/h is simulated. Also, it is considered three track cases (ballasted track over an embankment, an at-grade ballasted track and a slab track over an embankment), four soil types and distances $d = \{20, 30, 40, 50\}$ m from the track axis.

In an attempt to make a global comparison, Figure 3.2 shows for all the studied cases the discrepancy between the scoping and the reference model results. The error is estimated as $\Delta v = 20\log_{10}\left(v^P/v^R\right)$, where v^P and v^R are the response from the scoping and the reference model, respectively. Regarding the ballasted tracks, the at-grade and embankment results are combined and shown with superimposed envelope curves (Figure 3.2. (a)). The prediction is better in the mid frequency range for the ballasted and slab tracks than at low and high frequencies.

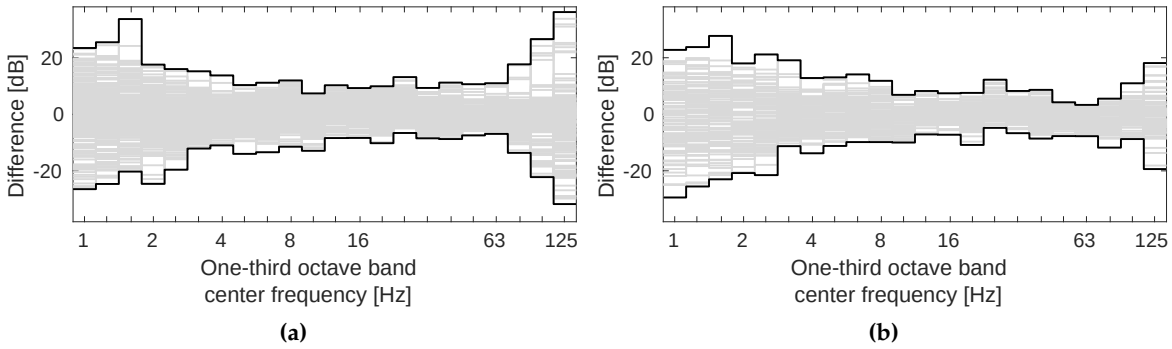

Figure 3.2: (Grey lines) one-third octave band center frequency of the differences Δv for all the cases of the (a) ballasted and (b) slab tracks. (Black lines) superimposed is the envelope of the highest discrepancies. **Paper B**.

The global uncertainty of the scoping model is determined using the Maximum Transient Vibration Value (MTVV) vibration metric [34]. Figure 3.3 represents the response for all the studied cases. A good agreement is observed with differences mainly found between -4.8 dB to 5.6 dB. Therefore the accuracy is similar to that found in previous research. These include Connolly et al. [20], who determined a mean error of ± 4.5 dB using a scoping model, with a largest error of 13.75 dB. Jones et al. [39] studied the uncertainty of considering different assumptions in underground railways (e.g. ignoring the presence of pile foundations, assuming the soil is a homogeneous half-space etc.). These simplifications can result in an uncertainty range between 5 dB to 20 dB. Also, Lombaert et al. [53] found differences of up to 10 dB in the free-field response for different realizations of track unevenness. Therefore the method proposed in this Thesis allows the scoping prediction with a similar accuracy found in previous researches using more comprehensive models.

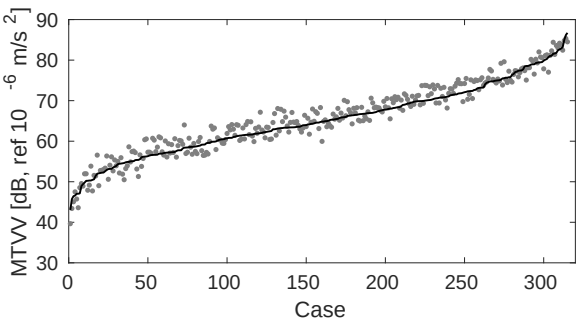

Figure 3.3: MTVV in the free-field due to a Renfe S-100 train passage at 20 m for all the cases, computed by (black line) the reference model and (grey points) the scoping model. **Paper B**.

3.2 BUILDING RESPONSE

The procedures proposed in Section 2.2 to solve the building immission problem, are numerically validated by comparison of the results with those obtained by the `SSIFiBo` toolbox [29]. This method is based on a comprehensive 3D time domain BEM-FEM methodology. The validation of the modal superposition approach described in **Paper A** considers four, eight and twelve storeys buildings. Moreover, the simplified method based on soil-structure transfer functions is validated using four, six and twelve storeys buildings (**Paper C**).

3.2.1 *Modal superposition*

A comparison between the proposed model and the `SSIFiBo` toolbox is developed in **Paper A** for multiple scenarios, where three homogeneous soils, three buildings, three train speeds and six distances from the track centreline are considered.

Figure 3.4 shows the response for the four, eight and twelve storey buildings obtained from the SSIFiBo toolbox. Superimposed is the contribution to the overall RMS value of the frequencies computed from the proposed model (Equation (23)). The agreement between both models is quite good at the dominant frequencies of the building response.

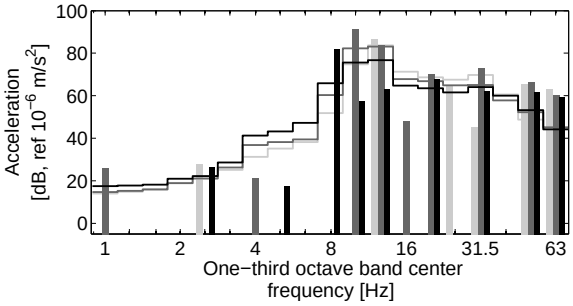

Figure 3.4: One-third octave band centre frequency content of the vertical relative acceleration due to a train passage at $v = 150\,\text{km/h}$ computed by the SSIFiBo toolbox (lines) and contribution of the modes to the overall RMS value of the vertical acceleration obtained from the scoping model (bars) at the top floor of the four-storey building (light grey color), eight-storey building (dark grey color) and twelve-storey building (black color). **Paper A**.

The overall RMS value of the acceleration for all the cases is computed using both models (scoping and SSIFiBo) to assess the accuracy of the proposed methodology. The difference is calculated as $\Delta a_{RMS}[\text{dB}] = 20\log\left(a^P_{RMS}/a^S_{RMS}\right)$, where a^P_{RMS} and a^S_{RMS} are the responses computed by the proposed model and the SSIFiBo toolbox, respectively. Figure 3.5 presented all the cases evaluated. The confidence region $[a^S_{RMS} + \mu \pm 2\sigma]$ and the expected value $a^S_{RMS} + \mu$ are superimposed, where μ and σ are the mean value and the standard deviation of the differences Δa_{RMS}. It is found that 96.45% of the results are within this confidence region, and overall the scoping model gives conservative predictions. The uncertainty of the predictions from the scoping model is within a range between $-3\,\text{dB}$ to $11\,\text{dB}$, and thus similar to the $5\,\text{dB}$ - $20\,\text{dB}$ values previously described [20, 39, 53].

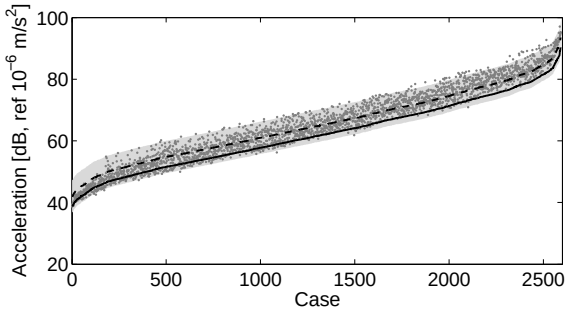

Figure 3.5: Overall RMS of the building for the 162 problems evaluated at the observation points A and B computed by the scoping model (grey points) and from the SSIFiBo toolbox (black line). Superimposed are the confidence region (grey area) and the expected value (black dashed line). **Paper A**.

3.2.2 *Soil-structure transfer function*

Next, the simplified method is numerically validated by analysing the buildings excited due to an incident wave field consisting of a uniform vertical displacement. The buildings are on a homogeneous soil with S-wave propagation velocity $c_s = 100\,\mathrm{m/s}$. The detailed description of this validation is given in **Paper C**.

In order to assess the accuracy of the simplified method predictions u^s, Figure 3.6 shows the differences $D^s = 20\log 10\,(u^s/u^r)$ with respect to the `SSIFiBo` toolbox u^r. Also, differences $\hat{D} = 20\log 10\,(\hat{u}/u^r)$ from solution ignoring SSI $\hat{u}$ are presented. It is seen that the agreement of the simplified method is reasonably good, whereas, as expected, the response ignoring SSI overestimates the results.

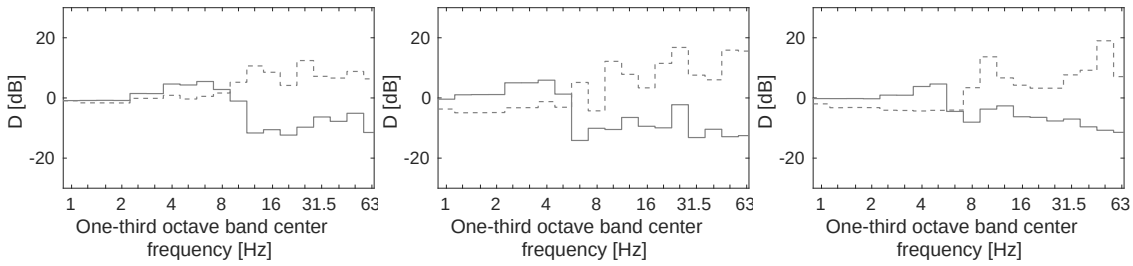

Figure 3.6: One-third octave band center frequency of the differences at the observation point A of the (a) four-storey, (b) six-storey and (c) twelve-storey buildings, at the top floor, from the (solid grey line) simplified methodology D^s and the (dashed grey line) solution ignoring SSI $\hat{D}$. **Paper C**.

These discrepancies in terms of MTVV [34] are shown in Figure 3.7 depending on the storey level. The amplification of the solution ignoring SSI is again observed. In spite of these discrepancies, the simplified method gives an acceptable prediction. Again, the accuracy is similar to the uncertainty range (5 dB to 20 dB) described above [20, 39, 53].

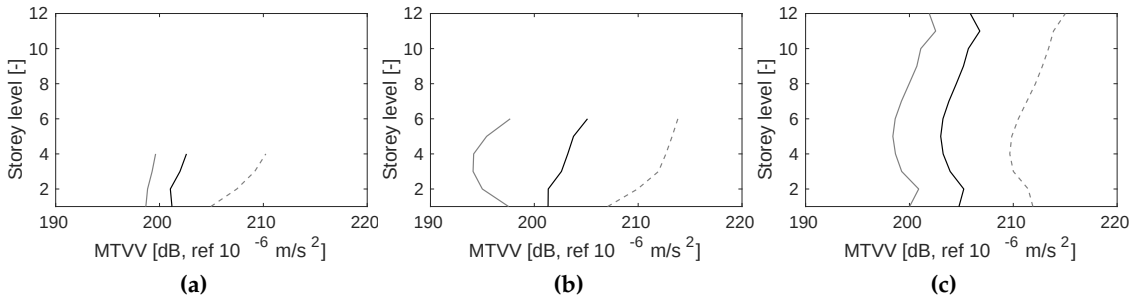

Figure 3.7: MTVV due to an incident wave field evaluated at the observation point A of the (a) four-storey, (b) six-storey and (c) twelve-storey buildings computed from the (black line) `SSIFiBo` toolbox and the (solid grey line) simplified method. Superimposed is the response (dashed grey line) ignoring SSI. **Paper C**.

3.3 ANALYSIS

Next, it is studied the effect of soil properties on the free-field and building vibrations by railway traffic using the scoping model (**Book Chapter**). Three homogeneous soils: soft, medium and stiff soils [23], are selected. Moreover, this analysis includes the influence of several track defect types on the building response (**Paper C**), because of the negative effects caused by railway traffic are more prominent in presence of local defects [45]. A twelve-storey building is considered.

3.3.1 *Soil properties*

Figure 3.8 shows the influence of soil stiffness on the rail receptance and the free-field mobility. The response decreases with increasing soil stiffness. Furthermore, the response is smoother and the dominant frequency increases as soil stiffness too. This is because of differences between the stiffness of the embankment and the ballast are lower for medium and stiff soils compared to the soft soil.

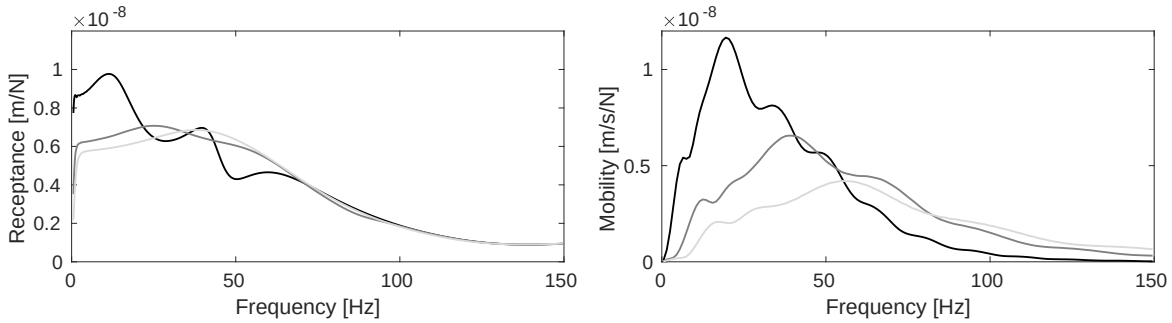

Figure 3.8: (a) The displacement of the rail and (b) free-field vertical mobility at 20 m from the ballasted for (black line) soft, (dark grey line) medium and (light grey line) stiff soils. **Book Chapter**.

The effect of soil stiffness in the ground-borne response spectra (Equation (21)) and building vibrations due to the train passage is presented in Figure 3.9. According to the previous results (Figure 3.8), the frequency content of the ground-borne response spectra (Figure 3.9. (a)) shows that dominant frequencies due to the dynamic excitation vary from 10 to 50 Hz for the soft soil, to 20 and 60 Hz for the medium and stiff soils. Building response is mainly distributed in frequencies from 8 Hz to 80 Hz. According to the differences in the ground-borne response spectra (Figure 3.9. (a)), building response is higher for the soft soil (Figure 3.9. (b,c)). A detailed description of the analysis is presented in the **Book Chapter**, that also includes the effect of track, building type, and train speed on building vibration.

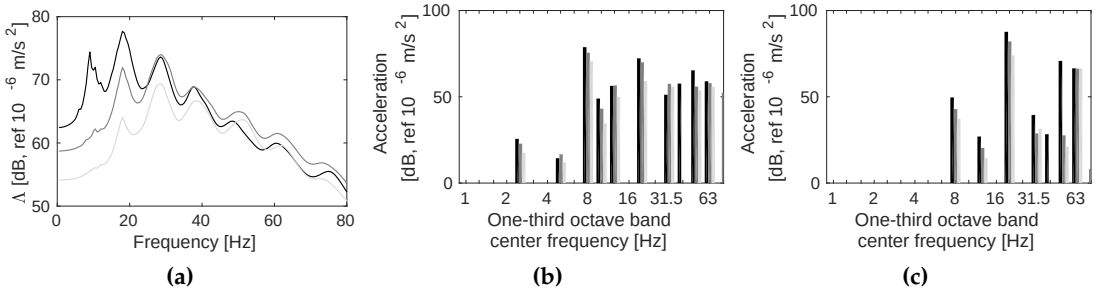

Figure 3.9: (a) Ground-borne response spectra $\Lambda_i^j(f_i)$ and (b and c) contribution of the modes to the overall RMS value of the vertical weighted acceleration at the top floor of the observation points (b) A and (c) B, due to a Renfe S-100 train passage at $v = 100\,\mathrm{km/h}$ at 20 m from the ballasted track for (black line) soft, (dark grey line) medium and (light grey line) stiff soils. **Book Chapter**.

3.3.2 *Local defects*

In this section, the influence of several defect types (Figure 3.10) on building vibrations is analysed for both the AM96 train and classic tram, on a homogeneous soil with $c_s = 100\,\mathrm{m/s}$. Free-field response is obtained using the methodology validated in Reference [21]. This study is completed in **Paper C** with the influence of defect size on building response.

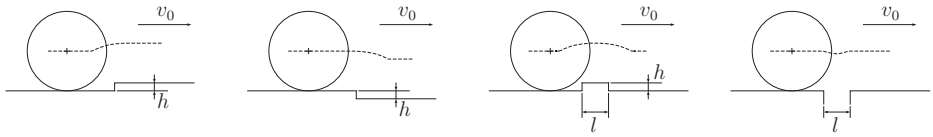

Figure 3.10: Local defect shape (from left to right: step up, step down, positive pulse and negative pulse). **Paper C**.

Figure 3.11 presents the building response due to both the AM96 passage over a ballasted track and the classic tram passage over a slab track. For the AM96 passage (Figure 3.11. (a)), it can be observed the step up joint induces higher vibrations at low frequencies, whereas the maximum values at mid and high frequencies are due to the positive pulse. Also, the running RMS values do not show a clear dependency on the defect type because the response due to the AM96 passage has similar amplitudes (Figure 3.11. (b)). Regarding the building vibrations induced by the classic tram passage, it is seen the frequency responses show a similar tendency for all defect types (Figure 3.11. (d)). However, it is more clearly shown in running RMS curves (Figure 3.11. (d)) that the highest responses are found for the positive pulse and the step up joint.

It can be concluded that the defect type influences the amplitude of the response more dominantly than the shape. Moreover, it is clear the correlation between defect type and building response. On the other hand, the differences between ballasted (Figure 3.11. (a,b))

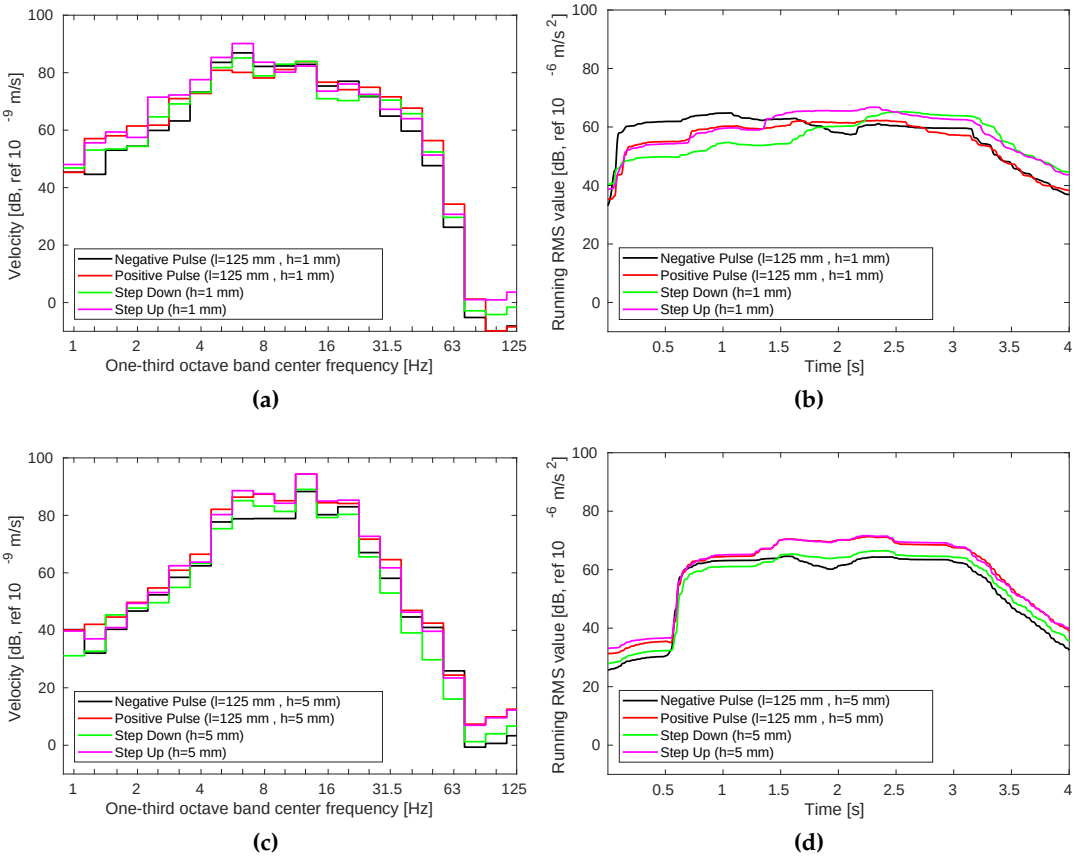

Figure 3.11: (a,c) One-third octave band center frequency of the z vertical velocity and (b,d) running RMS value of the weighted acceleration at the top floor of the twelve-storey building for several defect types due to a (a,b) AM96 train passage at $v_0 = 120\,\mathrm{km/h}$ and (c,d) a tram passage at $v_0 = 40\,\mathrm{km/h}$. **Paper C**.

and slab tracks (Figure 3.11. (c,d)) results show that the track type is an important parameter to model during vibration assessment.

4

CONCLUSIONS AND FUTURE DEVELOPMENTS

The previous sections of this Thesis consists of an extended summary of the research proposed. A more detailed description of the works carried out is given the appended publications.

4.1 CONCLUSIONS

In this Thesis, a simplified methodology to compute the propagation of railway vibrations into nearby buildings was presented. The model is novel because it was able to simulate the generation, propagation and immission of vibrations, for a complex vehicle, track, soil and building arrangements in a reduced time.

To do so, the source-propagation of wave energy through the ground has been decoupled from the immission of waves within buildings. Then, a simplified 2.5D FEM track model, a hybrid direct stiffness-neural network procedure (**Paper B**) and two sub-models to obtain building response have been combined to create an overall model describing the vehicle-track-soil-building problem (**Book Chapter**). A building-soil sub-model based on a modal superposition analysis was proposed (**Paper A**). This was designed to be conservative in nature, to ensure that it was able to identify any high risk vibration sites during scoping tests, thus avoiding the application of any safety factor (e.g. 10 dB is commonly added in practise). On the other hand, a more accurate SSI sub-model was also presented (**Paper C**), that allows obtaining the time history of the building response. This sub-model combined the soil-structure transfer functions with an arbitrary excitation to evaluate building vibrations.

A combination of experimental and numerical data was used to validate the vehicle-track-soil approach. Track receptance, free-field mobility and soil vibration due to train passage were analysed and the new model was found to have strong prediction capability (**Paper B**). Both soil-building sub-models were numerically verified against a detailed prediction model based on a 3D BEM-FEM formulation. The agreement was good and any discrepancies were mainly due to the assumed simplifications.

A sensitivity analysis was undertaken using the proposed model. Track type, soil stiffness, building height, train speed, track defect type and defect size effects were studied, and it was found that there was a strong relationship between vibration levels and these parameters.

Moreover, comparisons have been made to determine the accuracy of using a global database of V_{s30} soil properties to predict vibration levels (**Book Chapter**). Track receptance, free-field mobility, soil vibration, dominant building modes and overall building response

due to railway traffic have been analysed and it has been found that this simplification was only satisfactory for cases with smooth layer profile.

An important advantage of the proposed model compared to a comprehensive model is its computational efficiency. The comprehensive model selected for the comparison consists on the 2.5D BEM-FEM methodology in Reference [31] used to calculate the free-field response, and the 3D BEM-FEM `SSIFiBo` toolbox [29] used to evaluate building vibrations. The Table 4.1 shows the computational costs to obtain the response of the twelve storey building due to a Renfe S-100 train travelling at $v = 100\,\text{km/h}$ using an `Intel One Core i7@1.87 GHz` computer. The CPU time referred to the source-propagation problem in the soil and the immission problem in the building. Taking into account the scheme of the scoping model (Figures 2.1), Table 4.1 outlines the main calculation steps and their run times. Note that the time required to obtain free-field predictions (step 2.3) is not presented because both scoping and comprehensive models were the same. It should be noted that:

- The simplified track model (Figure 2.2) allows the scoping model to reduce the computations of the prediction of train-track excitation $\mathbf{g}$ (step 2.1). The comprehensive model uses a BEM-FEM methodology to calculate the train-track excitation, thus requiring additional computations.

- The time required to calculate the track-soil transfer function $\tilde{\mathbf{u}}_{\text{ff}}$ (step 2.2) using the scoping model was primarily due to the evaluation of the soil Green's function (step 2.2.2). The correction factor $\tilde{A}_g$ was estimated through a NN approach (step 2.2.1) and required a minimal computational cost. The combination of these two steps results in a run time that was much lower than that for the comprehensive model.

- The largest boost in computation efficiency comes from the prediction of the building response. Regarding the comprehensive model, it should be noted that the cost required to compute the soil BEM domain under the building foundation was not included. Also, the soil-structure transfer function was computed only once for a soil-building subsystem. Later, it was combined with a wide range of free-field vibration data to analyse multiple scenarios, requiring identical time that the modal superposition sub-model.

The difference in run times is mainly due to the BEM-FEM methodology used in the analysis of track-soil and soil-structure interaction. Alternatively, the time required for the scoping model to solve the whole vibration analysis is much lower than the necessary for the comprehensive model.

Considering these much reduced computational requirements, the range of uncertainty and the versatility of the proposed model, it is concluded that the scoping model acts as a powerful `MATLAB` toolbox that allows users to evaluate free-field and building vibrations due to train passage at the early design stage.

Table 4.1: Average running time.

Step	Comprehensive model	Scoping model	
		Modal superposition	Soil-structure transfer function
Train-track forces	25 min	38 s	
Track-soil transfer function	15 min	5 min	
Building response	7.5 h	12 s	19 min

4.2 FUTURE DEVELOPMENTS

In this Thesis, a highly effective tool to predict soil and building vibrations induced by railway traffic for an early stage of development for a new railway line, was presented. However, new challenges and researches might be developed. In this section some of these researches are briefly related:

- It would be interesting to analyse the additional parameters of the track model (Figure 2.2) in order to improve the vehicle-track-soil sub-model by adding these parameters as inputs to the NN approach. This allows extending the range of ballasted and slab tracks to study. A sensitivity analysis of these parameters would allow understanding the effect on the proposed model predictions. Later, the parameters with more influence would be selected as new inputs of the NN approach.

- The number of underground railway lines in modern urban cities and towns is growing rapidly. Therefore, it would be very useful to include a tunnel section model in the vehicle-track-soil sub-model. The tunnel section would be implemented following the proposed methodology presented in **Paper B**, developing a 2.5D FEM model of the track and training a NN to obtain the correction factor $\tilde{A}_g$ for the tunnel section.

- When a train wheel impacts a local irregularity, the dynamic wheel/rail interaction force is dominant in the generation of ground vibration [21, 45]. It would be worthwhile to improve the vehicle-track-soil sub-model by considering local track defects. These research would be built upon the methodology proposed in Reference [21].

- In this Thesis, it is studied the simplification to consider V_{s30} values for computing building vibrations in layered soils, and it was concluded that this assumption only gives good predictions for smooth profiles. Then, it would be advisable to develop a procedure to consider SSI in layered soils with better building vibration estimations. In **Paper C**, it is concluded that the properties of the uppermost layer have a dominant response in ground vibrations by railway. Then, it would be interesting to test if the averaged layer properties over the top 10 m of soil (V_{s10}) gives better results.

- It would be quite useful to improve the soil-building sub-model by adding several types of foundations (e.g. building with basement, deep foundations etc.). The re-

comendations of the NIST to consider SSI in buildings with a basement or supported by deep foundations, would be implemented in the proposed model.

- Building vibrations by railway traffic generate indoor noise, causing disturbance and annoyance in human. That annoyance is related to the level and frequency spectrum of the re-radiated noise level [38]. Then, it would be advisable to develop a simplified toolbox to evaluate the magnitude and the shape of the re-radiated noise. It would be a challenge to implement the 2.5D methodology presented by Romero et al. [67, 68] in the proposed model, considering some assumptions.

4.3 COLOPHON

This document is presented as a compendium of four publications to obtain the PhD degree for the Universidad de Sevilla. This procedure is according to Article 9, Agreement 9.1/CG12/04/19, that fixed the requirement of this manuscript. The previous sections of this Thesis consisted of an extended summary of the proposed research. A comprehensive description of this work is given in the appended publications.

BIBLIOGRAPHY

[1] L. Auersch. The excitation of ground vibration by rail traffic: theory of vehicle–track–soil interaction and measurements on high-speed lines. *Journal of Sound and Vibration*, 284:103–132, 2005. doi: https://doi.org/10.1016/j.jsv.2004.06.017.

[2] L. Auersch. Dynamic stiffness of foundations on inhomogeneous soils for a realistic prediction of vertical building resonance. *Journal of Geotechnical and Geoenvironmental Engineering*, 134(3):328–340, 2008. doi: http://dx.doi.org/10.1061/(ASCE)1090-0241(2008)134:3(328).

[3] L. Auersch. Wave propagation in the elastic half-space due to an interior load and its application to ground vibration problems and buildings on pile foundations. *Soil Dynamics and Earthquake Engineering*, 30:925–936, 2010. doi: https://doi.org/10.1016/j.soildyn.2010.04.003.

[4] L. Auersch. Building Response due to Ground Vibration–Simple Prediction Model Based on Experience with Detailed Models and Measurements. *International Journal of Acoustics and Vibration*, 15(3):101–112, 2010. doi: http://dx.doi.org/10.20855/ijav.2010.15.3262.

[5] L. Auersch, A. Romero, and P. Galvín. Respuesta dinámica de edificaciones producida por campos de onda incidentes considerando la interacción suelo-estructura. *Revista Internacional de Métodos Numéricos para Cálculo y Diseño en Ingeniería*, 30(4):256–263, 2014. doi: https://doi.org/10.1016/j.rimni.2013.09.001.

[6] D. Cantero, T. Arvidsson, E. OBrien, and R. Karoumi. Train–track–bridge modelling and review of parameters. *Structure and Infrastructure Engineering*, 12(9):1051 – 1064, 2016. doi: http://dx.doi.org/10.1080/15732479.2015.1076854.

[7] C.E. Hanson, D.A. Towers, and L.D. Meister. High-speed ground Transportation Noise and Vibration Impact Assessment, HMMH Report 293630-4. *U.S. Department of Transportation, Federal Railroad Administration, Office of Railroad Development*, 2005.

[8] C.E. Hanson, D.A. Towers, and L.D. Meister. Transit Noise and Vibration Impact Assessment, Report FTA-VA-90-1003-06. *U.S. Department of Transportation, Federal Transit Administration, Office of Planning and Environment*, 2006.

[9] R.W. Clough and J. Penzien. *Dynamic of Structures*. McGraw-Hill, New York, 1975.

[10] D.P. Connolly, G.P. Marecki, G. Kouroussis, I. Thalassinakis, and P.K. Woodward. The growth of railway ground vibration problems – A review. *Science of the Total Environment*, 568:1276–1282, 2015. doi: http://dx.doi.org/10.1016/j.scitotenv.2015.09.101.

[11] P. Coulier, G. Lombaert, and G. Degrande. The influence of source-receiver interaction on the numerical prediction of railway induced vibrations. *Journal of Sound and Vibration*, 333:2520–2538, 2014. doi: https://doi.org/10.1016/j.jsv.2014.01.017.

[12] D. E. Rumelhart and J. L. McClelland. *Parallel distributed processing: Explorations in the microstructure of cognition. Vol 1*. MIT Press, Cambridge, MA, 1986.

[13] *DIN 45672 Teil 2: Schwingungsmessungen in der Umgebung von Schienenverkehrswegen: Auswerteverfahren*. Deutsches Institut für Normung, 1995.

[14] *DIN 4150-2: Structural vibrations - Part 2: Human exposure to vibration inbuildings*. Deutsches Institut für Normung, 1999.

[15] *DIN 4150-3: Structural vibrations - Part 3: Effects of vibration on structures*. Deutsches Institut für Normung, 1999.

[16] A. Doménech, M.D. Martínez-Rodrigo, A. Romero, and P. Galvín. On the basic phenomenon of soil-structure interaction on the free vibration response of beams: Application to railway bridges. *Engineering Structures*, 125:254 – 265, 2016. ISSN 0141-0296. doi: http://dx.doi.org/10.1016/j.engstruct.2016.06.052.

[17] J. Domínguez. *Boundary elements in dynamics*. Computational Mechanics Publications and Elsevir Aplied Science, Southampton, 1993.

[18] D.P. Connolly, G. Kouroussis, A. Giannopoulos, O. Verlinden, P.K. Woodward, and M.C. Forde. Assesment of railway vibrations using an efficient scoping model. *Soil Dynamics and Earthquake Engineering*, 58:37–47, 2014. doi: https://doi.org/10.1016/j.soildyn.2013.12.003.

[19] D.P. Connolly, G. Kouroussis, P.K. Woodward, A. Giannopoulos, O. Verlinden, and M.C. Forde. Scoping prediction of re-radiated ground-borne noise and vibration near high speed rails lines with variable soils. *Soil Dynamics and Earthquake Engineering*, 66: 78–88, 2014. doi: https://doi.org/10.1016/j.soildyn.2014.06.021.

[20] D.P. Connolly, P. Alves Costa, G. Kouroussis, P. Galvín, P.K. Woodward, and O. Laghrouche. Large scale international testing of railway ground vibrations across Europe. *Soil Dynamics and Earthquake Engineering*, 71:1–12, 2015. doi: https://doi.org/10.1016/j.soildyn.2015.01.001.

[21] D.P. Connolly, P. Galvín, B. Olivier, A. Romero, and G. Kouroussis. A 2.5D time-frequency domain model for railway induced soil-building vibration due to railway defects. *Soil Dynamics and Earthquake Engineering*, 120:332 – 344, 2019. ISSN 0267-7261. doi: https://doi.org/10.1016/j.soildyn.2019.01.030.

[22] A.C. Eringen and E.S. Suhubi. *Elastodynamics, Volume 2, Linear theory*. Academic Press, New York, USA, 1975.

[23] *Eurocode 8: Design of structures for earthquake resistance–Part 1 : General rules, seismic actions and rules for buildings*. European Committee for Standardization, 1998.

[24] Federal Railroad Administration. *High-Speed Ground Transportation Noise and Vibration Impact Assessment*. U.S. Department of Transportation, 2012.

[25] P. Fiala, G. Degrande, and F. Augusztinovicz. Numerical modelling of ground-borne noise and vibration in buildings due to surface rail traffic. *Journal of Sound and Vibration*, 301:718–738, 2007. doi: https://doi.org/10.1016/j.jsv.2006.10.019.

[26] S. François, L. Pyl, H.R. Masoumi, and G. Degrande. The influence of dynamic soil-structure interaction on traffic induced vibrations in buildings. *Soil Dynamics and Earthquake Engineering*, 27:655–674, 2007. doi: https://doi.org/10.1016/j.soildyn.2006.11.008.

[27] S. François, M. Schevenels, P. Galvín, G. Lombaert, and G. Degrande. A 2.5d coupled fe–be methodology for the dynamic interaction between longitudinally invariant structures and a layered halfspace. *Computer Methods in Applied Mechanics and Engineering*, 199(23):1536 – 1548, 2010. ISSN 0045-7825. doi: https://doi.org/10.1016/j.cma.2010.01.001.

[28] P. Galvín and J. Domínguez. High-speed train-induced ground motion and interaction with structures. *Journal of Sound and Vibration*, 307:755–777, 2007. doi: https://doi.org/10.1016/j.jsv.2007.07.017.

[29] P. Galvín and A. Romero. A MATLAB toolbox for soil-structure interaction analysis with finite and boundary elements. *Soil Dynamics and Earthquake Engineering*, 57:10–14, 2014. doi: https://doi.org/10.1016/j.soildyn.2013.10.009.

[30] P. Galvín, A. Romero, and J. Domínguez. Fully three-dimensional analysis of high-speed train–track–soil–structure dynamic interaction. *Journal of Sound and Vibration*, 329:5147–5163, 2010. doi: https://doi.org/10.1016/j.jsv.2010.06.016.

[31] P. Galvín, S. François, M. Schevenels, E. Bongini, G. Degrande, and G. Lombaert. A 2.5d coupled fe-be model for the prediction of railway induced vibrations. *Soil Dynamics and Earthquake Engineering*, 30(12):1500 – 1512, 2010. ISSN 0267-7261. doi: https://doi.org/10.1016/j.soildyn.2010.07.001.

[32] P. Galvín, D. López-Mendoza, D.P. Connolly, G. Degrande, G. Lombaert, and A. Romero. Scoping assessment of free-field vibrations due to railway traffic. *Soil Dynamics and Earthquake Engineering*, 114:598–614, 2018. doi: https://doi.org/10.1016/j.soildyn.2018.07.046.

[33] M. Hussein, H. Hunt, K. Kuo, P. Alves Costa, and J. Barbosa. The use of sub-modelling technique to calculate vibration in buildings from underground railways. *Proceedings of the Institution of Mechanical Engineers, Part F: Journal of Rail and Rapid Transit*, 229(3):303 – 314, 2013. doi: https://doi.org/10.1177/0954409713511449.

[34] *ISO 2631-1:2003: Mechanical vibration and shock–Evaluation of human exposure to whole-body vibration–Part 1: General requirements*. International Organization for Standardization, 2003.

[35] *ISO 2631-2:2003: Mechanical vibration and shock–Evaluation of human exposure to whole-body vibration–Part 2: Vibration in buildings (1–80 Hz)*. International Organization for Standardization, 2003.

[36] *ISO 14837-1:2005 Mechanical vibration–Ground-borne noise and vibration arising from rail systems–Part 1: General guidance*. International Organization for Standardization, 2005.

[37] *ISO 8041-1:2017: Human response to vibration – Measuring instrumentation – Part 1: General purpose vibration meters*. International Organization for Standardization, 2017.

[38] J. G. Walker and M. F. K. Chan. Human response to structurally radiated noise due to underground railway operations. *Journal of Sound and Vibration*, 193(1):49 – 63, 1996. doi: https://doi.org/10.1006/jsvi.1996.0245.

[39] S. Jones, K. Kuo, M.F.M. Hussein, and H.E.M Hunt. Prediction uncertainties and inaccuracies resulting from common assumptions in modelling vibration from underground railways. *Proceedings of the Institution of Mechanical Engineers, Part F: Journal of Rail and Rapid Transit*, 226:501–512, 2012. doi: https://doi.org/10.1177/0954409712441744.

[40] J.T. Nelson and H.J. Sauernman. A prediction procedure for rail transportation groundborne noise and vibration. *Transportation Research Record: Journal of the Transportation Research Board*, 1143:26–35, 1987.

[41] E. Kausel. *Fundamental solutions in elastodynamics: a compendium*. Cambridge University Press, 2006.

[42] E. Kausel. Early history of soil-structute interaction. *Soil Dynamics and Earthquake Engineering*, 30:822–8328, 2010. doi: https://doi.org/10.1016/j.soildyn.2009.11.001.

[43] E. Kausel and J. M. Roësset. Stiffness matrices for layered soils. *Bulletin of the Seismological Society of America*, 71(6):1743, 1981.

[44] G. Kouroussis, L. Van Parys, C. Conti, and O. Verlinden. Prediction of ground vibrations induced by urban railway traffic: An analysis of the coupling assumptions between vehicle, track, soil, and buildings. *The International Journal of Acoustics and Vibration*, 18(4):163 – 172, 2013. ISSN 1027-5851. doi: https://doi.org/10.20855/ijav.2013.18.4330.

[45] G. Kouroussis, J. Florentin, and O. Verlinden. Ground vibrations induced by intercity/interregion trains: a numerical prediction based on the multibody/finite element modeling approach. *Journal of Vibration and Control*, 22:4192 – 4210, 2016. doi: https://doi.org/10.1177/1077546315573914.

[46] G. Kouroussis, K.E. Vogiatzis, and D.P. Connolly. A combined numerical/experimental prediction method for urban railway vibration. *Soil Dynamics and Earthquake Engineering*, 97:377 – 386, 2017. ISSN 0267-7261. doi: http://dx.doi.org/10.1016/j.soildyn.2017.03.030.

[47] G. Kouroussis, K.E. Vogiatzis, and D.P. Connolly. Assessment of railway ground vibration in urban area using in-situ transfer mobilities and simulated vehicle-track interaction. *International Journal of Rail Transportation*, 6:113 – 130, 2018. ISSN 2324-8378. doi: https://doi.org/10.1080/23248378.2017.1399093.

[48] G. Kouroussis, S. Zhu, B. Olivier, and D. Ainalis W. Zhai. Urban railway ground vibrations induced by localized defects: using dynamic vibration absorbers as a mitigation solution. *Journal of Zhejiang University-SCIENCE A*, 20(2):83 – 97, 2019. doi: https://doi.org/10.1631/jzus.A1800651.

[49] K.A. Kuo, H. Verbraken, G. Degrande, and G. Lombaert. Hybrid predictions of railway induced ground vibration using a combination of experimental measurements and numerical modelling. *Journal of Sound and Vibration*, 373:263–284, 2016. ISSN 0022-460X. doi: https://doi.org/10.1016/j.jsv.2016.03.007.

[50] K.A. Kuo, M. Papadopoulos, G. Lombaert, and G. Degrande. The coupling loss of a building subject to railway induced vibrations: Numerical modelling and experimental measurements. *Journal of Sound and Vibration*, 442:459–481, 2019. ISSN 0022-460X. doi: https://doi.org/10.1016/j.jsv.2018.10.048.

[51] G. Lombaert and G. Degrande. Ground-borne vibration due to static and dynamic axle loads of intercity and high-speed trains. *Journal of Sound and Vibration*, 319(3–5): 1036–1066, 2009. ISSN 0022-460X. doi: http://dx.doi.org/10.1016/j.jsv.2008.07.003.

[52] G. Lombaert, G. Degrande, J. Kogut, and S. François. The experimental validation of a numerical model for the prediction of railway induced vibrations. *Journal of Sound and Vibration*, 297(3):512 – 535, 2006. ISSN 0022-460X. doi: https://doi.org/10.1016/j.jsv.2006.03.048.

[53] G. Lombaert, P. Galvín, S. François, and G. Degrande. Quantification of uncertainty in the prediction of railway induced ground vibration due to the use of statistical track unevenness data. *Journal of Sound and Vibration*, 333(18):4232 – 4253, 2014. ISSN 0022-460X. doi: https://doi.org/10.1016/j.jsv.2014.04.052.

[54] P. Lopes, P. Alves Costa, M. Ferraz, R. Calçada, and A. Silva Cardoso. Numerical modeling of vibrations induced by railway traffic in tunnels: From the source to the nearby buildings. *Soil Dynamics and Earthquake Engineering*, 61–62:269–285, 2014. doi: https://doi.org/10.1016/j.soildyn.2014.02.013.

[55] P. Lopes, J. Fernández Ruiz, P. Alves Costa, L. Medina Rodríguez, and A. Silva Cardoso. Vibrations inside buildings due to subway railway traffic. experimental validation of a comprehensive prediction model. *Science of the Total Environment*, 568:1333–1343, 2016. doi: http://dx.doi.org/10.1016/j.scitotenv.2015.11.016.

[56] D. López-Mendoza, A. Romero, D.P. Connolly, and P. Galvín. Scoping assessment of building vibration induced by railway traffic. *Soil Dynamics and Earthquake Engineering*, 93:147–161, 2017. ISSN 0267-7261. doi: http://dx.doi.org/10.1016/j.soildyn.2016.12.008.

[57] M. H. Beale, M. T. Hagan, and H. B. Demuth. *Neural network toolbox User's guide*. Mathworks, Inc, 2017.

[58] M. T. Hagan and M. B. Menhaj. Training feedforward networks with the marquardt algorithm. *EEE Transactions on Neural Networks*, 5(6):989–993, 1994. doi: https://doi.org/10.1109/72.329697.

[59] C. Madshus, B. Bessason, and L. Harvik. Prediction model for low frequency vibration from high speed railways on soft ground. *Journal of Sound and Vibration*, 193(1):195–203, 1996. doi: https://doi.org/10.1006/jsvi.1996.0259.

[60] M. Monjezi, M. Ahmadi, M. Sheikhan, A. Bahrami, and A. R. Salimi. Predicting blast-induced ground vibration using various types of neural networks. *Soil Dynamics and Earthquake Engineering*, 30:1233–1236, 2010. doi: https://doi.org/10.1016/j.soildyn.2010.05.005.

[61] *NIST GCR 12-917-21 Soil-Structure Interaction for Building Structures*. National Institute of Standards and Technology U.S. Department of Commerce, 2012.

[62] N.M. Newmark. A method of computation for structural dynamics. *ASCE Journal of the Engineering Mechanics Division*, 85:67–94, 1959.

[63] V. Nourani and M. S. Fard. Sensitivity analysis of the artificial neural network outputs in simulation of the evaporation process at different climatologic regimes. *Advances in Engineering Software*, 47:127–146, 2012. doi: https://doi.org/10.1016/j.advengsoft.2011.12.014.

[64] B. Olivier, D.P. Connolly, P.Alves Costa, and G. Kouroussis. The effect of embankment on high speed rail ground vibrations. *International Journal of Rail Transportation*, 4(4):229–246, 2016. doi: 10.1080/23248378.2016.1220844.

[65] P. Alves Costa, R. Calçada, and A. Silva Cardoso. Track–ground vibrations induced by railway traffic: In-situ measurements and validation of a 2.5D FEM-BEM model. *Soil Dynamics and Earthquake Engineering*, 32:111–128, 2012. doi: https://doi.org/10.1016/j.soildyn.2011.09.002.

[66] A. Romero, M. Solís, J. Domínguez, and P. Galvín. Soil–structure interaction in resonant railway bridges. *Soil Dynamics and Earthquake Engineering*, 47:108 – 116, 2013. ISSN 0267-7261. doi: http://dx.doi.org/10.1016/j.soildyn.2012.07.014. SI: José Manuel Roësset.

[67] A. Romero, A. Tadeu, P. Galvín, and J. António. 2.5D coupled BEM–FEM used to model fluid and solid scattering wave. *International Journal for Numerical Methods in Engineering*, 101:148–164, 2015. doi: https://doi.org/10.1002/nme.4801.

[68] A. Romero, P. Galvín, J. António, J. Domínguez, and A. Tadeu. Modelling of acoustic and elastic wave propagation from underground structures using a 2.5d bem-fem approach. *Engineering Analysis with Boundary Elements*, 76:26 – 39, 2017. ISSN 0955-7997. doi: http://dx.doi.org/10.1016/j.enganabound.2016.12.008.

[69] F. Rossi and A. Nicolini. A simple model to predict train-induced vibration: theoretical formulation and experimental validation. *Enviornmental Impact Assesment Review*, 23: 305–322, 2003. doi: https://doi.org/10.1016/S0195-9255(03)00005-2.

[70] W. Rücker and L. Auersch. A user-friendly prediction tool for railway induced ground vibrations: Emission - transmission - immission. *Notes on Numerical Fluid Mechanics and Multidisciplinary Design*, 99:129–135, 2008. doi: https://dx.doi.org/10.1007/978-3-540-74893-9_18.

[71] S.B. Mezher, D.P. Connolly, P.K. Woodward, O. Laghrouche, J. Pombo, and P. Alves Costa. Railway critical velocity – analytical prediction and analysis. *Transportation Geotechnics*, 6:84 – 96, 2016. doi: https://doi.org/10.1016/j.trgeo.2015.09.002.

[72] Mattias Schevenels, Stijn François, and Geert Degrande. Edt: An elastodynamics toolbox for MATLAB. *Computers & Geosciences*, 35(8):1752 – 1754, 2009. ISSN 0098-3004. doi: http://dx.doi.org/10.1016/j.cageo.2008.10.012.

[73] X. Sheng, C.J.C. Jones, and D.J. Thompson. Prediction of ground vibration from trains using the wavenumber finite and boundary element methods. *Journal of Sound and Vibration*, 293:575–586, 2006. doi: https://doi.org/10.1016/j.jsv.2005.08.040.

[74] A. Tadeu and J. António. 2.5D Green's functions for elastodynamic problems in layered acoustic and elastic formations. *CMES-Comput Model Eng Sci*, 2(4):477–495, 2001.

[75] A. Triepaischajonsak and D.J. Thompson. A hybrid modelling approach for predicting ground vibration from trains. *Journal of Sound and Vibration*, 335:147 – 173, 2015. ISSN 0022-460X. doi: http://dx.doi.org/10.1016/j.jsv.2014.09.029.

[76] H. Verbraken, G. Lombaert, and G. Degrande. Verification of an empirical prediction method for railway induced vibrations by means of numerical simulations. *Journal of Sound and Vibration*, 330(8):1692–1703, 2011. doi: https://doi.org/10.1016/j.jsv.2010.10.026.

[77] K. Vogiatzis and H. Mouzakis. Ground-borne noise and vibration transmitted from subway networks to multi-storey reinforced concrete buildings. *Transport*, 33(2):446 – 453, 2018. doi: https://doi:10.3846/16484142.2017.1347895.

[78] K. Vogiatzis, H. Mouzakis, and V. Zafiropoulou. Assessing subway network ground borne noise and vibration using transfer function from tunnel wall to soil surface measured by muck train operation. *Science of the Total Environment*, 650:2888 – 2896, 2019. doi: https://doi:10.3846/16484142.2017.1347895.

[79] G.P. Wilson. *Noise and Vibration Characteristics of High Speed Transit Vehicles*. Office of Noise Abatement and Control, Environmental Protection Agency, Washington D.C., 1971.

[80] G.P. Wilson. *Ground-Borne Vibration Levels from Rock and Earth Based Subways.* DeLeuw, Cather and Company, Washington D.C., 1971.

[81] C. With, M. Bahrekazemi, and A. Bodare. Validation of an empirical model for prediction of train-induced ground vibrations. *Soil Dynamics and Earthquake Engineering*, 26: 983–990, 2006. doi: https://doi.org/10.1016/j.soildyn.2006.03.005.

[82] J.P. Wolf. *Dynamic soil-structure interaction*. Prentice-Hall, Englewood Cliffs, New Jersey, 1985.

[83] H. Xia, Y.M. Cao, and G. De Roeck. Theoretical modeling and characteristic analysis of moving-train induced ground vibrations. *Journal of Sound and Vibration*, 329:819–832, 2010. doi: https://doi.org/10.1016/j.jsv.2009.10.007.

[84] Y. L. Cun, I. Kanter, and S. A. Solla. Second order properties of error surfaces: Learning time and generalization. *Advances in Neural Information Processing Systems*, 3:918–924, 1991.

[85] Y.M. Cao and H. Xia. Analysis of green's functions in wavenumber–frequency domain for surface displacements of elastic layered half-space soil. *Journal of Computer Mechanics*, 25(6):833–838, 2008.

[86] M. Yurdakul and H. Akdas. Modeling uniaxial compressive strength of building stones using non-destructive test results as neural networks input parameters. *Construction and Building Materials*, 47:1010–1019, 2013. doi: https://doi.org/10.1016/j.conbuildmat.2013.05.109.

[87] S. Zhu, J. Wang, C. Cai, K. Wang, W. Zhai, J. Yang, and H. Yan. Development of a vibration attenuation track at low frequencies for urban rail transit. *Computer-Aided Civil and Infrastructure Engineering*, 32:713 – 726, 2017. doi: https://doi.org/10.1111/mice.12285.

[88] O.C. Zienkiewicz. *The finite element method*. McGraw-Hill, third edition, 1986.

APPENDED PUBLICATIONS

A

PAPER A: SCOPING ASSESSMENT OF BUILDING VIBRATION INDUCED BY RAILWAY TRAFFIC

The original version of this paper can be found in **www.elsevier.com**

- DOI: 10.1016/j.soildyn.2016.12.008
- Journal Name: Soil Dynamics and Earthquake Engineering
- ISSN: 0267-7261
- Journal Citation Reports (2017). Impact Factor: 2.077
  - Engineering, Geological: Q2 (17/36)
  - Geosciences, Multidisciplinary: Q2 (87/190)
- SCIMAGO (2017). Impact Factor: 1.08
  - Civil and Structural Engineering: Q1 (47/497)
  - Geotechnical Engineering and Engineering Geology: Q1 (30/367)

Scoping assessment of building vibration induced by railway traffic

Authors: Daniel López-Mendoza[a], Antonio Romero Ordóñez[a], David P. Connolly[b] and Pedro Galvín Barrera[a]

[a] Escuela Técnica Superior de Ingeniería, Universidad de Sevilla, Camino de los Descubrimientos, 41092 Sevilla, Spain
[b] Institute for Infrastructure and Environment, Heriot Watt University, Edinburgh, UK

ABSTRACT

This work presents a scoping model to predict ground-borne railway vibration levels within buildings considering Soil-Structure Interaction (SSI). It can predict the response of arbitrarily complex buildings in a fraction of the time typically required to analyse a complex SSI problem, and thus provides a practical tool to rapidly analyse the vibration response of numerous structures near railway lines. The tool is designed for use in cases where the ground-borne vibration is known, and thus can be used as model input. Therefore in practice, for the case of a new line, the ground motion can be computed numerically, or alternatively, for the case of new buildings to be constructed near an existing line, it can be recorded directly (e.g. using accelerometers) and used as model input. To achieve these large reductions in computational time, the model discretises the ground-borne vibration in the free field into a frequency range corresponding to the modes that characterize the dynamic building response. After the ground-borne response spectra that corresponds with the incident wave field is estimated, structural vibration levels are computed using modal superposition, thus avoiding intensive soil-structure interaction computations. The model is validated using a SSI problem and by comparing results against a more complex finite element-boundary element model. Finally, the new scoping model is then used to analyse the effect of soil properties, building height, train speed and distance between the building and the track on structural-borne vibration. The results show that the scoping model provides a powerful tool for use during the early design stages of a railway system when a large number of structures require analysis.

Keywords: Scoping assessment; Modal superposition; Railway traffic; High speed rail; Building vibrations; Ground-borne vibrations; Structural vibration; Railroad vibration; Environmental Impact Assesment (EIA).

A.1 INTRODUCTION

The expansion of High-Speed Rail (HSR) has been decisive for economic development across the world, however this growth has also led to an increase in those effected by ground-borne vibrations from railways [9]. The negative effects of this vibration are numerous and it is thus addressed in international standards. One of these standards is ISO2631 [24, 25], where indoor, whole-body human exposure to vibration is evaluated in the frequency range, 1 Hz to 80 Hz. The vibration evaluation is based on the Root-Mean-Square (RMS) value of the acceleration in the three orthogonal directions. Additionally, ISO14837 [26], a dedicated standard for the railway sector, is currently under development. This presents an overview of ground-borne vibration due to railway traffic, prediction techniques, experimental measurement, evaluation criteria and also mitigation.

It also discusses numerical modelling, including two-and-a-half-dimensional (2.5D) and three-dimensional (3D) models, which are referred to as detailed design models and can be used during the construction stage of new lines. 2.5D models are based on the assumption that the problem is homogeneous in the track direction, thus reducing the degrees of freedom. Several authors [1, 19, 22, 27, 31, 32, 36, 38, 40] have presented 2.5D methodologies to predict vibrations produced by railway traffic using Boundary Element Method (BEM)-Finite Element Method (FEM) coupled formulations. Three-dimensional models account for local soil discontinuities, underground constructions and structures that break the uniformity of the geometry along the track line [5, 20, 23, 34, 44], however, are more computationally expensive.

At the earlier stages of development for a new railway line, simpler and quicker methodologies are desirable. These models, called scoping models [26], allow engineers to asses long lengths of track in a reduced computational time, because typically, the train-track-soil interaction (source and propagation problem) is decoupled from soil-structure interaction (immission problem). Coulier et. al [10] studied the effect of assuming an uncoupled approach in a ballasted track and they concluded that it can be neglected for distances to the track longer than six times the Rayleigh wave length, thus validating this assumption.

Nelson and Sauernmann [29] presented a simple in-situ testing methodology based on impact-testing procedures to characterize soil vibrations and vehicle-track systems. Alternatively, Madshus et al. [35] developed a semi-empirical model from the statistical analysis of railway vibration measurements in Norway and Sweden. This model was used to study low frequency vibrations due to High Speed Trains HST on soft soils. Rossi and Nicolini [39] also presented an approach to predict train-induced vibration considering different train types, train speeds, track properties and distances to the track . The analytical expressions of the model were calibrated by experimental data. With et al. [43] proposed a scoping model to compute running RMS values of velocity based on the wheel force, the train speed and the distance to the track, while the Federal Railroad Administration (FRA) and the Federal Transit Administration (FTA) of the U.S. Department of Transportation have proposed empirical procedures to predict vibration levels due to railway traffic [6, 7]. Ver-

braken et al. [41] verified by means of a numerical method the assumptions introduced in these approaches. Later, Kuo et al. [30] developed two models using a combination of field measurements and numerical methods based on the use of separate source and propagation mechanism, and implemented them using the definitions proposed in references [6, 7]. Auersch [4] studied building induced vibrations using a simple soil-wall-floor model based on an empirical transfer fuction obtained from the characteristics of the structure. A soil modelled using a spring and a viscous damper was used to evaluate the effects of soil-structure interaction. François et al. [18] developed an analysis of building induced vibrations by employing simplified methods that discard SSI, but take into account the relative stiffness between the building and the soil. Recently, Conolly et al. [13, 14] presented a scoping tool, called Scoperail, to predict in-door noise in buildings and structural vibrations values due to high speed trains. A 3D FEM model was used to generate vibration records for a wide range of train speeds and soil types, and these results were combined with empirical factors in order to compute vibrations due to train passages.

The present paper builds upon these previous approaches and proposes a scoping methodology to evaluate building induced vibrations at the early development stage of railway lines using modal superposition and considering SSI. Free-field response due to train passages is the required model input data, and can be obtained from numerical models and experimental records, including conventional, freight and high speed trains. Therefore the model can be used to predict structural vibrations in the cases of both new and existing lines. The proposed method allows to assess the building response with a very low computational effort, and can be used in a general purpose FEM program. This paper is organized as follows. First, the scoping model is presented. Next, the proposed model is numerically validated comparing with a more comprehensive methodology. Finally, the effect of the soil properties, the building height, the train speed and the distance from the track to the building on the results from the scoping model is analysed.

A.2 NUMERICAL MODEL

This section describes the proposed scoping model. The dynamic analysis is carried out by modal superposition [8] of the structure subjected to support excitation, with the aim of computing the overall RMS value of the response due to an incident wavefield.

The dynamic equilibrium equation of a structure can be written as:

$$\mathbf{M}\ddot{\mathbf{u}}_t(t) + \mathbf{C}\dot{\mathbf{u}}_t(t) + \mathbf{K}\mathbf{u}_t(t) = \mathbf{F} \tag{1}$$

where $\mathbf{M}$, $\mathbf{C}$ and $\mathbf{K}$ are the mass, damping and stiffness matrices, respectively. $\mathbf{u}_t$, $\dot{\mathbf{u}}_t$, and $\ddot{\mathbf{u}}_t$ are the total displacements, velocities and accelerations, respectively, and $\mathbf{F}$ represents the external force. The total displacement can be decomposed as the sum of the ground motion $\mathbf{u}_g$ and that due to the structure deformation $\mathbf{u}$:

$$\mathbf{u}_t(t) = \mathbf{u}(t) + \mathbf{r}\mathbf{u}_g(t) \tag{2}$$

where the influence matrix $\mathbf{r}$ defines the wave incidence on the structure.

Substituting the Equation (2) into the Equation (1), and considering that the ground motion $\mathbf{u}_g$ does not produce either viscous force ($\mathbf{C}\dot{\mathbf{r}}\mathbf{u}_g = \mathbf{0}$) or elastic force ($\mathbf{K}\mathbf{r}\mathbf{u}_g = \mathbf{0}$), the following equation can be obtained:

$$\mathbf{M}\ddot{\mathbf{u}}(t) + \mathbf{C}\dot{\mathbf{u}}(t) + \mathbf{K}\mathbf{u}(t) = -\mathbf{M}\mathbf{r}\ddot{\mathbf{u}}_g(t) \tag{3}$$

The displacement vector $\mathbf{u}$ is obtained by modal superposition as:

$$\mathbf{u}(t) = \sum_{i=1}^{N}\sum_{j=1}^{3} \boldsymbol{\phi}_i q_i^j \tag{4}$$

where $\boldsymbol{\phi}_i$ is the i-th mode shape, q_i^j the i-th modal amplitude due to a ground motion at direction j and N is the number of modes considered to describe the structural response.

Then, Equation (3) can be rewritten for each direction j by the substitution of Equation (4) and pre-multipliying by the mode shape transpose vector $\boldsymbol{\phi}_j^T$:

$$\sum_{i=1}^{N}\left[\boldsymbol{\phi}_j^T\mathbf{M}\boldsymbol{\phi}_i\ddot{q}_i^j(t) + \boldsymbol{\phi}_j^T\mathbf{C}\boldsymbol{\phi}_i\dot{q}_i^j(t) + \boldsymbol{\phi}_j^T\mathbf{K}\boldsymbol{\phi}_i q_i^j(t)\right] = -\boldsymbol{\phi}_j^T\mathbf{M}\mathbf{r}\ddot{u}_g^j(t) \tag{5}$$

Equation (5) can be decomposed into a system of N uncoupled equations taking into account the mode shape orthogonality condition with respect to the stiffness and mass matrices. Also, it can be assumed that this condition can be applied to the damping matrix. Equation (5) then becomes:

$$\ddot{q}_i^j(t) + 4\pi\zeta_i f_i\dot{q}_i^j(t) + 4\pi^2 f_i^2 q_i^j(t) = -\Gamma_i^j\ddot{u}_g^j(t) \tag{6}$$

with

$$\Gamma_i^j = \frac{\boldsymbol{\phi}_i^T\mathbf{M}r^j}{\boldsymbol{\phi}_i^T\mathbf{M}\boldsymbol{\phi}_i} \tag{7}$$

where f_i is the natural frequency, ζ_i is the damping ratio, and Γ_i^j is the modal participation factor for the i-th mode at direction j.

The modal amplitude q_i^j can be written as:

$$q_i^j(t) = \Gamma_i^j\xi_i^j(t) \tag{8}$$

Introducing Equation (8) in Equation (6) yields:

$$\ddot{\xi}_i^j(t) + 4\pi\zeta_i f_i\dot{\xi}_i^j(t) + 4\pi^2 f_i^2\xi_i^j(t) = -\ddot{u}_g^j(t) \tag{9}$$

The solution of Equation (9) can be computed by means of the Duhamel's integral as [8]:

$$\xi_i^j(t) = \frac{1}{f_{di}}\int_0^t -\ddot{u}_g^j e^{-2\pi\zeta_i f_i(t-\tau)}\sin\left(f_{di}\left(t-\tau\right)\right)d\tau \tag{10}$$

where $f_{di} = f_i\sqrt{1-\zeta_i^2}$ is the damped natural frequency. Equation (10) is solved using the Generalized Single Solved (GSSSS) integration algorithm Uo-Vo developed by Zhou and Tamma [45]. This algorithm accurately calculates the low-frequency roots of Equation (10).

Once the modal amplitude is obtained, the structural response can be computed from Equations (2) and (4). Different international standards evaluate structural vibration level, such as standard ISO 2631 [24] which defines the overall RMS value of the frequency-weighted acceleration, or alternatively, the Vibration decibels (VdB) metric based on the running RMS value of the velocity [16]. Since the frequency weighting depends on the corresponding standard, it is not considered in the present work. Next, the procedure to asses the overall RMS value of the acceleration is developed. The VdB metric can also be estimated using a similar methodology.

The overall RMS value of the acceleration response is calculated as:

$$a_{RMS} = \sqrt{\frac{1}{T}\int_0^T \ddot{\mathbf{u}}_t^2(t)dt} \tag{11}$$

where T is the characteristic period defined by the DIN 45672-2 standard [12] where the structural response is assumed to be stationary. Then, the RMS value is obtained, accounting for the previously computed $\mathbf{u}_t(t)$ from Equations (2) and (4):

$$a_{RMS} = \sqrt{\frac{1}{T}\sum_{n=1}^{M}\left(\sum_{j=1}^{3}\left(r^j\ddot{u}_g^j(t_n) + \sum_{i=1}^{N}\boldsymbol{\phi}_i\Gamma_i^j\ddot{\xi}_i^j(t_n)\right)\right)^2\Delta t} \tag{12}$$

being $t = t_1, t_2, \ldots, t_n, \ldots, t_M$ with $\Delta t = t_n - t_{n-1}$.

After expanding, Equation (12) can be written as:

$$a_{RMS} = \sqrt{\frac{1}{T}\sum_{n=1}^{M}\left(\sum_{j=1}^{3}\left(r^j\ddot{u}_g^j(t_n)\right)^2 + \left(\sum_{i=1}^{N}\sum_{j=1}^{3}\left(\boldsymbol{\phi}_i\Gamma_i^j\ddot{\xi}_i^j(t_n)\right)\right)^2 + \sum_{i=1}^{N}\sum_{j=1}^{3}\sum_{k=1}^{3}\left(2r^k\boldsymbol{\phi}_i\Gamma_i^j\ddot{u}_g^k(t_n)\ddot{\xi}_i^j(t_n)\right)\right)\Delta t} \tag{13}$$

Bearing in mind $\frac{T}{\Delta t} = M$, Equation (13) is expressed in a compact form as:

$$a_{RMS} = \sqrt{H_g + H_b + H_{gb}} \tag{14}$$

with

$$H_g = \frac{1}{M}\sum_{n=1}^{M}\sum_{j=1}^{3}\left(r^j\ddot{u}_g^j(t_n)\right)^2 \tag{15}$$

$$H_b = \frac{1}{M}\sum_{n=1}^{M}\left(\sum_{i=1}^{N}\sum_{j=1}^{3}\left(\boldsymbol{\phi}_i\Gamma_i^j\ddot{\xi}_i^j(t_n)\right)\right)^2 \tag{16}$$

$$H_{gb} = \frac{1}{M}\sum_{n=1}^{M}\sum_{i=1}^{N}\sum_{j=1}^{3}\sum_{k=1}^{3}\left(2r^k\boldsymbol{\phi}_i\Gamma_i^j\ddot{u}_g^k(t_n)\ddot{\xi}_i^j(t_n)\right) \tag{17}$$

H_g, H_b and H_{gb} represent the contributions to the RMS value of the ground motion, the structural response and the coupling between both terms, respectively.

The generalization of Parseval's theorem for two time functions $f(t)$ and $g(t)$ whose Fourier transforms are $F(\omega)$ and $G(\omega)$ entails [11]:

$$\int_{-\infty}^{+\infty} f(t)g^*(t)dt = \frac{1}{2\pi}\int_{-\infty}^{+\infty} F(\omega)G^*(\omega)d\omega \tag{18}$$

where * means complex conjugate and ω is the angular frequency.

The application of the theorem for equally-spaced samples of two real functions $f(t_n)$ and $g(t_n)$ can be written as:

$$\sum_{n=1}^{M} f(t_n)g(t_n) = \frac{1}{M}\sum_{n=1}^{M}\left[\text{sgn}\{\Re(F(f_n)G^*(f_n))\}\,|F(f_n)G^*(f_n)|\right] \tag{19}$$

where $f_n = \frac{n}{M\Delta t}$.

The terms H_g, H_b and H_{gb} (Equations (15-17)) can be computed from Equation (19) as:

$$H_g = \frac{1}{M^2}\sum_{n=1}^{M}\sum_{j=1}^{3} r^{j^2}\left|\ddot{U}_g^j(f_n)\right|^2 \tag{20}$$

$$H_b = \frac{1}{M^2}\sum_{n=1}^{M}\left|\sum_{i=1}^{N}\sum_{j=1}^{3}\left(\boldsymbol{\phi}_i\Gamma_i^j\ddot{\Xi}_i^j(f_n)\right)\right|^2 \tag{21}$$

$$H_{gb} = \frac{1}{M^2}\sum_{n=1}^{M}\sum_{i=1}^{N}\sum_{j=1}^{3}\sum_{k=1}^{3}\left[2r^k\boldsymbol{\phi}_i\Gamma_i^j\,\text{sgn}\{\Re(\ddot{U}_g^k(f_n)\ddot{\Xi}_i^{j*}(f_n))\}\left|\ddot{U}_g^k(f_n)\ddot{\Xi}_i^{j*}(f_n)\right|\right] \tag{22}$$

where $\ddot{U}_g^j(f_n)$ and $\ddot{\Xi}_i^j(f_n)$ are the Discrete Fourier transforms of $\ddot{u}_g^j(t_n)$ and $\ddot{\xi}_i^j(t_n)$.

The present model uses some assumptions in the terms H_b and H_{gb} of the Equation (14) in order to developed a simple procedure that can be easily used in a general purpose FEM commercial program. The first simplification is that the cross product term H_{gb} is neglected. It is based on the assumption that the structural response $\ddot{\Xi}_i^j(f_n)$ amplifies the soil motion $\ddot{U}_g^k(f_n)$ and, therefore, the term $\ddot{U}_g^k(f_n)\ddot{\Xi}_i^{j*}(f_n)$ is much lower than $\ddot{\Xi}_i^{j^2}(f_n)$.

Moreover, the Equation (21) can be expanded as follows:

$$H_b = \frac{1}{M^2}\sum_{n=1}^{M}\left[\sum_{i=1}^{N}\sum_{j=1}^{3}\left(\boldsymbol{\phi}_i\Gamma_i^j\left|\ddot{\Xi}_i^j(f_n)\right|\right)^2 + \sum_{i=1}^{N}\prod_{\substack{j=1\\k=1\\j\neq k}}^{3}\boldsymbol{\phi}_i^2\Gamma_i^j\ddot{\Xi}_i^j(f_n)\Gamma_i^k\ddot{\Xi}_i^{k*}(f_n)\right.$$
$$\left. + \sum_{j=1}^{3}\sum_{k=1}^{3}\prod_{\substack{i=1\\l=1\\i\neq l}}^{N}\boldsymbol{\phi}_i\Gamma_i^j\ddot{\Xi}_i^j(f_n)\boldsymbol{\phi}_l\Gamma_l^k\ddot{\Xi}_l^{k*}(f_n)\right] \tag{23}$$

In the proposed methodology only the first term of Equation (23) is considered. This assumption is based on: i) the cross product $\Gamma_i^j\Gamma_i^k$ between the modal participation factor for the i-th mode at different directions j and k can be disregarded, and ii) since the functions $\ddot{\Xi}_i^j(f_n)$ and $\ddot{\Xi}_l^{k*}(f_n)$ are frequency responses of one-degree-of freedom systems, the cross product $\Xi_i^j(f_n)\Xi_l^{k*}(f_n)$ can be neglected if the modes are well separated and lightly damped. In the next section, the study of the uncertainties due to the simplifications carried out in the terms H_b and H_{gb} will be studied.

Then, the overall RMS value of the acceleration (Equation (14)) is given by:

$$a_{RMS} = \sqrt{H_g + H_b'} \tag{24}$$

being $H_b' = \sum_{i=1}^{N} H_{bi}'$, with $H_{bi}' = \boldsymbol{\phi}_i^2\sum_{j=1}^{3}\left(\Gamma_i^j\Lambda_i^j\right)^2$. In the previous expression:

$$\Lambda_i^j = \frac{1}{M}\sqrt{\sum_{n=1}^{M}\left|\ddot{\Xi}_i^j(f_n)\right|^2} \tag{25}$$

represents the ground-borne response spectra.

The spectra defined in Equation (25) allows for straightforward integration within commercial FEM software, by solving a Response Spectrum Analysis (RSA) [8], where the input is the ground-borne response spectra $\Lambda_i^j(f_i)$. The result of the RSA can be used to obtain the contribution to the response of the structural deformation H_b'. The contribution of the ground motion should be added according to Equation (24).

The contribution of the i-th mode to the overall RMS value of the acceleration can be estimated from Equation (24) as:

$$C_i = \sqrt{H_{bi}'} \tag{26}$$

In order to represent the structure's dynamic behaviour with accuracy, the proposed model calculates and combines the response for only those modes at frequencies (f_k) which meet the criterion:

$$\max\left(\frac{\Gamma_k^{j^2}}{\sum_{i=1}^{N}\Gamma_i^{j^2}}\right) \geq \varepsilon \qquad j = 1,2,3 \tag{27}$$

where ε is the required tolerance.

SSI is integrated into the proposed scoping model by adding spring k_f and damper c_f elements to the foundation of the building model. Alternative simplified solutions, depending on the type of foundation can be found in previous literature [2, 3, 4, 17]: isolated footing, continuous footing, isolated pile and pile group. In this work it was considered the following correlation for shallow foundations from the model presented by Auersch [4]: $k_f = 3.4G_s\sqrt{A_f}$ and $c_f = 1.6\sqrt{G_s\rho_s A_f}$, where G_s and ρ_s are the shear modulus and the mass density of the soil, respectively, and A_f is the foundation area.

A.3 NUMERICAL VERIFICATION

A.3.1 *Scoping model validation*

The proposed model was numerically validated by analysing the dynamic behaviour of a building due to an incident wavefield. To do so, the structural response as computed by the proposed scoping model was compared with that obtained by the `SSIFiBo` toolbox [21] based on a 3D time domain BEM-FEM methodology.

The structure was a three-storey building with dimensions 14.4 m × 10.8 m × 9 m (Figure A.1) [5]. It consisted of eight columns of width 0.3 m × 0.3 m, and a core wall with thickness of 0.15 m. The floors were modelled as slabs with a thickness of 0.2 m. The foundation was considered as a $h_f = 0.3$ m thick slab. All the structural elements consisted of concrete with a Young's modulus $E_c = 30 \times 10^9\,\mathrm{N/m^2}$, Poisson's ratio $\nu_c = 0.2$ and density $\rho_c = 2500\,\mathrm{kg/m^3}$. Structural damping of $\zeta = 0.02$ was used for all modes that contributed to the building response. In order to discretise the structure 180 two-node Euler-Bernoulli and 2118 four-node shell elements were used. The element size was small enough to adequately represent the structure dynamic behaviour below a maximum frequency of $f_{max} = 80$ Hz. The minimum wave length of the bending floor waves was given by $\lambda = \sqrt{2\pi}\left(\frac{D}{\rho_c h_f}\right)^{(1/4)}/f_{max} = 3.6\,m$, where $D = E_c h_f^3\left(1-\nu_c^2\right)/12$ was the bending stiffness of the floors. An element size of $l = 0.6$ m was used, resulting in 6 elements per wavelength.

The building was founded on a homogeneous soil with the following properties: P-wave velocity $c_p = 300\,\mathrm{m/s}$, S-wave velocity $c_s = 150\,\mathrm{m/s}$, material damping $\zeta_s = 0.06$ and density $\rho_s = 1750\,\mathrm{kg/m^3}$. Computations were solved using a time step $\Delta t = 0.002$ s

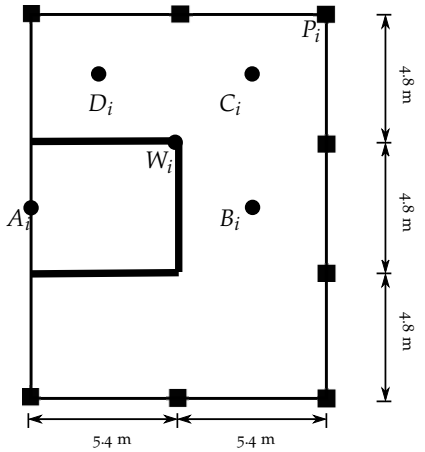

Figure A.1: Building plant geometry.

according to the stability criterion for the time domain formulation of the SSIFiBo toolbox [21]. The incident wave field corresponded with an uniform vertical displacement $\mathbf{u}_0 = \delta(t)$ m, where δ was the Dirac delta function.

In the case of the scoping model, the dynamic behaviour of the building was computed using the superposition of the dominant modes. A tolerance of $\varepsilon = 0.001$ was considered. Figure A.2 shows the bending mode shapes of the floors for the building on foundation springs at a frequency range between 0 Hz and 125 Hz.

Figure A.3 shows the one-third octave band spectra content of the vertical relative accelerations $\ddot{\mathbf{u}}(t)$ at the observation points located in every floor obtained using the SSIFiBo toolbox. Superimposed is the contribution to the overall RMS value of the vertical acceleration of the building modes, within a frequency band centred at Ω_j, computed from the proposed scoping model as:

$$C_j(\Omega_j) = \sum_i \sqrt{C_i^2(f_i)} \qquad \forall f_i \in [\Omega_{j0}, \Omega_{j1}] \tag{28}$$

where Ω_{j0} and Ω_{j1} are the limits of the one-third octave band Ω_j, and C_i is calculated from Equation (26).

The building response was evaluated at observation points A, B, C, D, P and W (Figure A.1) located at every storey of the building. This response was mainly distributed in the frequency range from 8 Hz to 125 Hz. The higher level of vibration was observed at the observation point A (Figure A.3. (a)) located at the part of the slabs supported on the core wall, where the bending stiffness of the floor was higher than in the remaining parts of the structure. The response at this point was found at frequencies of 30.40 Hz, 47.88 Hz and 94.92 Hz that correspond with those bending modes which present higher vertical displacements at the slabs bounded by the core wall (Figures A.2.(d,e,f)). Conversely, the response in the slabs at observation points B, C and D (Figures A.3.(b,c,d)) present lower

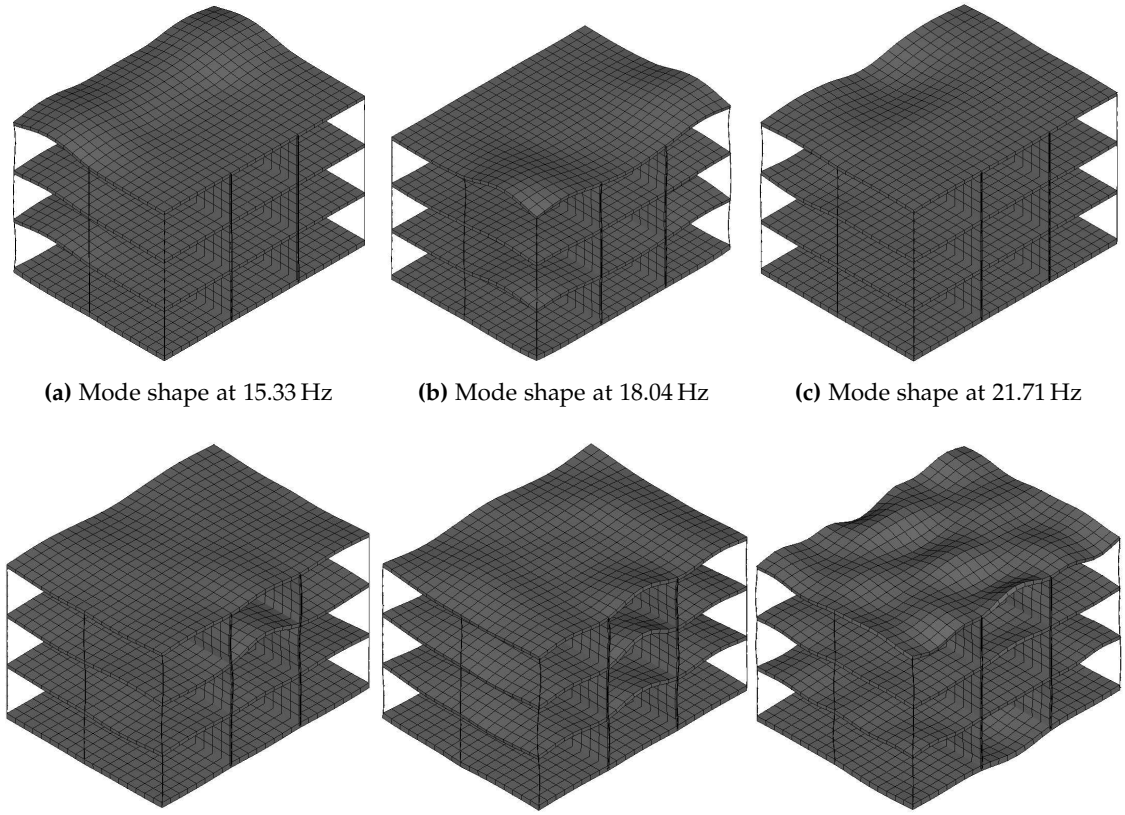

(a) Mode shape at 15.33 Hz **(b)** Mode shape at 18.04 Hz **(c)** Mode shape at 21.71 Hz

(d) Mode shape at 30.40 Hz **(e)** Mode shape at 47.88 Hz **(f)** Mode shape at 94.92 Hz

Figure A.2: Bending mode shapes of the floors.

value of vibration, and peaks (found at frequencies of 15.33 Hz and 18.04 Hz) match the two first bending vertical modes (Figures A.2.(a,b)). This is because the higher slab flexibility at these points causes an increased absorption of strain energy. The responses in the column (Figure A.3.(e)) and the core wall (Figure A.3.(f)) are distributed at approximately 47.88 Hz. It should be mentioned that the observation point *W* presents the lowest values of vibration. The agreement between the proposed scoping model and the `SSIFiBo` toolbox is good in the frequency range from 15 to 100 Hz.

The overall RMS value of the acceleration response computed using both the proposed scoping model (Equation (24)), the `SSIFiBo` toolbox, and Equation (14) are shown in Figure A.4. The discrepancies in the results obtained using Equation (14) and those computed without these simplifications are within a reasonable range of uncertainty, with the results obtained using Equation (24) being more accurate. The solution computed using the `SSIFiBo` toolbox shows a correlation between the building vibration and the storey level. However, this trend is not clearly observed in the scoping model solution. The differences

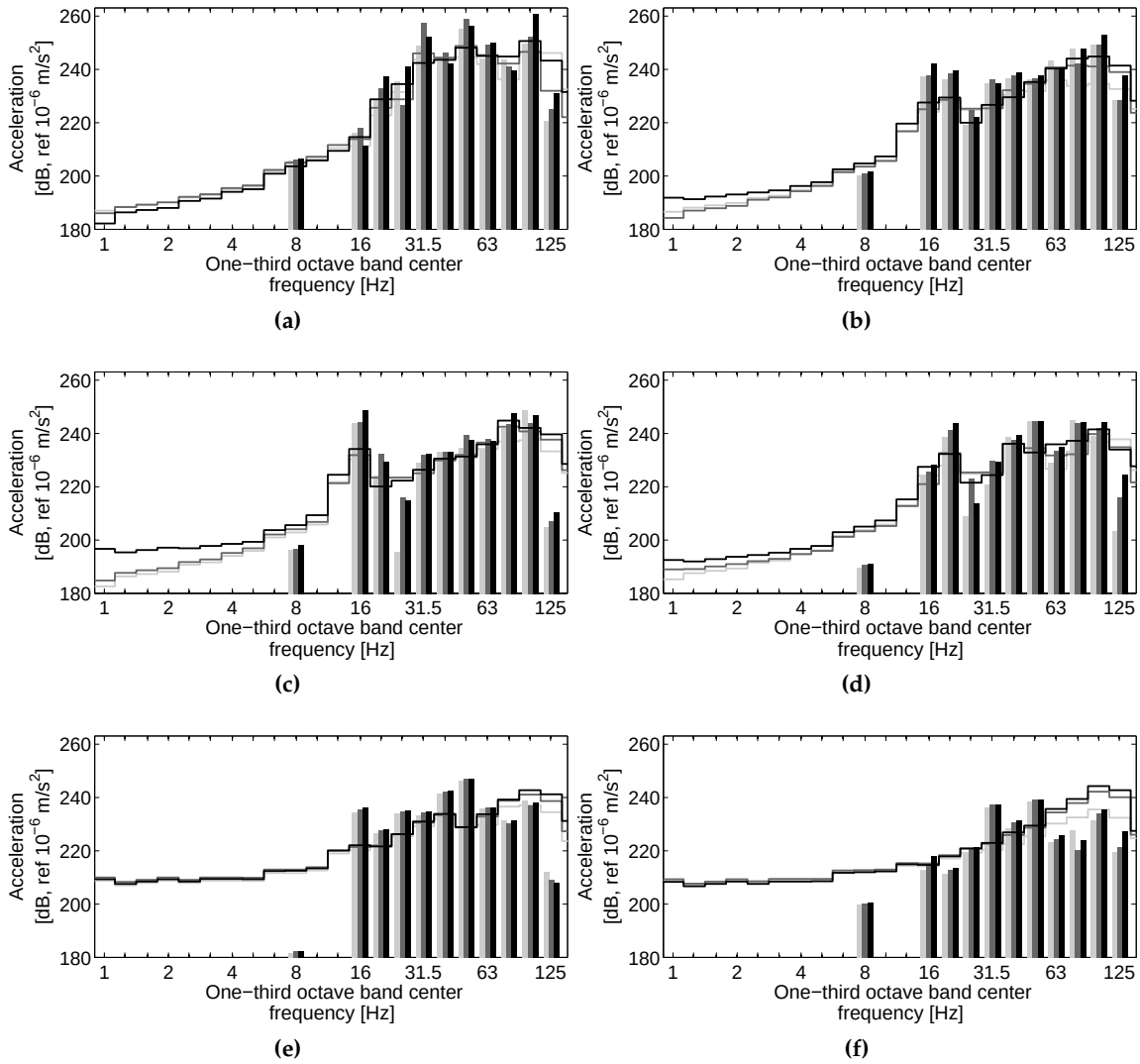

Figure A.3: One-third octave band centre frequency of the vertical relative acceleration computed $\ddot{\mathbf{u}}(t)$ by the `SSIFiBo` toolbox [21] (solid lines) and contribution C_j to the overall RMS value of the vertical acceleration of the modes within a frequency band centred in Ω_j obtained from the proposed scoping model (bars) at observation points (a) A, (b) B, (c) C, (d) D, (e) P and (f) W located at the first (light grey color), the second (dark grey color) and the third (black color) floors.

between both models reaches the highest value in the first floor. Nevertheless, the uncertainties are below 13 dB.

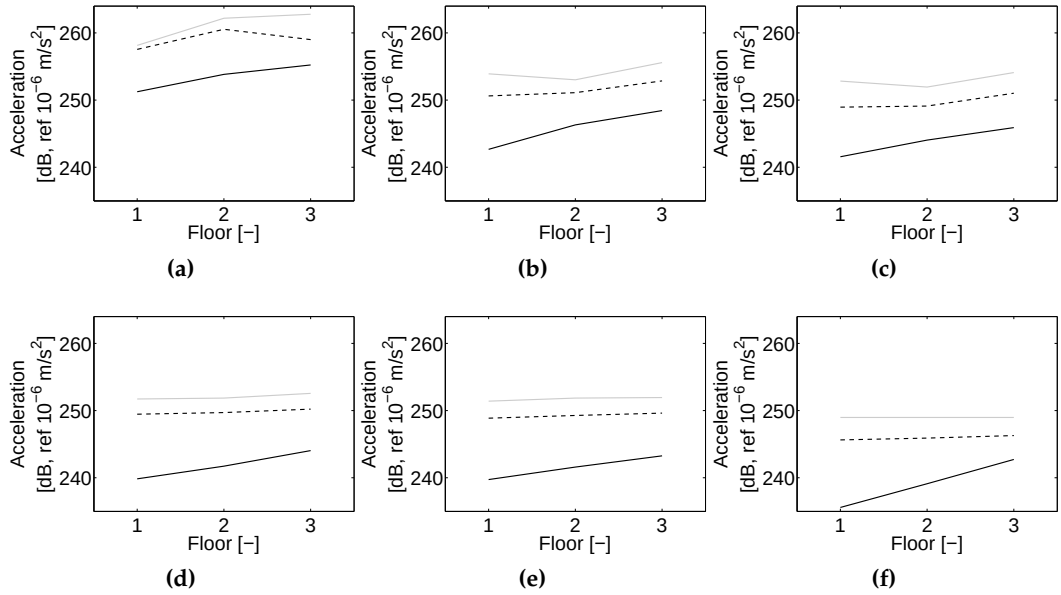

Figure A.4: Overall RMS value of the acceleration response against the storey level at the observation points (a) *A*, (b) *B*, (c) *C*, (d) *D*, (e) *P* and (f) *W* computed from the `SSIFiBo` toolbox [21] (black solid line), the scoping model (grey solid line) and the proposed model without simplifications (black dashed line).

A.3.2 *Parametric study: soil properties and type of foundation*

Secondly, for the purpose of determining the versatility of the model, the influence of soil properties and building design on structural response was studied. Three types of soil with the properties summarized in Table A.1 and five types of building were analysed. Each was similar to the generic building described in subsection A.3.1, but with the following changes:

1. Foundation consisting of a slab with a thickness of 0.3 m as in subsection A.3.1.
2. Foundation consisting of a slab with a thickness of 0.5 m.
3. Isolated footing of size 1.2 m $\times$ 1.2 m $\times$ 0.5 m.
4. Continuous footing of size 1.2 m $\times$ 0.5 m.
5. Absence of core wall.

Figure A.5 shows the overall RMS value of the building response at the top floor depending on the soil properties. The increment of building vibration with increasing soil stiffness observed in the solution computed from `SSIFiBo` toolbox it because the energy dissipation of soft soils is higher than stiff soils. This observation is not presented in the scoping model solution. Moreover the discrepancies between both models are higher in the

Table A.1: Soil properties.

Soil type	c_p [m/s]	c_s [m/s]	ξ [−]	ρ [kg/m^3]
Soft	300	150	0.06	1750
Medium	400	200	0.06	1750
Stiff	600	300	0.06	1750

soft soil. This is because the influence of SSI in the soft soil is dominant, and the scoping model uses a simplified calculation procedure in comparison to the `SSIFiBo` toolbox. In order to evaluate the uncertainty of the results, the simplifications assumed in Equation (14) and the methodology to evaluate the structural damping of the building in both models should be considered. Structural damping in the scoping model is determined using Equation (10), where the same damping $\zeta_i = \zeta$ for each i-th mode has been used. In comparison, the `SSIFiBo` toolbox considers viscous damping in the time domain, based on the Rayleigh model [8], and thus damping is not the same for all frequencies. In spite of this, the agreement between both models improves as soil stiffness increases and the uncertainty is within a reasonable range.

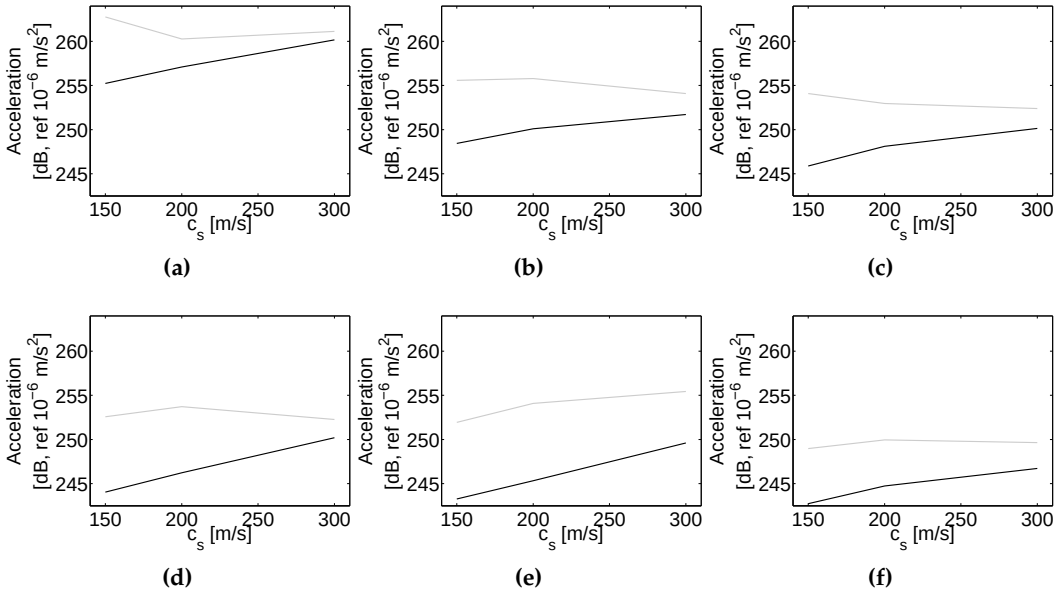

Figure A.5: Overall RMS value of the acceleration response depending of the soil properties at the top floor at the observation points (a) A, (b) B, (c) C, (d) D, (e) P and (f) W computed from the `SSIFiBo` toolbox (black line) and the scoping model (Equation (24)) (grey line).

Regarding the analysis of different building parameters, Table A.2 summarizes the obtained results. The influence of the thickness of the foundation slab causes only small changes to the building response as the thickness increased. Similar results were derived

in previous researches [5, 42]. The isolated and continuous footing foundations yield lower values of acceleration than the 0.5 m thick slab showing that vibration levels decrease with decreasing the stiffness of the foundation. This phenomenon is because the 0.5 m thick slab is the stiffest foundation, and has lower energy dissipation capacity than the remaining foundations. In comparison, the use of a core wall in the building increases the structural stiffness and the level of the response.

Considering the accuracy of the scoping model for a wide range of different soils and building parameters, it was concluded that it is suitable for use in a wide range of scenarios.

Table A.2: Maximum of the overall RMS value of the acceleration response for each observation point.

Problem	Point A	Point B	Point C	Point D	Point P	Point W	Maximum difference
	[dB]	[dB]	[dB]	[dB]	[dB]	[dB]	[dB]
Slab thickness $d = 0.3$ m	262.8	255.6	254.1	252.6	251.9	248.9	10.8
Slab thickness $d = 0.5$ m	264	255.7	256.2	254.8	254.8	249.9	11.5
Isolated footing	259.1	252.5	252.4	250.9	251.9	248.4	11.5
Continuous footing	259.6	255.2	254.4	255.1	254.9	248.6	11.4
Without core wall	256.1	254.7	255.1	255.1	249.9	251.8	9.1

A.4 SENSITIVITY ANALYSIS OF BUILDING INDUCED VIBRATION DUE TO TRAIN PASSAGE

In this section, vibrations induced by train passages in three multi-storey buildings are evaluated using the scoping model. The influence of soil properties, building height, train speed and the distance from the track to the building on the results are analysed. The midpoint foundation of the building was located at distances, $\{20, 30, 40, 50, 60, 70\}$ m from the track centreline and three different homogeneous soils were considered with the properties indicated in Table A.3. Table A.4 shows the carriage length L_t, the distance between bogies L_b, the axle distance L_a, the total axle mass M_t and the unsprung axle mass M_u for all carriages of the S-100 serie train considered in this paper. Train speeds of $\{100, 150, 200\}$ km/h were analysed. In all cases, train speed was found to be in a range between 10 % and 60 % of the critical velocity of the track system [37]. Therefore, it was assumed that the dynamic contribution (e.g. rail unevenness) would be dominant in the free-field response [31]. In total, the sensitivity study included the analysis of 162 problems (3 soil types $\times$ 3 buildings $\times$ 3 train speeds $\times$ 6 distances).

The structures were four, eight and twelve storeys buildings with the same floor plan dimensions 12 m $\times$ 12 m (Figure A.6.(a)). It consisted of eight concrete columns with 0.6 m $\times$ 0.4 m section, four edge beams with 0.6 m $\times$ 0.2 m section and two framed concrete walls with 2.4 m $\times$ 0.15 m section. The floors were simply supported concrete slabs with a thickness of 0.2 m. The floors consist of a two-dimensional frame with axial stiffness per

Table A.3: Soil properties.

Soil type	c_p [m/s]	c_s [m/s]	ξ [−]	ρ [kg/m^3]
Soft	250	100	0.06	1750
Medium	400	200	0.06	1800
Stiff	995	300	0.06	1850

Table A.4: Geometrical and mass characteristics of the S-100 train.

		No. of carriages	No. of axles	L_t[m]	L_b[m]	L_a[m]	M_t[kg]	M_u[kg]
S-100	Traction cars	2	4	22.15	14.00	3.00	17185	2048
	End carriages	2	3	21.84	18.70	3.00	11523	2003
	Central carriages	6	2	18.70	18.70	3.00	15523	2003

unit length $EA = 1.433 \times 10^9\,\mathrm{N/m}$, bending stiffness per unit length $EI = 9.935 \times 10^6\,\mathrm{Nm}$, and a mass per unit area of $m = 172\,\mathrm{kg/m^2}$. The structure was founded on a 1.0 m thick concrete slab. The concrete material had the following properties: Young's modulus $E = 20 \times 10^9\,\mathrm{N/m^2}$, Poisson's ratio $\nu = 0.2$, density $\rho = 2400\,\mathrm{kg/m^3}$ and the structural damping was considered using a Rayleigh model, where $\zeta = 0.05$ was set for all modes that contributed to the building response. The structure was discretised using two-node Euler-Bernoulli elements to represent columns and beams and four-node shell elements for the floors and the framed walls. Figure A.6.(b) shows the discretisation of the twelve-storey building.

The bending mode shapes of the floors computed without considering SSI are presented in Figure A.7. The mode shapes can be observed for increasing core wall (Figures A.7.(e,j,n)) and corner column (Figures A.7.(d,g,l,m,o)) deformations. Regarding the core wall, the displacements at the central zone of the floors are larger, while the corner columns involve the bending of the columns.

In the next subsection, before the sensitivity analysis, the dynamic behaviour of the buildings considering SSI will be studied.

The soil vibrations due to train passages were numerically obtained using the `SSIFiBo` toolbox [21]. The rails were represented by Euler-Bernoulli beams with a bending stiffness $E_\mathrm{r} I_\mathrm{r} = 6.45 \times 10^6\,\mathrm{N/m^2}$ and a mass per unit length $\rho_\mathrm{r} A_\mathrm{r} = 60.34\,\mathrm{kg/m}$ for each rail. The rail pads were modelled as continuous spring-damper connections. A rail pad stiffness $k_\mathrm{rp} = 150 \times 10^6\,\mathrm{N/m}$ and loss factor $\eta_\mathrm{rp} = 0.25$ to account for internal energy dissipation in the rail pad were used. The sleepers were of concrete monoblock type with a spacing of $d = 0.60\,\mathrm{m}$ and modelled as a uniformly distributed mass being $m_\mathrm{sl} = 300\,\mathrm{kg}$. The ballast bed was represented by a set of distributed linear springs and dampers. A ballast layer with a thickness h_b = 0.35 m, vertical stiffness $k_\mathrm{b} = 500 \times 10^6\,\mathrm{N/m}$ and density $\rho_b = 1550\,\mathrm{kg/m^3}$ was considered.

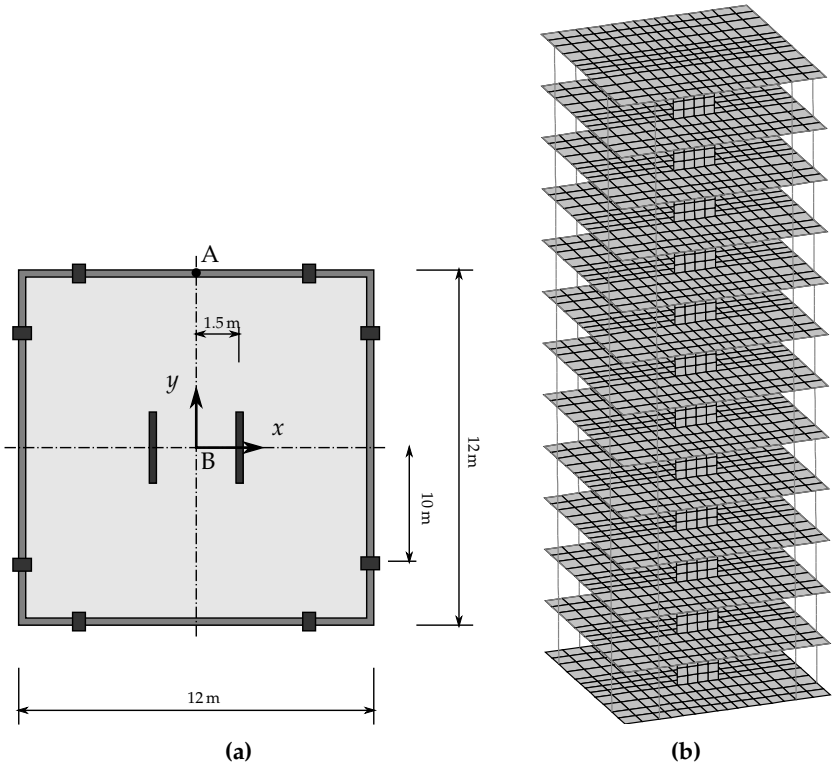

Figure A.6: (a) Four, eight and twelve-storey buildings plan geometry and (b) discretization of the twelve-storey building.

In the free-field predictions, both quasi-static excitation and dynamic excitation due to random track unevenness were taken into account [31]. The same track unevenness profile was considered for all the cases.

Once the free-field vibration was computed, ground-borne response spectra $\Lambda_i^j(f_i)$ for a damping ratio $\zeta = 0.05$ was obtained using Equation (25). Then, the building response was evaluated. The building response was obtained using a Single Point Response (SPR) excitation model, where the incident wave was transmitted simultaneously to all nodes of the structure foundation. The considered tolerance ($\varepsilon = 0.01$) was small enough to ensure that the building behaviour was accurately obtained. The building responses at the points A and B (Figure A.6.(a)) located along all the storey levels were analysed.

In this sensitivity analysis, the results from the scoping model were compared with those obtained by the `SSIFiBo` toolbox [21].

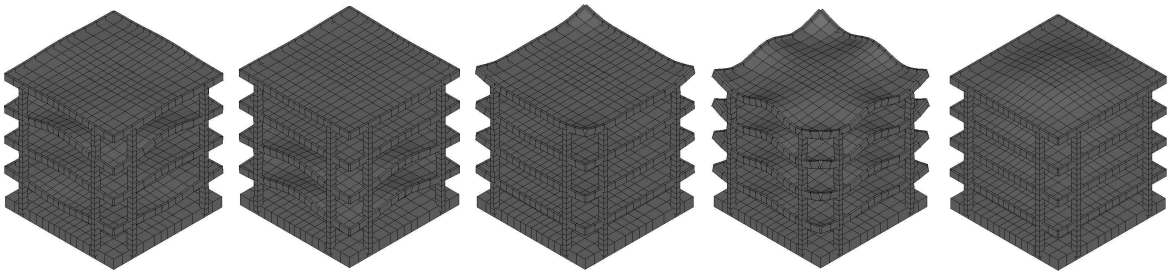

(a) Mode at 13.93 Hz **(b)** Mode at 14.25 Hz **(c)** Mode at 28.82 Hz **(d)** Mode at 50.63 Hz **(e)** Mode at 60.38 Hz

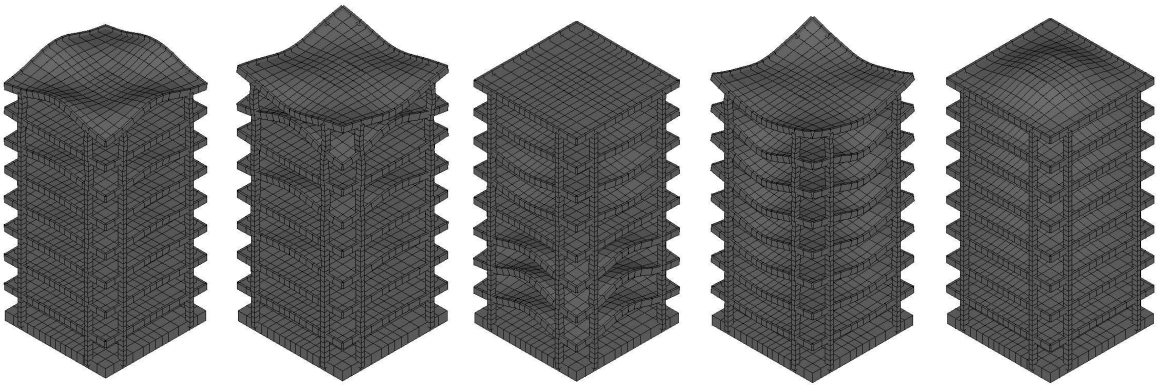

(f) Mode at 11.46 Hz **(g)** Mode at 12.35 Hz **(h)** Mode at 14.42 Hz **(i)** Mode at 20.67 Hz **(j)** Mode at 30.19 Hz

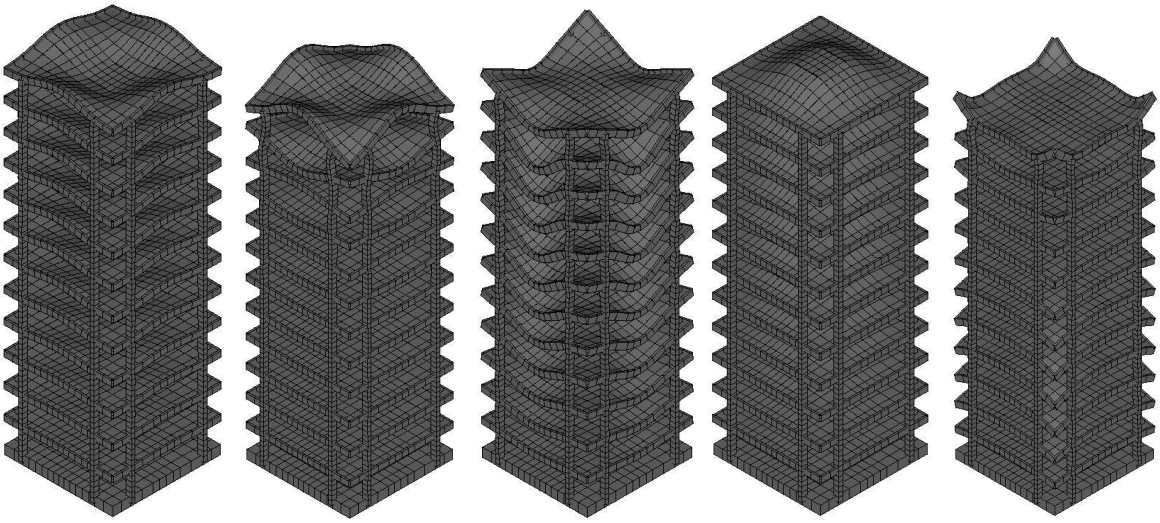

(k) Mode at 9.10 Hz **(l)** Mode at 12.04 Hz **(m)** Mode at 18.53 Hz **(n)** Mode at 20.14 Hz **(ñ)** Mode at 30.21 Hz

Figure A.7: Bending floor mode shapes of the (a,b,c,d,e) four-storey building, (f,g,h,i,j) eight-storey building and (k,l,m,n,o) twelve-storey building.

A.4.1 *Soil properties*

Before the sensitivity analysis, building response was characterized depending on the soil properties. For this purpose, the contribution of bending modes was obtained from the building response to an incident wave field acting in the vertical (z) direction using a ground-borne response spectra $\Lambda_i^j(f_n) = 1\text{m/s}^2$ (Equation 24). In this way, the contribution of each i-th mode to the building response $C_i = \sqrt{\boldsymbol{\phi}_i^2 \sum_{j=1}^{3} \Gamma_i^{j^2}}$ (Equation (26)) was not dependent of the excitation. Figure A.8 shows the contribution to the overall RMS value of the vertical acceleration at the different frequencies for the four, eight and twelve storey buildings obtained using Equation (28) and evaluated at the top floor, at observation points A and B (Figure A.6.(a)). The response was computed for the soils presented in Table A.3. The bending modes of the dominant floors were found in the frequency range below 80 Hz. It was observed that the contribution for each soil was different. At the observation point B, the fundamental frequency was different depending on the soil properties.

Next, the combination of the response spectra Λ_i^j (computed from the free-field predictions) and the characterization of the buildings for a load with constant amplitude at the studied frequency range (Figure A.8) is used to understand the building behaviour due to train passages. The effect of the soil properties on the scoping prediction for a building located at 20 m from the track due to a S-100 train travelling at $v = 150\,\text{km/h}$ was studied. Figure A.9 shows the ground-borne response spectra Λ_i^j computed from the free field vibrations. The ground-borne spectra exhibits elevated amplitudes in the frequency range between 10 Hz and 40 Hz. Peaks around the axle passing frequency $f_a = v/L_a = 13.9\,\text{Hz}$ and due to the dynamic excitation at 30 Hz can be observed. The highest value was reached in the vertical direction. The effect of the soil properties on the quasi-static contribution are clearly observed at lower frequencies. However, at the frequencies contributing to the dynamic response, the results do not show a clear correlation between the free field response and the soil properties.

Figure A.10 shows the influence of the soil on building vibration. It can be observed that the accelerations decrease as the soil stiffness increases, excluding the eight-storey building where the response in the medium soil is higher. This phenomenon can be explained from Λ_i^j (Figure A.9) and the eight-storey building response showed in Figure A.8. Ground-borne vertical response spectra Λ_i^j (Figure A.9.(c)) shows higher amplitudes in the medium soil at about 30 Hz because this is close to the the fundamental frequency for the observation point B (Figure A.8. (d)). In Figure A.8.(c) it is observed that the response at point A is concentrated around 10 Hz and the vibration level in the stiff soil is slightly higher than for the medium soil. However, the excitation Λ_i^j around 10 Hz (Figure A.9.(c)) presents a lower value for the stiff soil. Thus, the eight-storey building responses at point A for both the medium and the stiff soil are similar (Figure A.10. (b)).

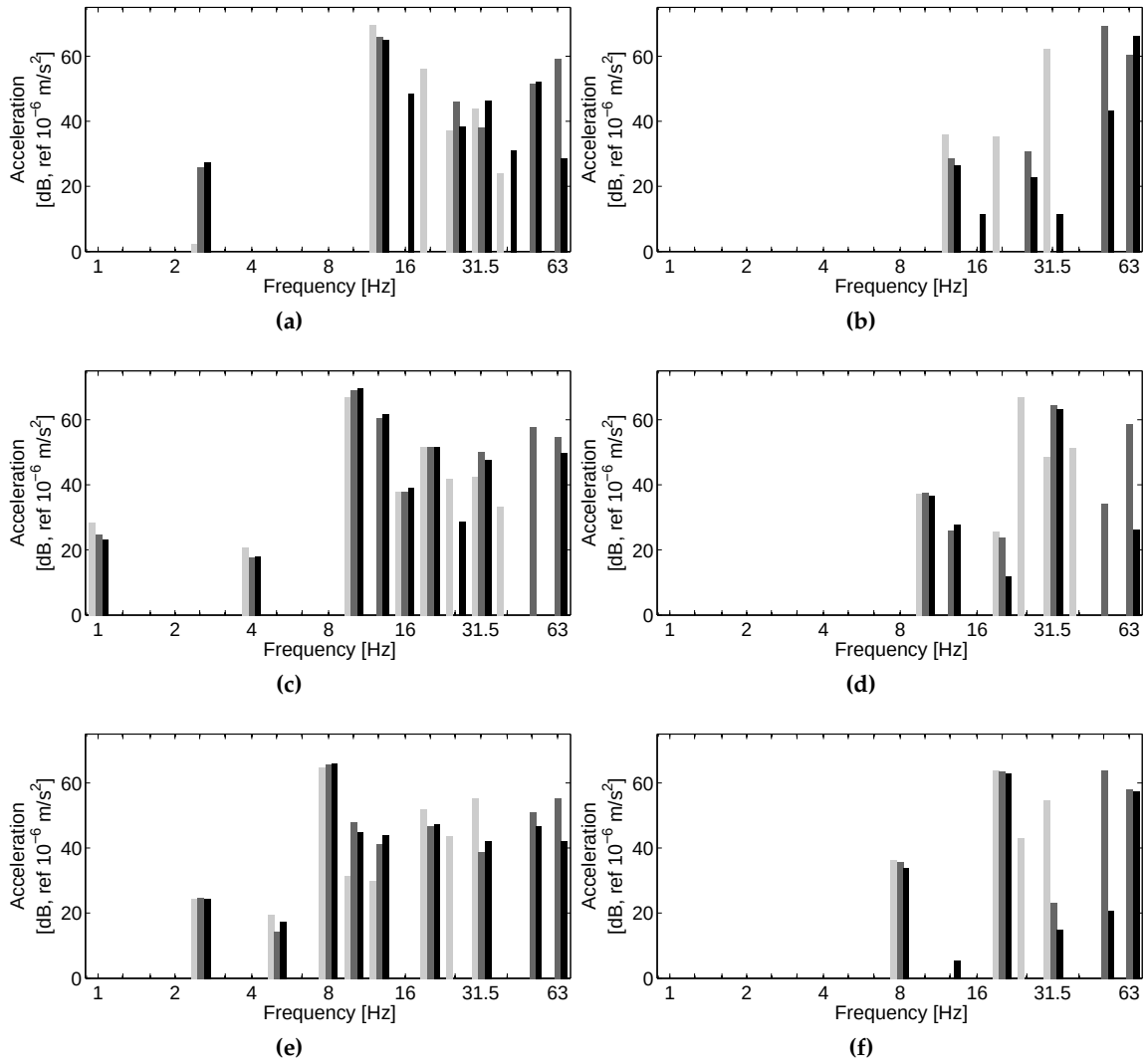

Figure A.8: Contribution of the modes to the overall RMS value of the vertical acceleration due to an incident wave with ground-borne response spectra $\Lambda_i^j = 1\mathrm{m/s}^2$ in the soft soil (light grey bar), medium soil (dark grey bar) and stiff soil (black bar) obtained from the proposed scoping model at the top floor of the observation points (a,c,e) *A* and (b,d,f) *B* for the (a,b) four-storey building, (c,d) eight-storey building and (e,f) twelve-storey building.

The scoping model predicted higher amplitudes than the `SSIFiBo` reference model. The differences between both models were dependent on the soil properties, but these uncertainties did not follow a clear trend. Thus, it can be concluded that soil properties are an important parameter for the accuracy of the proposed scoping model.

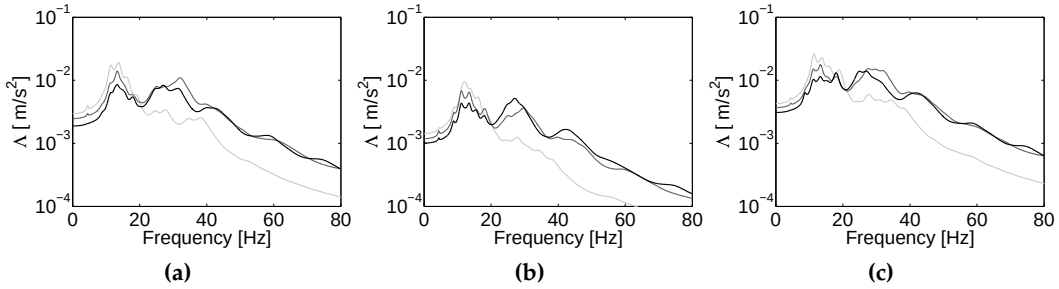

Figure A.9: (a) Transversal, (b) longitudinal and (c) vertical ground-borne response spectra Λ_i^j at 20 m from the track center due to a train passage at $v = 150$ km/h in the soft soil (light grey line), medium soil (dark grey line) and stiff soil (black line).

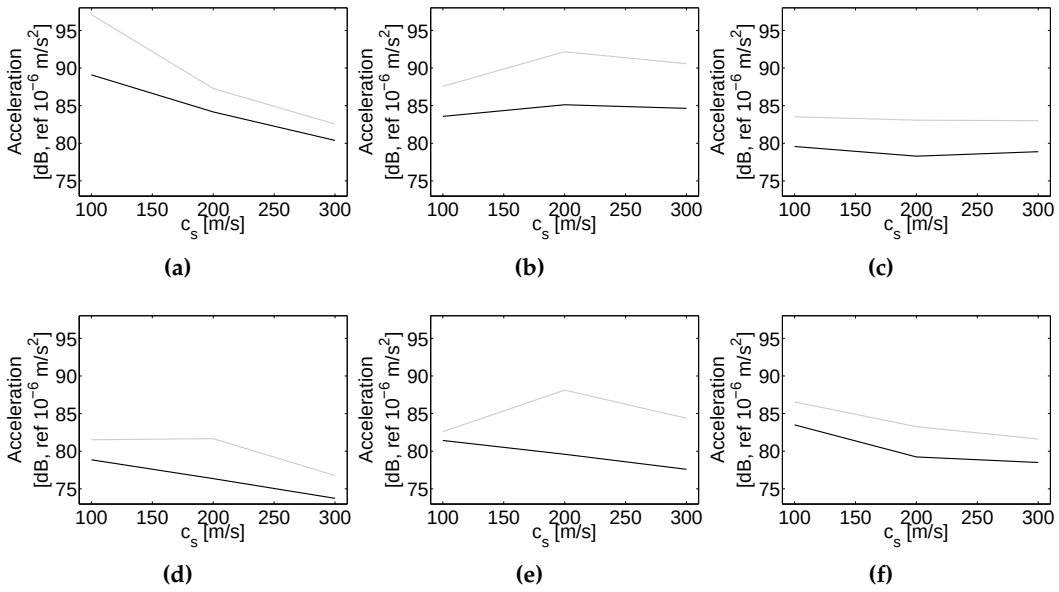

Figure A.10: Overall RMS value of the acceleration response due to a train passage at $v = 150$ km/h evaluated at the top floor at the observation points (a,b,c) A and (d,e,f) B computed from the `SSIFiBo` toolbox (black line) and the scoping model (Equation (24)) (grey line) for the (a,d) four-storey, (b,e) eight-story and (c,f) twelve-storey buildings.

A.4.2 *Building height*

Next, the effect of the building height on the results computed from the proposed methodology was analysed. The four, eight and twelve storey building responses due to the passage of a S-100 train travelling at $v = 150$ km/h was analysed. The buildings were located at 20 m from the track and the soil with $c_s = 200$ m/s was considered. Figure A.11 shows the one-third octave band spectra content of the vertical relative accelerations $\ddot{\mathbf{u}}(t)$ (Equation

(2)) at the observation points A and B located at the first, middle and top floors obtained from the SSIFiBo toolbox. Superimposed is the contribution to the overall RMS value of the frequencies computed from the scoping model. It can be seen that the mode with higher participation factor computed for the four, eight and twelve-storey buildings was found around the frequencies 12 Hz, 10 Hz and 8 Hz for the observation point A, and 50 Hz, 30 Hz and 20 Hz for the observation point B respectively. Thus, as expected, frequency reduced as the building height increased. The highest value of vibration was found at the top floor of the eight-storey building because the values of the soil response spectra Λ_i^j (Figure A.9.(c)) match with the natural frequencies of the eight-storey building at about 10 Hz and 30 Hz (Figure A.8. (c,d)). These are higher than those at the frequencies 8 Hz and 20 Hz that correspond to the natural frequencies of the twelve-storey building (Figures A.8.(e,f)). The agreement between both models was quite good at the frequencies that dominate the building response.

Figure A.12 presents the influence of building height on the overall RMS value of the response. The results computed from both models are shown for different storey levels. As expected, the response increases with storey level at the observation point B. However, this correlation is not observed at observation point A for the four and twelve-storey buildings. Regarding the response at the observation point A of the four-storey building, the response is at about 12 Hz that corresponds with the two first bending modes (Figure A.7. (a,b)). These modes present larger amplitudes at the middle floors of the building than at the top floor. The lack of correlation between storey level and the response computed from the SSIFiBo toolbox at the observation point A of the twelve-storey building can be explained since the second bending mode at 12 Hz (Figure A.7.(l)) presents lower amplitudes at the floors from one to six at observation point A. The maximum discrepancy between both models was found in the response of the eight-storey building, where a difference of 8.5 dB was found. This discrepancy is acceptable considering the simplified procedure used to formulate the scoping model, and the different structural damping approaches used for it compared to the detailed model.

A.4.3 *Train Speed*

Next the scoping model was used to assess the effect of the train speed on building response. The response of the three buildings located at 20 m to the track due to the passage of a S-100 train travelling at $\{100, 150, 200\}$ km/h was studied. The moderately stiff soil was again considered. Figure A.13 shows the vertical ground-borne response spectra Λ_i^j computed from the free-field vibrations. Peaks around the axle passing frequency $f_a = v/L_a = \{9.26, 13.9, 18.52\}$ Hz that involve the quasi-static contribution can be observed. The highest value was found in the ground-borne response spectra at $v = 200$ km/h around 18 Hz. The ground-borne response spectra due to a train passage at $v = 150$ km/h resulted in peaks around 13 Hz and 30 Hz.

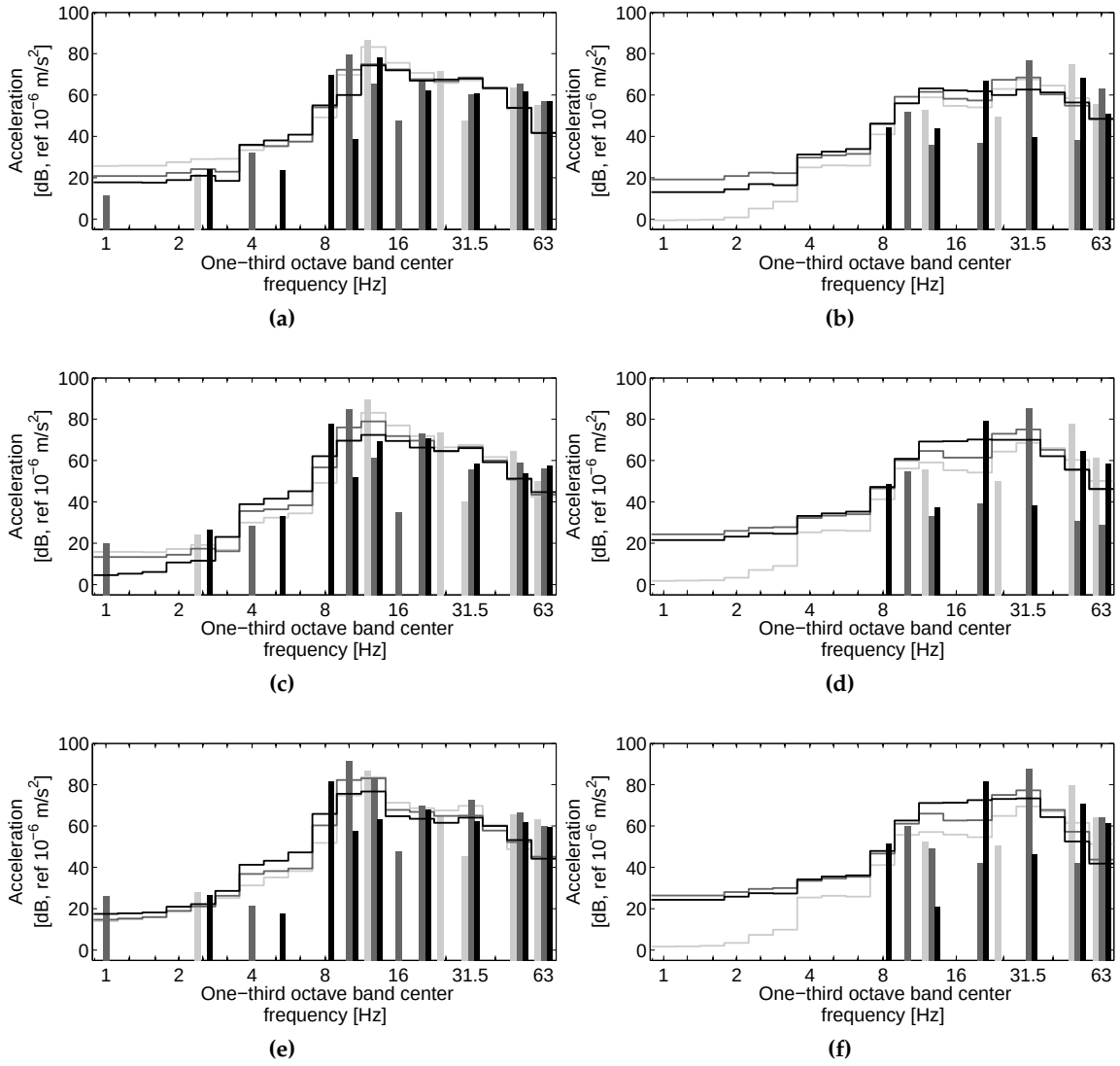

Figure A.11: One-third octave band centre frequency content of the vertical relative acceleration due to a train passage at $v = 150\,\mathrm{km/h}$ computed by the `SSIFiBo` toolbox (lines) and contribution of the modes to the overall RMS value of the vertical acceleration obtained from the scoping model (bars) at the observation points (a,c,e) A and (b,d,f) B located at (a,b) the first, (c,d) the middle and (e,f) the top floors of the four-storey building (light grey color), eight-storey building (dark grey color) and twelve-storey building (black color).

The overall RMS value of the building response is shown in Figure A.14. It can be seen that the level of vibration generally increased with increasing speed, except for the response at the observation point B of the eight-storey building, computed by the scoping model. Instead, at approximately 30 Hz the ground-borne response spectra $v = 150\,\mathrm{km/h}$ presents

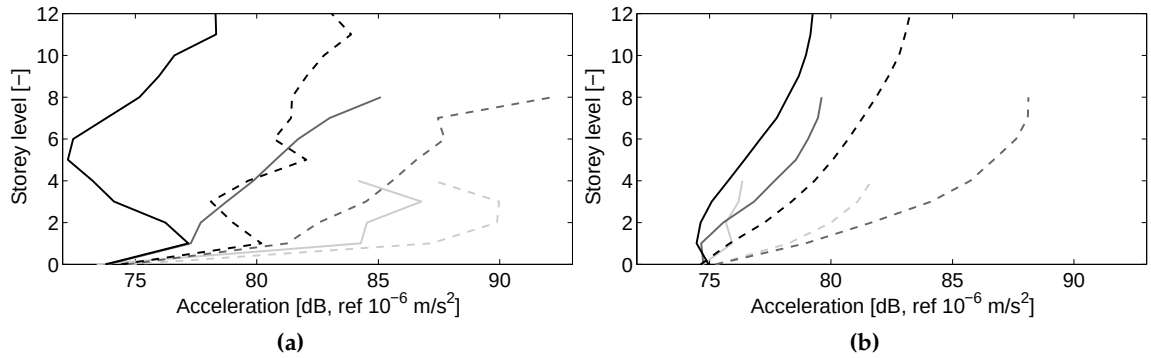

Figure A.12: Overall RMS value of the acceleration response due to a train passage at $v = 150\,\mathrm{km/h}$ evaluated at the observation points (a) A and (b) B computed from the `SSIFiBo` toolbox (solid line) and the scoping model (Equation (24)) (dashed line) for the four-storey building (light grey line), eight-storey (dark grey line) and twelve-storey building(black line).

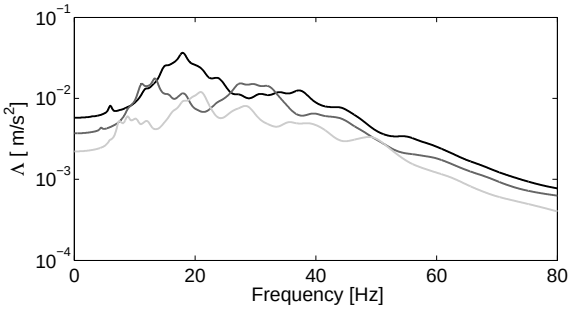

Figure A.13: Vertical ground-borne response spectra Λ_i^j at 20 m from the track center due to a train passage at $v = 100\,\mathrm{km/h}$ (light grey line), $v = 150\,\mathrm{km/h}$ (dark grey line) and $v = 200\,\mathrm{km/h}$ (black line) in the medium soil.

higher value. The differences between both models were not strongly influenced by train speed.

A.4.4 *Distance from the track*

Building response due to the passage of a S-100 train travelling at $v = 150\,\mathrm{km/h}$ was analysed for different distances between the track to the building. The moderately stiff soil type was again considered. Figure A.15 shows the vertical ground-borne response spectra Λ_i^j computed from the free-field vibration. As expected, ground-borne vibration levels were increasingly damped with increasing distance from the track.

Figure A.16 shows the effect of the distance from the track to the building on the overall RMS value of the response, where it is seen that the building response decreases with increasing distance. This correlation between distance from the track and the response

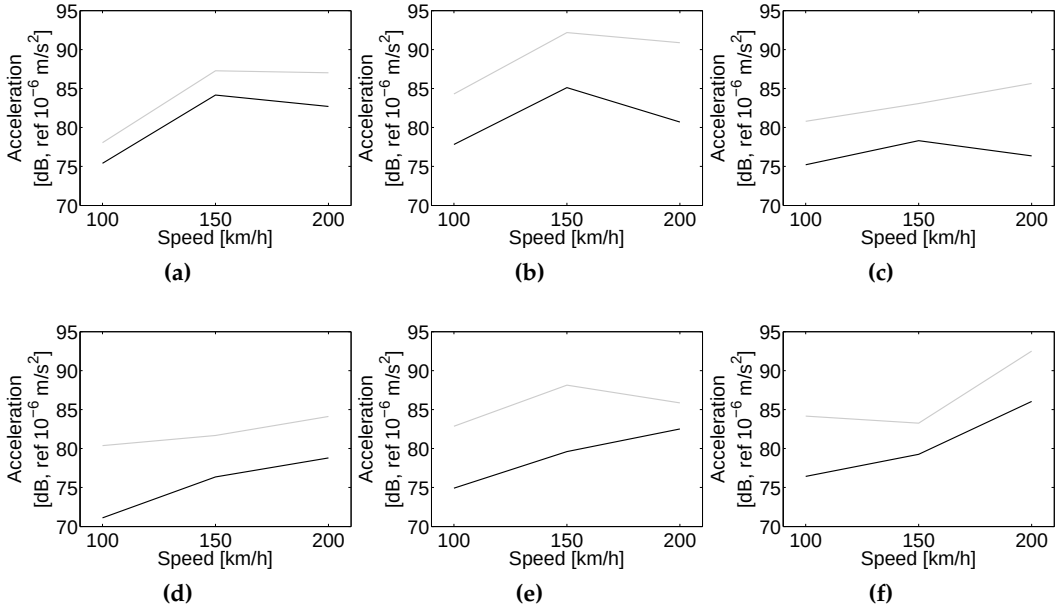

Figure A.14: Overall RMS value of the acceleration response due to a train passage at different speeds evaluated at the observation points (a,b,c) A and (d,e,f) B computed from the `SSIFiBo` toolbox (black line) and the scoping model (Equation (24)) (grey line) for the (a,d) four-storey building, (b,e) eight-storey building and (c,f) twelve-storey building.

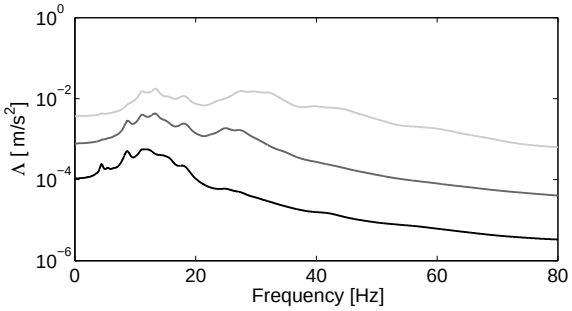

Figure A.15: Vertical ground-borne response spectra Λ_i^j at 20 m (light grey line), 40 m (dark grey line) and 70 m (black line) from the track center due to a train passage at $v = 150$ km/h.

both in the free field and in the building is consistent with previous research [42]. The scoping model predicted elevated values with regard to the `SSIFiBo` model, however, the accuracy of the scoping model remained broadly constant with distance.

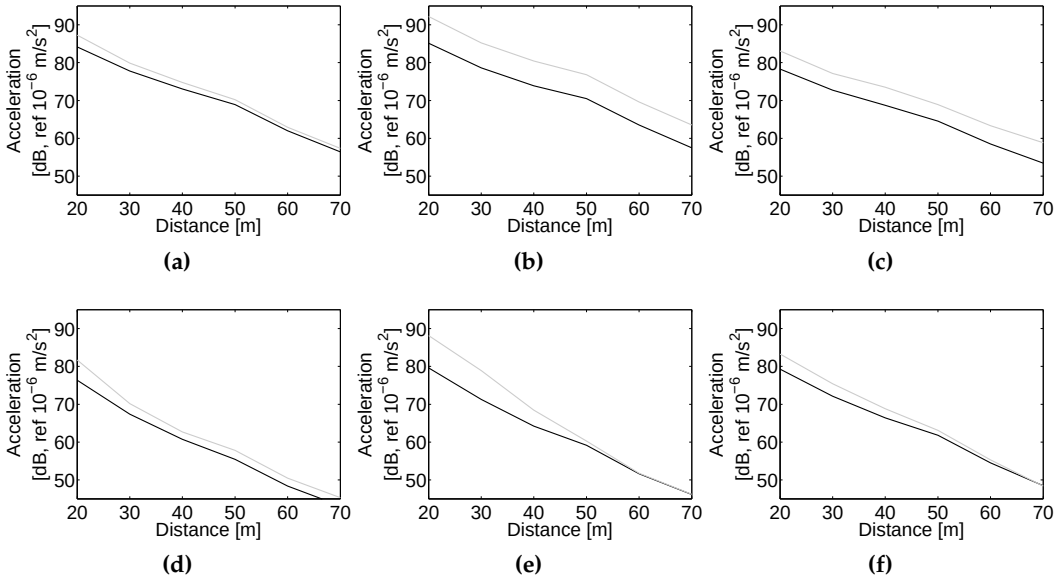

Figure A.16: Overall RMS value of the acceleration response evaluated at the observation points (a,b,c) A and (d,e,f) B computed from the `SSIFiBo` toolbox (black line) and the scoping model (Equation (24)) (grey line) for the (a,d) four-storey building, (b,e) eight-storey building and (c,f) twelve-storey building.

A.4.5 *Remarks of the sensitivity analysis*

The overall RMS value of the acceleration for the 162 problems were computed using both models (scoping and `SSIFiBo`) to assess the accuracy of the proposed methodology. The difference between the responses computed from both models was calculated as:

$$\Delta a_{RMS}[\text{dB}] = 20 \log \left(\frac{a^P_{RMS}}{a^S_{RMS}} \right) \tag{29}$$

where a^P_{RMS} and a^S_{RMS} were the responses computed by the proposed model and the `SSIFiBo` toolbox, respectively. Figure A.17 shows this difference for the 162 problems evaluated at the observation points A and B at all the storey levels that correspond with 2592 cases. It can be seen that the difference between both models is normally distributed (Figure A.17.(a)) with mean value $\mu = 3\,\text{dB}$ and standard deviation $\sigma = 2.6\,\text{dB}$ (Figure A.17.(b)).

Figure A.18 presented all the cases evaluated. The confidence region $[a^S_{RMS} + \mu \pm 2\sigma]$ and the expected value $a^S_{RMS} + \mu$ are superimposed. It was found that 96.45% of the results were within this confidence region, and that most of the results from the scoping model were higher in magnitude than those obtained from the detailed model. The uncertainty of the predictions from the scoping model were within a range between $-3\,\text{dB}$ to $11\,\text{dB}$ and thus similar to the $5\,\text{dB}$ - $20\,\text{dB}$ values found in previous research [15, 28, 33].

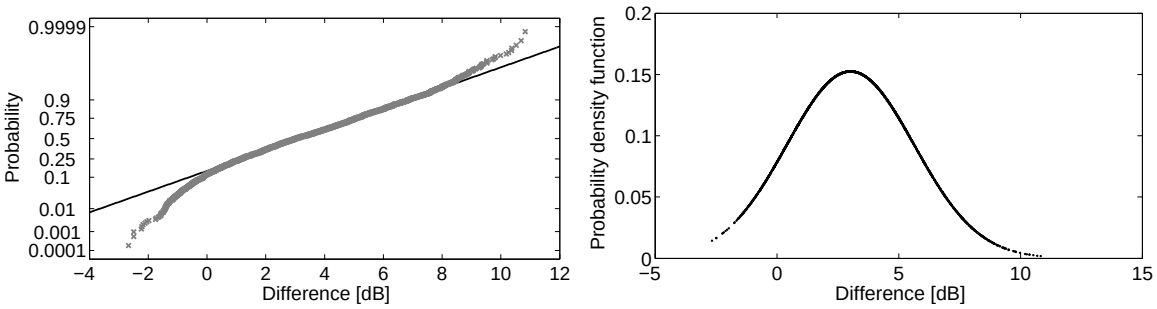

Figure A.17: (a) Distribution of the difference between both models (grey crosses) against the normal distribution (black line) and (b) probability density function of the difference.

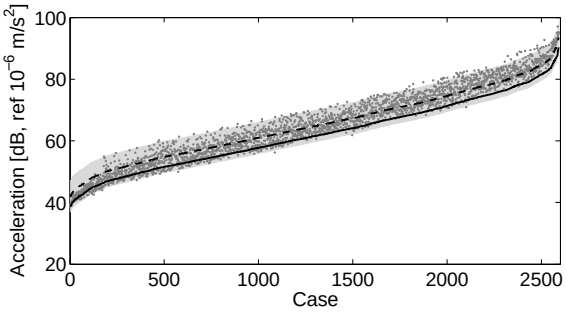

Figure A.18: Overall RMS of the building for the 162 problems evaluated at the observation points A and B computed by the scoping model (grey points) and from the `SSIFiBo` toolbox (black line). Superimposed are the confidence region (grey area) and the expected value (black dashed line).

The sensitivity analysis showed that soil material properties were a relevant parameter that could affect the accuracy of the vibration level prediction, due to the deviation shown in Figure A.10.

One of the advantages of the proposed method is its computational efficiency. Table A.5 shows the computational cost to obtain the results of the twelve-storey response for a S-100 train travelling at $v = 150\,\text{km/h}$ using an `Intel Core i7@1.87 GHz` computer. The running time shown refers to the immission problem of waves in the building. The cost needed to compute the BEM model in the `SSIFiBo` toolbox, the ground-borne response Λ_i^j in the scoping model and the FEM model of the building were not included. The difference between the running time required in both models was due to the more comprehensive BEM-FEM methodology used by the `SSIFiBo` toolbox to consider the SSI against the simple FEM procedure of the scoping model. The time using the proposed scoping model is much lower than the necessary for the detailed prediction model (between 45-135 times faster depending on soil stiffness). Therefore, the scoping model could be a powerful tool during the early design stages of railway lines where a large number of building vibrations assessment.

Table A.5: Average running time for a S-100 travelling at $v = 150$ km/h considering the twelve-storey building

	Average running time		
	Soft soil	Medium soil	Stiff soil
`SSIFiBo` toolbox	$t = 3\,\text{h}$	$t = 7.5\,\text{h}$	$t = 9\,\text{h}$
Proposed scoping Model	$t = 4\,\text{min}$		

A.5 CONCLUSIONS

In this paper, a scoping model to predict vibrations in buildings induced by railway traffic considering soil-structure interaction was proposed. The scoping model is attractive because the structural vibration induced by train passage can be assessed in minimal computational time.

The scoping model uses the ground-borne response spectra Λ_i^j computed from either numerical or experimentally free field vibrations (ground motion at the three orthogonal directions should be measured). Therefore, it is useful for cases of new lines, and also existing lines where new buildings are planned. To minimise calculation times, building response is obtained using modal superposition.

The proposed model was verified against a detailed prediction model based on a BEM-FEM formulation. The agreement was good and any discrepancies were mainly due to the simplifications assumed in the proposed formulation and the different procedure to consider the structural damping in both models. Therefore it can be considered a highly effective tool for early stage prediction.

The proposed methodology was used to analyse the dynamic behaviour of a building due to train passages, considering numerically generated free-field vibrations as input data. The effect of different parameters was analysed: soil properties, building height, train speed and distance from the track to the building. The building response showed a clear dependence on these parameters.

In conclusion, the scoping model allows engineers and designers to evaluate building response due to train passage at the early design stage with confidence. The proposed model involves a powerful tool easily implementable in general purpose commercial FEM software. The contribution of the dominant frequencies obtained using the scoping model were in good agreement with those obtained using a detailed design model, and the estimation of the overall RMS acceleration values were also strong. Generally, the new model provides conservative predictions of overall RMS values of the acceleration, with typical discrepancies between $-3\,\text{dB} + 11\,\text{dB}$.

ACKNOWLEDGMENTS

This research was funded by the Spanish Ministry of Economy and Competitiveness (Ministerio de Economía y Competitividad) through research project BIA2013-43085-P. Finan-

cial support is gratefully acknowledged. The support given by the Andalusian Scientific Computing Centre (CICA) is also gratefully.

REFERENCES

[1] L. Auersch. The excitation of ground vibration by rail traffic: theory of vehicle–track–soil interaction and measurements on high-speed lines. *Journal of Sound and Vibration*, 284:103–132, 2005. doi: https://doi.org/10.1016/j.jsv.2004.06.017.

[2] L. Auersch. Dynamic stiffness of foundations on inhomogeneous soils for a realistic prediction of vertical building resonance. *Journal of Geotechnical and Geoenvironmental Engineering*, 134(3):328–340, 2008. doi: http://dx.doi.org/10.1061/(ASCE)1090-0241(2008)134:3(328).

[3] L. Auersch. Wave propagation in the elastic half-space due to an interior load and its application to ground vibration problems and buildings on pile foundations. *Soil Dynamics and Earthquake Engineering*, 30:925–936, 2010. doi: https://doi.org/10.1016/j.soildyn.2010.04.003.

[4] L. Auersch. Building Response due to Ground Vibration–Simple Prediction Model Based on Experience with Detailed Models and Measurements. *International Journal of Acoustics and Vibration*, 15(3):101–112, 2010. doi: http://dx.doi.org/10.20855/ijav.2010.15.3262.

[5] L. Auersch, A. Romero, and P. Galvín. Respuesta dinámica de edificaciones producida por campos de onda incidentes considerando la interacción suelo-estructura. *Revista Internacional de Métodos Numéricos para Cálculo y Diseño en Ingeniería*, 30(4):256–263, 2014. doi: https://doi.org/10.1016/j.rimni.2013.09.001.

[6] C.E. Hanson, D.A. Towers, and L.D. Meister. High-speed ground Transportation Noise and Vibration Impact Assessment, HMMH Report 293630-4. *U.S. Department of Transportation, Federal Railroad Administration, Office of Railroad Development*, 2005.

[7] C.E. Hanson, D.A. Towers, and L.D. Meister. Transit Noise and Vibration Impact Assessment, Report FTA-VA-90-1003-06. *U.S. Department of Transportation, Federal Transit Administration, Office of Planning and Environment*, 2006.

[8] R.W. Clough and J. Penzien. *Dynamic of Structures*. McGraw-Hill, New York, 1975.

[9] D.P. Connolly, G.P. Marecki, G. Kouroussis, I. Thalassinakis, and P.K. Woodward. The growth of railway ground vibration problems – A review. *Science of the Total Environment*, 568:1276–1282, 2015. doi: http://dx.doi.org/10.1016/j.scitotenv.2015.09.101.

[10] P. Coullier, G. Lombaert, and G. Degrande. The influence of source-receiver interaction on the numerical prediction of railway induced vibrations. *Journal of Sound and Vibration*, 333:2520–2538, 2014. doi: https://doi.org/10.1016/j.jsv.2014.01.017.

[11] B. Davies. *Integral Transforms and Their Applications*. Springer Science, New York, 1985.

[12] *DIN 45672 Teil 2: Schwingungsmessungen in der Umgebung von Schienenverkehrswegen: Auswerteverfahren*. Deutsches Institut für Normung, 1995.

[13] D.P. Connolly, G. Kouroussis, A. Giannopoulos, O. Verlinden, P.K. Woodward, and M.C. Forde. Assesment of railway vibrations using an efficient scoping model. *Soil Dynamics and Earthquake Engineering*, 58:37–47, 2014. doi: https://doi.org/10.1016/j.soildyn.2013.12.003.

[14] D.P. Connolly, G. Kouroussis, P.K. Woodward, A. Giannopoulos, O. Verlinden, and M.C. Forde. Scoping prediction of re-radiated ground-borne noise and vibration near high speed rails lines with variable soils. *Soil Dynamics and Earthquake Engineering*, 66: 78–88, 2014. doi: https://doi.org/10.1016/j.soildyn.2014.06.021.

[15] D.P. Connolly, P. Alves Costa, G. Kouroussis, P. Galvín, P.K. Woodward, and O. Laghrouche. Large scale international testing of railway ground vibrations across Europe. *Soil Dynamics and Earthquake Engineering*, 71:1–12, 2015. doi: https://doi.org/10.1016/j.soildyn.2015.01.001.

[16] Federal Railroad Administration. *High-Speed Ground Transportation Noise and Vibration Impact Assessment*. U.S. Department of Transportation, 2012.

[17] P. Fiala, G. Degrande, and F. Augusztinovicz. Numerical modelling of ground-borne noise and vibration in buildings due to surface rail traffic. *Journal of Sound and Vibration*, 301:718–738, 2007. doi: https://doi.org/10.1016/j.jsv.2006.10.019.

[18] S. François, L. Pyl, H.R. Masoumi, and G. Degrande. The influence of dynamic soil-structure interaction on traffic induced vibrations in buildings. *Soil Dynamics and Earthquake Engineering*, 27:655–674, 2007. doi: https://doi.org/10.1016/j.soildyn.2006.11.008.

[19] S. François, M. Schevenels, P. Galvín, G. Lombaert, and G. Degrande. A 2.5D coupled FE-BE methodology for the dynamic interaction between longitudinally invariant structures and a layered halfspace. *Computer Methods in Applied Mechanics and Engineering*, 199:1536–1548, 2010. doi: https://doi.org/10.1016/j.cma.2010.01.001.

[20] P. Galvín and J. Domínguez. High-speed train-induced ground motion and interaction with structures. *Journal of Sound and Vibration*, 307:755–777, 2007. doi: https://doi.org/10.1016/j.jsv.2007.07.017.

[21] P. Galvín and A. Romero. A MATLAB toolbox for soil-structure interaction analysis with finite and boundary elements. *Soil Dynamics and Earthquake Engineering*, 57:10–14, 2014. doi: https://doi.org/10.1016/j.soildyn.2013.10.009.

[22] P. Galvín, S. François, M. Schevenels, E. Bongini, G. Degrande, and G. Lombaert. A 2.5D coupled FE-BE model for the prediction of railway induced vibrations. *Soil Dynamics and Earthquake Engineering*, 30:1500–1512, 2010. doi: https://doi.org/10.1016/j.soildyn.2010.07.001.

[23] P. Galvín, A. Romero, and J. Domínguez. Fully three-dimensional analysis of high-speed train–track–soil–structure dynamic interaction. *Journal of Sound and Vibration*, 329:5147–5163, 2010. doi: https://doi.org/10.1016/j.jsv.2010.06.016.

[24] *ISO 2631-1:2003: Mechanical vibration and shock–Evaluation of human exposure to whole-body vibration–Part 1: General requirements*. International Organization for Standardization, 2003.

[25] *ISO 2631-2:2003: Mechanical vibration and shock–Evaluation of human exposure to whole-body vibration–Part 2: Vibration in buildings (1–80 Hz)*. International Organization for Standardization, 2003.

[26] *ISO 14837-1:2005 Mechanical vibration–Ground-borne noise and vibration arising from rail systems–Part 1: General guidance*. International Organization for Standardization, 2005.

[27] P. Jean, C. Guigou, and M. Villot. A 2.5D BEM Model for Ground-Structure Interaction. *Building Acoustics*, 11(3):1–17, 2004. doi: https://doi.org/10.1260/1351010042250376.

[28] S. Jones, K. Kuo, M.F.M. Hussein, and H.E.M Hunt. Prediction uncertainties and inaccuracies resulting from common assumptions in modelling vibration from underground railways. *Proceedings of the Institution of Mechanical Engineers, Part F: Journal of Rail and Rapid Transit*, 226:501–512, 2012. doi: https://doi.org/10.1177/0954409712441744.

[29] J.T. Nelson and H.J. Sauernman. A prediction procedure for rail transportation ground-borne noise and vibration. *Transportation Research Record: Journal of the Transportation Research Board*, 1143:26–35, 1987.

[30] K.A. Kuo, H. Verbraken, G. Degrande, and G. Lombaert. Hybrid predictions of railway induced ground vibration using a combination of experimental measurements and numerical modelling. *Journal of Sound and Vibration*, 373:263–284, 2016. doi: https://doi.org/10.1016/j.jsv.2016.03.007.

[31] G. Lombaert and G. Degrande. Ground-borne vibration due to static and dynamic axle loads of InterCity and high-speed trains. *Journal of Sound and Vibration*, 319:1036–1066, 2009. doi: http://dx.doi.org/10.1016/j.jsv.2008.07.003.

[32] G. Lombaert, G. Degrande, J. Kogut, and S. François. The experimental validation of a numerical model for the prediction of railway induced vibrations. *Journal of Sound and Vibration*, 297:512–535, 2006. doi: https://doi.org/10.1016/j.jsv.2006.03.048.

[33] G. Lombaert, P. Galvín, S. François, and G. Degrande. Quantification of uncertainty in the prediction of railway induced ground vibration due to the use of statistical track unevenness data. *Journal of Sound and Vibration*, 333:4232–4253, 2014. doi: https://doi.org/10.1016/j.jsv.2014.04.052.

[34] P. Lopes, P. Alves Costa, M. Ferraz, R. Calçada, and A. Silva Cardoso. Numerical modeling of vibrations induced by railway traffic in tunnels: From the source to the nearby buildings. *Soil Dynamics and Earthquake Engineering*, 61–62:269–285, 2014. doi: https://doi.org/10.1016/j.soildyn.2014.02.013.

[35] C. Madshus, B. Bessason, and L. Harvik. Prediction model for low frequency vibration from high speed railways on soft ground. *Journal of Sound and Vibration*, 193(1):195–203, 1996. doi: https://doi.org/10.1006/jsvi.1996.0259.

[36] P. Alves Costa, R. Calçada, and A. Silva Cardoso. Track–ground vibrations induced by railway traffic: In-situ measurements and validation of a 2.5D FEM-BEM model. *Soil Dynamics and Earthquake Engineering*, 32:111–128, 2012. doi: https://doi.org/10.1016/j.soildyn.2011.09.002.

[37] P. Alves Costa, A. Colaço, R. Calçada, and A. Silva Cardoso. Critical speed of railway tracks. Detailed and simplified approaches. *Transportation Geotechnics*, 2:30–46, 2015. doi: https://doi.org/10.1016/j.trgeo.2014.09.003.

[38] A. Romero, A. Tadeu, P. Galvín, and J. António. 2.5D coupled BEM–FEM used to model fluid and solid scattering wave. *International Journal for Numerical Methods in Engineering*, 101:148–164, 2015. doi: https://doi.org/10.1002/nme.4801.

[39] F. Rossi and A. Nicolini. A simple model to predict train-induced vibration: theoretical formulation and experimental validation. *Enviornmental Impact Assesment Review*, 23:305–322, 2003. doi: https://doi.org/10.1016/S0195-9255(03)00005-2.

[40] X. Sheng, C.J.C. Jones, and D.J. Thompson. Prediction of ground vibration from trains using the wavenumber finite and boundary element methods. *Journal of Sound and Vibration*, 293:575–586, 2006. doi: https://doi.org/10.1016/j.jsv.2005.08.040.

[41] H. Verbraken, G. Lombaert, and G. Degrande. Verification of an empirical prediction method for railway induced vibrations by means of numerical simulations. *Journal of Sound and Vibration*, 330(8):1692–1703, 2011. doi: https://doi.org/10.1016/j.jsv.2010.10.026.

[42] M. Villot, P. Ropars, P. Jean, E. Bongini, and F. Poisson. Modeling the influence of structural modifications on the response of a building to railway vibration. *Noise Control Engineering Journal*, 11:641–651, 2011. doi: https://doi.org/10.3397/1.3633330.

[43] C. With, M. Bahrekazemi, and A. Bodare. Validation of an empirical model for prediction of train-induced ground vibrations. *Soil Dynamics and Earthquake Engineering*, 26: 983–990, 2006. doi: https://doi.org/10.1016/j.soildyn.2006.03.005.

[44] H. Xia, Y.M. Cao, and G. De Roeck. Theoretical modeling and characteristic analysis of moving-train induced ground vibrations. *Journal of Sound and Vibration*, 329:819–832, 2010. doi: https://doi.org/10.1016/j.jsv.2009.10.007.

[45] X. Zhou and K. K. Tamma. Design, analysis, and synthesis of generalized single step single solve and optimal algorithms for structural dynamics. *International Journal for Numerical Methods in Engineering*, 59:597–668, 2004. doi: https://doi.org/10.1002/nme.873.

B

PAPER B: SCOPING ASSESSMENT OF FREE-FIELD VIBRATIONS DUE TO RAILWAY TRAFFIC

The original version of this paper can be found in **www.elsevier.com**

- DOI: 10.1016/j.soildyn.2018.07.046
- Journal Name: Soil Dynamics and Earthquake Engineering
- ISSN: 0267-7261
- Journal Citation Reports (2017). Impact Factor: 2.077
  - Engineering, Geological: Q2 (17/36)
  - Geosciences, Multidisciplinary: Q2 (87/190)
- SCIMAGO (2017). Impact Factor: 1.08
  - Civil and Structural Engineering: Q1 (47/497)
  - Geotechnical Engineering and Engineering Geology: Q1 (30/367)

Scoping assessment of free-field vibrations due to railway traffic

Authors: Pedro Galvín Barrera[a], Daniel López-Mendoza[a], David P. Connolly[b], Geert Degrande[c], Geert Lombaert[c] and Antonio Romero Ordóñez[a]

[a] Escuela Técnica Superior de Ingeniería, Universidad de Sevilla, Camino de los Descubrimientos, 41092 Sevilla, Spain
[b] Institute for High Speed Rail, Leeds University, LS2 9JT Leeds, UK
[c] Department of Civil Engineering, K.U.Leuven, Kasteelpark Arenberg 40, B-3001 Leuven, Belgium

ABSTRACT

The number of railway lines both operational and under construction is growing rapidly, leading to an increase in the number of buildings adversely affected by ground-borne vibration (e.g. shaking and indoor noise). Post-construction mitigation measures are expensive, thus driving the need for early stage prediction, during project planning/development phases. To achieve this, scoping models (i.e. desktop studies) are used to assess long stretches of track quickly, in absence of detailed design information. This paper presents a new, highly customisable scoping model, which can analyse the effect of detailed changes to train, track and soil on ground vibration levels. The methodology considers soil stiffness and the combination of both the dynamic and static forces generated due to train passage. It has low computational cost and can predict free-field vibration levels in accordance with the most common international standards. The model uses the direct stiffness method to compute the soil Green's function, and a novel two-and-a-half dimensional (2.5D) finite element strategy for train-track interaction. The soil Green's function is modulated using a Neural Network (NN) procedure to remove the need for the time consuming computation of track-soil coupling. This modulation factor combined with the new train-track approach results in a large reduction in computational time. The proposed model is validated by comparing track receptance, free-field mobility and soil vibration with both field experiments and a more comprehensive 2.5D combined Finite Element Method (FEM)-Boundary Element Method (BEM) model. A sensitivity analysis is undertaken and it is shown that track type, soil properties and train speed have a dominant effect on ground vibration levels. Finally, the possibility of using average shear wave velocity introduced for seismic site response analysis to predict vibration levels is investigated and shown to be reasonable for certain smooth stratigraphy's.

Keywords: Scoping assessment; Free-field vibrations; Soil vibrations; Neural network; V_{s30} profile; Railroad vibration; Railway traffic; High speed rail; Ground-borne vibrations; Environmental Impact Assessment (EIA).

B.1 INTRODUCTION

The emergence of High-Speed Rail (HSR) has stimulated economic development in Europe, America and Asia. This has also caused an increasing number of properties and structures affected by ground-borne railway vibrations [8]. International standard ISO2631 [23, 24] addresses these negative effects and evaluates the whole-body human exposure to vibration. In addition, ISO14837 [25] is focused on the emission-propagation-immission mechanisms of waves from the train-track system (source) to the building (receiver). It provides a guide on the measurement of experimental data, vibration evaluation and mitigation.

ISO14837 [25] also outlines suggested numerical modelling approaches. At the construction stage of a new railway line, comprehensive and detailed design models are recommended. These are typically computationally expensive, and include three-dimensional (3D) [3, 17, 18, 40, 63] models with full coupling between the train-track-soil-structure system. One alternative to 3D modelling is to use a two-and-a-half-dimensional (2.5D) approach [2, 16, 19, 26, 37, 38, 48, 50, 51, 55]. These models assume the problem is continuous in the track direction and are not as such well suited for modelling transition zones, etc.

If the vibration assessment is to be undertaken at an earlier stage of railway line development, simplified scoping models [25] are often more useful. This is because they are faster running and often do not require as many input parameters.

Nelson and Sauernmann [28] presented such an empirical model to assess re-radiated ground-borne noise and vibration in buildings by combining line source response and force density. Field impact-testing procedures were used to evaluate line source transfer functions, while vehicle-track force density was indirectly obtained. Madshus et al. [44] developed a semi-empirical model to predict both expected values and confidence regions of building vibrations. To do so, a statistical analysis of recorded vibrations due to high-speed trains was undertaken. This model was focused on the low frequency vibrations of buildings founded in soft soil. Alternatively, Rossi and Nicolini [52] presented an analytical approach calibrated using railway field vibration measurements. This allowed for the quantification of train type, train speed, track properties and distance to the track, on the free-field vibrations induced by railway traffic. With et al. [62] proposed an empirical model to predict train-induced ground vibrations considering wheel force, train speed and distance to the track. Also, empirical approaches to estimate soil and building vibrations due to a train passage [6, 7] have been proposed by the Federal Railroad Administration (FRA) and the Federal Transit Administration (FTA) of the US Department of Transportation. The simplifications considered in these procedures [6, 7] were verified by the numerical model presented in reference [59]. Later, Hussein et al. [22] proposed a

sub-modelling method to couple a train-track-soil 3D model with a building, using a 2D frame made of beam elements. Kouroussis et al. [31] developed a decoupled approach, using only the finite element modelling, for characterizing building vibrations induced by adjacent tramway network with an important rail unevenness (local defect). Connolly et al. [12, 13] presented a scoping tool, called Scoperail, to instantly compute vibrations due to train passages. A machine learning approach to obtain free-field vibrations was developed by using numerical records for a wide range of train speeds and soil types. These soil vibrations were coupled with empirical factors in order to predict indoor noise in buildings and structural vibrations levels due to high speed trains. A hybrid model was described by Triepaischajonsak et al. [58], that combined a detailed vehicle-track model formulated in the time domain with a layered ground model operating in the frequency domain, based on the formulation outlined by Kausel et al. [30]. Then, forces acting on the ground were obtained from the train-track model and used in the ground model to calculate free-field vibrations. Kuo et al. [33] developed a hybrid model where the source and propagation mechanisms are decoupled. The model combined recorded data and numerical predictions considering the definitions proposed in references [6, 7]. Recently, Kouroussis et al. [32] developed a hybrid experimental-numerical model to predict vibrations from urban railway traffic. The level of vibration was calculated by combining the force density obtained from a numerical train-track model with the mobility function measured through an experimental approach.

Building upon this previous body of scoping model research, this paper presents a new scoping methodology to evaluate the free-field vibrations, aimed at aiding vibration assessments undertaken during the planning stages of a new railway line. It is able to model the effect of a large variety of input variables using minimal computational effort. To do so, track-soil interaction to define the vibration transmission is modelled by modulating the soil Green's function [29, 30, 54] with a correction factor obtained using a Neural Network (NN) approach. This allows for the coupled track-soil response to be simulated in only the time it takes to compute the soils Green's function. Then, free-field predictions are assessed by combining this track-soil model with train-track excitations. The proposed method allows for the estimation of the ground vibration descriptors presented in references [12, 13], but also the soil response in the time and frequency domains (with low computational effort).

This paper is organised as follows. First, the scoping model is presented. Next, an experimental and numerical validation of the scoping model is undertaken. A sensitivity analysis is then carried out to showcase the model and determine the effect of several key parameters on vibration propagation. Finally, the accuracy of using the average shear wave velocity of a layered soil as defined in Eurocode 8 [15] and denoted as V_{s30} is quantified.

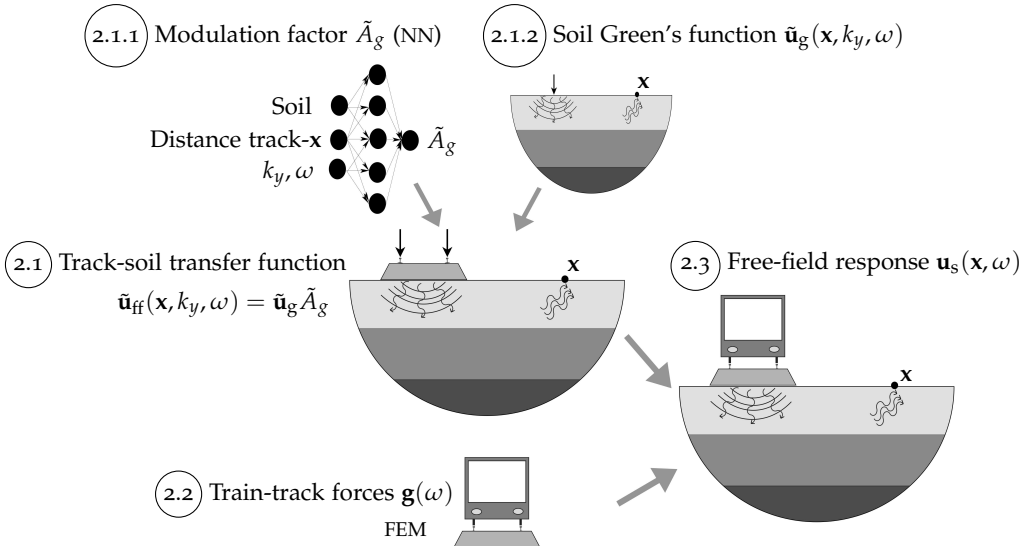

Figure B.1: Scheme of the scoping model.

B.2 NUMERICAL MODELLING

To calculate the field response (Figure B.1), the train-track-soil system was divided into two primary sub-models: a track-soil sub-model (step 2.1) and a train-track sub-model (step 2.2). To minimise the computational demand required to compute these sub-models, the following modelling strategies were used:

- To calculate the track-soil transfer function $\tilde{\mathbf{u}}_{ff}$ (Figure B.1, step 2.1) the soil Green's function $\tilde{\mathbf{u}}_g$ is computed in the absence of track. Then, to approximate the response of a combined track-ground system, the Green's function is modulated using a correction factor, calculated via a neural network procedure.
- The train-track forces $\mathbf{g}$ are calculated using a simplified Finite Element Method (FEM) track model where the underlying soil is modelled using a spring-damper element that approximates the underlying soil response (Figure B.1, step 2.2).

The free field response $\mathbf{u}_s$ (Figure B.1, step 2.3) is then computed using the formulation in the frequency-wavenumber domain presented by Lombaert et al. [38]. The train-track forces and the track-soil transfer function are described below.

B.2.1 *Track-soil transfer function*

Many vibration prediction models consider track-soil interaction using comprehensive methodologies. However, these require a high computational cost. In order to avoid this, the proposed model estimates the track-soil transfer function $\tilde{\mathbf{u}}_{ff}(\mathbf{x}, k_y, \omega)$ (Figure B.1 step 2.1) by combining the Green's functions $\tilde{\mathbf{u}}_g(\mathbf{x}, k_y, \omega)$ [30] (Figure B.1 step 2.1.2) for

a homogeneous or layered soil with a correction factor $\tilde{A}_g$ obtained using a neural network (Figure B.1 step 2.1.1). Note that the sub-indices ff and g indicate free-field response and Green's functions, respectively, and a tilde indicates a variable in the frequency-wavenumber domain. The track-soil transfer function $\tilde{\mathbf{u}}_{\mathrm{ff}}(\mathbf{x}, k_y, \omega)$ represents the response at a point $\mathbf{x} = \{d, y, 0\}$ located at the soil surface due to an impulsive vertical load at the rail. Correction factor $\tilde{A}_g$ depends on the track type and the soil properties. It is evaluated for a point $\mathbf{x}$ located at a distance d from the track centreline, a frequency ω and a wavenumber k_y. The track-soil transfer function at a point $\mathbf{x}$ can be obtained as:

$$\tilde{\mathbf{u}}_{\mathrm{ff}}(\mathbf{x}, k_y, \omega) = \tilde{A}_g(d, k_y, \omega)\tilde{\mathbf{u}}_{\mathrm{g}}(\mathbf{x}, k_y, \omega) \tag{1}$$

A NN approach to assess the correction factor $\tilde{A}_g(d, k_y, \omega)$ was selected because NN procedures are suitable methods to capture wave propagation models due to their ability for non-linear regression. NN approaches have been used to predict strong motion duration in earthquake engineering [9], to evaluate the effectiveness of trenches to reduce ground-borne vibration [21], to estimate fundamental period of vibration and maximum displacement of a building [34], to assess acceleration response spectra from tremors in the mining industry [35] and to detect damage on a railway bridge due to train passage [57].

B.2.1.1 *NN architecture*

In order to estimate the correction factor $\tilde{A}_g$ (Equation (1)), a Multilayer Perceptron (MLP) neural network architecture with a back-propagation training algorithm [10] was chosen (Figure B.2). One, two and three hidden layers were tested. A NN framework with four layers (one input, two hidden and one output) was chosen to construct the proposed model.

The correction factor $\tilde{A}_g$ modulates the Green's function $\tilde{\mathbf{u}}_{\mathrm{g}}(\mathbf{x}, k_y, \omega)$ to evaluate the track-soil function $\tilde{\mathbf{u}}_{\mathrm{ff}}(\mathbf{x}, k_y, \omega)$ at a point $\mathbf{x}$, a frequency ω and a wavenumber k_y. Coefficient $\tilde{A}_g$ depends on the track type and the soil properties. To build NN architecture ballasted and slab tracks were considered. Simplified soil profiles were used to build the NN model, using the average shear wave velocity V_{s30} as defined in Eurocode 8 [15], and computed as:

$$V_{s30} = \frac{30\ [\mathrm{m}]}{\sum_i^{N_s} \frac{h_i}{c_{s_i}}} \tag{2}$$

where h_i is the thickness of the $i-$th layer, N_s the total number of layers in the top 30 m and c_{s_i} the shear wave velocity of the $i-$th layer.

V_{s30} can be used to define a homogeneous soil, however it is non-unique because a variety of layered soils can be represented using the same value of V_{s30}. Therefore to further define the soil, the proposed model uses two additional variables: the depth h_1, and the shear wave velocity c_{s_1} of the upper layer. Then, the input layer (Figure B.2) contains six inputs parameter: soil parameters c_{s_1}, h_1, V_{s30}, the distance d between the evaluated point $\mathbf{x}$ and the track, frequency ω and wavenumber. The wavenumber is represented by the non-dimensional wavenumber $k_{dy} = k_y c_{s_1}/\omega$. In the case of a homogeneous soil, the shear wave velocity of the upper layer matches with the V_{s30} parameter $c_{s_1} = V_{s30}$, with $h_1 = 30$ m.

In order to optimise the NN architecture, successive tests were developed modifying the number of neurons in the hidden layers. It was observed that 20 and 10 neurons in the first and second hidden layer, respectively, wee optimal because performance did not improve when a larger number was used. The output layer has two parameters because the correction factor $\tilde{A}_g$ is a complex number. Therefore it is defined using its modulus $\left|\tilde{A}_g\right|$ and argument $arg\left(\tilde{A}_g\right)$:

$$\tilde{A}_g = \left|\tilde{A}_g\right| e^{\arg\left(\tilde{A}_g\right)i} \tag{3}$$

The objective of the NN procedure is to ensure the free-field response of the modulated

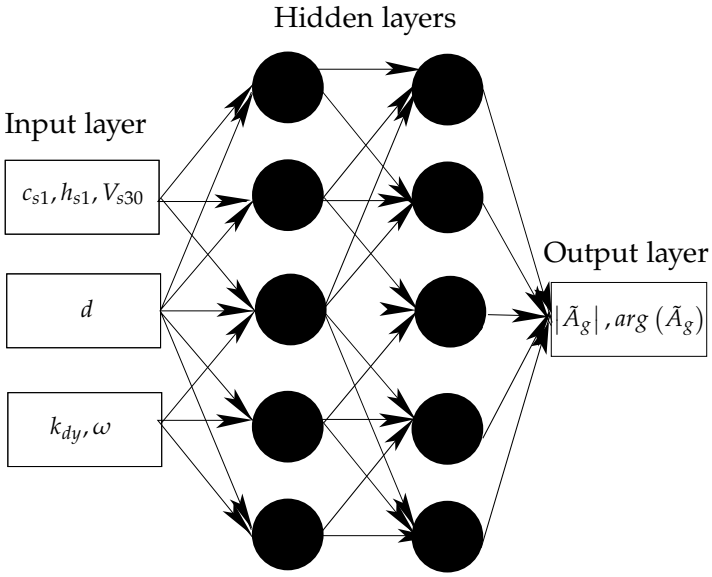

Figure B.2: Neural network model schematic.

track-soil model is equal to the response of the true, coupled track-soil model, i.e.:

$$\tilde{\mathbf{u}}_{\mathrm{ff}}^{p} = \tilde{\mathbf{u}}_{\mathrm{ff}}^{r} \tag{4}$$

being $\tilde{\mathbf{u}}_{\mathrm{ff}}^{p}$ and $\tilde{\mathbf{u}}_{\mathrm{ff}}^{r}$ the track-soil transfer function obtained from the proposed model (super-index p) (Equation (1)) and computed by using the reference model [19] (super-index r), respectively. Substituting Equations (3) and (4) into Equation (1) and considering the exponential forms of the track-soil transfer function $\tilde{\mathbf{u}}_{\mathrm{ff}}^{r}$ and the Green's functions $\tilde{\mathbf{u}}_{\mathrm{g}}$, the following expression can be obtained:

$$\left|\tilde{\mathbf{u}}_{\mathrm{ff}}^{r}\right| e^{\arg\left(\tilde{\mathbf{u}}_{\mathrm{ff}}^{r}\right)i} = \left|\tilde{A}_g\right| e^{\arg\left(\tilde{A}_g\right)i} \left|\tilde{\mathbf{u}}_{\mathrm{g}}\right| e^{\arg\left(\tilde{\mathbf{u}}_{\mathrm{g}}\right)i} \tag{5}$$

To obtain the reference values required to train the neural network, the modulus $\left|\tilde{A}_g\right|$ and argument $\arg\left(\tilde{A}_g\right)$ are obtained using Equation (5):

$$\left|\tilde{A}_g\right| = \frac{\left|\tilde{\mathbf{u}}_{\mathrm{ff}}^r\right|}{\left|\tilde{\mathbf{u}}_{\mathrm{g}}\right|} \tag{6}$$

$$\arg\left(\tilde{A}_g\right) = \arg\left(\tilde{\mathbf{u}}_{\mathrm{ff}}^r\right) - \arg\left(\tilde{\mathbf{u}}_{\mathrm{g}}\right) \tag{7}$$

The aim of the NN procedure is to map the weighted inputs (e.g. distance) to outputs (i.e. vibration). First, weighted inputs are assumed and the resulting predicted outputs are compared against the known outputs to quantify the error. This error is fed back through the network using a back-propagation training algorithm. The input weightings are then modified and the process is repeated until convergence.

The NN approach was developed by using the `Matlab Neural Network Toolbox` [42]. A tangent hyperbolic function was used as the activation function in the hidden layers due to its faster convergence compared to nonsymmetric functions [64]. The NN architecture was trained using the Levenberg-Marquardt algorithm that has been shown to be one of the fastest methods for training NNs [43]. Also, to evaluate the performance of the NN model and select the best framework, mean squared error (MSE) and coefficient of determination (R^2) were used, which are defined as follows:

$$MSE = \frac{1}{N_n}\sum_{i=1}^{N_n}\left(X_i - \hat{X}_i\right)^2 \tag{8}$$

$$R^2 = 1 - \frac{\sum_{i=1}^{N_n}\left(X_i - \hat{X}_i\right)^2}{\sum_{i=1}^{N_n}\left(X_i - \mathrm{mean}(X)\right)^2} \tag{9}$$

where X_i and $\hat{X}_i$ are the output targets and predicted outputs, respectively, and N_n is the size of the sample. These statistical indices allow the proposed model to be adjusted to approximate the reference model defined in Equation (4). When MSE and R^2 approach 0 and 1, respectively, accurate predictions of the track-soil function $\tilde{\mathbf{u}}_{\mathrm{ff}}^r$ are obtained [45, 46, 65].

To reduce the prediction error, tests were performed by transforming the raw input and output target data [56]:

- Re $\left(\tilde{A}_g\right)$ and Im $\left(\tilde{A}_g\right)$ parts were used as the output parameters.
- Modulus $\left|\tilde{A}_g\right|$ and argument $\arg\left(\tilde{A}_g\right)$ ("wrapped" and "unwrapped") were used as the output parameters.
- Input data were normalised to the interval $[-1, 1]$.
- Output target data were normalised to the interval $[-1, 1]$ and $[0, 1]$.
- Output target data modulus $\left|\tilde{A}_g\right|$ were transformed to logarithmic scale.

Unfortunately these modifications did not improve performance so were discarded. However, results were improved when output target data argument was wrapped to 2π rad and output target data modulus was presented as:

$$K_g = 20\log_{10}\left|\tilde{A}_g\right| \tag{10}$$

Then, Equations (7) and (10) were used to build the output targets.

NN DATABASE CONSTRUCTION A large number of data points are required to train and evaluate a NN. A discussion about this issue is done in Section B.6. To do so, observation points were chosen at distances d from 10 to 50 m. Three types of soil were considered: soft, medium and stiff, corresponding to types D, C and B, as classified in Eurocode 8 [15] (Table B.1). Rock type A was discarded because it is less commonly found in railway lines.

Table B.1: Soil types based on Eurocode 8.

	Description	V_{s30} [m/s]
A	Rock outcrop	> 800
B	Very dense sand or gravel, or very stiff clay	$360 - 800$
C	Dense to medium-dense sand or gravel, or stiff clay	$180 - 360$
D	Loose-to-medium sand or gravel	< 180

A sample of 60 different layered soils was randomly generated considering the following parameters:

- Number of layers N was considered to be within the range $1 - 4$.
- To avoid locating the half-space at large depths where V_{s30} is not a good estimator of soil conditions [61], the sum of layer depths was considered to be below 30 m: $\sum_{i=1}^{N} h_i \leq 30\,\text{m}$.
- In order to obtain layered soils properties compatible with (Table B.1), the shear wave velocity of each layer was considered to be in the range $c_s = 100 - 800\,\text{m/s}$.
- Layer stiffness increased with the depth.
- Density and Poisson's ratio were $\rho = 1800\,\text{kg/m}^3$ and $\nu = 0.33$, for all layers.

Figure B.3 shows the breakdown of the characteristics of the generated layered soils in the form of histograms. It can be observed that several soils presented an upper layer with depth below $h_1 = 10\,\text{m}$ and shear wave velocity around $c_{s_1} = 200\,\text{m/s}$ (Figures B.3.(a) and B.3.(b)). Also medium and stiff soils with V_{s30} values from 280 m/s to 500 m/s were mainly found in the sample of soils (Figure B.3 (c)).

Another sample of 60 homogeneous soils was built upon this previous sample of layered soils considering shear wave velocity $c_s = V_{s30}$, where V_{s30} was obtained from the sample of layered soils. So, the database set was constructed from 120 soils.

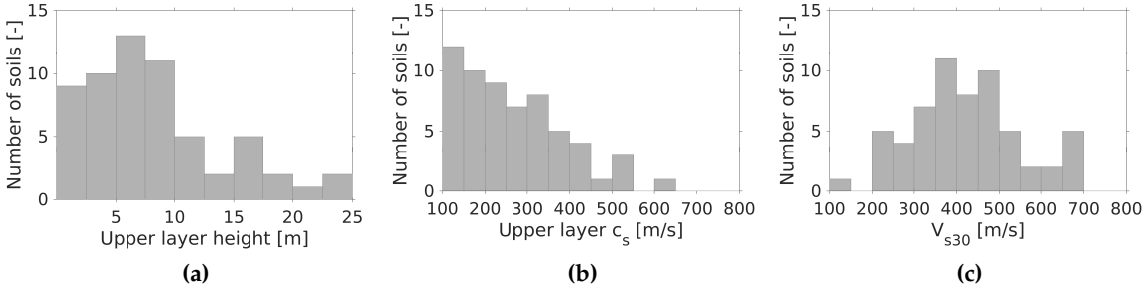

Figure B.3: Histograms of sample of soils properties: (a) upper layer height, (b) upper layer shear wave velocity and (c) V_{s30}.

The output targets (Equations (7) and (10)) were calculated using the Green's functions $\tilde{\mathbf{u}}_{\mathrm{g}}(\mathbf{x}, k_y, \omega)$ computed for the sample of layered and homogeneous soils. The reference model [19] used to obtain the track-soil transfer functions $\tilde{\mathbf{u}}^r_{\mathrm{ff}}(\mathbf{x}, k_y, \omega)$ considered ballasted and slab tracks situated on top of an embankment, supported by this sample of soils. Table B.2 summarises the properties of the ballasted and slab tracks (Figures B.5 and B.6). The material properties of the embankment were chosen equal to those of the top layer of the soil. A linear hysteretic damping model was used for all constituents of the ballasted and slab track structure. The properties were obtained from published literature (among them [18]).

Output targets were obtained for the sample of 120 soils and considering distances d : $\{10, 20, 30, 40, 50\}$ m from the track centreline. The sample of 75 frequencies was within the range 0.5 Hz - 150 Hz. A sample of 98 non-dimensional wavenumber k_{dy} values from 0 to 100 was employed. This resulted in: 120 soil types $\times$ 5 distances $\times$ 75 frequencies $\times$ 98 wavenumbers $=$ 4410000 data points. These output targets were divided in two subsamples: three-quarters for NN training and one-quarter for NN testing.

NN TESTING Once the NN was trained and its architecture finalised, model performance was evaluated. Figure B.4 shows a scatter plot to evaluate the agreement in the predictions of the correction factor $\tilde{A}_g$. The indices R^2 and MSE are related in Table B.3. It can be observed that the agreement in the estimation of the modulus parameter K_g is quite good (Figure B.4.(a)). Regarding the argument parameter $arg\left(\tilde{A}_g\right)$, the agreement is not quite as strong (Figure B.4.(b)). However, as shown in the next section, the NN predictions of the correction factor $\tilde{A}_g$ provide a reasonable estimate of the track-soil transfer function $\tilde{\mathbf{u}}_{\mathrm{ff}}$.

Table B.2: Ballasted and slab track properties.

RAIL	
Bending stiffness $E_\mathrm{r} I_\mathrm{r}$ $\left[\mathrm{N/m^2}\right]$	6.18×10^6
Mass per unit length $\rho_\mathrm{r} A_\mathrm{r}$ [kg/m]	60.83
Loss factor η_r	0.05
RAIL PAD	
Equivalent stiffness $\overline{k}_\mathrm{rp}$ $\left[\mathrm{N/m^2}\right]$	150×10^6
Loss factor η_rp	0.25
SLEEPER	
Spacing d_sl [m]	0.60
Length l_sl [m]	2.60
Width b_sl [m]	0.35
Height h_sl [m]	0.22
Mass per sleeper m_sl [kg]	300
Rotational inertia $\rho_\mathrm{sl}\overline{I}_\mathrm{sl}$ $\left[\mathrm{kgm^2/m}\right]$	567
BALLAST	
Length at the top l_b1 [m]	2.60
Length at the bottom l_b2 [m]	2.87
Width b_b [m]	0.35
Height h_b [m]	0.3
Equivalent mass $\overline{m}_\mathrm{b}$ [kg/m]	796
Vertical stiffness k_b [N/m]	500×10^6
Loss factor η_b	1.0
SLAB	
Length l_slab [m]	2.60
Height h_slab [m]	0.30
Bending stiffness $E_\mathrm{slab} I_\mathrm{slab}$ $\left[\mathrm{Nm^2}\right]$	117×10^6
Mass per unit length $\rho_\mathrm{slab} A_\mathrm{slab}$ [kg/m]	1950
Loss factor η_slab	0.01
EMBANKMENT	
Length at the top l_e1 [m]	3.50
Length at the soil surface l_e2 [m]	7.00
Height h_e [m]	1.50

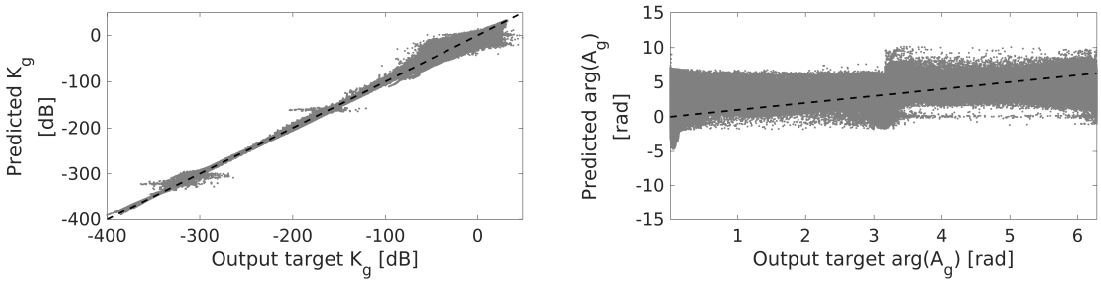

(a) **(b)**

Figure B.4: Results of neural network model of the (a) K_g and (b) $arg\left(\tilde{A}_g\right)$ parameters.

Table B.3: NN performance.

		Training set		Testing set	
		R^2	MSE	R^2	MSE
Ballasted track	K_g	0.99	3.7 dB^2	0.99	3.7 dB^2
	$arg\left(\tilde{A}_g\right)$	0.64	1.2 rad^2	0.64	1.2 rad^2
Slab track	K_g	0.99	5.9 dB^2	0.99	5.9 dB^2
	$arg\left(\tilde{A}_g\right)$	0.75	1.6 rad^2	0.75	1.6 rad^2

B.2.2 *Track-soil forces*

B.2.2.1 *Track model*

The track-soil forces (Figure B.1 step 2.2) are calculated using a simplified 2.5D FEM model (Figures B.5 and B.6). The model allows both linear hysteretic or viscous damping models for the constituents in the ballasted and slab track structure.

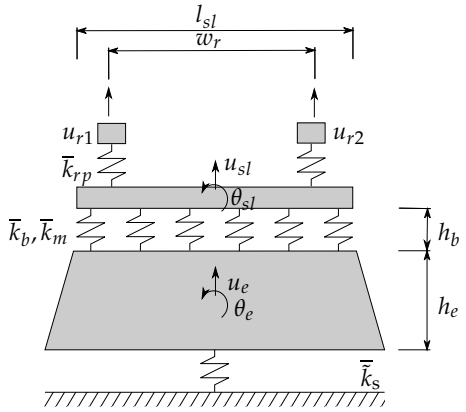

Figure B.5: Cross section of ballasted track model.

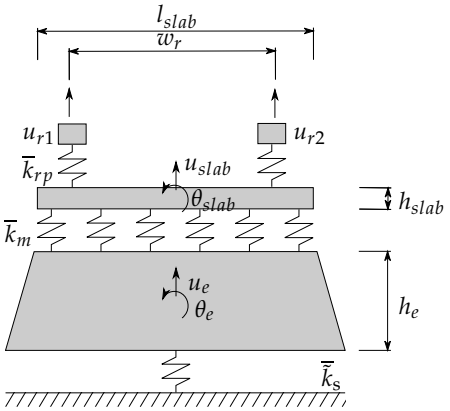

Figure B.6: Cross section of slab track model.

For the ballasted track model, the rails are represented using Euler-Bernoulli beams with a bending stiffness $E_\mathrm{r} I_\mathrm{r}$ and a mass $\rho_\mathrm{r} A_\mathrm{r}$ per unit length. The rail displacements are denoted as $u_{\mathrm{r}1}(x_1, t)$ and $u_{\mathrm{r}2}(x_2, t)$. The position of the rails is determined by x_1 and x_2, with $x_2 - x_1$ equal to the track gauge w_r. The internal energy dissipation in the rail is modelled using a loss factor η_r.

The rail pads are modelled as continuous spring-damper connections. The rail pad stiffness k_rp and damping coefficient c_rp of a single rail pad are used to calculate the equivalent stiffness $\overline{k}_\mathrm{rp} = k_\mathrm{rp}/d_\mathrm{sl}$ and damping $\overline{c}_\mathrm{rp} = c_\mathrm{rp}/d_\mathrm{sl}$ where d_sl is the sleeper spacing. Alternatively, a loss factor η_rp can be used to describe rail pad behaviour as, $\overline{k}_\mathrm{rp} = \overline{k}_\mathrm{rp}(1 + i\eta_\mathrm{rp})$.

The concrete sleepers are assumed to be rigid in the plane of the track cross section, so that the vertical sleeper displacements along the track are determined by the vertical displacement $u_\mathrm{sl}(x, t)$ and rotation $\theta_\mathrm{sl}(x, t)$ at the centre of gravity of the sleeper. The sleepers are modelled as a uniformly distributed mass $\overline{m}_\mathrm{sl} = m_\mathrm{sl}/d_\mathrm{sl}$. The rotational inertia of the sleeper is estimated as $\rho_\mathrm{sl}\overline{I}_\mathrm{sl} = \rho_\mathrm{sl} I_\mathrm{sl}/d_\mathrm{sl}$.

The ballast bed is modelled using a set of distributed linear springs and dampers. The smeared ballast stiffness $\overline{k}_\mathrm{b}$ is computed from the vertical spring stiffness k_b per sleeper as $k_\mathrm{b}/d_\mathrm{sl}$. The viscous damping in the ballast bed is accounted for by a ballast impedance and equals $\overline{k}_\mathrm{b} + i\omega\overline{c}_\mathrm{b}$. Alternatively, a loss factor η_b can be used to describe ballast behaviour as $\overline{k}_\mathrm{b} = \overline{k}_\mathrm{b}(1 + i\eta_\mathrm{b})$. The equivalent ballast mass $\overline{m}_\mathrm{b}$ is computed using the ballast mass m_b under each sleeper as $m_\mathrm{b}/d_\mathrm{sl}$. The ballast mass m_b is estimated from the height h_b of the ballast layer and lengths $l_{\mathrm{b}1} = l_\mathrm{sl}$ and $l_{\mathrm{b}2}$ at the top and the bottom of the ballast layer, respectively, as $m_\mathrm{b} = 0.5\rho_\mathrm{b} h_\mathrm{b}(l_{\mathrm{b}1} + l_{\mathrm{b}2})b_\mathrm{sl}$.

The embankment is represented using an Euler-Bernoulli beam with a bending stiffness $E_\mathrm{e} I_\mathrm{e}$, a torsional rigidity $G_\mathrm{e} J_\mathrm{e}$, a loss factor η_e, a rotational inertia $\rho_\mathrm{e} I_{pe}$, and a mass $\rho_\mathrm{e} A_\mathrm{e}$ per unit length. The embankment properties are approximated to be equal to the uppermost soil layer. The effect of the embankment on ground vibrations due to railway traffic has been previously studied by other authors (among them [19, 47]).

A ballast mat can be simulated using spring-damper elements between the embankment and the ballast with equivalent stiffness and damping (or loss factor) $\overline{k}_{\mathrm{m}}$ and $\overline{c}_{\mathrm{m}}$ (or η_{m}), respectively.

For the slab track model, the rails, rail pads and embankment are modelled as in the ballasted track model. The slab is represented by an Euler-Bernoulli beam with a bending stiffness $E_{\mathrm{slab}}I_{\mathrm{slab}}$, a torsional rigidity $G_{\mathrm{slab}}J_{\mathrm{slab}}$, a rotational inertia $\rho_{\mathrm{slab}}I_{p\mathrm{slab}}$, a loss factor η_{slab} and a mass per unit length $\rho_{\mathrm{slab}}A_{\mathrm{slab}}$. A floating slab track can be represented as in the case of the ballast mat.

The underlying soil is represented using a spring-damper element with stiffness $\overline{\tilde{k}}_{\mathrm{s}}(k_y,\omega)$. The equivalent stiffness and damping of the soil is estimated by the vertical soil response computed from the Green's function for a homogeneous or layered half-space. The soil flexibility $1/\overline{\tilde{k}}_{\mathrm{s}}(k_y,\omega)$ is obtained from the soil response induced by a unit vertical load applied at the soil surface and evaluated at a point located at a distance $d = w_{\mathrm{r}}/2$ from the track centerline (under the rail). Note that because the spring-damper element does not consider the effect of a moving load, the model ignores the dynamic effects that may be induced when approaching critical velocity [53]. The continuity of displacement is fulfilled between the soil and the track.

2.5D FEM FORMULATION The 2.5D FEM formulation follows that outlined in [19]:

$$\left[-\omega^2\mathbf{M}_{\mathrm{bb}} + \mathbf{K}^0_{\mathrm{bb}} - ik_y\mathbf{K}^1_{\mathrm{bb}} - k_y^2\mathbf{K}^2_{\mathrm{bb}} + ik_y^3\mathbf{K}^3_{\mathrm{bb}} + k_y^4\mathbf{K}^4_{\mathrm{bb}} + \tilde{\mathbf{K}}^{\mathrm{s}}_{\mathrm{bb}}(k_y,\omega)\right]\tilde{\mathbf{u}}_{\mathrm{b}}(k_y,\omega) = \tilde{\mathbf{f}}_{\mathrm{b}}(k_y,\omega) \tag{11}$$

where $\mathbf{K}^0_{\mathrm{bb}}$, $\mathbf{K}^1_{\mathrm{bb}}$, $\mathbf{K}^2_{\mathrm{bb}}$, $\mathbf{K}^3_{\mathrm{bb}}$ and $\mathbf{K}^4_{\mathrm{bb}}$ are the stiffness matrices, $\mathbf{M}_{\mathrm{bb}}$ is the mass matrix, $\tilde{\mathbf{f}}_{\mathrm{b}}(k_y,\omega)$ is the external load vector, and $\mathbf{K}^{\mathrm{s}}_{\mathrm{bb}}(k_y,\omega)$ represents the dynamic soil stiffness matrix. For simplicity, matrices $\mathbf{K}^1_{\mathrm{bb}}$, $\mathbf{K}^2_{\mathrm{bb}}$ and $\mathbf{K}^3_{\mathrm{bb}}$ are discarded so that the proposed model does not contain any volume or shell elements. The finite element matrices $\mathbf{M}_{\mathrm{bb}}$, $\mathbf{K}^0_{\mathrm{bb}}$ and $\mathbf{K}^4_{\mathrm{bb}}$ in Equation (11) are independent of wavenumber k_y and frequency ω, and are only assembled once. Equation (11) is now further elaborated by dividing the finite element degrees of freedom $\tilde{\mathbf{u}}_{\mathrm{b}}(k_y,\omega)$ into internal degrees of freedom $\tilde{\mathbf{u}}_{\mathrm{b}_1}(k_y,\omega)$ and degrees of freedom $\tilde{\mathbf{u}}_{\mathrm{b}_2}(k_y,\omega)$ on the soil-structure interface:

$$\left(-\omega^2\begin{bmatrix}\mathbf{M}_{\mathrm{b}_1\mathrm{b}_1} & \mathbf{M}_{\mathrm{b}_1\mathrm{b}_2}\\ \mathbf{M}_{\mathrm{b}_2\mathrm{b}_1} & \mathbf{M}_{\mathrm{b}_2\mathrm{b}_2}\end{bmatrix} + \begin{bmatrix}\mathbf{K}^0_{\mathrm{b}_1\mathrm{b}_1} & \mathbf{K}^0_{\mathrm{b}_1\mathrm{b}_2}\\ \mathbf{K}^0_{\mathrm{b}_2\mathrm{b}_1} & \mathbf{K}^0_{\mathrm{b}_2\mathrm{b}_2}\end{bmatrix} + k_y^4\begin{bmatrix}\mathbf{K}^4_{\mathrm{b}_1\mathrm{b}_1} & \mathbf{K}^4_{\mathrm{b}_1\mathrm{b}_2}\\ \mathbf{K}^4_{\mathrm{b}_2\mathrm{b}_1} & \mathbf{K}^4_{\mathrm{b}_2\mathrm{b}_2}\end{bmatrix} + \begin{bmatrix}0 & 0\\ 0 & \tilde{\mathbf{K}}^{\mathrm{s}}_{\mathrm{b}_2\mathrm{b}_2}(k_y,\omega)\end{bmatrix}\right)\begin{bmatrix}\tilde{\mathbf{u}}_{\mathrm{b}_1}(k_y,\omega)\\ \tilde{\mathbf{u}}_{\mathrm{b}_2}(k_y,\omega)\end{bmatrix} = \begin{bmatrix}\tilde{\mathbf{f}}_{\mathrm{b}_1}(k_y,\omega)\\ \tilde{\mathbf{f}}_{\mathrm{b}_2}(k_y,\omega)\end{bmatrix} \tag{12}$$

The dynamic soil stiffness matrix $\tilde{\mathbf{K}}^{\mathrm{s}}_{\mathrm{b}_2\mathrm{b}_2}(k_y,\omega) = \overline{\tilde{k}}_{\mathrm{s}}(k_y,\omega)$ is computed by means of the Green's function [30] (Figure B.1 step 2.1.2).

The following describes the evaluation of train-track interaction forces (Figure B.1 step 2.2). Both quasi-static excitation and dynamic excitation due to random track unevenness are taken into account [39], and the dynamic contributions depend upon the rail displacements $\tilde{\mathbf{u}}_{\mathrm{r}}(k_y, \omega)$ obtained using Equation (12).

B.2.2.2 *Vehicle loading*

Firstly, a Power Spectral Density (PSD) function is assumed for the random track unevenness:

$$\tilde{S}_{\mathrm{rzz}}(k_y) \quad = \quad \tilde{S}_{\mathrm{rzz}}(k_{y0}) \left(\frac{k_y}{k_{y0}} \right)^{-w} \tag{13}$$

where $\tilde{S}_{\mathrm{rzz}}(k_{y0})$ is the reference value of the PSD at k_{y0} and w is the exponent that determines how strong the PSD function decreases with increasing wavenumber k_y. The coefficients $\tilde{S}_{\mathrm{rzz}}(k_{y0})$ and w are obtained from standards [1]. $w = 3.5$ and $k_{y0} = 1\,\mathrm{rad/m}$ are commonly assumed for railway unevenness. The value of $\tilde{S}_{\mathrm{rzz}}(k_{y0})$ depends on the track maintenance [20]: $5 \times 10^{-7}\,\mathrm{m}^3$ (poor), $1.25 \times 10^{-7}\,\mathrm{m}^3$ (medium) and $1 \times 10^{-9}\,\mathrm{m}^3$ (good).

The rail unevenness $\mathbf{u}_{\mathrm{w/r}}(\omega)$ is evaluated as:

$$\mathbf{u}_{\mathrm{w/r}}(\omega) = \mathbf{T}(\omega) \frac{1}{v} \tilde{u}_{rz} \left(-\frac{\omega}{v} \right) \tag{14}$$

where $\tilde{u}_{rz}(k_y)$ is the wavenumber transform of the rail unevenness $u_{rz}(y)$ and $\mathbf{T}(\omega)$ is a vector that collects the phase shift for each axle moving at a constant speed v, being:

$$u_{rz}(y) = \sum_{m=1}^{n} \sqrt{2 \tilde{S}_{rzz}(k_{ym}) \Delta k_y} \cos(k_{ym} y - \theta_m) \tag{15}$$

where $k_{ym} = m \Delta k_y$ is the wavenumber sampling, Δk_y the wavenumber bin and θ_m represents random phase angles uniformly distributed in the interval $[0, 2\pi]$. The dynamic forces $\mathbf{g}_d(\omega)$ are computed from the track and vehicle compliances assuming a perfect contact between both [38]:

$$\mathbf{u}_{\mathrm{c}}(\omega) \quad = \quad \mathbf{u}_{\mathrm{r}}(\omega) + \mathbf{u}_{\mathrm{w/r}}(\omega) \tag{16}$$

where $\mathbf{u}_{\mathrm{c}}$ represents the displacements at the vehicle-track interface and, both the rail displacements $\mathbf{u}_{\mathrm{r}}(\omega)$ and the rail unevenness $\mathbf{u}_{\mathrm{w/r}}(\omega)$ are evaluated at a fixed position in the moving frame of reference. The dynamic loads are computed as:

$$\left[\mathbf{C}^t(\omega) + \mathbf{C}^v(\omega) \right] \mathbf{g}_d(\omega) = -\mathbf{u}_{\mathrm{w/r}}(\omega) \tag{17}$$

where $\mathbf{C}^v(\omega)$ is the vehicle compliance and $\mathbf{C}^t(\omega)$ is the track compliance.

The vehicle's unsprung mass is the train mass that influences mainly vertical dynamic loads [37], meaning vehicle compliance can be assessed as $\mathbf{C}^v(\omega) = \mathrm{diag}(-1/(M_u \omega^2))$, where M_u is the unsprung axle mass.

Additionally, the track compliance C^t_{lk} relates the track displacement at the position of axle k due to a unit load at axle l. The track compliance is obtained from the rail impulse response $\tilde{u}_\mathrm{r}$ using the following equation [38]:

$$\mathbf{C}^t_{lk}(\tilde{\omega}) = \frac{1}{2\pi}\int_{-\infty}^{+\infty} \tilde{u}_\mathrm{r}(k_y, \tilde{\omega} + k_y v) e^{-\mathrm{i}k_y(y_l - y_k)} \mathrm{d}k_y \tag{18}$$

where y_l and y_k are the positions of l-th and k-th axles respectively. Also, $\tilde{\omega} = \omega - k_y v$ and v is the train speed.

The quasi-static load of the k-th axle is determined by the weight w_k carried by the axle [38]:

$$g_{q_k}(\tilde{\omega}) = w_k 2\pi\delta(\tilde{\omega}) \tag{19}$$

B.2.3 *Free-field response*

Once the track-soil transfer function $\tilde{\mathbf{u}}_\mathrm{ff}$ (Equation (1)), the dynamic excitation $\mathbf{g}_d$ (Equation (17)) and the quasi-static excitation $\mathbf{g}_q$ (Equation (19)) are obtained, the soil response $\mathbf{u}_\mathrm{s}(\mathbf{x}, \omega)$ due a train passage at speed v is determined by following the 2.5D formulation in the wavenumber-frequency domain described in reference [38]. The free-field response $\mathbf{u}_\mathrm{s}(\mathbf{x}, \omega)$ is decomposed into its static $\mathbf{u}_\mathrm{qs}$ and dynamic $\mathbf{u}_\mathrm{ds}$ components $\mathbf{u}_\mathrm{s}(\mathbf{x}, \omega) = \mathbf{u}_\mathrm{qs}(\mathbf{x}, \omega) + \mathbf{u}_\mathrm{ds}(\mathbf{x}, \omega)$. The static and dynamic contributions, u_qsi and u_dsi, in the i-th direction at a point $\mathbf{x}$ can be evaluated as:

$$u_\mathrm{qsi}(\mathbf{x}, \omega) = \sum_{k=1}^{n_a} w_k \tilde{h}_\mathrm{ffi}(y - y_k, \omega, 0) \tag{20}$$

$$u_\mathrm{dsi}(\mathbf{x}, \omega) = \frac{1}{2\pi}\sum_{k=1}^{n_a}\int_{-\infty}^{+\infty} \tilde{h}_\mathrm{ffi}(y - y_k, \omega, \tilde{\omega}) g_{\mathrm{d}_k}(\tilde{\omega}) \mathrm{d}\tilde{\omega} \tag{21}$$

where n_a is the number of axles and w_k, y_k and g_{d_k} refer to weight carried, position and dynamic load of the k-th axle respectively. A change of variables $\tilde{\omega} = \omega - k_y v$ is again considered and the relation $\tilde{h}_\mathrm{ffi}(y - y_k, \omega, \tilde{\omega}) = \frac{1}{v}\tilde{u}_\mathrm{ffi}(\mathbf{x}, \frac{\omega - \tilde{\omega}}{v}, \omega) \exp\left[-i\frac{\omega - \tilde{\omega}}{v}(y - y_k)\right]$ is used to express Equations (20) and (21) in compact forms.

B.2.4 *Building response*

After obtaining the free-field response, it can be used to compute the vibration within buildings located close to the line. To do so, the free-field response can be used as an input for a soil-structure interaction model such as [41]. This entire train-track-soil-building model has been combined into a `MATLAB` toolbox, however this present work focuses on the calculation of free-field vibration.

B.3 EXPERIMENTAL AND NUMERICAL VALIDATION

In this section an experimental (i.e. field testing) and numerical validation of the proposed scoping model is undertaken.

B.3.1 *Experimental validation*

A field experiment was undertaken on the High Speed Train (HST) line between Brussels and Köln. Accelerometers were used to record rail and sleeper receptances, free-field mobility and also the free-field vibrations generated during the passage of Thalys HST at a speed of $v = 294\,\mathrm{km/h}$. Table B.6 shows the carriage length L_t, the distance between bogies L_b, the axle distance L_a, the total axle mass M_t and the unsprung axle mass M_u for all carriages. A ballasted track with the properties shown in Table B.4 and supported by a layered subgrade with the characteristics shown in Table B.5 was studied. A detailed description of the field work campaign is give in [38]. To validate the scoping model against the field data, both track response and free-field response were analysed.

Table B.4: HST track Brussels-Köln.

RAIL	
Bending stiffness $E_\mathrm{r} I_\mathrm{r}$ $\left[\mathrm{N/m^2}\right]$	6.45×10^6
Mass per unit length $\rho_\mathrm{r} A_\mathrm{r}$ [kg/m]	60.3
RAIL PAD	
Stiffness k_rp [N/m]	153.4×10^6
Damping c_rp [Ns/m]	13.5×10^3
SLEEPER	
Spacing d_sl [m]	0.6
Length l_sl [m]	2.5
Width b_sl [m]	0.235
Height h_sl [m]	0.205
Mass per sleeper m_sl [kg]	300
BALLAST	
Height h_b [m]	0.35
Equivalent mass $\overline{m}_\mathrm{b}$ [kg/m]	582.6
Vertical stiffness k_b [N/m]	920.7×10^6
Damping c_b [Ns/m]	16.6×10^3

Table B.5: Soil characteristics.

	h [m]	c_p [m/s]	c_s [m/s]	ξ [-]	ρ [kg/m^3]	ν
Layer 1	3	300	150	0.03	2000	0.333
Half-space	∞	560	280	0.03	2000	0.333

Table B.6: Geometrical and mass characteristics of the Thalys HST.

	No.of carriages	No.of axles	L_t[m]	L_b[m]	L_a[m]	M_t[kg]	M_u[kg]
Traction cars	2	4	22.15	14.00	3.00	17000	2027
End carriages	2	3	21.84	18.70	3.00	17000	2027
Central carriages	6	2	18.70	18.70	3.00	17000	2027

A track unevenness profile (Equation (13)) with reference value $\tilde{S}_{\mathrm{rzz}}(k_{y0}) = 1.36 \times 10^{-8}\,\mathrm{m}^3$ of the PSD at $k_{y0} = 1\,\mathrm{rad/m}$ and an exponent $w = 3.5$ was considered. A more detailed experimental description is found in the original work [38].

B.3.1.1 *Track-soil system*

Figure B.7 shows a comparison between rail receptances calculated using the scoping model and those measured experimentally. The results presented in reference [38] are also presented. It is seen that the scoping model slightly overestimates experimental rail receptance up to 27 Hz. On the other hand, the curves from the scoping model are under the experimental response at mid and high frequencies. The agreement with the experimental result is less good than in those presented in reference [38], however this is expected due to the underlying simplifications and considered acceptable for a scoping model. A difference between both models of -22 dB at 100 Hz was found. In addition to the rail displacement $\tilde{\mathbf{u}}_{\mathrm{r}}$ the model can also compute sleeper receptance, as shown in Figures B.7.(c) and B.7.(d). A similar accuracy is found.

Figure B.8 shows experimental and computed mobilities of the track-soil system at distances $\{8, 16, 24, 32, 48, 64\}$ m from the track centreline. The free-field mobility predictions are overestimated, but the agreement is good and the computed results exhibit a similar frequency dependence compared to the experimental data. Differences between the scoping model and reference [38] increase with the frequency up to a value of -15 dB. The discrepancies at short distances from the track (Figures B.8.(a) and B.8.(b)) are because the NN approach was trained for a ballasted track over an embankment, while the HST line between Brussels and Köln is an at-grade track. The effect of the embankment is significant at the locations closer to the track [19, 47].

Figure B.8 shows the effect of a $\pm 10\%$ variation in $|\tilde{A}_g|$-values, on the predicted vibration from the scoping model. The predictions are not highly affected by small changes in $|\tilde{A}_g|$-values and they present a consistent behaviour.

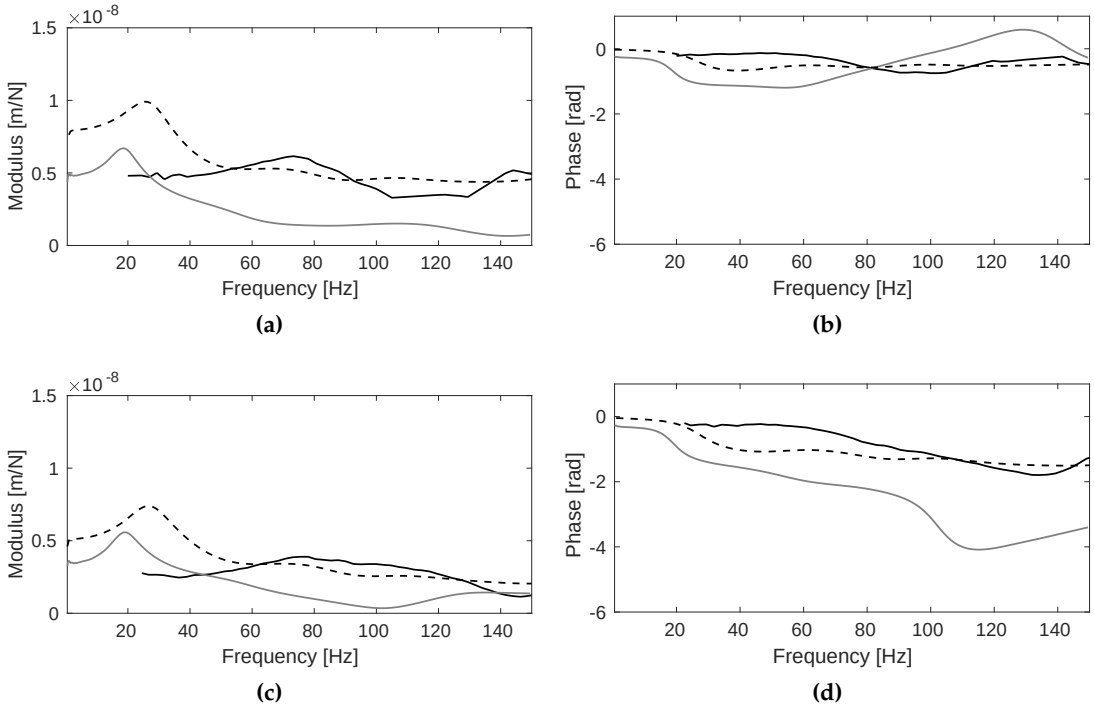

Figure B.7: (Black line) experimental and (grey line) computed with the scoping model (a, b) rail and (c, d) sleeper receptances. Superimposed (dashed black line) the solution presented in reference [38].

B.3.1.2 *Free-field response*

The one-third octave band center frequencies of the free-field response at distances $\{8, 16, 24, 32, 48, 64\}$ m from the track centreline due to a Thalys HST passage at $v = 294$ km/h are presented in Figure B.9. The response from [38] is superimposed. The one-third octave band spectrum has been computed according to the German standard DIN 45672-2 [11] for a reference period T2 during which the response is considered to be stationary. The frequency content is concentrated at frequencies below 100 Hz, for both the scoping model and experimental results. In general, the computed response from the scoping model underestimates the experimental results. The discrepancies between both results computed using the scoping model and presented in [38] are in accordance with Figure B.8.

Figure B.10 shows the time history of the free-field response due to a Thalys passage at $v = 294$ km/h. The time domain response was evaluated from an inverse Fourier transform of the frequency response in the range from 0.5 to 150 Hz, with a frequency sampling of $\Delta f = 0.01$ Hz. The duration of both experimental and computed responses are increasing with the distance from the track. The accuracy to predict the amplitude of the free-field response due to a train passage is sufficient for the purpose of a preliminary study.

In accordance with the comparison shown in this section, it can be concluded that the scoping model presents a good agreement with the experimental results.

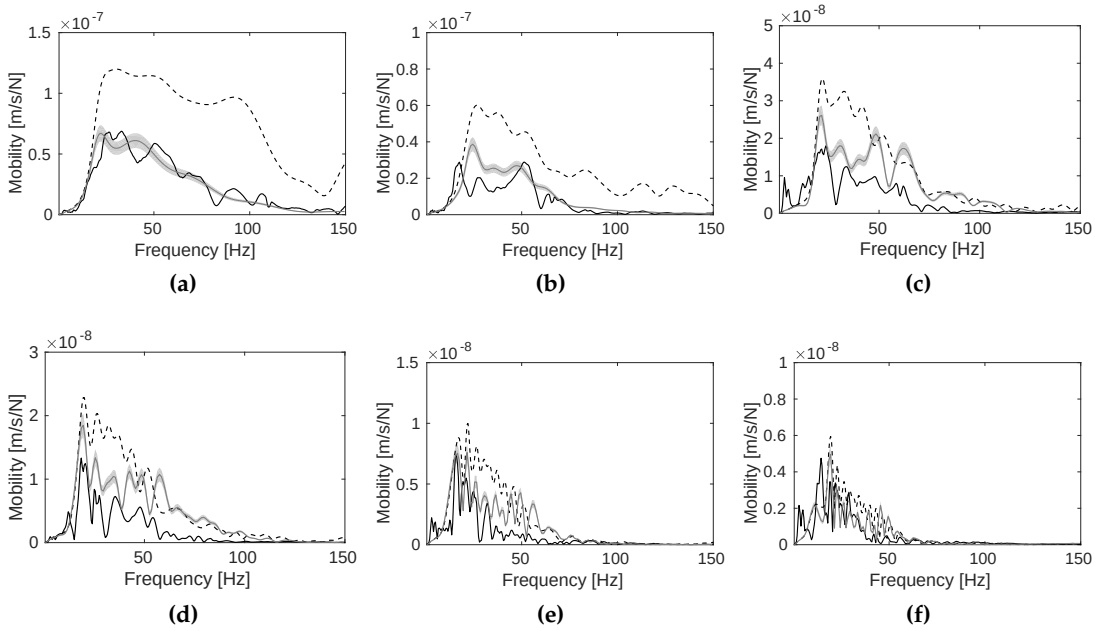

Figure B.8: (Black line) the experimental and (grey line) computed with the scoping model free-field vertical mobility at a distance of: (a) 8 m; (b) 16 m; (c) 24 m; (d) 32 m; (e) 48 m and (f) 64 m from the track centerline. The effect of a $\pm 10\%$ variation in $|\tilde{A}_g|$-values is represented by the grey area. Superimposed (dashed black line) the solution presented in reference [38].

B.3.2 *Numerical validation*

To further validate the scoping model, its predictions were compared against a more comprehensive, 'reference' model. The reference model (Figure B.11) is based upon a 2.5D boundary element-finite element methodology in the frequency-wavenumber domain [38, 19]. It was designed to compute the generation of railway vibrations and their propagation through the neighbouring soil. First, the track-soil transfer function $\tilde{\mathbf{u}}_{\mathrm{ff}}$ is calculated by modelling the track using FEM and the soil using the Boundary Element Method (BEM). This result corresponds to the soil response due to an impulse load applied on the rails (Figure B.11 step 2.1). Next, the train-track forces $\mathbf{g}(\omega)$ are calculated considering both quasi-static and dynamic contributions (Figure B.11 step 2.2). Finally, the train-track interaction forces are combined with the track-soil transfer function, resulting in the free-field response due to train passage $\mathbf{u}_{\mathrm{s}}$ at a point $\mathbf{x}$ (Figure B.11, step 2.3).

The scoping model has two main novelties: the use of a simplified 2.5D FEM track model, and a NN procedure to convert the soil Green's fuctions to the track-soil response. Therefore, a series of tests were performed to assess the accuracy of each new sub-model. To do so, a variety of modelling scenarios were analysed. Three track cases (ballasted track over an embankment, an at-grade ballasted track and a slab track over an embankment), four soil types and a train speed $v = 100\,\mathrm{km/h}$ were considered. Quasi-static excitation

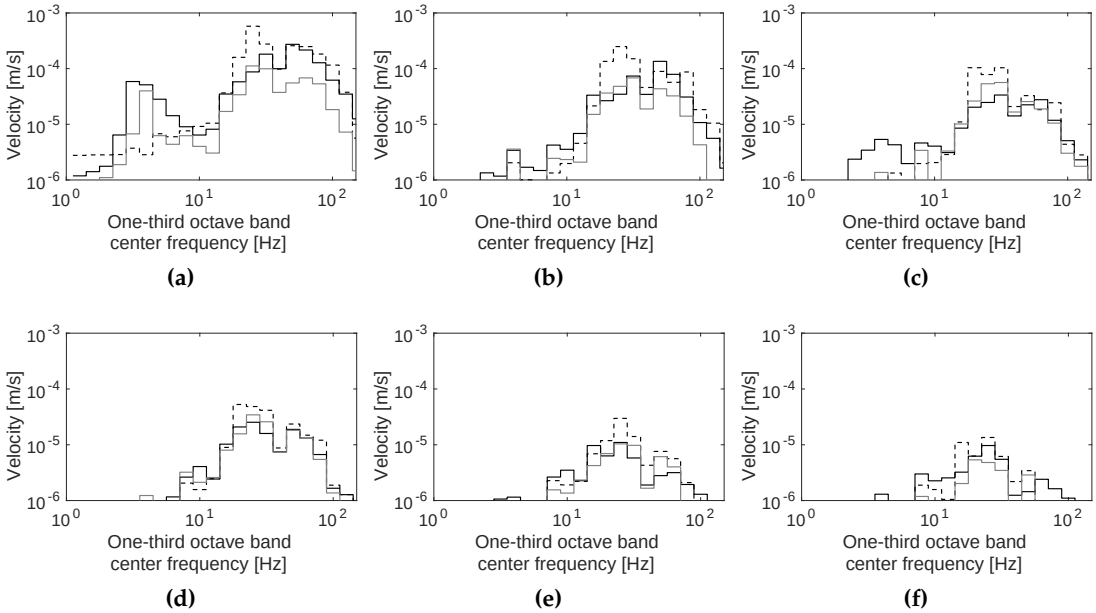

Figure B.9: (Black line) the experimental and (grey line) computed with the scoping model one-third octave band center frequency of the vertical velocity at the free field at a distance of: (a) 8 m; (b) 16 m; (c) 24 m; (d) 32 m; (e) 48 m and (f) 64 m from the track centerline during the passage of the Thalys HST at a speed $v = 294\,\mathrm{km/h}$. Superimposed (dashed black line) the solution presented in reference [38]

.

and dynamic excitation due to random track unevenness were taken into account [37], and the same track unevenness profile was considered for all cases. The free-field mobility and free-field response due to railway traffic were obtained at a point located at a distance of $d = 20\,\mathrm{m}$ from the track centreline.

Regarding the vehicle, a S-100 series train (Table B.7) was simulated. It should be noted that because the train speed is below the critical velocity of the track system [49], the dynamic contribution will be dominant in the free-field response [37].

Table B.7: Geometrical and mass characteristics of the S-100 train.

	No.of carriages	No.of axles	L_t[m]	L_b[m]	L_a[m]	M_t[kg]	M_u[kg]
Traction cars	2	4	22.15	14.00	3.00	17185	2048
End carriages	2	3	21.84	18.70	3.00	11523	2003
Central carriages	6	2	18.70	18.70	3.00	15523	2003

B.3.2.1 *Train-track forces*

To thoroughly validate the train-track forces sub-model, three track types were analysed. Track 1 was a classical ballasted track (Section B.2.1.1 (Table B.2)) supported by an embank-

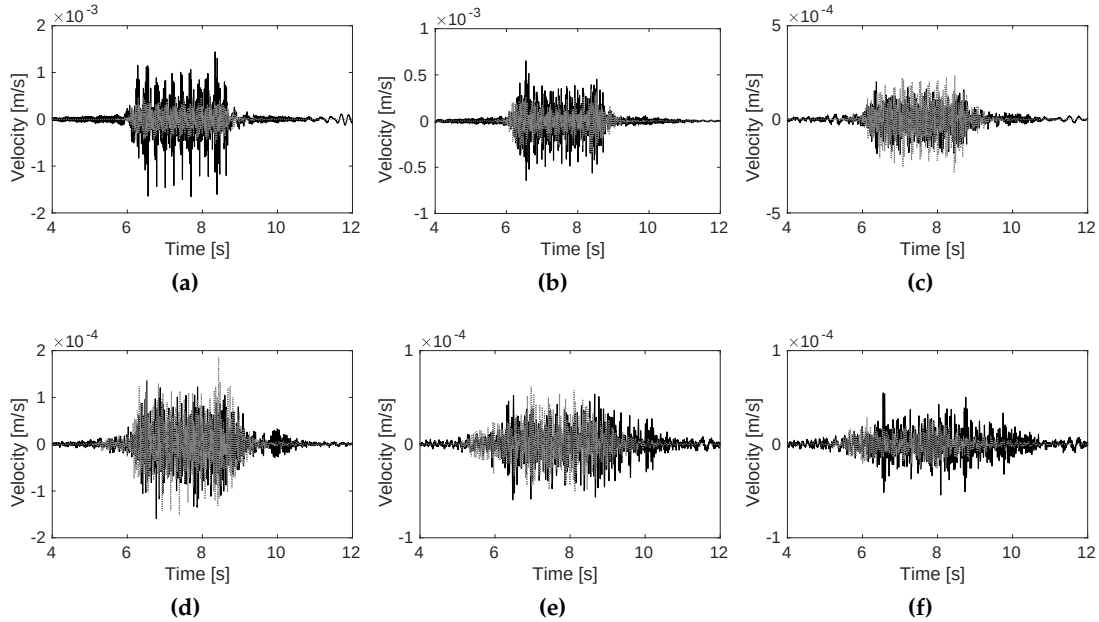

Figure B.10: (Black line) the experimental and (grey line) computed with the scoping model time history of the vertical velocity at the free field at a distance of: (a) 8 m; (b) 16 m; (c) 24 m; (d) 32 m; (e) 48 m and (f) 64 m from the track centerline during the passage of the Thalys HST at a speed $v = 294\,\mathrm{km/h}$.

ment with identical mechanical properties as the underlying soil. Track 2 was a slab track (Figure B.6) with identical rails, rail pads and embankment as Track 1 (Section B.2.1.1 (Table B.2)). Track 3 was identical to Track 1, however at-grade (i.e. without an embankment).

The soil was modelled as a homogeneous elastic half-space with a shear wave velocity $c_\mathrm{s} = 200\,\mathrm{m/s}$, a dilatational wave velocity $c_\mathrm{p} = 400\,\mathrm{m/s}$ and density $\rho = 1800\,\mathrm{kg/m^3}$. The material damping ratio ξ ($\eta/2 = \xi$) for both deviatoric and volumetric deformation had a value of 0.05.

Figure B.12 shows rail receptances for the three type of tracks. It is seen that the low frequency response is slightly overestimated, but the agreement improves with increasing frequency. This is due to the dominant influence of track-soil interaction, in which the reference and scoping models differ. The reference method rigorously models the soil using BEM, while the scoping model uses a simplified methodology with a linear spring-damper to significantly reduce computational time.

Free-field mobilities for the three tracks are presented in Figure B.13. It is seen that the shape and magnitude of response of both models match well. The ballasted track models overestimate the response up to 50 Hz (Figures B.13.(a) and B.13.(c)), whereas the response of the slab track system is underestimated at mid frequency range. However, in general, considering the degree of input uncertainty for ground vibration models, the scoping model is within a reasonable range of accuracy.

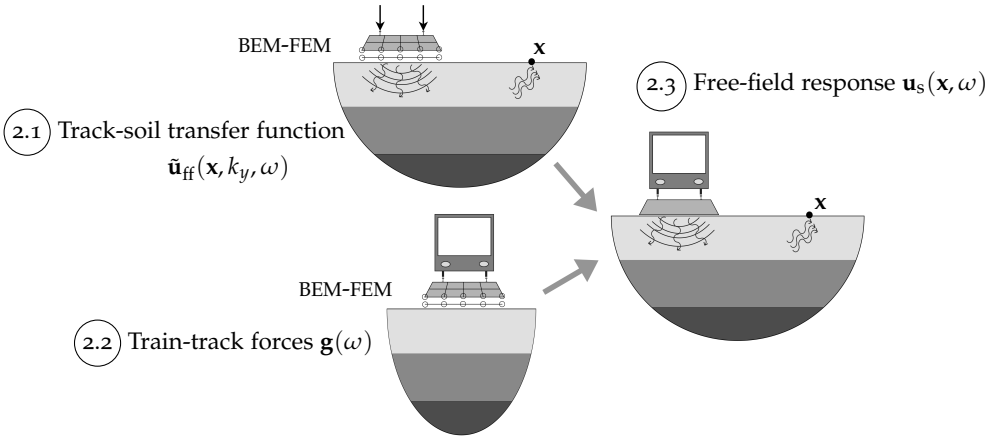

Figure B.11: Scheme of the reference model.

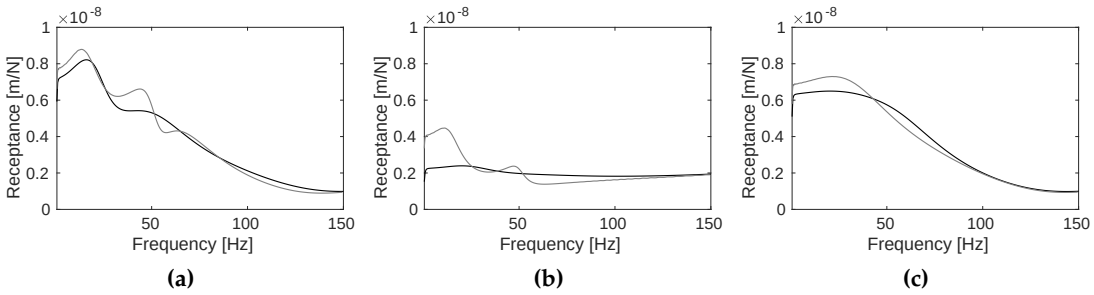

Figure B.12: The displacement of the rail of the (a) ballasted track on an embankment, (b) slab track and (c) at-grade track, computed by (black line) the reference model and (grey line) the scoping model.

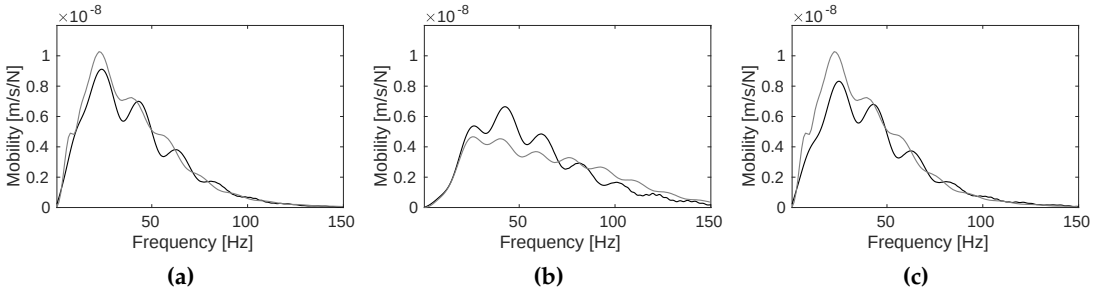

Figure B.13: Free-field vertical mobility at a distance of 20 m from the (a) ballasted track on an embankment, (b) slab track and (c) at-grade track, computed by (black line) the reference model and (grey line) the scoping model.

Figure B.14 presents the frequency contents in one-third octave bands of the dynamic load of an axle computed using both models. The estimation of the dynamic load from the proposed model coincides very strongly with those obtained using the reference model.

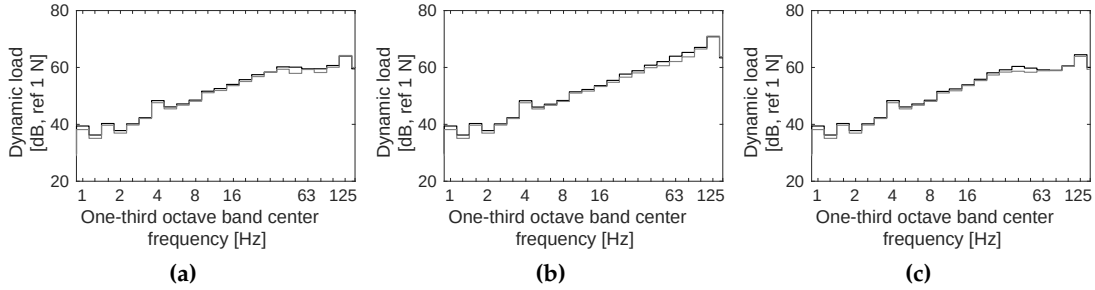

Figure B.14: One-third octave band center frequency of the dynamic load of an axle with unsprung mass $m_s = 2048\,\text{kg}$ at $v = 100\,\text{km/h}$ for the (a) ballasted track on an embankment, (b) slab track and (c) at-grade track computed by (black line) the reference model and (grey line) the scoping model.

Figure B.15 shows the frequency contents and the running RMS values of the free-field response, due to a S-100 train passage at $v = 100\,\text{km/h}$. The running RMS value has been computed from the weighted acceleration with a time window of 1 s as prescribed by the ISO 2631 standard [23]. The discrepancies between models are low and in accordance with those observed in the mobility results (Figure B.13). The running RMS curves present a similar agreement with differences in the range of $\{-4\,\text{dB}, 1.5\,\text{dB}\}$.

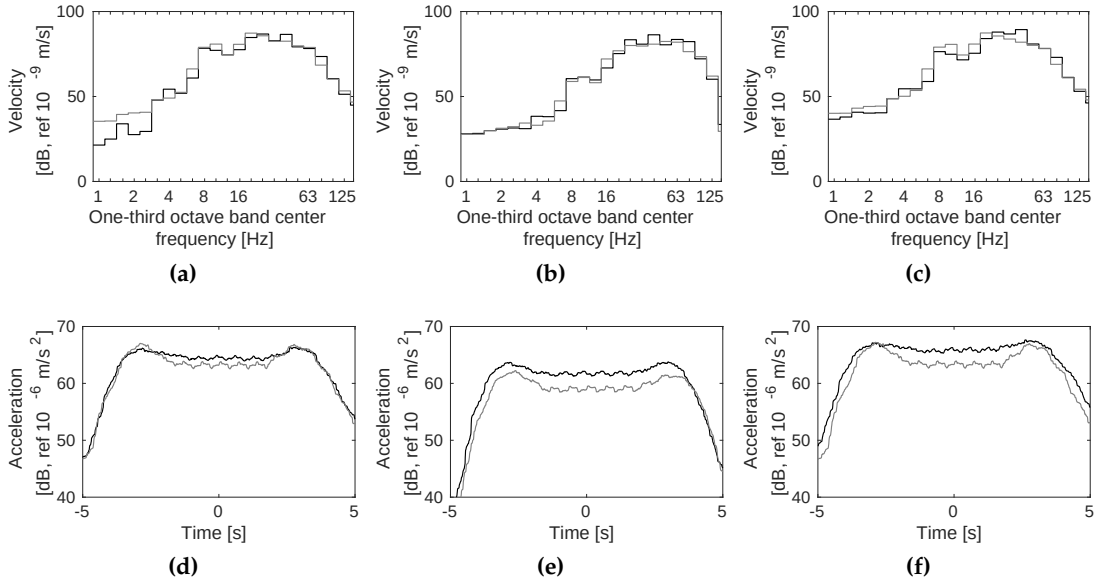

Figure B.15: (a-c) One-third octave band center frequency of the vertical velocity and (d-f) running RMS value of the vertical weighted acceleration in the free-field at a distance of 20 m for the (a,d) ballasted track on an embankment, (b,e) slab track and (c,f) at-grade track due to a S-100 train passage at $v = 100\,\text{km/h}$ computed by (black line) the reference model and (grey line) the scoping model.

Overall there is strong agreement between the reference and scoping model with regard to receptance, mobility, dynamic load, frequency contents in one-third octave bands and running RMS values. This is true for the ballasted and slab tracks. Therefore it is concluded that the scoping model is capable of predicting train track forces.

B.3.2.2 *Track-soil transfer function*

The scoping model uses a NN to convert the Green's function for a soil into the response of a coupled track-soil system. To determine the accuracy of this approach, three homogenous soil cases were investigated, each corresponding to Eurocode 8 [15] (Table B.1): soft, medium and stiff. Their exact properties are shown in Table B.8, and the train speed used was $v = 100\,\mathrm{km/h}$.

Table B.8: Homogeneous soil properties.

	h [m]	c_p [m/s]	c_s [m/s]	ξ [-]	ρ $\left[\mathrm{kg/m^3}\right]$
Soft soil	∞	345.2	172.6	0.05	1800
Medium soil	∞	669.8	334.9	0.05	1800
Stiff soil	∞	993.6	496.8	0.05	1800

Figure B.16 shows the influence of soil stiffness on the rail receptances from both models. The accuracy of the proposed model in the estimations is good, particularly for the medium and stiff soils. There is some small discrepancy at low frequency for the soft soil, however in general accuracy seems relatively independent from soil stiffness.

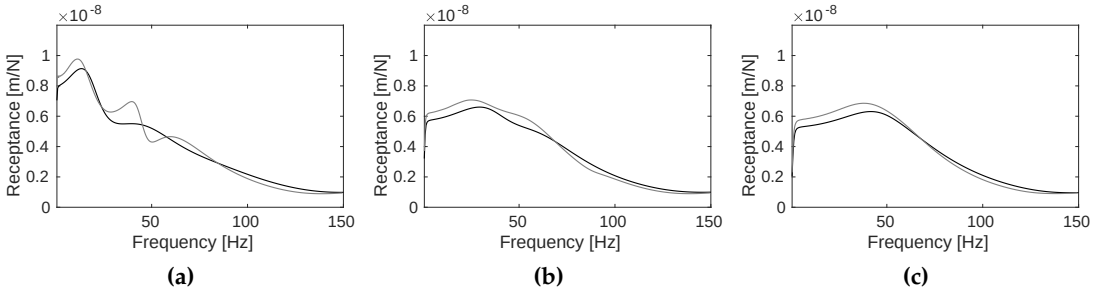

Figure B.16: The displacement of the rail of the ballasted track for the homogeneous (a) soft, (b) medium and (c) stiff soils, computed by (black line) the reference model and (grey line) the scoping model.

Free-field mobilities at a distance of 20 m from the track are presented in Figure B.17 for three homogeneous soils. Although there are some discrepancies between both prediction models, the magnitude and trend of results is good and it does not depend on soil stiffness.

The effect of soil stiffness on free-field vibrations due to the train passage is presented in Figure B.18. According to the previous results (Figures B.16 and B.17), the frequency contents of the soil vibrations (Figure B.18) show that the dominant frequencies due to the

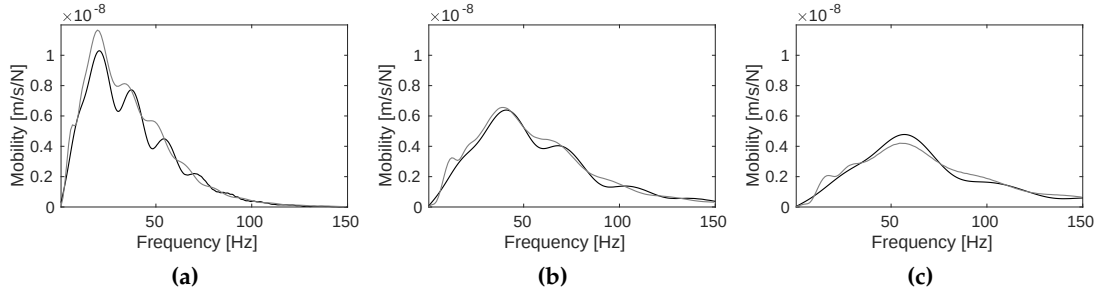

Figure B.17: Free-field vertical mobility at 20 m of the ballasted track for the homogeneous (a) soft, (b) medium and (c) stiff soils, computed by (black line) the reference model and (grey line) the scoping model.

excitation vary from 10 to 40 Hz for the soft soil to 30 and 70 Hz for the stiff soil. The highest discrepancies between both models are concentrated in the lower frequencies.

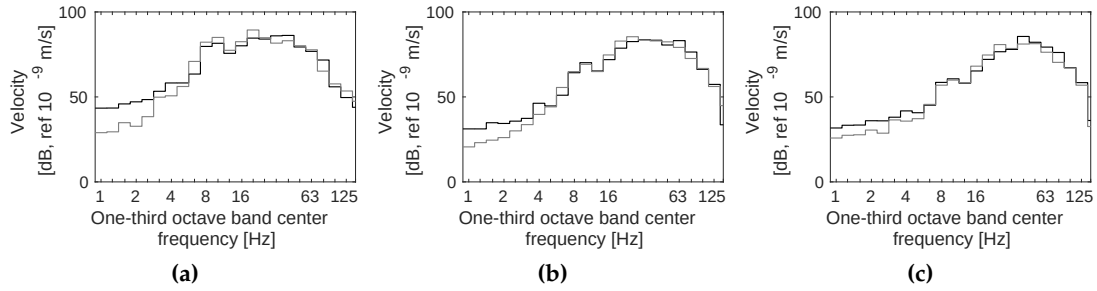

Figure B.18: Frequency content of the vertical velocity at 20 m from the ballasted track due to a S-100 train passage at $v = 100$ km/h for the homogeneous (a) soft, (b) medium and (c) stiff soils, computed by (black line) the reference model and (grey line) the scoping model.

A similar analysis to the presented in Section B.3.2 was performed considering layered soils. However, the results are not included because the conclusions are the same as those obtained previously.

Bearing in mind the differences between both models are dependent on the soil stiffness, but these uncertainties do not follow a clear trend, it can be concluded that soil properties are important parameters for the accuracy of the scoping model predictions.

B.4 ANALYSIS

This section presents a brief sensitivity analysis on the effect of track properties and train speed on vibration levels, as calculated using the scoping model.

Figure B.19 shows the modulation of the dynamic loads and free-field response due to the track type. It can be seen that the dynamic slab track loads are higher at frequencies above 40 Hz. This is because the slab track had a higher stiffness which causes an increase

of the free field response at the high frequency range. However, the soil response due to the train passage at the low and medium frequency ranges is attenuated by the slab track due to the effect of the free-field mobility (Figure B.20).

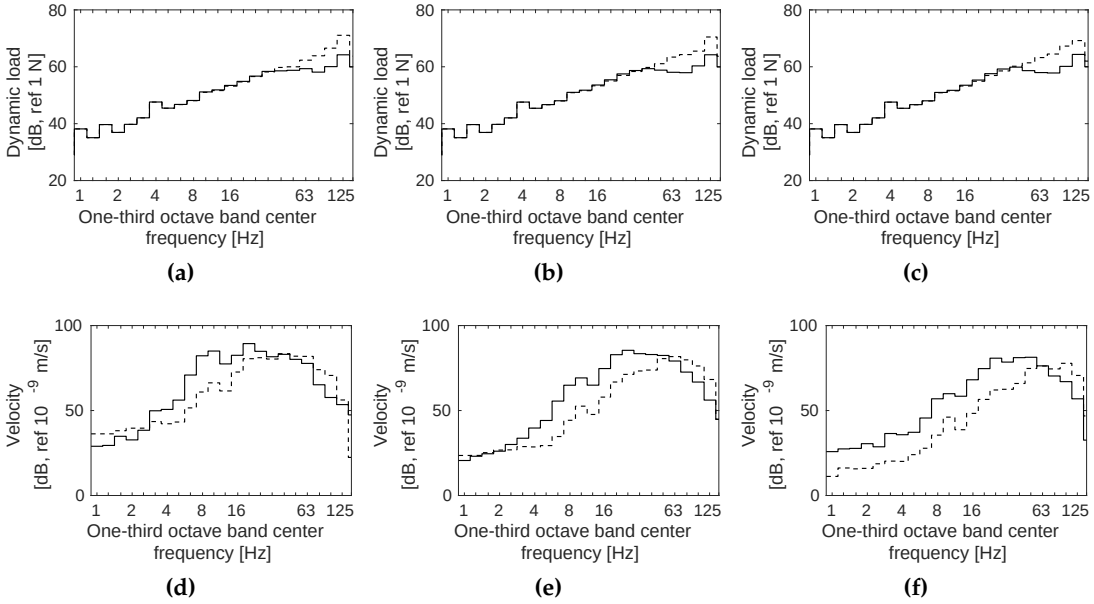

Figure B.19: Frequency content of the (a-c) dynamic load of an axle with unsprung mass $m_s = 2048\,\text{kg}$ and (d-f) the vertical velocity in the free-field at 20 m from the track due to a S-100 train passage, at $v = 100\,\text{km/h}$ for the homogeneous (a,d) soft, (b,e) medium and (c,f) stiff soils (Table B.8): (solid line) ballasted and (dashed line) slab tracks.

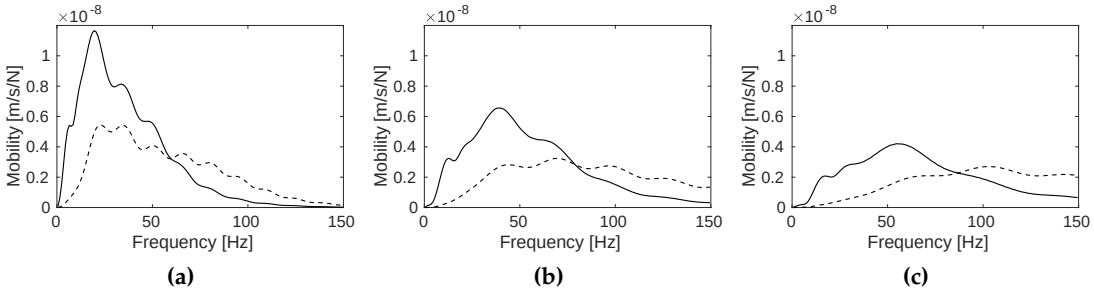

Figure B.20: Free-field vertical mobility at 20 m from the track centerline for the homogeneous (a) soft, (b) medium and (c) stiff soils (Table B.8): (solid line) ballasted and (dashed line) slab tracks.

Next, the scoping model was used to assess the effect of train speed on railway vibrations. Free-field response due to the passage of a S-100 train travelling at $\{100,\, 150\,,200\}$ km/h on the generic ballasted track was analysed. A homogeneous medium soil with $c_s = 200\,\text{m/s}$ as described in the previous Section B.3.2.1 was considered.

Figure B.21 presents the influence of the train speed on the free-field predictions computed by the proposed model. The quasi-static contribution can be observed in the frequency content around the axle passing frequency $f_a = v/L_a = \{9.26, 13.9, 18.52\}$ Hz. The dominant frequency due to the dynamic excitation remains in the range between 20 and 40 Hz for the different train speeds. Both quasi-static and dynamic contributions increase with train speed, however it is more pronounced for the quasi-static case.

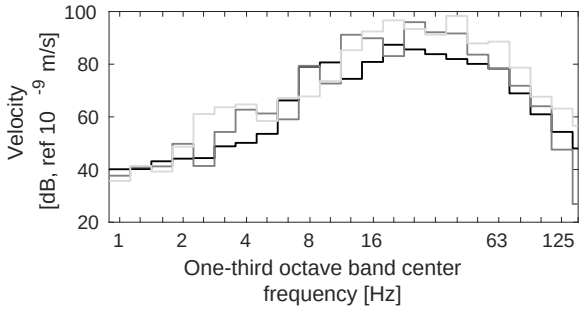

Figure B.21: One-third octave band center frequency of the vertical velocity in the free-field due to a S-100 train passage at (black line) $v = 100$ km/h, (dark grey line) $v = 150$ km/h and (light grey line) $v = 200$ km/h at 20 m computed by the scoping model.

Finally, Figure B.22 shows the relationship between train speed and the Maximum Transient Vibration Value (MTVV) [23] of the free field acceleration. The predicted vibration response has been weighted according to ISO2631 [23] to obtain the MTVV metric. A clear trend is observed with vibration levels increasing with train speed.

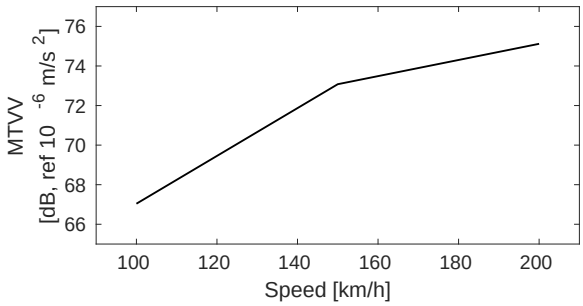

Figure B.22: MTVV in the free-field due to a S-100 train passage at 20 m depending on the speed of train, computed by the scoping model.

B.5 v_{s30} PARAMETER

V_{s30} is a measure of the mean shear wave speed in the top 30m of soil [15]. It is a property commonly used in earthquake engineering as an estimate of surface shear wave velocity. Databases of V_{s30} values exist that cover the entire earth's landmass, meaning that V_{s30} can potentially be used to increase the accuracy of desktop vibration scoping studies. However,

a challenge is that the mean shear wave velocity over a 30m depth is typically higher than the shear wave speed at the uppermost soil surface (i.e. where ground-borne vibration is most efficient). Although the parameter V_{s30} is recognised in international standards [4, 15], there have been studies about its limitations [5, 36, 60, 61]. Therefore the accuracy of using V_{s30} to approximate layered soils, within a railway vibration setting was investigated.

To do so, results for each layered soil were compared with those obtained for a homogeneous soil considering $c_s = V_{s30}$. Hereafter the homogeneous soil with $c_s = V_{s30}$ is called equivalent homogeneous soil.

Figure B.23 shows the rail receptances from the scoping model considering again the ballasted track (Table B.2) for the three layered soils (Table B.9) and the equivalent homogeneous soil. The layered soil properties were chosen to ensure the V_{s30} matched the c_s properties shown in Table B.8. It is observed that peaks in the track response for the three layered soils are found in the frequency range 12 Hz to 16 Hz. This is because the dominant frequency is strongly dependent upon the properties of the uppermost soil layer, which are similar for the three layered soils. A better agreement in terms of peak amplitudes is obtained at high frequencies. Regarding the three different soils, the homogeneous approximation performs best for the soft soil. This is because it has a smoother soil stratigraphy, characterised by a smaller discrepancy between the upper and lower layers' stiffness.

Table B.9: Layered soil properties.

		h [m]	c_p [m/s]	c_s [m/s]	ξ [-]	ρ [kg/m^3]	V_{s30} [m/s]
Soft	Layer 1	24.1	318.9	159.5	0.05	1800	172.6
	Half-space	∞	518.1	259.1	0.05	1800	
Medium	Layer 1	1.7	220.9	110.5	0.05	1800	334.9
	Layer 2	7.8	479.4	239.7	0.05	1800	
	Layer 3	2.7	726	363	0.05	1800	
	Half-space	∞	1038	519	0.05	1800	
Stiff	Layer 1	2	361.5	180.7	0.05	1800	496.8
	Layer 2	3.6	660.4	330.2	0.05	1800	
	Layer 3	1.8	1113.2	556.6	0.05	1800	
	Half-space	∞	1291.6	645.8	0.05	1800	

Figure B.24 shows the influence of soil stratigraphy on free-field mobility. In these results, it should be remembered that the neural network approach only utilises the upper layer properties (h_1 and c_{s_1}) and the V_{s30} parameter (Figure B.2), meaning the full soil profile is not considered. Regarding mobility results the level of error is similar to the receptance results, with the soft soil showing better agreement compared to the medium and stiff soils.

Figure B.25 shows the free-field vibrations due to the S-100 train passage at $v = 100\,\mathrm{km/h}$ computed from the proposed model. Some differences are seen for the soft and stiff soils

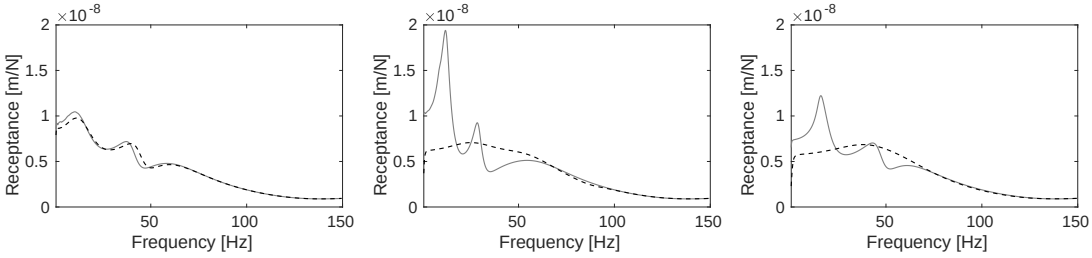

Figure B.23: The displacement of the rail for the layered (a) soft, (b) medium and (c) stiff soils, computed by (grey line) the scoping model. Superimposed is the solution for (black dashed line) the equivalent homogeneous soil.

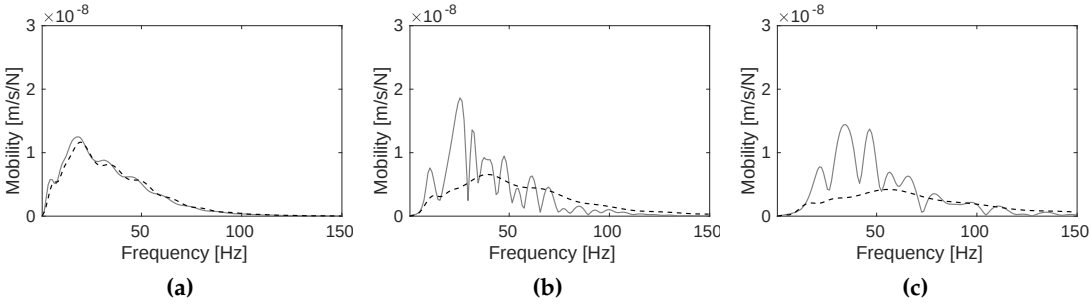

Figure B.24: Free-field vertical mobility at 20 m for the layered (a) soft, (b) medium and (c) stiff soils, computed by (grey line) the scoping model. (Black dashed line) superimposed is the solution for the equivalent homogeneous soil.

at low frequencies, and medium and stiff soils in the mid frequency range. In general the agreement is reasonable, although at some frequencies there are errors of up to 14 dB.

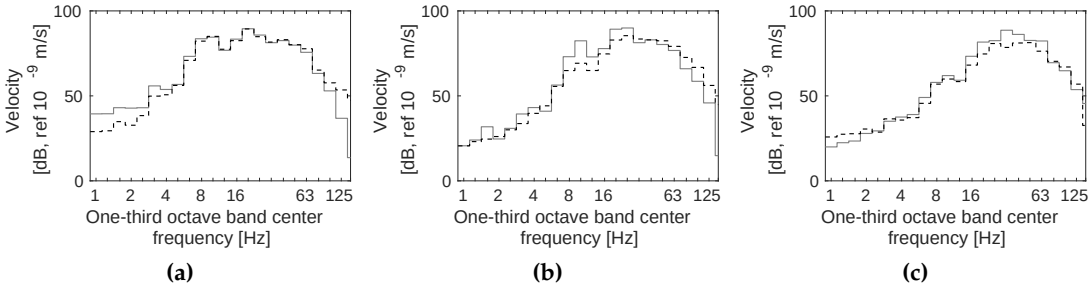

Figure B.25: One-third octave band center frequency of the vertical velocity in the free-field due to a S-100 train passage at $v = 100$ km/h at 20 m for the layered (a) soft, (b) medium and (c) stiff soils, computed by (grey line) the scoping model. (Black dashed line) superimposed is the solution for the equivalent homogeneous soil.

Figure B.26 presents the MTVV [23] at different distances from the ballasted track, considering different V_{s30} values. The response for homogeneous soils decrease as the soil stiffness increase as expected, however, the layered soils show the opposite behaviour. This is due to the shear wave velocity of the upper layer in each soil (Table B.9). In all cases, this shear wave velocity is lower than the V_{s30} parameter and the difference between both increases from the soft to the stiff soil. The soil response is higher for the stiff layered soil since the free-field response is mainly influenced by surface waves. Therefore, it can be concluded that characterising soils using the V_{s30} parameter should be performed carefully and only for cases with straightforward stratigraphies.

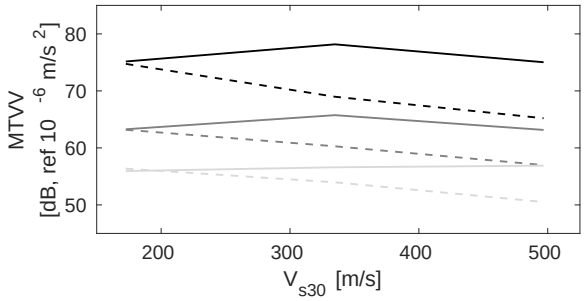

Figure B.26: MTVV in the free-field at distances from the ballasted track of (black line) 10 m, (dark grey line) 30 m and (light grey line) 50 m due to a S-100 train passage at $v = 100$ km/h considering (solid lines) layered and (dashed lines) homogeneous soils charecterized by their V_{s30} parameter.

B.6 DISCUSSION

Quantification of scoping model accuracy is challenging because of limited field data and the unknown error levels inherent within the reference model. Therefore, in an attempt to make a global comparison, Figure B.27 shows the discrepancy between scoping and reference model results, for all the cases previously presented in this study. The error was calculated as $\Delta v = 20\log_{10}\left(v^P/v^R\right)$, where v^P and v^R were the response from the scoping and the reference model respectively.

Regarding the ballasted tracks, the at-grade and embankment results have been combined, and shown with superimposed envelope curves. It is seen that prediction ability is better in the mid frequency range. As for the slab track, best performance is also in the mid-frequency range.

The global uncertainty of the scoping model was determined using the MTVV vibration metric [23]. Figure B.28 presents the response for all the cases. A good agreement is found with differences mainly found between -4.8 dB to 5.6 dB. Therefore the accuracy is similar to the uncertainty range between 5 dB to 20 dB as found in previous research [39, 27, 14].

A dataset of 4410000 data points was used to create the NN model. A discussion on the minimum number of data points needed to achieve sufficient NN model accuracy is important if it is to be developed for other cases (e.g. tracks, soil conditions, embankment

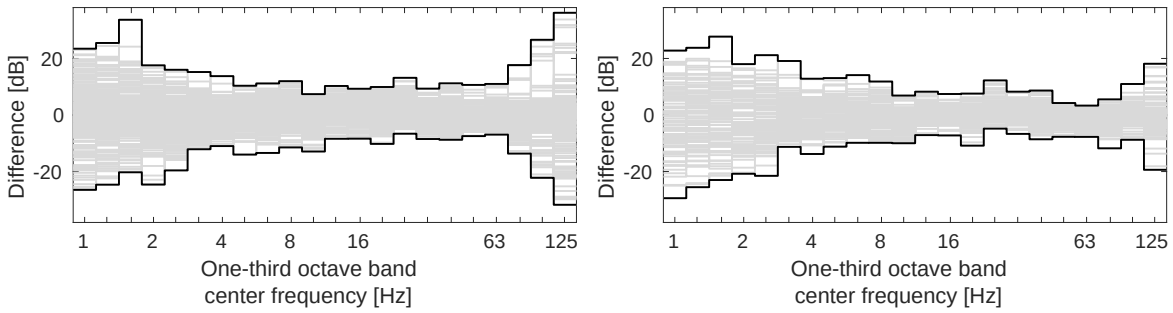

Figure B.27: (Grey lines) one-third octave band center frequency of the differences Δv for all the cases of the (a) ballasted and (b) slab tracks. (Black lines) superimposed is the envelope of the highest discrepancies.

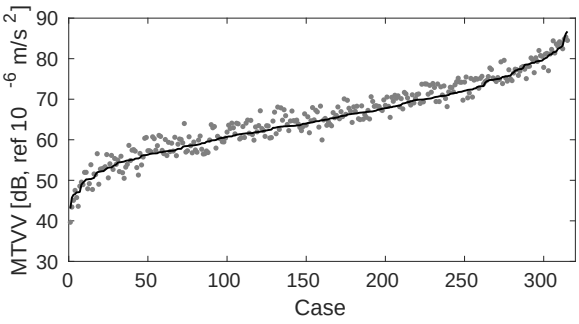

Figure B.28: MTVV in the free-field due to a S-100 train passage at 20 m for all the cases, computed by (black line) the reference model and (grey points) the scoping model.

types, etc.). Figure B.29 shows the predictions for all the cases computed using the scoping model with a NN approach trained with four times the number of original data points (120 soil types $\times$ 5 distances $\times$ 150 frequencies $\times$ 196 wavenumbers $=$ 17640000) and the reference model. The larger dataset required a significant increase in computation effort, however results did not improve. Therefore is concluded that increasing the number of data points does not signify a more accuracy model.

An important advantage of the new scoping model compared to alternative models is its computational efficiency. Table B.10 shows the computational costs to obtain the free-field response for a S-100 train travelling at $v = 100\,\text{km/h}$ using an `Intel One Core i7@1.87 GHz` computer. The run times refer to the source-propagation problem of waves in the soil. The running time does not depend on the soil's properties. Taking into account the architecture of the scoping and reference models (Figures B.1 and B.11), Table B.10 outlines the main calculation steps and their run times. It should be noted that:

- The time required to calculate the track-soil transfer function $\tilde{\mathbf{u}}_{\text{ff}}$ (step 2.1) using the scoping model was primarily due to the evaluation of the soil Green's function (step 2.1.2). The estimation of the correction factor $\tilde{A}_g$ through the NN approach (step 2.1.1)

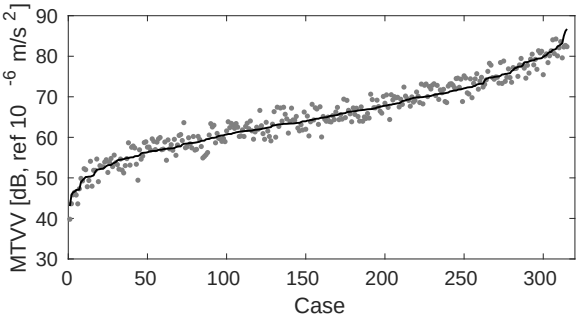

Figure B.29: MTVV in the free-field due to a S-100 train passage at 20 m for all the cases, computed by (black line) the reference model and (grey points) the scoping model with a NN approach trained with four times of the original data points.

required minimal cost. The combination of these two steps resulted in a run time that was lower than that for the reference model which relied on a FEM-BEM formulation.

- The simplified track model (Figure B.5) allowed the scoping model to reduce computations of train-track excitations $\mathbf{g}$ (step 2.2) since the soil-track interaction was represented by a spring-damper element. Again, the reference model used a BEM-FEM methodology to calculate the train-track excitations and track-soil transfer function $\tilde{\mathbf{u}}_{\mathrm{ff}}$, thus requiring additional computation.
- Running times for obtaining free-field predictions are identical.
- Moreover, the preprocessing in the scoping model involves a minimal time.

Table B.10: Average running time.

Step	Reference model	Scoping model
Track-soil transfer function	15 min	5 min
Train-track forces	25 min	38 s
Free-field predictions	30 s	30 s

Considering these much reduced computational requirements, strong accuracy and the versatility of the proposed scoping model, it is concluded that it could be a powerful tool during the early design stages of railway lines.

B.7 CONCLUSIONS

In this work, a simplified methodology to compute the propagation of railway vibrations from track to free-field was presented. The model is novel because it is able to simulate the generation, propagation and immission of vibrations, for complex vehicle, track and soil arrangements in minimal time. To do so, a 2.5D FEM track model was combined with a

hybrid direct stiffness-neural network procedure to create an overall model describing the vehicle-track-soil problem.

To validate the model, a combination of experimental and numerical data was used. Track receptance, free-field mobility and soil vibration due to train passage were analysed and the new model was found to have strong prediction ability.

A sensitivity analysis was undertaken using the validated model. Track type and train speed effects were compared and it was found that there was a strong relationship between vibration levels and both soil properties and track type. Also, comparisons were made to determine the accuracy of using a global database of V_{s30} soil properties to predict vibration levels. It was found that this simplification was only satisfactory for cases with smooth stratigraphies.

ACKNOWLEDGEMENTS

This research was funded by the Spanish Ministry of Economy and Competitiveness (Ministerio de Economía y Competitividad) through research project BIA2016-75042-C2-1-R. Financial support is gratefully acknowledged. The support given by the Andalusian Scientific Computing Centre (CICA) and the Leverhulme Trust (UK) is also gratefully acknowledged.

The first author would like to thank the Spanish Ministry of Education, Culture and Sport (Ministerio de Educación, Cultura y Deporte) for the financial support of his research stay at the School of Civil Engineering of the University of Leeds through the scholarship "Salvador de Madariaga" Reference PRX18/00115.

REFERENCES

[1] ISO 8608. *Mechanical vibration – road surface profiles – Reporting of measured data*. International Organization for Standardization, 1995.

[2] L. Auersch. The excitation of ground vibration by rail traffic: theory of vehicle–track–soil interaction and measurements on high-speed lines. *Journal of Sound and Vibration*, 284:103–132, 2005. doi: https://doi.org/10.1016/j.jsv.2004.06.017.

[3] L. Auersch, A. Romero, and P. Galvín. Respuesta dinámica de edificaciones producida por campos de onda incidentes considerando la interacción suelo-estructura. *Revista Internacional de Métodos Numéricos para Cálculo y Diseño en Ingeniería*, 30(4):256–263, 2014. doi: https://doi.org/10.1016/j.rimni.2013.09.001.

[4] *NEHRP Recommended Seismic Provisions for New Buildings and Other Structures, FEMA P-1050*. Building Seismic Safety Council, 2015.

[5] S. Castellaro, F. Mulargia, and P.L. Rossi. Vs30: Proxy for seismic amplification? *Seismological Research Letters*, 79(4):540–543, 2008. doi: http://dx.doi.org/10.1785/gssrl.79.4.540.

[6] C.E. Hanson, D.A. Towers, and L.D. Meister. High-speed ground Transportation Noise and Vibration Impact Assessment, HMMH Report 293630-4. *U.S. Department of Transportation, Federal Railroad Administration, Office of Railroad Development*, 2005.

[7] C.E. Hanson, D.A. Towers, and L.D. Meister. Transit Noise and Vibration Impact Assessment, Report FTA-VA-90-1003-06. *U.S. Department of Transportation, Federal Transit Administration, Office of Planning and Environment*, 2006.

[8] D.P. Connolly, G.P. Marecki, G. Kouroussis, I. Thalassinakis, and P.K. Woodward. The growth of railway ground vibration problems – A review. *Science of the Total Environment*, 568:1276–1282, 2015. doi: http://dx.doi.org/10.1016/j.scitotenv.2015.09.101.

[9] C.R. Arjun and A. Kumar. Neural network estimation of duration of strong ground motion using japanese earthquake records. *Soil Dynamics and Earthquake Engineering*, 31:866–872, 2011. doi: https://doi.org/10.1016/j.soildyn.2011.01.001.

[10] D. E. Rumelhart and J. L. McClelland. *Parallel distributed processing: Explorations in the microstructure of cognition. Vol 1*. MIT Press, Cambridge, MA, 1986.

[11] *DIN 45672 Teil 2: Schwingungsmessungen in der Umgebung von Schienenverkehrswegen: Auswerteverfahren*. Deutsches Institut für Normung, 1995.

[12] D.P. Connolly, G. Kouroussis, A. Giannopoulos, O. Verlinden, P.K. Woodward, and M.C. Forde. Assesment of railway vibrations using an efficient scoping model. *Soil Dynamics and Earthquake Engineering*, 58:37–47, 2014. doi: https://doi.org/10.1016/j.soildyn.2013.12.003.

[13] D.P. Connolly, G. Kouroussis, P.K. Woodward, A. Giannopoulos, O. Verlinden, and M.C. Forde. Scoping prediction of re-radiated ground-borne noise and vibration near high speed rails lines with variable soils. *Soil Dynamics and Earthquake Engineering*, 66: 78–88, 2014. doi: https://doi.org/10.1016/j.soildyn.2014.06.021.

[14] D.P. Connolly, P. Alves Costa, G. Kouroussis, P. Galvín, P.K. Woodward, and O. Laghrouche. Large scale international testing of railway ground vibrations across Europe. *Soil Dynamics and Earthquake Engineering*, 71:1–12, 2015. doi: https://doi.org/10.1016/j.soildyn.2015.01.001.

[15] *Eurocode 8: Design of structures for earthquake resistance–Part 1 : General rules, seismic actions and rules for buildings*. European Committee for Standardization, 1998.

[16] S. François, M. Schevenels, P. Galvín, G. Lombaert, and G. Degrande. A 2.5d coupled fe–be methodology for the dynamic interaction between longitudinally invariant structures and a layered halfspace. *Computer Methods in Applied Mechanics and Engineering*, 199(23):1536 – 1548, 2010. doi: https://doi.org/10.1016/j.cma.2010.01.001.

[17] P. Galvín and J. Domínguez. High-speed train-induced ground motion and interaction with structures. *Journal of Sound and Vibration*, 307:755–777, 2007. doi: https://doi.org/10.1016/j.jsv.2007.07.017.

[18] P. Galvín, A. Romero, and J. Domínguez. Fully three-dimensional analysis of high-speed train–track–soil–structure dynamic interaction. *Journal of Sound and Vibration*, 329:5147–5163, 2010. doi: https://doi.org/10.1016/j.jsv.2010.06.016.

[19] P. Galvín, S. François, M. Schevenels, E. Bongini, G. Degrande, and G. Lombaert. A 2.5d coupled fe-be model for the prediction of railway induced vibrations. *Soil Dynamics and Earthquake Engineering*, 30(12):1500 – 1512, 2010. doi: https://doi.org/10.1016/j.soildyn.2010.07.001.

[20] H.Braun and T.Hellenbroich. Messergebnisse von strassenunebenheiten. *VDI Berichte*, 877:47–80, 1991.

[21] C. Hung and S. Ni. Using multiple neural networks to estimate the screening effect of surface waves by in-filled trenches. *Computers and Geotechnics*, 34:397–409, 2007. doi: https://doi.org/10.1016/j.compgeo.2007.06.005.

[22] M. Hussein, H. Hunt, K. Kuo, P. Alves Costa, and J. Barbosa. The use of sub-modelling technique to calculate vibration in buildings from underground railways. *Proceedings*

of the Institution of Mechanical Engineers, Part F: Journal of Rail and Rapid Transit, 229(3): 303 – 314, 2013. doi: https://doi.org/10.1177/0954409713511449.

[23] *ISO 2631-1:2003: Mechanical vibration and shock–Evaluation of human exposure to whole-body vibration–Part 1: General requirements*. International Organization for Standardization, 2003.

[24] *ISO 2631-2:2003: Mechanical vibration and shock–Evaluation of human exposure to whole-body vibration–Part 2: Vibration in buildings (1–80 Hz)*. International Organization for Standardization, 2003.

[25] *ISO 14837-1:2005 Mechanical vibration–Ground-borne noise and vibration arising from rail systems–Part 1: General guidance*. International Organization for Standardization, 2005.

[26] P. Jean, C. Guigou, and M. Villot. A 2.5D BEM Model for Ground-Structure Interaction. *Building Acoustics*, 11(3):1–17, 2004. doi: https://doi.org/10.1260/1351010042250376.

[27] S. Jones, K. Kuo, M.F.M. Hussein, and H.E.M Hunt. Prediction uncertainties and inaccuracies resulting from common assumptions in modelling vibration from underground railways. *Proceedings of the Institution of Mechanical Engineers, Part F: Journal of Rail and Rapid Transit*, 226:501–512, 2012. doi: https://doi.org/10.1177/0954409712441744.

[28] J.T. Nelson and H.J. Sauernman. A prediction procedure for rail transportation ground-borne noise and vibration. *Transportation Research Record: Journal of the Transportation Research Board*, 1143:26–35, 1987.

[29] E. Kausel. *Fundamental solutions in elastodynamics: a compendium*. Cambridge University Press, 2006.

[30] E. Kausel and J.M. Roësset. Stiffness matrices for layered soils. *Bulletin of the Seismological Society of America*, 71(6):1743, 1981.

[31] G. Kouroussis, L. Van Parys, C. Conti, and O. Verlinden. Prediction of ground vibrations induced by urban railway traffic: An analysis of the coupling assumptions between vehicle, track, soil, and buildings. *The International Journal of Acoustics and Vibration*, 18(4):163 – 172, 2013. doi: https://doi.org/10.20855/ijav.2013.18.4330.

[32] G. Kouroussis, K.E. Vogiatzis, and D.P. Connolly. A combined numerical/experimental prediction method for urban railway vibration. *Soil Dynamics and Earthquake Engineering*, 97:377 – 386, 2017. doi: http://dx.doi.org/10.1016/j.soildyn.2017.03.030.

[33] K.A. Kuo, H. Verbraken, G. Degrande, and G. Lombaert. Hybrid predictions of railway induced ground vibration using a combination of experimental measurements and numerical modelling. *Journal of Sound and Vibration*, 373:263–284, 2016. doi: https://doi.org/10.1016/j.jsv.2016.03.007.

[34] K. Kuźniar and Z. Waszczyszyn. Neural analysis of vibration problems of real flat buildings and data pre-processing. *Engineering Structures*, 24:1327–1335, 2002. doi: https://doi.org/10.1016/S0141-0296(02)00067-6.

[35] K. Kuźniar, E. Maciąg, and Z. Waszczyszyn. Computation of response spectra from mining tremors using neural networks. *Soil Dynamics and Earthquake Engineering*, 25: 331–339, 2005. doi: https://doi.org/10.1016/j.soildyn.2005.02.001.

[36] L.A. Wald and J. Mori. Evaluation of methods for estimating linear site-response amplifications in the los angeles region. *Bulletin of the Seismological Society of America*, 90(6B):S32–S42, 2000. doi: https://doi.org/10.1785/0119970170.

[37] G. Lombaert and G. Degrande. Ground-borne vibration due to static and dynamic axle loads of intercity and high-speed trains. *Journal of Sound and Vibration*, 319(3–5): 1036–1066, 2009. doi: http://dx.doi.org/10.1016/j.jsv.2008.07.003.

[38] G. Lombaert, G. Degrande, J. Kogut, and S. François. The experimental validation of a numerical model for the prediction of railway induced vibrations. *Journal of Sound and Vibration*, 297(3):512 – 535, 2006. doi: https://doi.org/10.1016/j.jsv.2006.03.048.

[39] G. Lombaert, P. Galvín, S. François, and G. Degrande. Quantification of uncertainty in the prediction of railway induced ground vibration due to the use of statistical track unevenness data. *Journal of Sound and Vibration*, 333(18):4232 – 4253, 2014. doi: https://doi.org/10.1016/j.jsv.2014.04.052.

[40] P. Lopes, P. Alves Costa, M. Ferraz, R. Calçada, and A. Silva Cardoso. Numerical modeling of vibrations induced by railway traffic in tunnels: From the source to the nearby buildings. *Soil Dynamics and Earthquake Engineering*, 61–62:269–285, 2014. doi: https://doi.org/10.1016/j.soildyn.2014.02.013.

[41] D. López-Mendoza, A. Romero, D.P. Connolly, and P. Galvín. Scoping assessment of building vibration induced by railway traffic. *Soil Dynamics and Earthquake Engineering*, 93:147–161, 2017. doi: http://dx.doi.org/10.1016/j.soildyn.2016.12.008.

[42] M. H. Beale, M. T. Hagan, and H. B. Demuth. *Neural network toolbox User's guide*. Mathworks, Inc, 2017.

[43] M. T. Hagan and M. B. Menhaj. Training feedforward networks with the marquardt algorithm. *EEE Transactions on Neural Networks*, 5(6):989–993, 1994. doi: https://doi.org/10.1109/72.329697.

[44] C. Madshus, B. Bessason, and L. Harvik. Prediction model for low frequency vibration from high speed railways on soft ground. *Journal of Sound and Vibration*, 193(1):195–203, 1996. doi: https://doi.org/10.1006/jsvi.1996.0259.

[45] M. Monjezi, M. Ahmadi, M. Sheikhan, A. Bahrami, and A. R. Salimi. Predicting blast-induced ground vibration using various types of neural networks. *Soil Dynamics and Earthquake Engineering*, 30:1233–1236, 2010. doi: https://doi.org/10.1016/j.soildyn.2010.05.005.

[46] V. Nourani and M. S. Fard. Sensitivity analysis of the artificial neural network outputs in simulation of the evaporation process at different climatologic regimes. *Advances in Engineering Software*, 47:127–146, 2012. doi: https://doi.org/10.1016/j.advengsoft.2011.12.014.

[47] B. Olivier, D.P. Connolly, P. Alves Costa, and G. Kouroussis. The effect of embankment on high speed rail ground vibrations. *International Journal of Rail Transportation*, 4(4):229–246, 2016. doi: 10.1080/23248378.2016.1220844.

[48] P. Alves Costa, R. Calçada, and A. Silva Cardoso. Track–ground vibrations induced by railway traffic: In-situ measurements and validation of a 2.5D FEM-BEM model. *Soil Dynamics and Earthquake Engineering*, 32:111–128, 2012. doi: https://doi.org/10.1016/j.soildyn.2011.09.002.

[49] P. Alves Costa, A. Colaço, R. Calçada, and A. Silva Cardoso. Critical speed of railway tracks. Detailed and simplified approaches. *Transportation Geotechnics*, 2:30–46, 2015. doi: https://doi.org/10.1016/j.trgeo.2014.09.003.

[50] A. Romero, A. Tadeu, P. Galvín, and J. António. 2.5D coupled BEM–FEM used to model fluid and solid scattering wave. *International Journal for Numerical Methods in Engineering*, 101:148–164, 2015. doi: https://doi.org/10.1002/nme.4801.

[51] A. Romero, P. Galvín, J. António, J. Domínguez, and A. Tadeu. Modelling of acoustic and elastic wave propagation from underground structures using a 2.5d bem-fem approach. *Engineering Analysis with Boundary Elements*, 76:26 – 39, 2017. doi: http://dx.doi.org/10.1016/j.enganabound.2016.12.008.

[52] F. Rossi and A. Nicolini. A simple model to predict train-induced vibration: theoretical formulation and experimental validation. *Enviornmental Impact Assesment Review*, 23:305–322, 2003. doi: https://doi.org/10.1016/S0195-9255(03)00005-2.

[53] S.B. Mezher, D.P. Connolly, P.K. Woodward, O. Laghrouche, J. Pombo, and P. Alves Costa. Railway critical velocity – analytical prediction and analysis. *Transportation Geotechnics*, 6:84 – 96, 2016. doi: https://doi.org/10.1016/j.trgeo.2015.09.002.

[54] M. Schevenels, S. François, and G. Degrande. Edt: An elastodynamics toolbox for MATLAB. *Computers & Geosciences*, 35(8):1752 – 1754, 2009. doi: http://dx.doi.org/10.1016/j.cageo.2008.10.012.

[55] X. Sheng, C.J.C. Jones, and D.J. Thompson. Prediction of ground vibration from trains using the wavenumber finite and boundary element methods. *Journal of Sound and Vibration*, 293:575–586, 2006. doi: https://doi.org/10.1016/j.jsv.2005.08.040.

[56] J.J. Shi. Reducing prediction error by transforming input data neural networks. *Journal of Computing in Civil Engineering*, 14(2):109 – 116, 2000. doi: https://doi.org/10.1061/(ASCE)0887-3801(2000)14:2(109).

[57] J. Shu, Z. Zhang, I. Gonzalez, and R. Karoumi. The application of a damage detection method using artificial neural network and train-induced vibrations on a simplified railway bridge model. *Engineering Structures*, 52:408–421, 2013. doi: https://doi.org/10.1016/j.engstruct.2013.02.031.

[58] A. Triepaischajonsak and D.J. Thompson. A hybrid modelling approach for predicting ground vibration from trains. *Journal of Sound and Vibration*, 335:147 – 173, 2015. doi: http://dx.doi.org/10.1016/j.jsv.2014.09.029.

[59] H. Verbraken, G. Lombaert, and G. Degrande. Verification of an empirical prediction method for railway induced vibrations by means of numerical simulations. *Journal of Sound and Vibration*, 330(8):1692–1703, 2011. doi: https://doi.org/10.1016/j.jsv.2010.10.026.

[60] T. Volti, D. Burbidge, C. Collins, M.W. Asten, J.K. Odum, W.J. Stephenson, C. Pascal, and J. Holzschuh. Comparisons between V_{S30} and spectral response for 30 sites in newcastle, australia, from collocated seismic cone penetrometer, active- and passive-source V_S data. *Bulletin of the Seismological Society of America*, 106(4):1690–1709, 2016. doi: https://doi.org/10.1785/0120150073.

[61] V.W. Lee and M.D. Triufnac. Should average shear-wave velocity in the top 30 m of soil be used to describe seismic amplification? *Soil Dynamics and Earthquake Engineering*, 30:1250–1258, 2010. doi: https://doi.org/10.1016/j.soildyn.2010.05.007.

[62] C. With, M. Bahrekazemi, and A. Bodare. Validation of an empirical model for prediction of train-induced ground vibrations. *Soil Dynamics and Earthquake Engineering*, 26:983–990, 2006. doi: https://doi.org/10.1016/j.soildyn.2006.03.005.

[63] H. Xia, Y.M. Cao, and G. De Roeck. Theoretical modeling and characteristic analysis of moving-train induced ground vibrations. *Journal of Sound and Vibration*, 329:819–832, 2010. doi: https://doi.org/10.1016/j.jsv.2009.10.007.

[64] Y. L. Cun, I. Kanter, and S. A. Solla. Second order properties of error surfaces: Learning time and generalization. *Advances in Neural Information Processing Systems*, 3:918–924, 1991.

[65] M. Yurdakul and H. Akdas. Modeling uniaxial compressive strength of building stones using non-destructive test results as neural networks input parameters. *Construction and Building Materials*, 47:1010–1019, 2013. doi: https://doi.org/10.1016/j.conbuildmat.2013.05.109.

C

PAPER C: A TRANSFER FUNCTION METHOD TO PREDICT BUILDING VIBRATION AND ITS APPLICATION TO RAILWAY DEFECTS

- Status: Submitted
- Journal Name: Construction and Building Materials
- ISSN: 0950-0618
- Journal Citation Reports (2017). Impact Factor: 3.485
    - Engineering, Civil: Q1 (11/128)
    - Construction and Building Technology: Q1 (10/62)
    - Materials Science, Multidisciplinay: Q2 (72/284)
- SCIMAGO (2017). Impact Factor: 1.607
    - Building and Construction: Q1 (14/321)
    - Civil and Structural Engineering: Q1 (25/497)
    - Materials Science (miscellaneous): Q1 (60/630)

A transfer function method to predict building vibration and its application to railway defects

Authors: Daniel López-Mendoza[a], David P. Connolly[b], Antonio Romero Ordóñez[a], Georges Kouroussis[c] and Pedro Galvín Barrera[a]

[a] Escuela Técnica Superior de Ingeniería, Universidad de Sevilla, Camino de los Descubrimientos, 41092 Sevilla, Spain
[b] Institute for High Speed Rail, Leeds University, LS2 9JT Leeds, UK
[c] Faculty of Engineering, Department of Theoretical Mechanics, Dynamics and Vibrations, Université de Mons, Belgium

ABSTRACT

This work presents a simplified method to evaluate building shaking due to arbitrary base excitations, and an example application to railway problems. The model requires minimal computational effort and can be applied to a wide range of footing shapes, thus making it attractive for scoping-type analysis. It uses the soil excitation spectrum at the building footing location as it's input, and computes the building response at any arbitrary location within it's 3D structure. To show an application of the model versatility, it is used to compute building response due to a variety of singular railway defects (e.g. switches/crossings). It is however suitable for more general applications including railway problems. The approach is novel because current railway scoping models do not use soil-structure transfer functions combined with free-field response to estimate building vibration by railway defects. First the soil-structure interaction approach is outlined for both rigid and flexible footings. Then it is validated by comparing results against a comprehensive fully-coupled 3D FEM-BEM model. Finally, it is used to analyse the effect of a variety of variables (soil properties, defect type, defect size and train speed) on 3 different building types. Overall the new approach allows for the computation of building vibrations with high accuracy, using minimal computational effort.

Keywords: Ground-borne vibrations; Railway traffic; High speed rail; Building vibrations; Structural vibration; Environmental Impact Assesment (EIA); Railway singular defects.

C.1 INTRODUCTION

The response of structures to ground-borne waves induced by blasting, earthquake, road and railway traffic, are examples where Soil-Structure Interaction (SSI) is an important issue [33, 59].

This was addressed by Wu and Hao [26, 60] who investigated blast-induced ground excitation. They proposed a numerical model to predict surface ground motion due to underground blasting. The free-field response was used as an input to obtain the building response using a simple approach, where the source (blasting)-receiver (building) interaction was neglected. Alternatively, Bayraktar et al. [4] developed a detailed nonlinear dynamic model to simulate concrete and masonry structures using an hybrid approach. Ground excitations due to blasting were measured and combined with a numerical building model, informed using experimental dynamic characteristics. Dogan et al. [12] also presented a combined experimental/numerical procedure to obtain building response due to blasting. Ground motion was measured while building vibration was computed using a 3D model ignoring SSI. A comparison between underground and surface blasting was made and it was found that vibrations were lower for the underground case.

Alternatively, the effect of SSI on the seismic response of buildings in soft layered soils was analysed by Savin et al. [53], using a detailed 3D model. Also, Gatti et al. [25] presented a complete approach to model the full path from the source (earthquake) to a nuclear reactor. To do so, wave-motion was used as an input for a SSI Boundary Element Method (BEM)-Finite Element Method (FEM) model. Alternatively, simplified procedures [49, 55, 56] have been proposed to model SSI for seismic applications.

Numerical models to compute building vibrations due to road traffic include Pyl et. al [50, 51] who presented a coupled BEM-FEM methodology to analyse the road-soil-structure system. Alternatively, François et al. [22] studied dynamic building behaviour considering the relative stiffness between the building and the soil, with the aim of simplifying the soil-structure interaction.

Regarding the rail sector, the growth of urban railway track infrastructure has led to an increase in the number of properties affected by ground-borne railway vibrations [9, 39, 57, 58, 61]. The negative effects caused by railway traffic are more prominent in the presence of local irregularities [36] and are addressed in international standards [29, 30, 31]. Thus, it is desirable to estimate the potential increase in vibrations levels in nearby buildings.

To do so, a variety of numerical models have been proposed to compute building induced vibrations due to railway traffic. Prior to the construction stage of a new railway project or the construction of a building near an existing line, a detailed design is required [31] possibly using comprehensive 3D models with high computational cost. These include Fiala et al. [21] who developed a comprehensive BEM-FEM model to calculate building vibration and indoor noise. Alternatively, Galvín et al. [24] presented a coupled train–track–soil-structure 3D BEM-FEM model formulated in the time domain where nonlinear behaviour of structures could be also considered. Moreover, the problem of vibration in bridges was

studied by comprehensive models [5, 13]. Coulier et al. [10] studied the source (track) and receiver (building) interaction in order to determine the uncertainty of using uncoupled approaches. It was concluded that for a ballasted track the assumption of uncoupling was acceptable for distances from the track greater than six times the Rayleigh wave length.

Uncoupled simplified procedures are normally used at an earlier stage of railway line development [31]. These represent useful tools, because their lower computation times. Two such methods to evaluate building vibrations due to a train passage have been proposed by the Federal Railroad Administration (FRA) and the Federal Transit Administration (FTA) of the U.S. Department of Transportation [6, 7, 20]. Rücker et al. [52] developed a simplified prediction tool that allows to evaluate free-field and building vibrations. Auersch [1] analysed building vibration in inhomogeneous soils and proposed a simplified methodology to consider SSI in a layered ground. He studied building induced vibrations using a simple soil-wall-floor model based on an empirical transfer function obtained from the characteristics of the structure [3]. Moreover, this also included with a simple method to estimate vibration in buildings on pile foundations [2]. Hussein et al. [27] developed a sub-modelling method where a train-track-soil 3D model was coupled with a 2D building approach based on beam elements. Hussein also presented a 3D model to calculate vibrations in a piled foundation building due to railway traffic from a nearby underground tunnel [28]. Later, Kouroussis et al. [34] proposed a decoupled FE model to predict building vibrations due to tramway traffic with local irregularities. Also a hybrid numerical/experimental model to assess ground and building vibration was presented [37, 38]. In this a vehicle-track numerical approach which simulated vibration generation due to a variety of railroad artefacts was combined with a experimental procedure based on multiple single source transfer mobilities that modelled the transmission mechanism between rail and nearby structures. Lopes et al. [42, 43] developed an uncoupled model to evaluate building vibrations induced by railway traffic in tunnels. Free-field response was computed using a 2.5D FEM-Perfectly Matched Layers (PML) model and combined with a 3D FEM model to evaluate the building response. Connolly et al. [15, 16] proposed a scoping model to predict vibrations and in-door noise in buildings due to railway traffic. A wide range of soil vibration records generated by a 3D FEM model was used to build a machine learning approach. This procedure was combined with empirical factors [20] to compute building vibrations. López-Mendoza et al. [44] presented a scoping model based on modal superposition analysis. The free-field vibration was discretised into the frequency range corresponding to the modes of the structure. Kuo et al. [40] presented a hybrid model that combined recorded data and numerical predictions considering the definitions proposed by the FRA [20]. The source, propagation and receiver mechanisms were uncoupled. Recently Connolly et al. [18] presented a decoupled procedure to analyse soil-building vibrations due to railway irregularities. A 2.5D time-frequency domain model to compute soil vibrations was combined with a 3D FEM procedure to obtain building vibrations induced by railway defects.

This paper uses a simple procedure where the source (ground motion) and the receiver (building) are uncoupled. It is focused on the receiver model and proposes soil-structure

transfer functions considering SSI. These soil-structure transfer functions are combined with free-field vibrations to compare building vibration with low computational effort. The model is numerically verified comparing with a comprehensive BEM-FEM model. Finally, the proposed model is used to analyse building vibrations due to local irregularities.

C.2 METHODOLOGY

ISO 14837-1 standard [31] defines the magnitude of building vibration $A(f)$ in the frequency domain f as a function that the source $S(f)$, the propagation $P(f)$ and the receiver $R(f)$. Considering the assumption that all the three terms are uncoupled (Figure C.1), the magnitude of the building vibration $A(f)$ can be expressed as:

$$A(f) = S(f)P(f)R(f) \tag{1}$$

The procedure developed by the Federal Railroad Administration (FRA) [20] to estimate

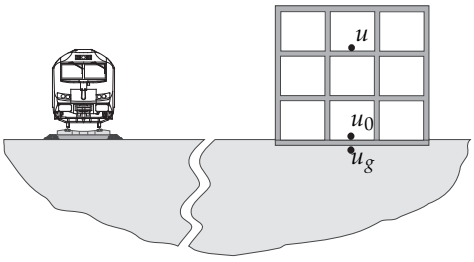

Figure C.1: Scheme of decoupled model.

building response due to railway traffic proposes two factors influencing the receiver: 1) the floor-to-floor attenuation, and, 2) the amplification due to the resonance of floors, walls and ceilings. The present work includes these factors defining the floor amplification F_a as the increment in the building response u with respect to the foundation response u_0 (Figure C.1). The floor amplification is computed as:

$$F_a(f) = u(f)/u_0(f) \tag{2}$$

Also, the effect of the building foundation should be considered using the coupling loss C_l [20]. The coupling loss is related to the soil-foundation interaction. Therefore it is the ratio between the building foundation response u_0 and the free-field vibration u_g (Figure C.1). In this work, the coupling is evaluated as:

$$C_l(f) = u_0(f)/u_g(f) \tag{3}$$

The following expression to calculate the building response u can be obtained by combining Equations (2) and (3):

$$u(f) = F_a(f)C_l(f)u_g(f) \tag{4}$$

Comparing Equations (1) and (4), it can be seen that the source $S(f)$ and the propagation $P(f)$ terms are included in the free-field vibration u_g, whereas the receiver term $R(f)$ is part of the floor amplification F_a and the coupling loss C_l. The main novelty of this work is applying the soil-structure transfer functions $u/u_g = F_a(f)C_l(f)$ depending only on the receiver, to predict building vibration by railway traffic. The soil-structure transfer function represents the building response due to a displacement impulse applied at the building foundation. A key advantage of this approach is the computational efficiency arising because the soil-structure transfer function is computed only once for a soil-building subsystem and later it is combined with a wide range of free-field vibration data to analyse multiple scenarios. These low requirements mean the approach is well-suited to early stage railway projects. On the other hand, although this work is focused on the application of soil-structure transfer functions to assess building vibrations by railway traffic, these soil-structure transfer functions can be used to predict building vibration due to diverse sources (e.g. construction, earthquake, road traffic, blast) where the free-field vibration spectrum is known.

This work uses the methodology presented in reference [18] to model the source - propagation subsystem ($S(f)$, $P(f)$). Once it is solved for the source-propagation subsystem, it can be used to compute the building vibration $A(f)$. To do so, the building foundation is excited by the free-field response u_g. The SSI is integrated in the proposed methodology using a simplified method. Below, it will be related the procedure to model the receiver soil-structure subsystem ($R(f)$).

C.2.1 *Simplified building-soil coupling model*

The simplified method is a 3D time domain FEM model. The dynamic equilibrium equation of a structure can be written as:

$$\mathbf{M}\ddot{\mathbf{u}}(t) + \mathbf{C}\dot{\mathbf{u}}(t) + \mathbf{K}\mathbf{u}(t) = \mathbf{F} \tag{5}$$

where $\mathbf{M}$, $\mathbf{C}$ and $\mathbf{K}$ are the mass, damping and stiffness matrices, respectively. $\mathbf{u}(t)$, $\dot{\mathbf{u}}(t)$, and $\ddot{\mathbf{u}}(t)$ are the building displacement, velocity and acceleration, respectively, while $\mathbf{F}$ represents the external force. The FEM equation is solved at each time step following an implicit time integration GN22 Newmark method [46, 62]. Structural damping is considered following a Rayleigh model [8], where the damping matrix $\mathbf{C}$ is proportional to the the mass $\mathbf{M}$ and stiffness $\mathbf{K}$ matrices as $\mathbf{C} = d_m\mathbf{M} + d_k\mathbf{K}$. Constants d_m and d_k are chosen depending on the modal damping of the structure.

Next a brief description of the simplified methodology to model SSI focused on the case of a building with a slab foundation on the surface of a homogeneous soil is presented. The

foundation consisting of a slab. A drawback of the approach is that it can not be applied to deep foundations. In order to consider SSI for layered soils, equivalent homogeneous soils are obtained depending on the average shear wave velocity V_{s30} as defined in Eurocode 8 [19], and computed as:

$$V_{s30} = \frac{30\ [\mathrm{m}]}{\sum_i^{N_s} \frac{h_i}{c_{s_i}}} \tag{6}$$

where h_i is the thickness of the i th layer, N_s the total number of layers in the top 30 m and c_{s_i} the shear wave velocity of the i th layer. Therefore, equivalent homogeneous soils with $c_s = V_{s30}$ are considered to model layered soils.

The simplified method is based on recommendations from the National Institute of Standards and Technology (NIST) [45]. This proposes to integrate SSI by adding spring-damper elements to the foundation of the building. As the building is not embedded in the soil, expressions to define horizontal spring-damper elements are discarded. The formulation to calculate vertical spring-damper elements is below.

To explain the simplified model, consider a rectangular building with floor plan dimensions $2L \times 2B$, where $L \geq B$ (Figure C.2). Note that in the following formulation, the sub-indices x, y and z are related to the translation along the respective axis. Also the sub-indices xx and yy refer the rocking about the x and y respectively, whereas sub-index zz is related to the torsion about the z axis (Figure C.2). Hereafter, the formulation considers the x axis to be the largest dimension of the foundation ($2L$).

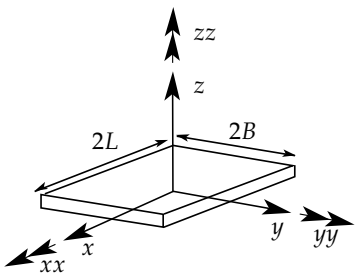

Figure C.2: Scheme of the plan geometry of the building foundation.

A spring-damper system is added to the foundation allowing it to be modelled as rigid or flexible. For the rigid case, a single spring-damper element defined by its stiffness k_z and the dashpot coefficient c_z. On the other hand, flexible foundations are simulated using spring-damper elements (k_z^i , c_z^i) spread across the foundation area, where k_z^i and c_z^i are the properties of the i^{th} spring-damper element.

C.2.1.1 *Rigid foundation*

If the foundation is rigid, it can be represented by a single spring-damper element (k_z , c_z). The vertical stiffness of the full system k_z, is evaluated using the formulation presented in reference [48]:

$$k_z = K_{z,surf}\alpha_z \tag{7}$$

where $K_{z,surf}$ is the vertical static stiffness of the surface foundation and α_z is the dynamic stiffness modifier. The vertical static stiffness $K_{z,surf}$ is obtained from the shear modulus G and Poison's ratio of the soil ν, and the foundation dimensions L and B, using:

$$K_{z,surf} = \frac{GB}{1-\nu}\left(3.1\left(\frac{L}{B}\right)^{0.75} + 1.6\right) \tag{8}$$

Also the dynamic stiffness modifier α_z depends on the structural properties and is evaluated as:

$$\alpha_z = 1 - \frac{\left(0.4 + \frac{0.2}{\frac{L}{B}}\right)a_0^2}{\frac{10}{1+3\left(\frac{L}{B}-1\right)} + a_0^2} \tag{9}$$

where a_0 is the dimensionless frequency computed from the S-wave velocity c_s and the angular frequency of the first bending mode ω_1 (discarding SSI), as:

$$a_0 = \frac{\omega_1 B}{c_s} \tag{10}$$

Once the vertical stiffness k_z is obtained, the dashpot coefficient of the full foundation c_z can be computed using [45]:

$$c_z = 2k_z\frac{\beta_z + \beta_s}{\omega_1} \tag{11}$$

where β_s is the damping ratio of the soil and β_z is the radiation damping ratio obtained as [48]:

$$\beta_z = \frac{4\psi\frac{L}{B}}{\frac{K_{z,surf}}{GB}}\frac{a_0}{2\alpha_z} \tag{12}$$

where $\psi = \sqrt{2\left(1-\nu\right)\left(1-2\nu\right)}$, limited to $\psi \leq 2.5$.

Following the same procedure to calculate the vertical stiffness k_z (Eq. (7)), the rocking stiffness can be obtained as [48]:

$$k_{yy} = K_{yy,surf}\alpha_{yy} \qquad k_{xx} = K_{xx,surf}\alpha_{xx} \tag{13}$$

The rocking static stiffnesses ($K_{xx,surf}$, $K_{yy,surf}$) and the dynamic stiffness modifiers (α_{xx}, α_{yy}) are evaluated as:

$$K_{yy,surf} = \frac{GB^3}{1-\nu}\left(3.73\left(\frac{L}{B}\right)^{2.4} + 0.27\right) \qquad K_{xx,surf} = \frac{GB^3}{1-\nu}\left(3.2\left(\frac{L}{B}\right) + 0.8\right) \tag{14}$$

$$\alpha_{yy} = 1 - \frac{0.55a_0^2}{0.6 + \frac{1.4}{\left(\frac{L}{B}\right)^3} + a_0^2} \qquad \alpha_{xx} = 1 - \frac{\left(0.55 + 0.01\sqrt{\frac{L}{B} - 1}\right)a_0^2}{2.4 - \frac{0.4}{\left(\frac{L}{B}\right)^3} + a_0^2} \tag{15}$$

In the same way as for the vertical dashpot (Eq. (11)), the rocking dashpot is computed as [48]:

$$c_{yy} = 2k_{yy}\frac{\beta_{yy} + \beta_s}{\omega_1} \qquad c_{xx} = 2k_{xx}\frac{\beta_{xx} + \beta_s}{\omega_1} \tag{16}$$

where the radiation damping ratios β_{xx} and β_{yy} are calculated as:

$$\beta_{yy} = \frac{\frac{4\psi}{3}\left(\frac{L}{B}\right)^3 a_0^2}{\frac{K_{yy,surf}}{GB^3}\left(\frac{1.8}{1+1.75\left(\frac{L}{B}-1\right)} + a_0^2\right)}\frac{a_0}{2\alpha_{xx}} \qquad \beta_{xx} = \frac{\frac{4\psi}{3}\frac{L}{B}a_0^2}{\frac{K_{xx,surf}}{GB^3}\left(2.2 - \frac{0.4}{\left(\frac{L}{B}\right)^3} + a_0^2\right)}\frac{a_0}{2\alpha_{yy}} \tag{17}$$

C.2.1.2 *Flexible foundation*

Equations 7 and 11 compute the spring-damper element (k_z, c_z) properties for rigid foundations. However, in order to consider the effect of a flexible foundation, the NIST proposes smeared spring and damper elements. To do so, the vertical values k_z and c_z are normalized by the foundation area to obtain the stiffness intensity $\tilde{k}_z^i = k_z/4BL$ and dashpot intensity $\tilde{c}_z^i = c_z/4BL$. Then, the stiffness k_z^i and dashpot c_z^i of a vertical spring-damper element in the interior of the foundation can be computed as:

$$k_z^i = \tilde{k}_z^i dA^i \qquad c_z^i = \tilde{c}_z^i dA^i \tag{18}$$

where dA^i is the individual area for the i^{th} spring-damper element (Figure C.3).

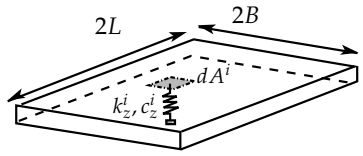

Figure C.3: Individual area dA^i for the i spring-damper element.

If these expressions (Eq. (18)) are used across the full foundation, the rotational stiffness would be underestimated and the rotational damping would be overestimated [45]. To correct these effects, factors R_k and R_c are applied to the spring-damper elements along a strip area on the the foundation edge. To do so, the stiffness and damping of a vertical spring-damper element at the foundation edge are estimated as:

$$k_z^i = R_k \tilde{k}_z^i dA^i \qquad c_z^i = R_c \tilde{c}_z^i dA^i \tag{19}$$

The width of the foundation edge strip is computed from the foundation end ratio R_e as $R_e L$ and $R_e B$ for the x and y axes, respectively. A value in the range from 0.3 to 0.5 is usually selected for the foundation end ratio R_e. In this work an end ratio $R_e = 0.5$ is used. Figure C.4 shows the spring-damper element properties (k_z^i, c_z^i) depending on the position of the i^{th} element across the foundation.

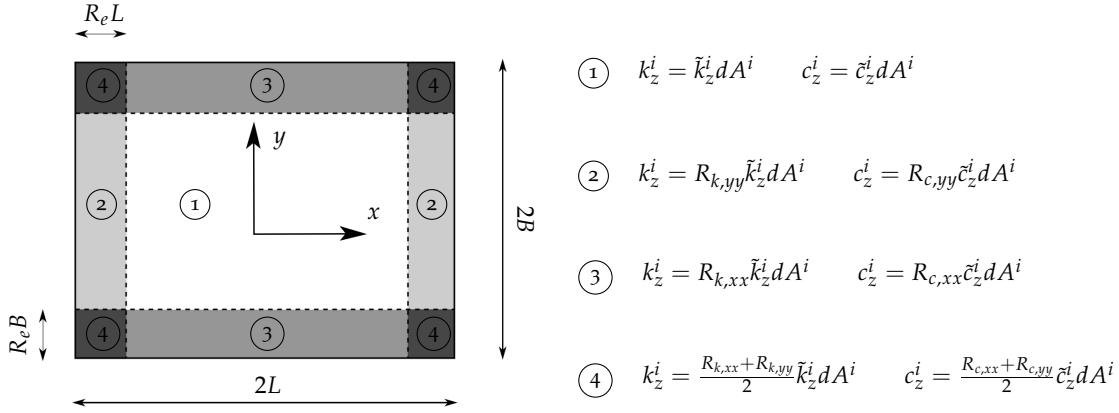

Figure C.4: Spring-damper element properties across the foundation.

Regarding the estimation of the correction factors R_k and R_c, the following expressions are proposed by the NIST:

$$R_{k,yy} = \frac{\frac{3k_{yy}}{4\tilde{k}_z^i BL^3} - (1-R_e)^3}{1-(1-R_e)^3} \qquad R_{k,xx} = \frac{\frac{3k_{xx}}{4\tilde{k}_z^i B^3 L} - (1-R_e)^3}{1-(1-R_e)^3} \tag{20}$$

$$R_{c,yy} = \frac{\frac{3c_{yy}}{4\tilde{c}_z^i BL^3}}{R_{k,yy}\left(1-(1-R_e)^3\right)+(1-R_e)^3} \qquad R_{c,xx} = \frac{\frac{3c_{xx}}{4\tilde{c}_z^i BL^3}}{R_{k,xx}\left(1-(1-R_e)^3\right)+(1-R_e)^3} \tag{21}$$

where k_{xx} and k_{yy} are the rotational stiffnesses about the x and y axes respectively, considering a rigid foundation. Also the dashpot coefficients c_{xx} and c_{yy} represent the rotational damping about the x and y axes respectively.

C.2.2 *Methodology summary*

1. The spring-damper system supporting the building foundation is computed using soil properties (c_s, G, ν, β_s), foundation geometry (B, L) and first bending mode (ω_1).
2. These inputs are used to obtain the spring-damper system properties for either a rigid foundation (Equations (7) and (11)) or a flexible foundation (Equations (18) and (19)).
3. The spring-damper system is assembled/combined with the building model. This allows for the construction of the global mass, damping and stiffness matrices (**M**, **C**, **K**).
4. The soil-structure transfer function $u/u_g = F_a(f)C_l(f)$ is computed by solving the dynamic equilibrium equation of the structure due to a displacement impulse applied at its foundation (Equation (5)).
5. The soil-structure transfer function is combined with the free-field vibration u_g [18] to obtain the building response u due to an arbitrary excitation (Equation (4)).

C.3 BUILDING-SOIL MODEL VALIDATION

In this section, the dynamic behaviour of three buildings are compared with those obtained from the `SSIFiBo` toolbox [23]. The `SSIFiBo` toolbox represents a comprehensive model based on a 3D time domain BEM-FEM methodology. The solution u^r represents the building response from `SSIFiBo` toolbox, hereafter called the 'reference' solution, whereas u^s is the solution computed using the simplified method considering flexible foundation. A third solution is also computed for each case, where SSI $\tilde{u}$ is ignored.

To quantify the effect of SSI, it is studied using the ratios:

$$\Delta u^r(f) = \frac{u^r(f)}{\tilde{u}(f)} \qquad \Delta u^s(f) = \frac{u^s(f)}{\tilde{u}(f)} \tag{22}$$

Substituting Equation (4) into Equation (22) and remembering that the coupling loss $\tilde{C}_l$ for the solution without SSI is equal to 1, the SSI effect can be rewritten as:

$$\Delta u^r = C_l^r F_a^r / \tilde{F}_a \qquad \Delta u^s = C_l^s F_a^s / \tilde{F}_a \tag{23}$$

This work analyses the assumption that SSI depends only on the coupling loss $\Delta u^r \approx C_l^r$ and $\Delta u^s \approx C_l^s$. Substituting this simplification in Equation (23) involves that the solution ignoring SSI presents floor amplifications close to those obtained using the reference model $F_a^r/\tilde{F}_a \approx 1$ and the simplified method $F_a^s/\tilde{F}_a \approx 1$. This assumption allows for the analysis of two simplified solutions u^I and u^{II}, where the coupling loss is computed using the reference C_l^r and the simplified C_l^s models, respectively.

Therefore, to summarise, the following solutions are analysed in this work:

$$
\begin{aligned}
u^r(f) &= F_a^r(f) C_l^r(f) u_g(f) \\
u^s(f) &= F_a^s(f) C_l^s(f) u_g(f) \\
\tilde{u}(f) &= \tilde{F}_a(f) u_g(f) \\
u^I(f) &= \tilde{F}_a(f) C_l^r(f) u_g(f) \\
u^{II}(f) &= \tilde{F}_a(f) C_l^s(f) u_g(f)
\end{aligned}
$$

The analysis of the buildings excited due to an incident wavefield allows for the evaluation of the accuracy of the simplified method (Section C.2.1) and the assumption described above.

The three types of building consist of four, six and twelve storey concrete buildings founded on a slab, with framed walls (Figure C.5). Floor plan dimensions of 12m $\times$ 40m, 20m $\times$ 20m and 12m $\times$ 12m are considered for the four, six and twelve storey buildings, respectively. The floors are simply supported concrete slabs. Four edge beams are considered in the twelve storey building. The concrete material has the following properties: Young's modulus $E = 20 \times 10^9\,\mathrm{N/m^2}$, Poisson's ratio $\nu = 0.2$ and density $\rho = 2400\,\mathrm{kg/m^3}$. A structural damping, $\zeta = 5\,\%$ is set for the dominant mode shapes (Figure C.6). The structures are discretised using two-node Euler-Bernoulli elements to represent columns and beams and four-node shell elements for the floors and the framed walls. Table C.1 summarises the building properties.

Table C.1: Building properties.

	4-storey	6-storey	12-storey
Column section $[\mathrm{m^2}]$	0.3×0.3	0.3×0.3	0.6×0.4
Edge beam section $[\mathrm{m^2}]$	–	–	0.6×0.2
Frame wall thickness [m]	0.25	0.25	0.15
Floor slab thickness [m]	0.25	0.25	0.2
Foundation slab thickness [m]	0.5	1	1

The dominant bending mode shapes computed without considering SSI can be observed in Figure C.6.

The buildings are on a homogeneous soil with P-wave velocity $c_p = 250\,\mathrm{m/s}$, S-wave velocity $c_s = 100\,\mathrm{m/s}$, material damping $\xi = 0.06$ and density $\rho = 1750\,\mathrm{kg/m^3}$. The building responses are presented for the observation points A and B (Figure C.5).

The incident wave field consists of a uniform vertical displacement $\tilde{\mathbf{u}}_g = \delta(t)$ m, where δ is the Dirac delta function. Therefore, the incident wave field in the frequency domain presents a constant value. This incident wave field allows for the calculation of the building response solely in terms of the receiver $u(f) = F_a(f) C_l(f)$ (Equation (4)). Also the coupling loss represents the foundation response $C_l(f) = u_0(f)$ (Equation (3)).

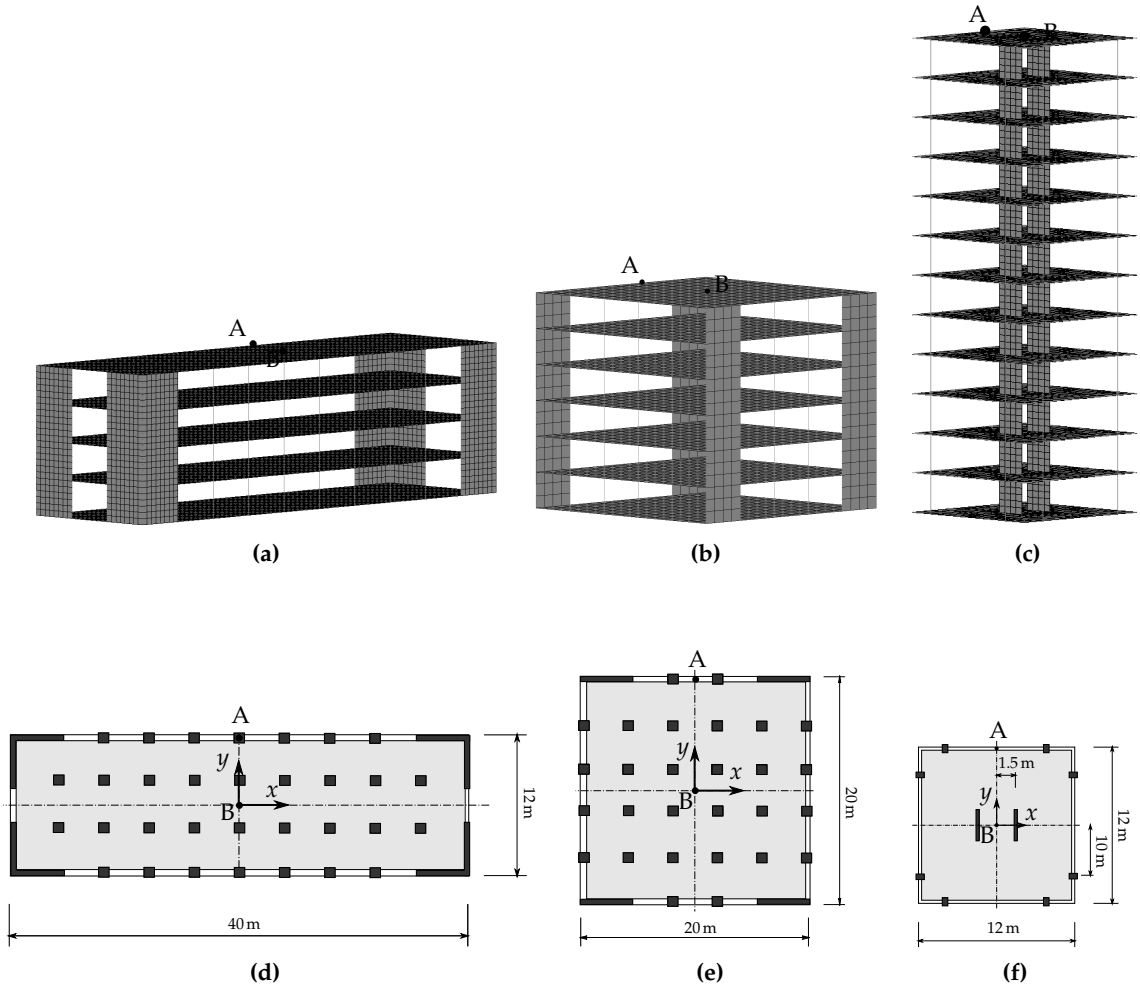

Figure C.5: Discretization and plan geometry of the (a, d) four, (b, e) six and (c, f) twelve-storey buildings.

Figure C.7 shows the one-third octave band representation [11] of the coupling loss computed using the reference model and the simplified method. Overall it is seen that the presence of the building attenuates the soil vibration, while the simplified method presents an acceptable estimation of the coupling loss. Moreover, the coupling loss does not depend strongly on the type of building or the observation point.

The floor amplification (Equation 2) is shown in Figures C.8 and C.9 from the first to fourth floors, for the simplified and reference models, and the case of ignoring SSI. Overall the floor amplification increases with the storey level in the low frequency range, while the excitation is filtered at higher frequencies according to the modal parameters of the buildings. It is seen that the floor amplification of each storey level is within the same order of magnitude. Although the simplified methodology presents a better agreement with

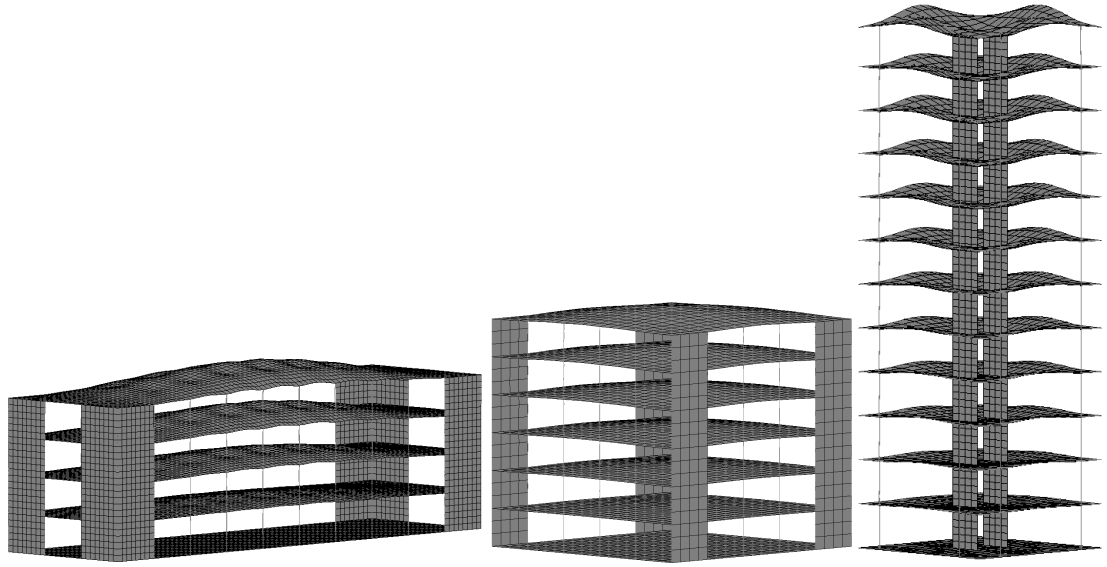

(a) Mode at 9.5 Hz **(b)** Mode at 6.9 Hz **(c)** Mode at 9.1 Hz

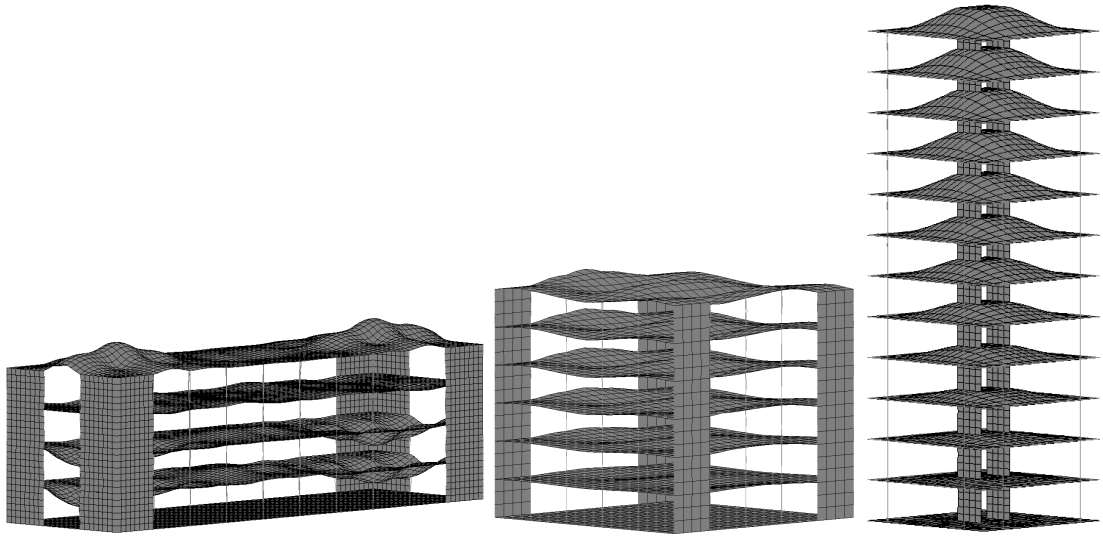

(d) Mode at 17.8 Hz **(e)** Mode at 14.2 Hz **(f)** Mode at 20.1 Hz

Figure C.6: Dominant bending mode shapes of the (a,d) four-storey building, (b,e) and (c,f) twelve-storey building.

the reference model results, the response from the solution ignoring SSI $\tilde{F}_a$ also matches acceptably well.

Figures C.10 and C.11 present the soil-structure transfer function $u(f)/u_g(f)$ for all 3 models. This soil-structure transfer function is obtained from the receivers terms $u(f)/u_g(f)$

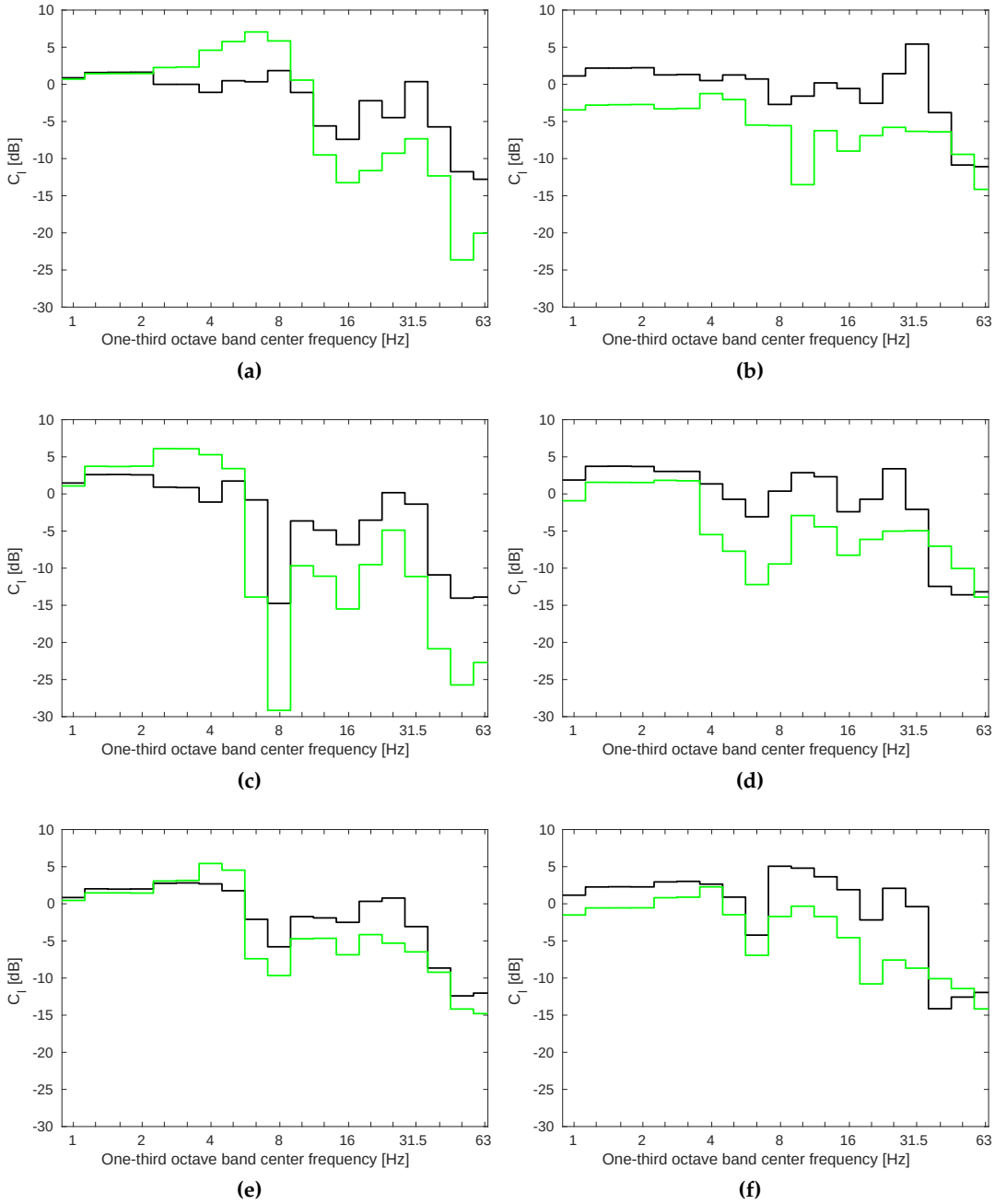

Figure C.7: One-third octave band center frequency of the coupling loss due to an incident wave field, at the observation points (a,c,e) A and (b,d,f) B of the (a,b) four-storey, (c,d) six-storey and (e,f) twelve-storey buildings, from the (black line) `SSIFiBo` toolbox and the (green line) simplified methodology.

$= F_a(f)C_l(f)$ (Equation (4)). It can be concluded that the shape and magnitude of the response from the simplified method match reasonable well with those obtained from the

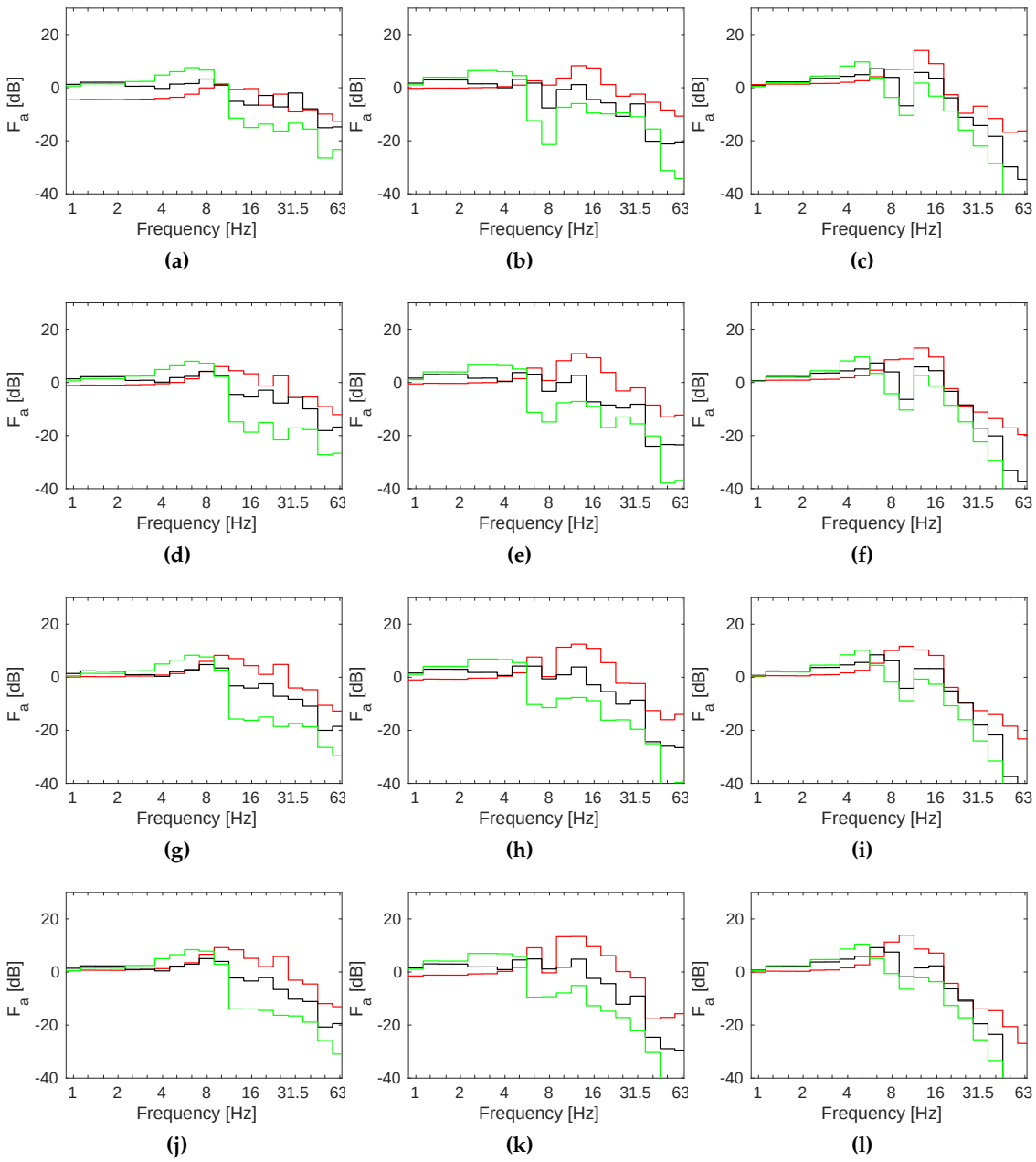

Figure C.8: One-third octave band center frequency of the floor amplification due to an incident wave field, at the observation point *A* of the (a,d,g,j) four-storey, (b,e,h,k,) six-storey and (c,f,i,l) twelve-storey buildings, at the (a,b,c) first, (d,e,f) second, (g,h,i) third and (j,k,l) fourth floors, from the (black line) `SSIFiBo` toolbox , the (green line) simplified methodology and (red line) ignoring SSI.

reference model, although the results from the simplified method are underestimated. The response ignoring SSI overestimates the result.

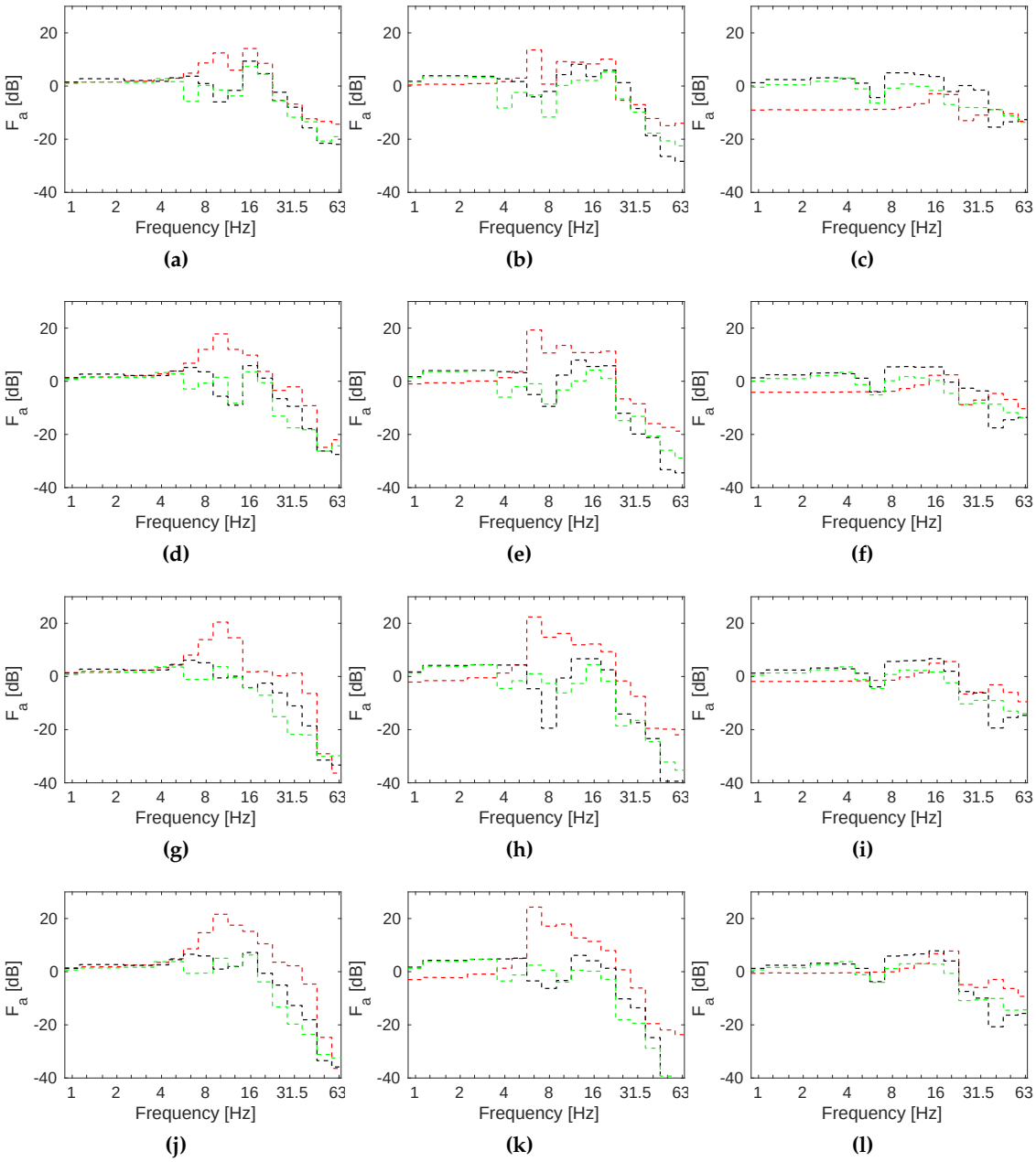

Figure C.9: One-third octave band center frequency of the floor amplification due to an incident wave field, at the observation point B of the (a,d,g,j) four-storey, (b,e,h,k,) six-storey and (c,f,i,l) twelve-storey buildings, at the (a,b,c) first, (d,e,f) second, (g,h,i) third and (j,k,l) fourth floors, from the (black line) `SSIFiBo` toolbox , the (green line) simplified methodology and (red line) ignoring SSI.

The effect of SSI is shown in Figure C.12 which displays the ratios Δu^r and Δu^s (Equation (22)) for all the storey levels of the buildings. Also, it superimposes the coupling loss factors

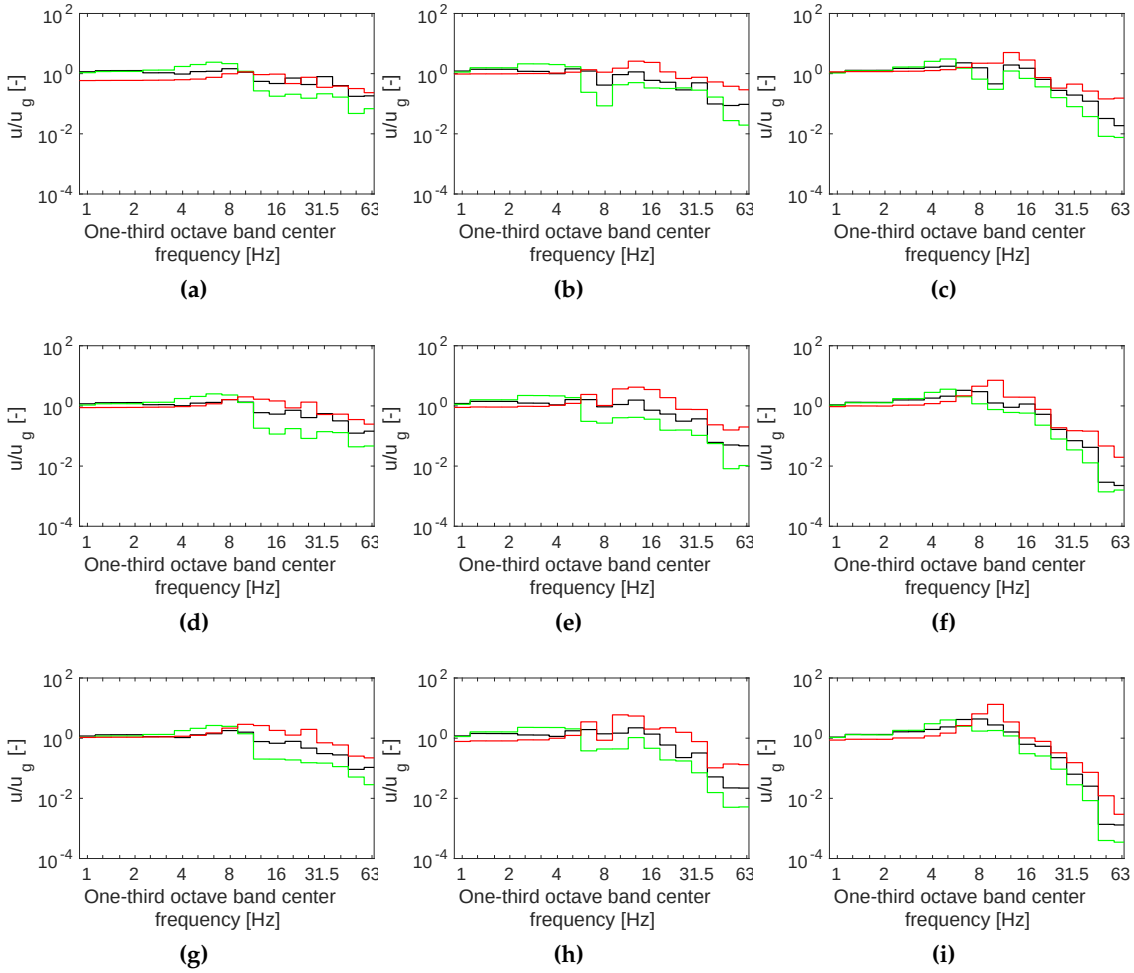

Figure C.10: One-third octave band center frequency of the soil-structure transfer function due to an incident wave field, at the observation point A of the (a,d,g) four-storey, (b,e,h) six-storey and (c,f,i) twelve-storey buildings, at the (a,b,c) first, (d,e,f) middle and (g,h,i) top floors, from the (black line) `SSIFiBo` toolbox, the (green line) simplified methodology and (red line) ignoring SSI.

C_l^r and C_l^s to evaluate the accuracy of the approximations $\Delta u^r \approx C_l^r$ and $\Delta u^s \approx C_l^s$, defined above. Although there are amplifications at low frequencies, it can be seen that there are attenuations at mid and high frequencies due to SSI. It is observed that the effect of SSI depends minorly on storey level. However, it is valid to approximate the SSI effect using the coupling loss factor.

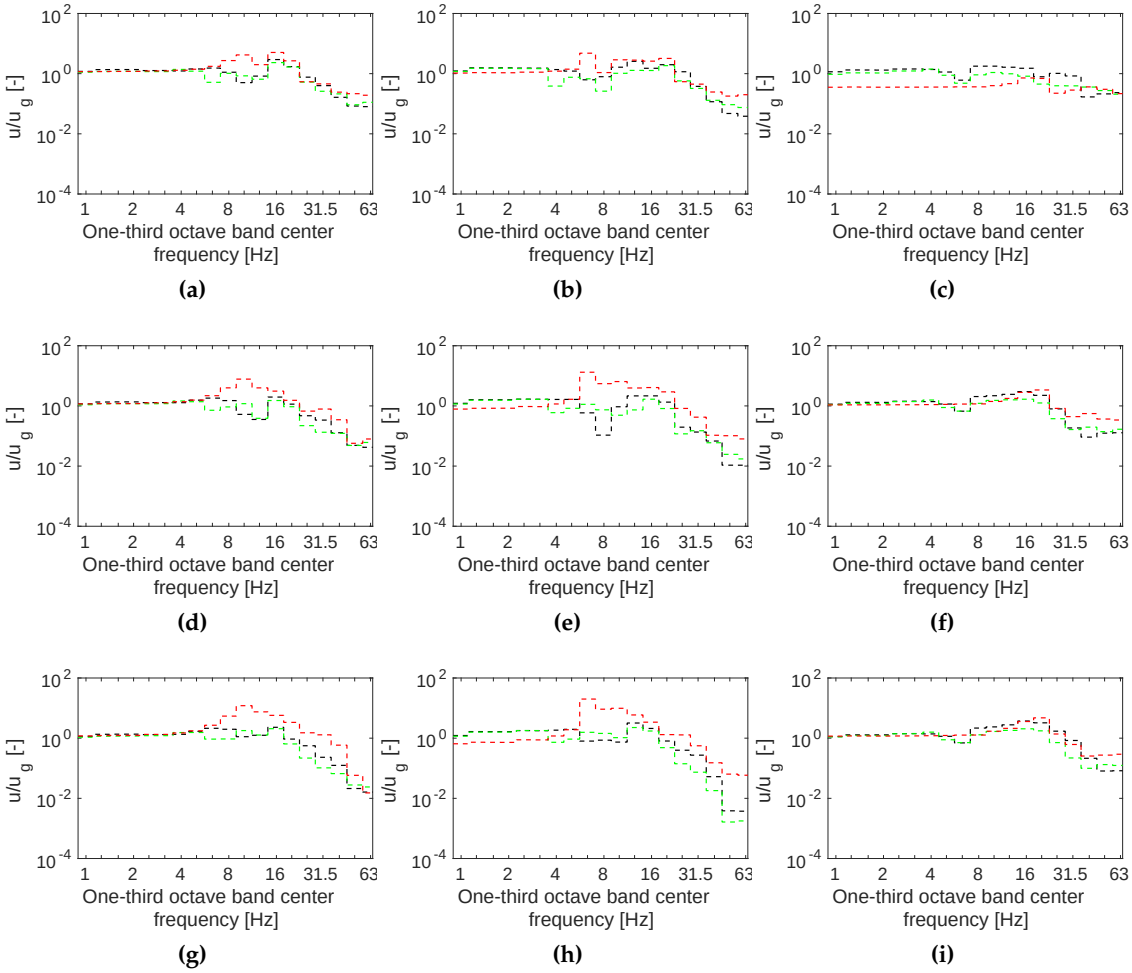

Figure C.11: One-third octave band center frequency of the soil-structure transfer function due to an incident wave field, at the observation point B of the (a,d,g) four-storey, (b,e,h) six-storey and (c,f,i) twelve-storey buildings, at the (a,b,c) first, (d,e,f) middle and (g,h,i) top floors, from the (black line) `SSIFiBo` toolbox, the (green line) simplified methodology and (red line) ignoring SSI.

In order to assess the accuracy of the proposed solutions described in Section C.2.2, Figures C.13 and C.14 show the differences with respect to the reference model. These differences are evaluated as:

$$D^s = 20 \log 10 \left(u^s / u^r \right)$$
$$\tilde{D}^s = 20 \log 10 \left(\tilde{u} / u^r \right)$$
$$D^I = 20 \log 10 \left(u^I / u^r \right)$$
$$D^{II} = 20 \log 10 \left(u^{II} / u^r \right)$$

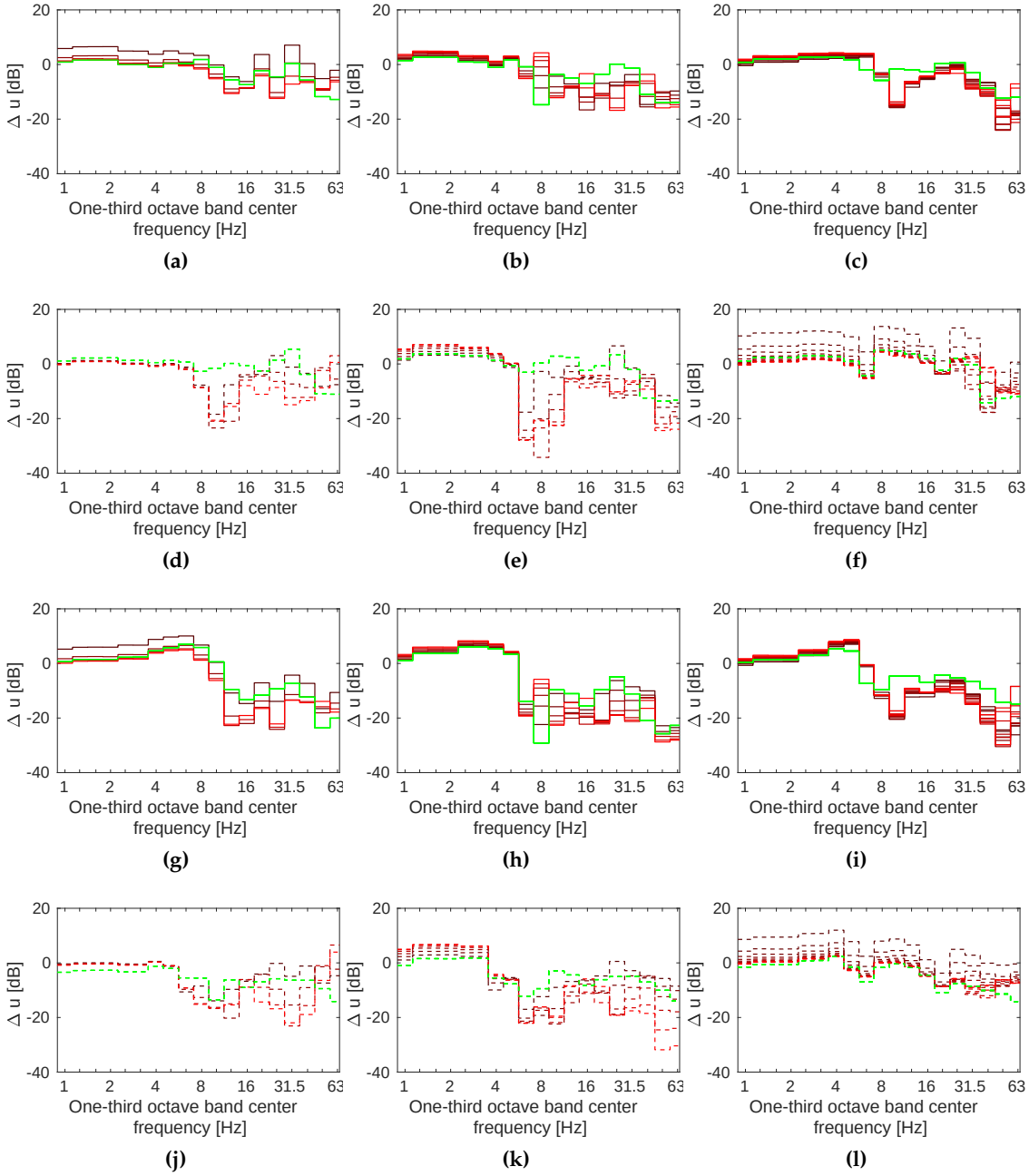

Figure C.12: One-third octave band center frequency of the (solid line) ratios (a-f) Δu^r and (g-l) Δu^s at the observation points (a,b,c,g,h,i, solid line) A and (d,e,f,j,k,l, dashed line) B of the (a,d,g,j) four-storey, (b,e,h,k) six-storey and (c,f,i,l) twelve-storey buildings. SSI attenuation from the (darkest line) first floor to the (red line) top floor. Superimposed is the (green line) coupling loss computed from the (a-f) `SSIFiBo` toolbox and the (g-l) simplified method.

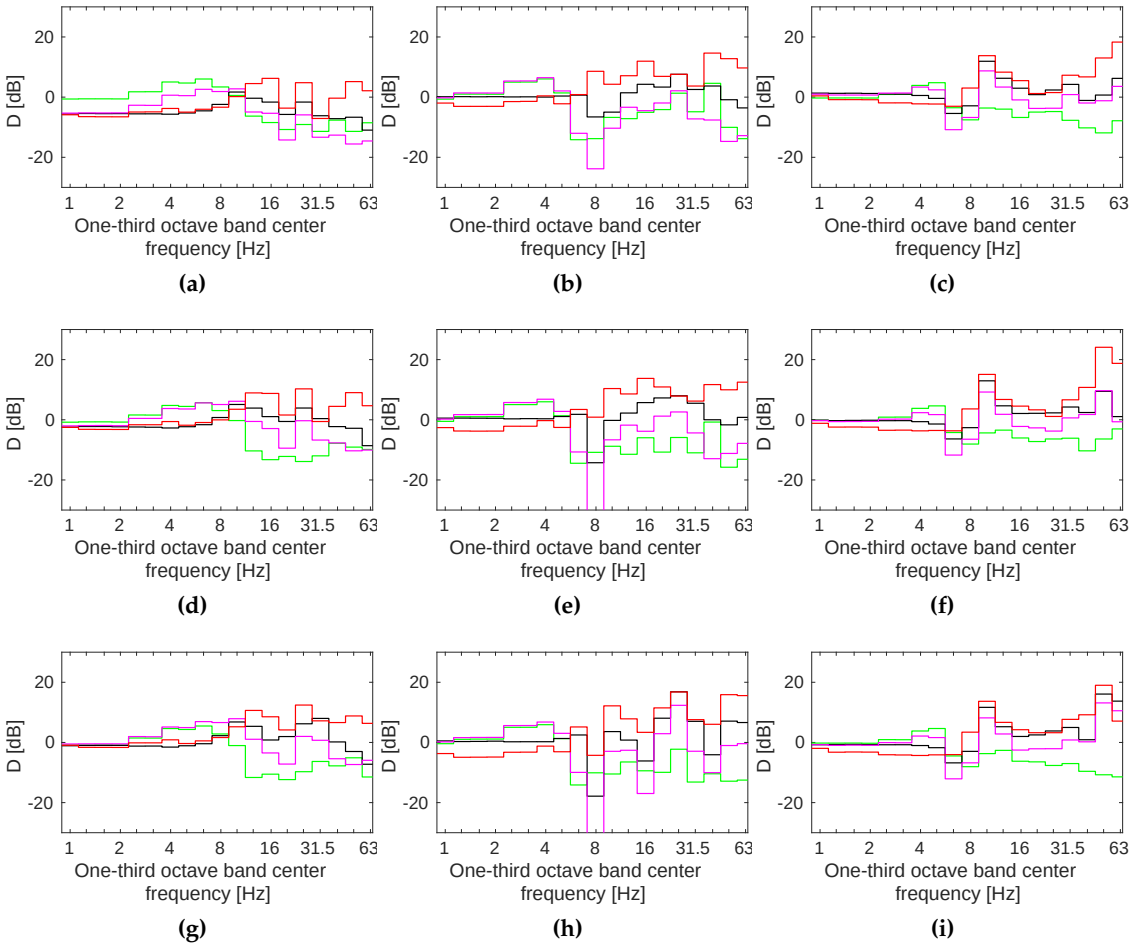

Figure C.13: One-third octave band center frequency of the differences at the observation point A of the (a,d,g) four-storey, (b,e,h) six-storey and (c,f,i) twelve-storey buildings, at the (a,b,c) first, (d,e,f) middle and (g,h,i) top floors, from the (green line) simplified methodology D^s, the (black line) approximation I D^I, the (magenta line) approximation II D^{II} and the (red line) solution ignoring SSI $\tilde{D}$.

It is seen that the agreement of the simplified method is reasonably good and this presents the better approximation with discrepancies up to 16 dB. As expected, the response ignoring SSI overestimates the result. These amplifications are partly modulated with the coupling loss C_l^r computed from the reference model as shown by the curve D^I. Also, the proposed solutions u^s, u^I and u^{II} are in the same range of uncertainty.

The discrepancies between the reference model Maximum Transient Vibration Value (MTVV) [29] response u^r and the solutions u^s, $\tilde{u}$, u^I and u^{II} are shown in Figure C.15, depending on storey level. The amplification of the solution ignoring SSI is not greatly modulated by the coupling loss C_l^r proposed in the solution u^I. In spite of the discrepancies, the solutions u^r, u^I and u^{II} give acceptable predictions. The accuracy is similar to the

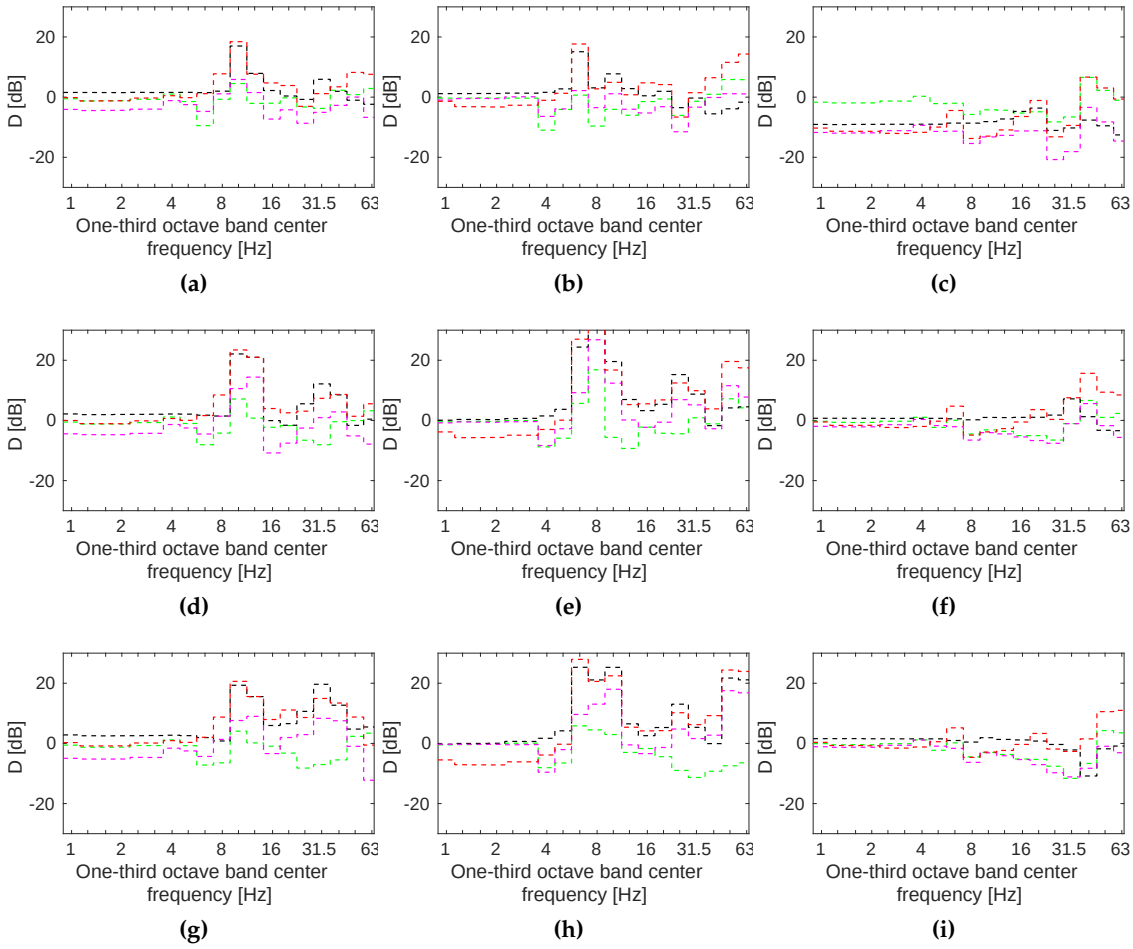

Figure C.14: One-third octave band center frequency of the differences at the observation point B of the (a,d,g) four-storey, (b,e,h) six-storey and (c,f,i) twelve-storey buildings, at the (a,b,c) first, (d,e,f) middle and (g,h,i) top floors, from the (green line) simplified methodology D^s, the (black line) approximation I D^I, the (magenta line) approximation II D^{II} and the (red line) solution ignoring SSI $\tilde{D}$.

uncertainty range (5 dB to 20 dB) as found in previous research [41, 32, 17]. The simplified method presents improved better results compared to the alternative solutions, so therefore is used for analysis in the next section.

C.4 CASE STUDY: RAILWAY TRACK DEFECTS

The proposed methodology is now used to analyse building vibration due to local track defects. The building response is calculated by combining the free-field u_g response due to railway traffic with the soil-structure transfer function $u(f)/u_g(f) = F_a(f)C_l(f)$ (Equation (4)) due to an incident wave field. Free-field response is calculated using a methodology

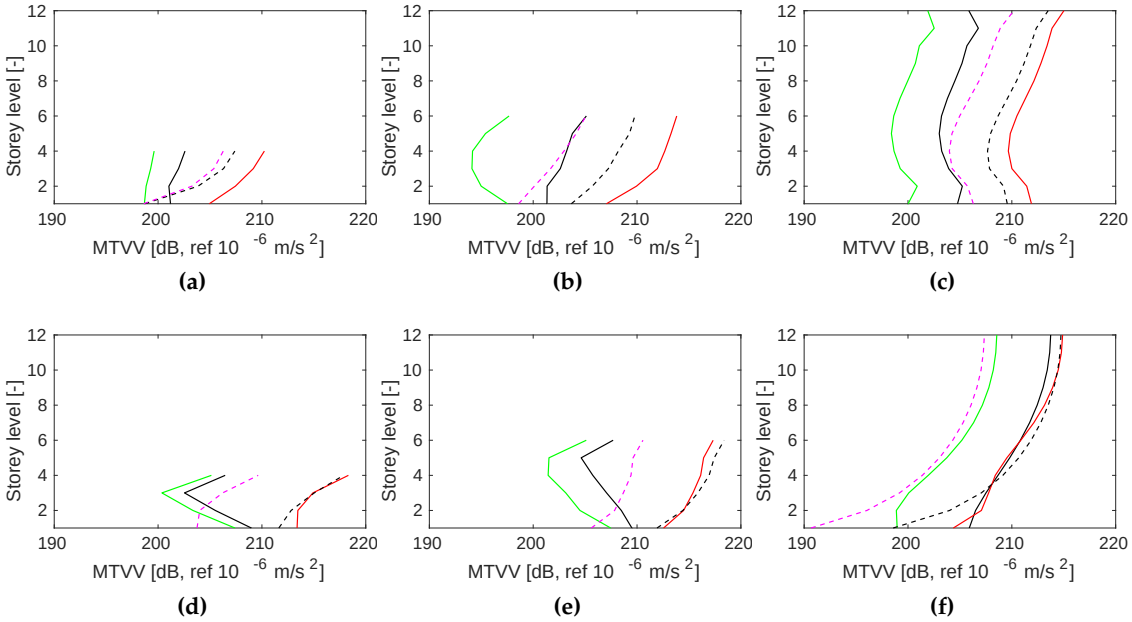

Figure C.15: MTVV due to an incident wave field evaluated at the observation points (a,b,c) A and (d,e,f) B of the (a,d) four-storey, (b,e) six-storey and (c,f) twelve-storey buildings computed from the (solid black line) `SSIFiBo` toolbox and the (green line) simplified method. Superimposed are the responses of the (dashed black line) approximation I, the (dashed magenta line) approximation II and (red line) ignoring SSI.

validated in reference [18]. Therefore this paper aims to use these excitation time histories as example datasets, rather than to validate or address the assumptions associated with the underlying excitation generation model.

Using a pre-determined source excitation facilitates reduced computational times because the soil-structure transfer function $u(f)/u_g(f)$ does not depend on the train passage and is only evaluated once for each soil. It should be noted that a comparison between the proposed methodology and the reference model is not included. This is because the free-field vibration u_g is the same for both models. Therefore, the discrepancies

$$\begin{aligned} D^s &= 20\log 10\left(\left(F_a^s(f)C_l^s(f)u_g(f)\right)/\left(F_a^r(f)C_l^r(f)u_g(f)\right)\right) \\ &= 20\log 10\left(\left(F_a^s(f)C_l^s(f)\right)/\left(F_a^r(f)C_l^r(f)\right)\right) \end{aligned}$$

are identical to those obtained previously (Figures C.13 and C.14), meaning the simplified method can be used to perform the analysis with acceptable accuracy.

A sensitivity analysis of the effect of soil properties, defect type, defect size and train speed is presented. Vibrations are obtained for the buildings analysed previously in Section C.3 (Figure C.5).

The influence of soil properties on the building response is studied using 3 homogeneous and 2 layered soils. Table C.2 contains their properties.

Table C.2: Soil properties.

		h [m]	E [MPa]	ν [−]	ξ [−]	ρ [kg/m^3]	V_{s30} [m/s]
Soil 1	Half-space	∞	50	0.35	0.05	2000	96.2
Soil 2	Half-space	∞	100	0.35	0.05	2000	136.1
Soil 3	Half-space	∞	200	0.35	0.05	2000	192.5
Soil 4	Layer 1	2	50	0.35	0.05	2000	180.4
	Half-space	∞	200	0.35	0.05	2000	
Soil 5	Layer 1	2	200	0.35	0.05	2000	99.5
	Half-space	∞	50	0.35	0.05	2000	

Figure C.16 shows the singular defects considered in the analysis, where v_0 is the train speed, h the defect height and l the defect length.

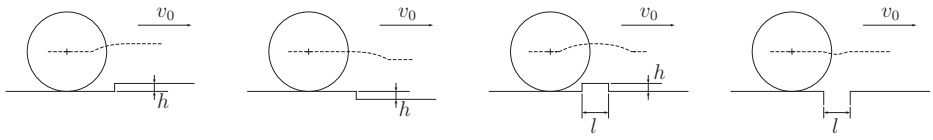

Figure C.16: Local defect shape (from left to right: step up, step down, positive pulse, negative pulse).

Moreover the defect size influence on building vibrations is analysed considering several defect lengths $l = \{80, 110, 140, 170, 200\}$ mm.

Regarding the vehicle, an AM96 intercity train (Figure C.17) travelling on a ballasted track is considered (Table C.4). Additionally the passage of a classic tram (Figure C.19) on an urban slab track (Table C.5) is studied. The vehicles are modelled using a detailed multibody vehicle approach [35] (Figure C.18). The AM96 and classic tram properties are shown in Table C.3.

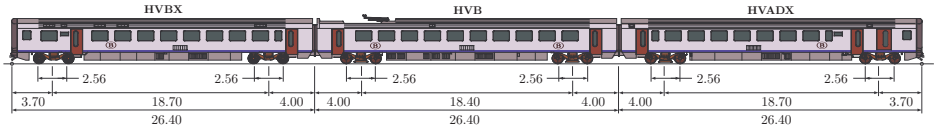

Figure C.17: AM96 train dimensions.

Train passages at $v_0 = \{60,90,120,150\}$ km/h and $v_0 = \{20,30,40,50\}$ km/h for the AM96 train and the classic tram are analysed respectively. The train speeds are below the critical velocity of the track-ground system [14, 47, 54].

The midpoint of the building foundation is located at a distance $d = 20$ m from the track centreline and the observation point B (Figure C.5) is selected because it presents the highest response (Figure C.15). Also, building vibrations are calculated considering a Single Point Response (SPR) excitation model, where the free-field vibration is transmitted simultaneously to the whole building foundation.

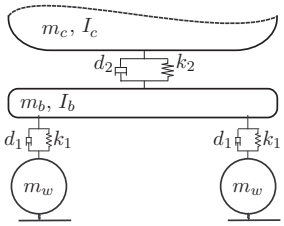

Figure C.18: Bogie modelling of AM 96 train and classic tram.

Table C.3: AM96 train properties.

		m_c [kg]	I_c [kg m^2]	m_b [kg]	I_b [kg m^2]	m_w [kg]	k_1 [MN/m]	d_1 [kNs/m]	k_2 [MN/m]	d_2 [kNs/m]
AM 96	HVB	25200	1.26×10^6	6900	1.52×10^3	1700	1.3	3.7	0.69	22.6
	HVADX	28900	1.45×10^6	7050	1.58×10^3	1700	1.3	3.7	0.69	22.6
	HVBX	25930	1.3×10^6	11800	2.6×10^3	1700	1.81	1.14	0.69	14
Classic tram		7580	8.75×10^4	3530	6.0×10^2	160	5.876	6	0.96	56.25

Table C.4: Ballasted track properties.

Ballast track properties (2 rails)	
Track gauge [m]	1.435
Rail 2nd moment of area $\left[\mathrm{m}^4\right]$	3.09×10^{-5}
Rail Young's modulus $\left[\mathrm{N/m}^2\right]$	2.1×10^{11}
Rail density $\left[\mathrm{kg/m}^3\right]$	7850
Railpad stiffness per unit length (2 rails) $\left[\mathrm{N/m}^2\right]$	6.15×10^8
Railpad damping per unit length (2 rails) $\left[\mathrm{Ns/m}^2\right]$	1.2×10^4
Sleeper spacing [m]	0.65
Sleeper mass per unit length [kg/m]	461.5
Ballast stiffness $\left[\mathrm{N/m}^2\right]$	1.3×10^8
Ballast damping $\left[\mathrm{Ns/m}^2\right]$	1.3×10^5
Ballast density $\left[\mathrm{kg/m}^3\right]$	1700
Ballast height (below sleeper) [m]	0.3
Ballast cross-sectional area $\left[\mathrm{m}^2\right]$	0.59
Ballast Poisson's ratio	0.3

C.4.1 *Soil properties*

This section analyses the effect of soil properties on building vibrations, considering the passage of the AM96 train at $v_0 = 120\,\mathrm{km/h}$, over a ballasted track, in the presence of a negative pulse defect.

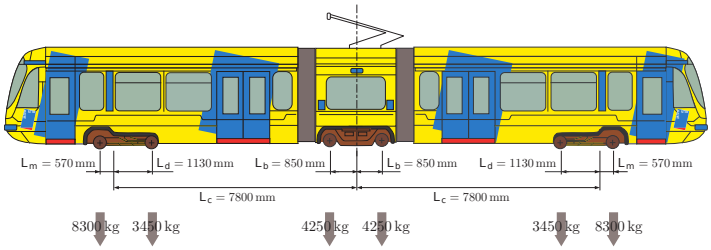

Figure C.19: Geometrical configuration of the classic tram.

Table C.5: Slab track properties.

Slab track properties (2 rails)	
Track gauge [m]	1.435
Rail 2nd moment of area $\left[\mathrm{m}^4\right]$	3.09×10^{-5}
Rail Young's modulus $\left[\mathrm{N/m}^2\right]$	2.1×10^{11}
Rail density $\left[\mathrm{kg/m}^3\right]$	7850
Railpad stiffness per unit length (2 rails) $\left[\mathrm{N/m}^2\right]$	4×10^8
Railpad damping per unit length (2 rails) $\left[\mathrm{Ns/m}^2\right]$	1.2×10^4
Slab thickness [m]	0.3
Slab width [m]	2.5
Slab stiffness (concrete) $\left[\mathrm{N/m}^2\right]$	3×10^{10}
Slab 2nd moment of area $\left[\mathrm{m}^4\right]$	5.63×10^{-3}
Slab density (concrete) $\left[\mathrm{kg/m}^3\right]$	2500
Slab Poison's ratio (concrete)	0.2

The free-field response v_g and the simplified method to consider SSI both depend on the soil properties. Figure C.20 shows the free-field velocity v_g and the soil-structure transfer function v/v_g in the frequency domain. In the free-field response (Figure C.20. (a)), dominant frequencies are located at mid frequencies due to dynamic excitation. These dominant frequencies increase with the soil stiffness varying from 14 to 22 Hz for the softest soil, to 35 and 56 Hz for the stiffest soils. Moreover, the influence of soil stratigraphy in the free field is shown. In spite of the small thickness of the uppermost layer ($h_1 = 2\,\mathrm{m}$), the dominant frequencies at the medium-high range depends on strongly the properties of this layer. The dominant frequencies of layered soil 4 (Table C.2) match with those observed in homogeneous soil 1, because both soils have the same properties in the uppermost layer. A similar effect can be observed between layered soil 5 and homogeneous soil 3. At the low frequency range, the dominant frequencies are controlled by the halfspace properties because of the long wavelengths.

In contrast, soil properties have a high influence on the amplitude of the soil-structure transfer function (Figure C.20. (b-d)), but the trend of the response is similar for all the

soils. The soil-structure transfer function shows amplifications at low and mid frequencies up to 30 Hz, whereas the response is damped at high frequencies. These amplifications are concentrated at 9 and 17 Hz for the four-storey building (Figure C.20. (b)), 6 and 14 Hz for the six-storey building (Figure C.20. (c)) and 20 Hz for the twelve-storey building (Figure C.20. (d)). These frequencies correspond with the natural frequencies of the buildings (Figure C.6). The effect of soil stratigraphy on the building response is not observed due to the assumption of considering an equivalent homogeneous soil to model the SSI.

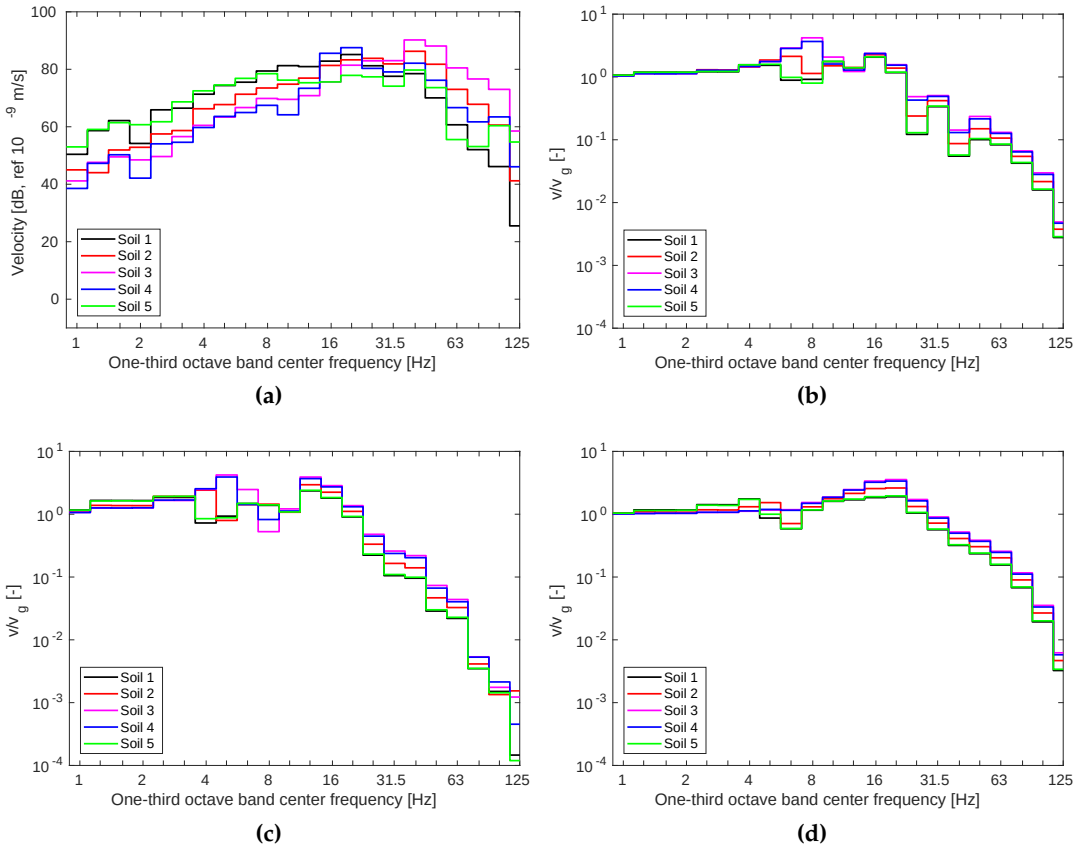

Figure C.20: (a) One-third octave band center frequency of the vertical velocity of the free field response v_g at 20 m to the ballasted track due to a AM96 train passage at $v_0 = 120$ km/h and (b-d) soil-structure transfer function v/v_g at the top floor of the (b) four-storey, (c) six-storey and (d) twelve-storey buildings for several soil properties.

Building vibration due to a railway defect is obtained by combining the free-field response v_g and the soil-structure transfer function shown previously (Figures C.20). Figure C.21 shows the frequency content and the running RMS value [29] of the building response. At low frequencies, building vibration decreases with soil stiffness (Figure C.21. (a,c,e)). This is as expected because the response depends on long wavelengths. In contrast, at high frequencies it is observed an increment of the building response with the soil stiffness. This

is consistent with the free-field response v_g (Figure C.20. (a)). In addition to the dominant frequencies indicated above, in the soil-structure transfer function v/v_g (Figure C.20. (b-d)), the additional frequencies due to the source are significant. Regarding the RMS running value (Figure C.21. (b,d,f)), the response of the layered soil with the softest uppermost layer yields the highest vibrations. This is due to the highest free-field response for this soil being approximately 20 Hz (Figure C.20. (a)). Although there are higher responses for other soils in the mid-high frequency range, these frequency contents are damped when the responses are weighted to obtain the running RMS values.

C.4.2 *Defect type*

This section analyses the influence of defect type on building vibrations for both the AM96 train and the classic tram, on homogeneous soil 2, considering several defect types (Figure C.16).

Figure C.22 presents the building response due to the AM96 passage over a ballasted track. Overall it can be observed the step up joint induces higher vibrations at low frequencies, whereas the maximum values at mid and high frequencies are due to the positive pulse. Also the defect type influences the amplitude of the response more dominantly than the shape (Figure C.22. (a,c,e)). The running RMS values (Figure C.22. (b,d,f)) do not show a clear dependency on the defect type because the responses have similar amplitudes.

The building vibrations induced by the classic tram passage over a slab track can be observed in Figure C.23. The frequency responses show a similar tendency for all defect types. However, it is more clearly shown in running RMS curves (Figure C.23. (b,d,f)) that the highest responses are found for the positive pulse and the step up joint. This is because the response (Figure C.23. (a,c,e)) for both defect types yields similar magnitudes in the dominant frequency range from 8 Hz to 20 Hz.

These differences between ballasted (Figure C.22) and slab tracks (Figure C.23) results show that the type of track is an important parameter to model during vibration assessment.

C.4.3 *Defect size*

This section analyses the effect of defect size on building vibrations. Negative pulse defect lengths spanning $l = \{80, 110, 140, 170, 200\}$ mm are considered in the presence of homogeneous soil 2 (Table C.2).

Figure C.24 shows the building response due to the classic tram passing over a slab track. The correlation between the response amplitude and the defect size is clearly observed in both frequency and time domain curves. The level of vibration increases significantly with the defect size from $l = 80$ to $l = 140$ mm, whereas the building response increases slightly for higher values of defect size.

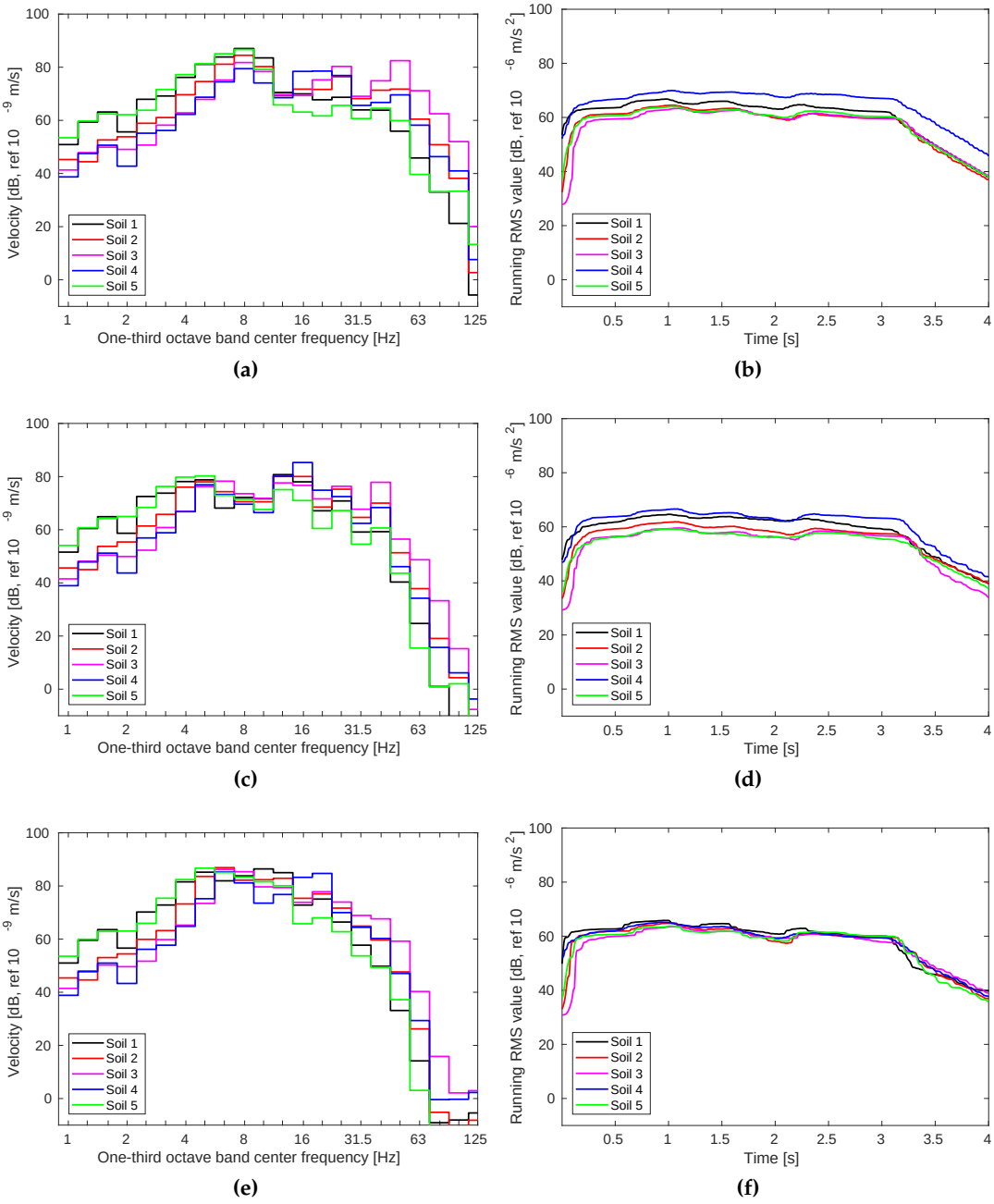

Figure C.21: (a,c,e) One-third octave band center frequency of the z vertical velocity and (b,d,f) running RMS value of the weighted acceleration at the top floor of the (a,b) four-storey, (c,d) six-storey and (e,f) twelve-storey buildings for several soil properties due to a AM96 train passage at $v_0 = 120\,\mathrm{km/h}$.

C.4.4 *Train speed*

This section computes several speeds of the AM96 train and the classic tram over the ballasted and slab tracks. The soil is type 2 (Table C.2) and the defect is a negative pulse defect. The train speed influence on building vibrations is analysed.

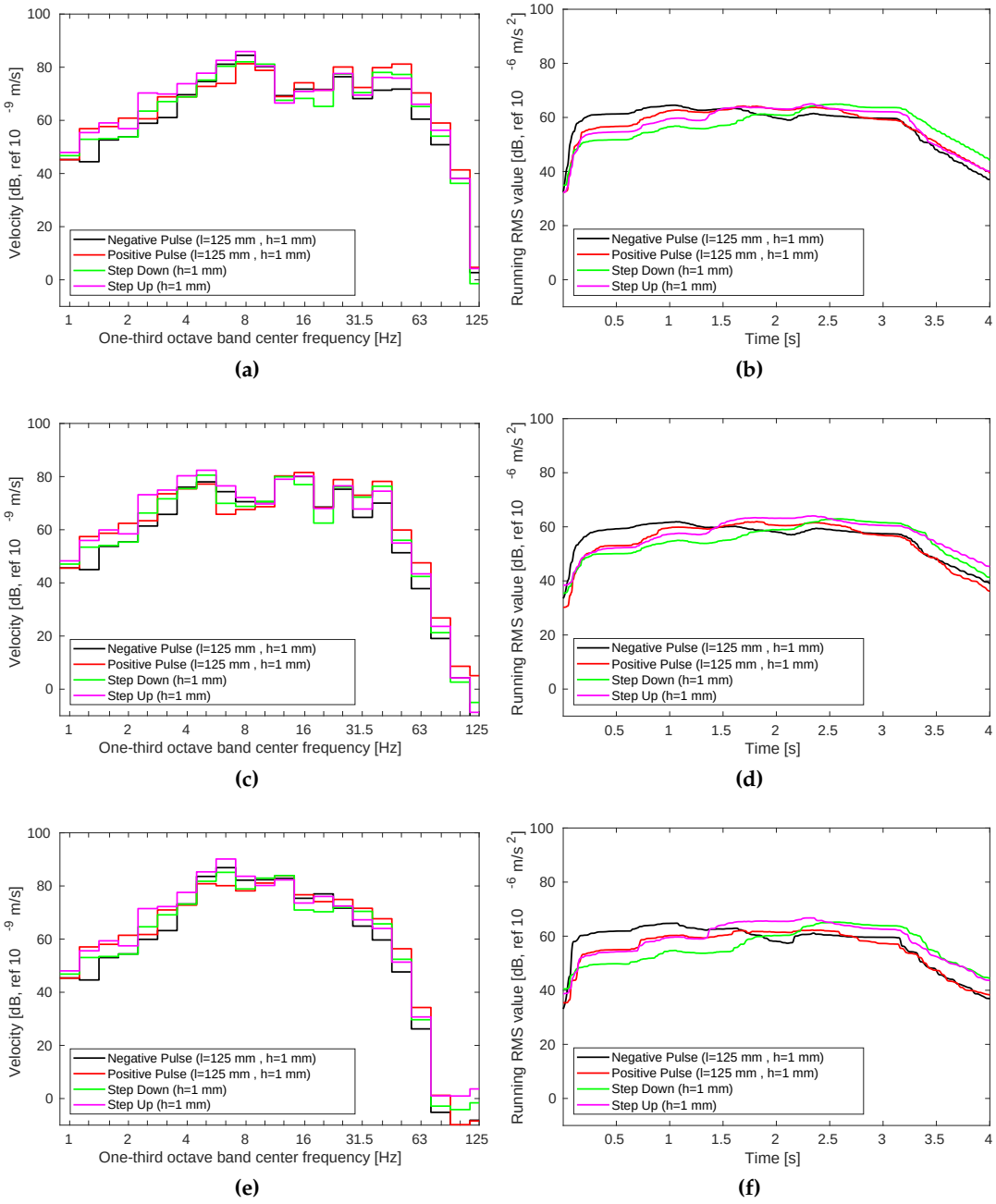

Figure C.22: (a,c,e) One-third octave band center frequency of the z vertical velocity and (b,d,f) running RMS value of the weighted acceleration at the top floor of the (a,b) four-storey, (c,d) six-storey and (e,f) twelve-storey buildings for several defect types due to a AM96 train passage at $v_0 = 120\,\mathrm{km/h}$.

Figure C.25 presents building vibrations induced by the AM96 train passage at speeds $v_0 = \{60,\ 90,\ 120,\ 150\}\,\mathrm{km/h}$. In the frequency domain response (Figure C.25. (a,c,e)),

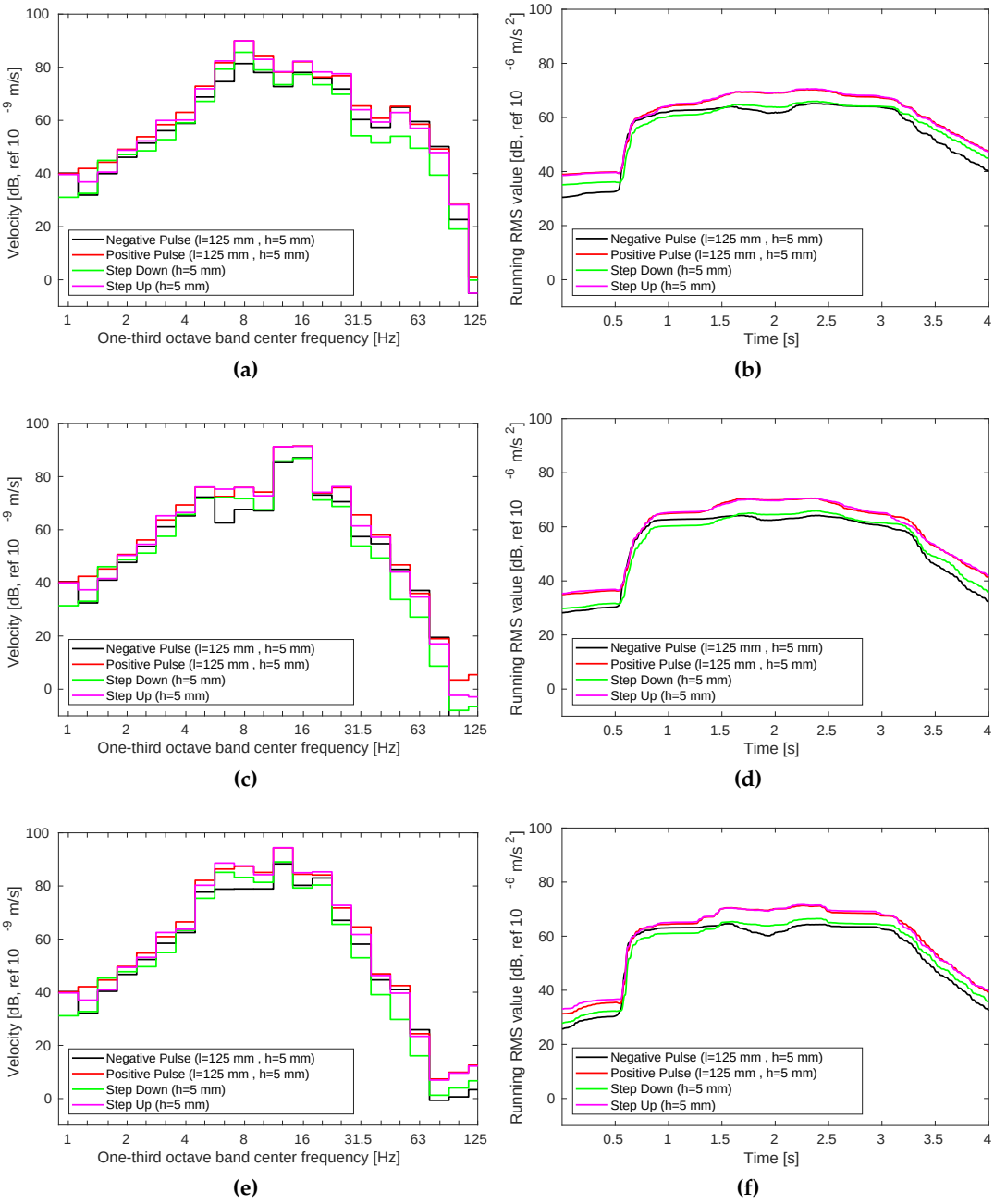

Figure C.23: (a,c,e) One-third octave band center frequency of the z vertical velocity and (b,d,f) running RMS value of the weighted acceleration at the top floor of the (a,b) four-storey, (c,d) six-storey and (e,f) twelve-storey buildings for several defect types due to a tram passage at $v_0 = 40\,\mathrm{km/h}$.

the effect of train speed is more clearly shown at low frequencies up to 10 Hz, where the building vibrations increase with the train speed. This trend is not found at mid and high

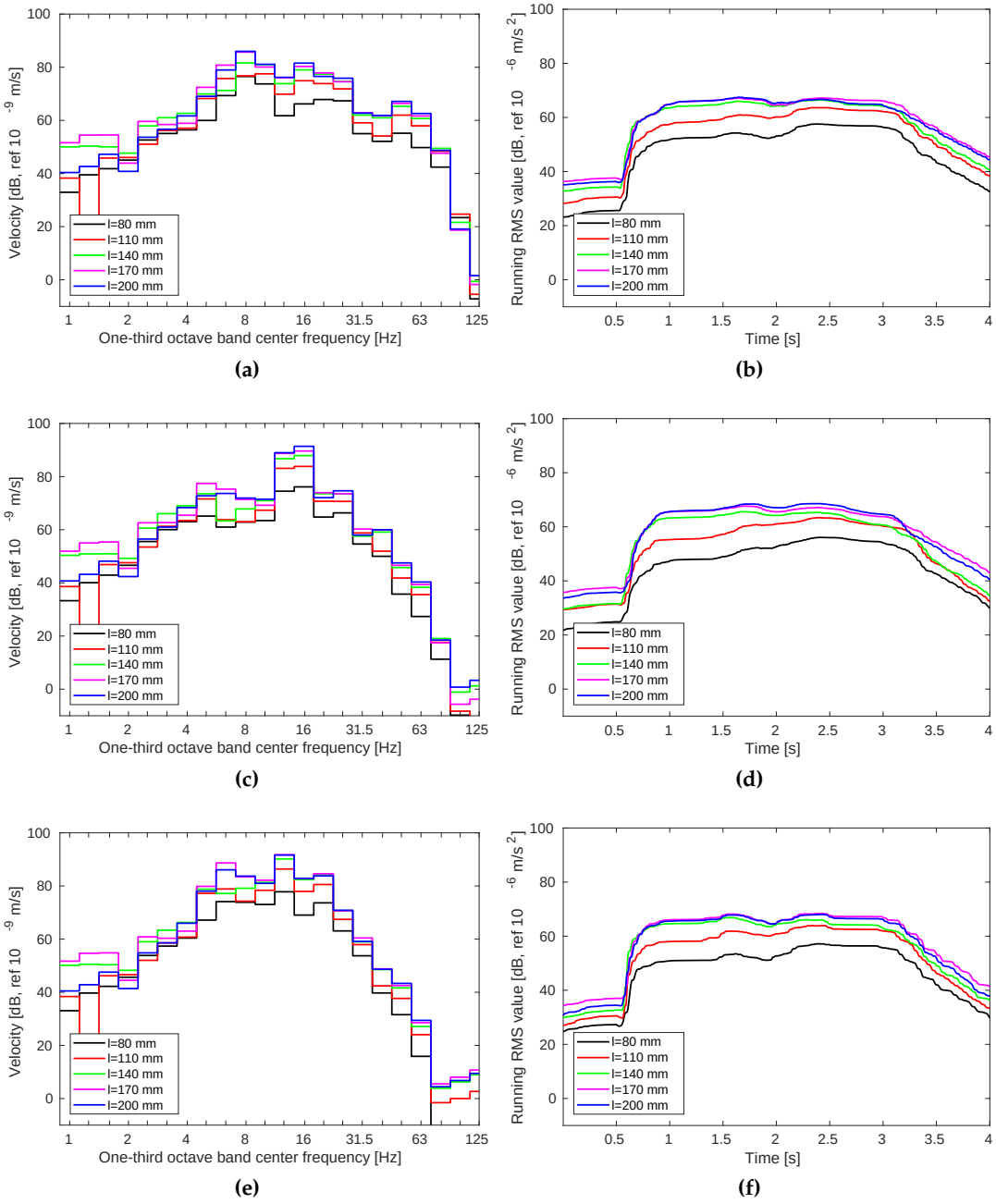

Figure C.24: (a,c,e) One-third octave band center frequency of the z vertical velocity and (b,d,f) running RMS value of the weighted acceleration at the top floor of the (a,b) four-storey, (c,d) six-storey and (e,f) twelve-storey buildings for several negative pulse defect sizes due to a tram passage at $v_0 = 40\,\mathrm{km/h}$.

frequencies. The running RMS value curves (Figure C.25. (b,d,f)) show again that the level of vibration increases with train speed.

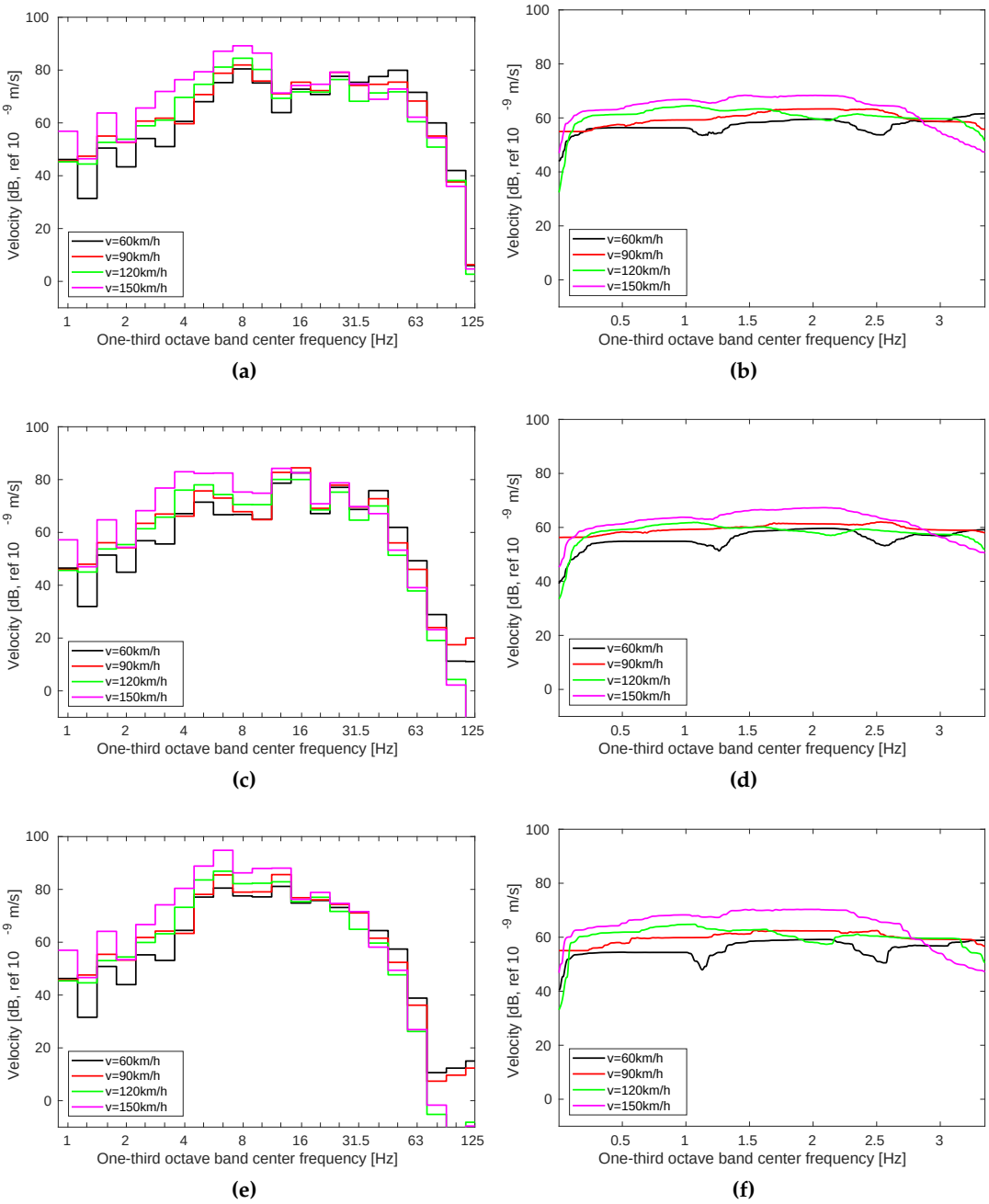

Figure C.25: (a,c,e) One-third octave band center frequency of the z vertical velocity and (b,d,f) running RMS value of the weighted acceleration at the top floor of the (a,b) four-storey, (c,d) six-storey and (e,f) twelve-storey buildings due to a AM96 train passage at several speeds and a negative pulse defect.

The previous correlation is not evident in the building response due to the classic tram analysis where the speed range is lower (20 versus 50 km/h) (Figure C.26). The response is

concentrated at frequencies (Figure C.26. (a,c,e)) that approximately match with the natural frequencies of the buildings (Figure C.6), but the level of vibration at these frequencies has a low correlation with train speed. Thus, the tram speed has a low influence on the running RMS values (Figure C.26. (b,d,f)).

C.5 CONCLUSIONS

Building vibration induced by railway traffic is a problem that requires study, during project planning/development phases. To do so, efficient methods are useful to assess building vibration quickly, considering multiple scenarios. In this work, a simplified method is presented to do this. It consists of a decoupled model, where the free-field vibration (source and propagation path) and the building vibration (receiver) are computed independently. This proposed paper is focused on the receiver sub-model. The soil-structure transfer function depending on the structural characteristics, and soil properties is obtained. This soil-structure transfer function is combined with the free-field response to obtain the building induced vibration in a computationally efficient manner. The proposed method is verified numerically by comparing results with a comprehensive model. The dynamic building response due to railway defects is studied. It is found that soil properties, defect type, defect size and train speed have a strong influence on building vibrations.

ACKNOWLEDGEMENTS

The authors would like to acknowledge the financial support provided by the Spanish Ministry of Economy and Competitiveness (Ministerio de Economía y Competitividad) through research project BIA2016-75042-C2-1-R, the Andalusian Scientific Computing Centre (CICA), the University of Leeds Cheney Award Scheme and the Leverhulme Trust (UK). They also acknowledge the support of Seville, Mons and Leeds Universities, who, without their support, this research would not have been possible.

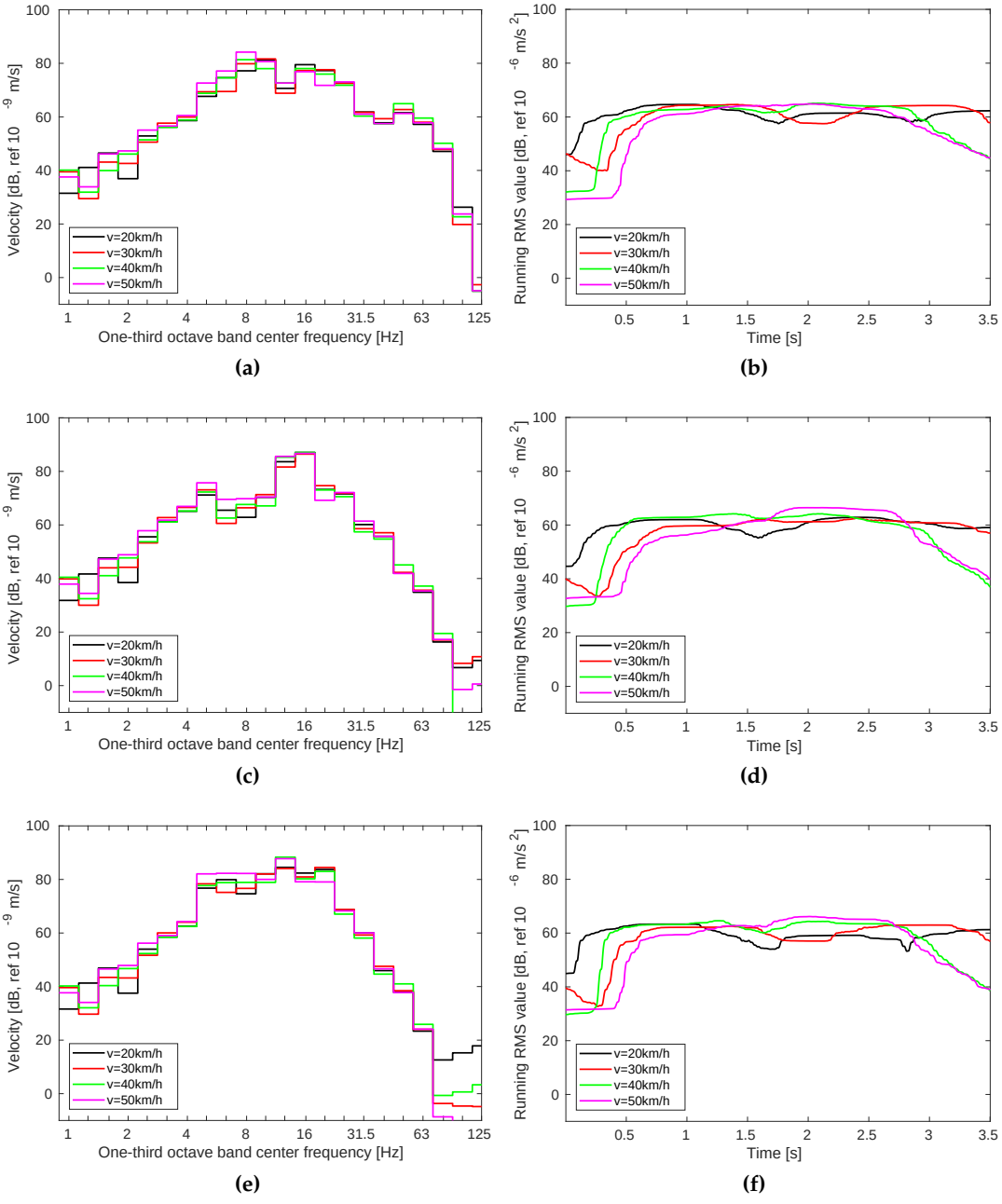

Figure C.26: (a,c,e) One-third octave band center frequency of the z vertical velocity and (b,d,f) running RMS value of the weighted acceleration at the top floor of the (a,b) four-storey, (c,d) six-storey and (e,f) twelve-storey buildings due to a tram passage at several speeds and a negative pulse defect.

REFERENCES

[1] L. Auersch. Dynamic stiffness of foundations on inhomogeneous soils for a realistic prediction of vertical building resonance. *Journal of Geotechnical and Geoenvironmental Engineering*, 134(3):328–340, 2008. doi: http://dx.doi.org/10.1061/(ASCE)1090-0241(2008)134:3(328).

[2] L. Auersch. Wave propagation in the elastic half-space due to an interior load and its application to ground vibration problems and buildings on pile foundations. *Soil Dynamics and Earthquake Engineering*, 30:925–936, 2010. doi: https://doi.org/10.1016/j.soildyn.2010.04.003.

[3] L. Auersch. Building Response due to Ground Vibration–Simple Prediction Model Based on Experience with Detailed Models and Measurements. *International Journal of Acoustics and Vibration*, 15(3):101–112, 2010. doi: http://dx.doi.org/10.20855/ijav.2010.15.3262.

[4] A. Bayraktar, A. Can Altunis, and M. Özcan. Safety assessment of structures for near-field blast-induced ground excitations using operational modal analysis. *Soil Dynamics and Earthquake Engineering*, 39:23 – 36, 2012. ISSN 0267-7261. doi: dx.doi.org/10.1016/j.soildyn.2012.02.005.

[5] D. Cantero, T. Arvidsson, E. OBrien, and R. Karoumi. Train–track–bridge modelling and review of parameters. *Structure and Infrastructure Engineering*, 12(9):1051 – 1064, 2016. doi: http://dx.doi.org/10.1080/15732479.2015.1076854.

[6] C.E. Hanson, D.A. Towers, and L.D. Meister. High-speed ground Transportation Noise and Vibration Impact Assessment, HMMH Report 293630-4. *U.S. Department of Transportation, Federal Railroad Administration, Office of Railroad Development*, 2005.

[7] C.E. Hanson, D.A. Towers, and L.D. Meister. Transit Noise and Vibration Impact Assessment, Report FTA-VA-90-1003-06. *U.S. Department of Transportation, Federal Transit Administration, Office of Planning and Environment*, 2006.

[8] R.W. Clough and J. Penzien. *Dynamic of Structures*. McGraw-Hill, New York, 1975.

[9] D.P. Connolly, G.P. Marecki, G. Kouroussis, I. Thalassinakis, and P.K. Woodward. The growth of railway ground vibration problems – A review. *Science of the Total Environment*, 568:1276–1282, 2015. doi: http://dx.doi.org/10.1016/j.scitotenv.2015.09.101.

[10] P. Coulier, G. Lombaert, and G. Degrande. The influence of source-receiver interaction on the numerical prediction of railway induced vibrations. *Journal of Sound and Vibration*, 333:2520–2538, 2014. doi: https://doi.org/10.1016/j.jsv.2014.01.017.

[11] *DIN 45672 Teil 2: Schwingungsmessungen in der Umgebung von Schienenverkehrswegen: Auswerteverfahren*. Deutsches Institut für Normung, 1995.

[12] O. Dogan, O. Anil, S.O. Akbas, E. Kantar, and R.T. Erdem. Evaluation of blast-induced ground vibration effects in a new residential zone. *Soil Dynamics and Earthquake Engineering*, 50:168 – 181, 2013. ISSN 0267-7261. doi: http://dx.doi.org/10.1016/j.soildyn.2013.03.005.

[13] A. Doménech, M.D. Martínez-Rodrigo, A. Romero, and P. Galvín. On the basic phenomenon of soil-structure interaction on the free vibration response of beams: Application to railway bridges. *Engineering Structures*, 125:254 – 265, 2016. ISSN 0141-0296. doi: http://dx.doi.org/10.1016/j.engstruct.2016.06.052.

[14] K. Dong, D. P. Connolly, O. Laghrouche, P.K. Woodward, and P. Alves Costa. The stiffening of soft soils on railway lines. *Transportation Geotechnics*, 17(A):178 – 191, 2018. ISSN 2214-3912. doi: https://doi.org/10.1016/j.trgeo.2018.09.004.

[15] D.P. Connolly, G. Kouroussis, A. Giannopoulos, O. Verlinden, P.K. Woodward, and M.C. Forde. Assesment of railway vibrations using an efficient scoping model. *Soil Dynamics and Earthquake Engineering*, 58:37–47, 2014. doi: https://doi.org/10.1016/j.soildyn.2013.12.003.

[16] D.P. Connolly, G. Kouroussis, P.K. Woodward, A. Giannopoulos, O. Verlinden, and M.C. Forde. Scoping prediction of re-radiated ground-borne noise and vibration near high speed rails lines with variable soils. *Soil Dynamics and Earthquake Engineering*, 66:78–88, 2014. doi: https://doi.org/10.1016/j.soildyn.2014.06.021.

[17] D.P. Connolly, P. Alves Costa, G. Kouroussis, P. Galvín, P.K. Woodward, and O. Laghrouche. Large scale international testing of railway ground vibrations across Europe. *Soil Dynamics and Earthquake Engineering*, 71:1–12, 2015. doi: https://doi.org/10.1016/j.soildyn.2015.01.001.

[18] D.P. Connolly, P. Galvín, B. Olivier, A. Romero, and G. Kouroussis. A 2.5D time-frequency domain model for railway induced soil-building vibration due to railway defects. *Soil Dynamics and Earthquake Engineering*, 120:332 – 344, 2019. ISSN 0267-7261. doi: https://doi.org/10.1016/j.soildyn.2019.01.030.

[19] *Eurocode 8: Design of structures for earthquake resistance–Part 1 : General rules, seismic actions and rules for buildings*. European Committee for Standardization, 1998.

[20] Federal Railroad Administration. *High-Speed Ground Transportation Noise and Vibration Impact Assessment*. U.S. Department of Transportation, 2012.

[21] P. Fiala, G. Degrande, and F. Augusztinovicz. Numerical modelling of ground-borne noise and vibration in buildings due to surface rail traffic. *Journal of Sound and Vibration*, 301:718–738, 2007. doi: https://doi.org/10.1016/j.jsv.2006.10.019.

[22] S. François, L. Pyl, H.R. Masoumi, and G. Degrande. The influence of dynamic soil-structure interaction on traffic induced vibrations in buildings. *Soil Dynamics and Earthquake Engineering*, 27:655–674, 2007. doi: https://doi.org/10.1016/j.soildyn.2006.11.008.

[23] P. Galvín and A. Romero. A MATLAB toolbox for soil-structure interaction analysis with finite and boundary elements. *Soil Dynamics and Earthquake Engineering*, 57:10–14, 2014. doi: https://doi.org/10.1016/j.soildyn.2013.10.009.

[24] P. Galvín, A. Romero, and J. Domínguez. Fully three-dimensional analysis of high-speed train–track–soil–structure dynamic interaction. *Journal of Sound and Vibration*, 329:5147–5163, 2010. doi: https://doi.org/10.1016/j.jsv.2010.06.016.

[25] F. Gatti, S. Touhami, F. Lopez-Caballero, R. Paolucci, D. Clouteau, V. Alves Fernandes, M. Kham, and F. Voldoire. Broad-band 3-D earthquake simulation at nuclear site by an all-embracing source-to-structure approach. *Soil Dynamics and Earthquake Engineering*, 115:263 – 280, 2018. ISSN 0267-7261. doi: https://doi.org/10.1016/j.soildyn.2018.08.028.

[26] H. Hao and C. Wu. Numerical study of characteristics of underground blast induced surface ground motion and their effect on above-ground structures. part ii. effects on structural responses. *Soil Dynamics and Earthquake Engineering*, 25:39 – 53, 2005. ISSN 0267-7261. doi: doi:10.1016/j.soildyn.2004.08.002.

[27] M. Hussein, H. Hunt, K. Kuo, P. Alves Costa, and J. Barbosa. The use of sub-modelling technique to calculate vibration in buildings from underground railways. *Proceedings of the Institution of Mechanical Engineers, Part F: Journal of Rail and Rapid Transit*, 229(3): 303 – 314, 2013. doi: https://doi.org/10.1177/0954409713511449.

[28] M. Hussein, H. Hunt, K. Kuo, P. Alves Costa, and J. Barbosa. The dynamic effect of piled-foundation building on an incicident vibration field from an underground railway tunnel. *20th International Congress on Sound & Vibration. ICSV 20*, 2013.

[29] *ISO 2631-1:2003: Mechanical vibration and shock–Evaluation of human exposure to whole-body vibration–Part 1: General requirements*. International Organization for Standardization, 2003.

[30] *ISO 2631-2:2003: Mechanical vibration and shock–Evaluation of human exposure to whole-body vibration–Part 2: Vibration in buildings (1–80 Hz)*. International Organization for Standardization, 2003.

[31] *ISO 14837-1:2005 Mechanical vibration–Ground-borne noise and vibration arising from rail systems–Part 1: General guidance*. International Organization for Standardization, 2005.

[32] S. Jones, K. Kuo, M.F.M. Hussein, and H.E.M Hunt. Prediction uncertainties and inaccuracies resulting from common assumptions in modelling vibration from underground railways. *Proceedings of the Institution of Mechanical Engineers, Part F: Journal of Rail and Rapid Transit*, 226:501–512, 2012. doi: https://doi.org/10.1177/0954409712441744.

[33] E. Kausel. Early history of soil-structute interaction. *Soil Dynamics and Earthquake Engineering*, 30:822–8328, 2010. doi: https://doi.org/10.1016/j.soildyn.2009.11.001.

[34] G. Kouroussis, L. Van Parys, C. Conti, and O. Verlinden. Prediction of ground vibrations induced by urban railway traffic: An analysis of the coupling assumptions between vehicle, track, soil, and buildings. *The International Journal of Acoustics and Vibration*, 18(4):163 – 172, 2013. ISSN 1027-5851. doi: https://doi.org/10.20855/ijav.2013.18.4330.

[35] G. Kouroussis, D.P. Connolly, K.E. Vogiatzis, and O. Verlinden. Modelling the environmental effects of railway vibrations from different types of rolling stock: a numerical study. *Shock and Vibration*, 6, 2015. doi: http://dx.doi.org/10.1155/2015/142807.

[36] G. Kouroussis, J. Florentin, and O. Verlinden. Ground vibrations induced by intercity/interregion trains: a numerical prediction based on the multibody/finite element modeling approach. *Journal of Vibration and Control*, 22:4192 – 4210, 2016. doi: https://doi.org/10.1177/1077546315573914.

[37] G. Kouroussis, K.E. Vogiatzis, and D.P. Connolly. A combined numerical/experimental prediction method for urban railway vibration. *Soil Dynamics and Earthquake Engineering*, 97:377 – 386, 2017. ISSN 0267-7261. doi: http://dx.doi.org/10.1016/j.soildyn.2017.03.030.

[38] G. Kouroussis, K.E. Vogiatzis, and D.P. Connolly. Assessment of railway ground vibration in urban area using in-situ transfer mobilities and simulated vehicle-track interaction. *International Journal of Rail Transportation*, 6:113 – 130, 2018. ISSN 2324-8378. doi: https://doi.org/10.1080/23248378.2017.1399093.

[39] G. Kouroussis, S. Zhu, B. Olivier, and D. Ainalis W. Zhai. Urban railway ground vibrations induced by localized defects: using dynamic vibration absorbers as a mitigation solution. *Journal of Zhejiang University-SCIENCE A*, 20(2):83 – 97, 2019. doi: https://doi.org/10.1631/jzus.A1800651.

[40] K.A. Kuo, M. Papadopoulos, G. Lombaert, and G. Degrande. The coupling loss of a building subject to railway induced vibrations: Numerical modelling and experimental measurements. *Journal of Sound and Vibration*, 442:459–481, 2019. ISSN 0022-460X. doi: https://doi.org/10.1016/j.jsv.2018.10.048.

[41] G. Lombaert, P. Galvín, S. François, and G. Degrande. Quantification of uncertainty in the prediction of railway induced ground vibration due to the use of statistical track unevenness data. *Journal of Sound and Vibration*, 333(18):4232 – 4253, 2014. ISSN 0022-460X. doi: https://doi.org/10.1016/j.jsv.2014.04.052.

[42] P. Lopes, P. Alves Costa, M. Ferraz, R. Calçada, and A. Silva Cardoso. Numerical modeling of vibrations induced by railway traffic in tunnels: From the source to the nearby buildings. *Soil Dynamics and Earthquake Engineering*, 61–62:269–285, 2014. doi: https://doi.org/10.1016/j.soildyn.2014.02.013.

[43] P. Lopes, J. Fernández Ruiz, P. Alves Costa, L. Medina Rodríguez, and A. Silva Cardoso. Vibrations inside buildings due to subway railway traffic. experimental validation of a comprehensive prediction model. *Science of the Total Environment*, 568: 1333–1343, 2016. doi: http://dx.doi.org/10.1016/j.scitotenv.2015.11.016.

[44] D. López-Mendoza, A. Romero, D.P. Connolly, and P. Galvín. Scoping assessment of building vibration induced by railway traffic. *Soil Dynamics and Earthquake Engineering*, 93:147–161, 2017. ISSN 0267-7261. doi: http://dx.doi.org/10.1016/j.soildyn.2016.12.008.

[45] *NIST GCR 12-917-21 Soil-Structure Interaction for Building Structures*. National Institute of Standards and Technology U.S. Department of Commerce, 2012.

[46] N.M. Newmark. A method of computation for structural dynamics. *ASCE Journal of the Engineering Mechanics Division*, 85:67–94, 1959.

[47] P. Alves Costa, A. Colaço, R. Calçada, and A. Silva Cardoso. Critical speed of railway tracks. Detailed and simplified approaches. *Transportation Geotechnics*, 2:30–46, 2015. doi: https://doi.org/10.1016/j.trgeo.2014.09.003.

[48] A. Pais and E. Kausel. Approximate formulas for dynamic stiffness of rigid foundations. *Soil Dynamics and Earthquake Engineering*, 7(4):213–227, 1988. doi: http://dx.doi.org/10.1016/S0267-7261(88)80005-8.

[49] D. Pitilakis and D. Clouteau. Equivalent linear substructure approximation of soil–foundation–structure interaction: model presentation and validation. *Bulletin of Earthquake Engineering*, 8(2):257 – 282, 2010. ISSN 1570-761X. doi: https://doi.org/10.1007/s10518-009-9128-3.

[50] L. Pyl, G. Degrande, and D. Clouteau. Validation of a source–receiver model for road traffic- induced vibrations in buildings. ii: Receiver model. *Journal of Engineering Mechanics*, 130:1394 – 1406, 2004. doi: https://doi.org/10.1061/(ASCE)0733-9399(2004)130:12(1394).

[51] L. Pyl, G. Degrande, G. Lombaert, and W. Haegeman. Validation of a source–receiver model for road traffic- induced vibrations in buildings. i: Source model. *Journal of Engineering Mechanics*, 130:1377 – 1393, 2004. doi: https://doi.org/10.1061/(ASCE)0733-9399(2004)130:12(1377).

[52] W. Rücker and L. Auersch. A user-friendly prediction tool for railway induced ground vibrations: Emission - transmission - immission. *Notes on Numerical Fluid Mechanics and Multidisciplinary Design*, 99:129–135, 2008. doi: https://dx.doi.org/10.1007/978-3-540-74893-9_18.

[53] E. Savin and D. Clouteau. Elastic wave propagation in a 3-D unbounded random heterogeneous medium coupled with a bounded medium. application to seismic soil–structure interaction (sssi). *International Journal for Numerical Methods in Engineering*, 54:607 – 630, 2002. doi: https://doi.org/10.1002/nme.442.

[54] S.B. Mezher, D.P. Connolly, P.K. Woodward, O. Laghrouche, J. Pombo, and P. Alves Costa. Railway critical velocity – analytical prediction and analysis. *Transportation Geotechnics*, 6:84 – 96, 2016. doi: https://doi.org/10.1016/j.trgeo.2015.09.002.

[55] R. Taherzadeh, D. Clouteau, and R. Cottereau. Simple formulas for the dynamic stiffness of pile groups. *Earthquake Engineering and Structural Dynamics*, 38:1665 – 1685, 2009. doi: https://doi.org/10.1002/eqe.918.

[56] H. Torabi and M.T. Rayhani. Three dimensional finite element modeling of seismic soil–structure interaction in soft soil. *Computers and Geotechnics*, 60:9 – 19, 2014. ISSN 0266-352X. doi: http://dx.doi.org/10.1016/j.compgeo.2014.03.014.

[57] K. Vogiatzis and H. Mouzakis. Ground-borne noise and vibration transmitted from subway networks to multi-storey reinforced concrete buildings. *Transport*, 33(2):446 – 453, 2018. doi: https://doi:10.3846/16484142.2017.1347895.

[58] K. Vogiatzis, H. Mouzakis, and V. Zafiropoulou. Assessing subway network ground borne noise and vibration using transfer function from tunnel wall to soil surface measured by muck train operation. *Science of the Total Environment*, 650:2888 – 2896, 2019. doi: https://doi:10.3846/16484142.2017.1347895.

[59] J.P. Wolf. *Dynamic soil-structure interaction*. Prentice-Hall, Englewood Cliffs, New Jersey, 1985.

[60] C. Wu and H. Hao. Numerical study of characteristics of underground blast induced surface ground motion and their effect on above-ground structures. part i. ground motion characteristics. *Soil Dynamics and Earthquake Engineering*, 25:27 – 38, 2005. ISSN 0267-7261. doi: doi:10.1016/j.soildyn.2004.08.001.

[61] S. Zhu, J. Wang, C. Cai, K. Wang, W. Zhai, J. Yang, and H. Yan. Development of a vibration attenuation track at low frequencies for urban rail transit. *Computer-Aided Civil and Infrastructure Engineering*, 32:713 – 726, 2017. doi: https://doi.org/10.1111/mice.12285.

[62] O.C. Zienkiewicz. *The finite element method*. McGraw-Hill, third edition, 1986.

D

BOOK CHAPTER: SCOPING ASSESSMENT OF GROUND AND BUILDING VIBRATIONS DUE TO RAILWAY TRAFFIC

The original version of this book chapterr can be found in **https://www.icevirtuallibrary.com/**

- ISBN: 9780727763792
- Book: Book on ground vibrations from high-speed railways
- Publisher: Institution of Civil Engineers
- General quality indicators: ie-CSIC (Índice de Editoriales y Editores CSIC). Valor: bajo.

Scoping assessment of building vibrations due to railway traffic

Authors: Pedro Galvín Barrera[1], Daniel López-Mendoza[1], David P. Connolly[2], and Antonio Romero Ordóñez[1]

[1] Escuela Técnica Superior de Ingeniería, Universidad de Sevilla, Camino de los Descubrimientos, 41092 Sevilla, Spain
[2] Institute for High Speed Rail, Leeds University, LS2 9JT Leeds, UK

D.1 INTRODUCTION

Globally, the number of high speed railway (HSR) lines both operational and under construction is growing rapidly (e.g. HS2, UK). This has led to an increase in real estate located close to lines, and thus the number of properties effected by ground-borne vibrations [9]. Ground-borne vibrations are vibrational waves generated within the track structure that propagate to nearby structures, causing shaking and in-door noise. These effects are undesirable and post-construction mitigation measures are expensive. Therefore vibration levels require prediction during early stages of planning/development, typically in the form of a desktop study.

International standard ISO 2631 [24, 25] addresses these negative effects and evaluates the whole-body human exposure to vibration. In addition, ISO 14837 [26] is railway focused and describes the emission-propagation-immission mechanisms of waves from the train-track system (source) to the building (receiver). It provides a guide on the measurement of experimental data, vibration evaluation and mitigation. ISO 14837 [26] also outlines suggested numerical modelling approaches.

At locations of sensitive receptors (e.g. theatres) or where vibration has identified to likely to be a problem, comprehensive and detailed design models are often used. These are typically computationally expensive, and include three-dimensional (3D) models with full coupling between the train-track-soil-structure system [3, 18, 20, 37, 54]. One alternative to 3D modelling is to use a two-and-a-half-dimensional (2.5D) approach [1, 17, 21, 27, 34, 35, 43, 45, 46, 49]. These models assume the problem is continuous in the track direction and as such not well suited to modelling transition zones, etc.

At the earlier stage, when attempting to identify line sections where vibration is likely to cause problems in nearby buildings, simplified scoping models are often used. This is because they are faster running and allow engineers to assess long lengths of track quickly, in absence of detailed design information.

Empirical approaches to estimate soil and building vibrations due to a train passage have been proposed by the Federal Railroad Administration (FRA) and Federal Transit Adminis-

tration (FTA) of the U.S. Department of Transportation [6, 7]. The simplifications considered in these procedures have been verified by the numerical model presented by Verbraken et al. [51]. Alternatively, some scoping models have been recently proposed. Connolly et al. [12, 13] presented a scoping tool, called Scoperail, to instantly compute vibrations due to train passages. A machine learning approach to obtain free-field vibrations was developed using numerically records for a wide range of train speeds and soil types. These soil vibrations were coupled with empirical factors in order to predict in-door noise and structural vibrations due to high speed trains. A hybrid model has been proposed by Triepaischajonsak and Thompson [50], that combined a detailed vehicle-track model formulated in the time domain with a layered ground model operating in the frequency domain, based on the formulation outlined by Kausel and Roësset [30]. Then, forces acting on the ground were obtained from the train-track model and later used to calculate ground free-field vibrations. Kuo et al. [32] developed a hybrid model where the source and propagation mechanisms were decoupled. The model combined experimental tests and numerical predictions considering the definitions proposed in [6, 7]. Kouroussis et al. [31] developed a hybrid experimental-numerical model to predict vibrations from urban railway traffic. The level of vibration was calculated by combining the force density obtained from a numerical train-track model with the mobility function measured through an experimental approach.

Research has also been performed to investigate the propagation of free-field vibration into buildings. Auersch [2] studied building responses using a simple soil-wall-floor model based on an empirical transfer fuction obtained from the characteristics of the structure. The soil was modelled using a spring and a viscous damper to evaluate the effects of soil-structure interaction. François et al. [16] analysed building induced vibrations by employing simplified methods that ignore Soil-Structure Interaction (SSI), but take into account the relative stiffness between the building and the soil. Later, Hussein et al. [23] proposed a sub-modelling method to couple a 3D train-track-soil model with a 2D frame building. López- Mendoza et al. [38] presented a scoping model, considering SSI, to predict vibrations in buildings induced by railway traffic from the ground-borne response spectra computed from either numerical or experimentally free field vibrations.

One challenge with the majority of vibration models, whether being used to predict free-field or structural vibration, is the unknown level of uncertainty in absolute levels. Therefore, in practise, it is common for vibration consultants to add a significant safety factor to predicted values. This is commonly of the order of 10 dB, and means some areas where vibration will not be a problem, are then considered problematic. This can result in elevated project costs (e.g. unwarrented abatement measures).

Therefore this chapter presents a methodology to construct a conservative vibration scoping model, that does not require a safety factor to be applied to predicted values. The train-track-soil-building methodology considers soil stiffness, the combination of both the dynamic and static forces generated due to high speed train passage and SSI. It can be used to predict the vibration levels in the free-field and nearby buildings, using metrics compatible with international standards. These predictions need a fraction of the time

typically required to analyse a complex SSI problem, and thus provides a practical tool to rapidly analyse the vibration response of several structures near railway lines.

The model uses the direct stiffness method to compute the soil's Green function [29, 30, 48], and a novel 2.5D finite element strategy for train-track interaction. The soil Green's function is modulated using a Neural Network (NN) to reduce the computation effort of track-soil interaction. This modulation factor combined with the new train-track approach results in a large reduction in computational time. The excitation of the building foundation corresponds with the soil response due to railway traffic. Structural vibration levels are computed using modal superposition, thus avoiding intensive computations.

In this chapter, the proposed scoping model is used to predict track receptance, free-field mobility, soil vibration and building response depending on track type, soil stiffness, building height and train speed. Also, the possibility of using the average shear wave velocity of a layered soil as defined in Eurocode 8 [15] and denoted as V_{s30}, to predict vibration levels, is investigated.

D.2 NUMERICAL MODELLING

A wide variety of modelling approaches can be used to predict ground and building vibrations due to railway traffic. Typically, due to the large size of the modelling domain, the train-track-soil-building problem is divided into sub-models (Figure D.1). These sub-models typically use simplified strategies, that can achieve similar accuracy, but in much reduced time.

The proposed model (available as a `MATLAB` toolbox on the website `http://personal.us.es/pedrogalvin/scoping.en.html`) assumes the train-track-soil interaction (source - propagation problem, Figure D.1, step 2.3) can be decoupled from soil-structure interaction (immission problem, Figure D.1, step 2.4). The simplified methodology presented by Galvín et al. [22] is followed to calculate the free-field response (Figure D.1, step 2.3). The train-track-soil system is divided into two primary sub-models: a train-track sub-model (Figure D.1, step 2.1) and a track-soil sub-model (Figure D.1, step 2.2). These sub-models are described below.

After obtaining the free-field response, it is used to compute the vibration within buildings located close to the line (Figure D.1, step 2.4). To do so, the free-field response is the input for the soil-structure interaction model described in [38].

To minimise the computational demand required, the following strategies are used:

- The train-track forces $\mathbf{g}$ are calculated using a simplified Finite Element Method (FEM) track model where the underlying soil is modelled using a spring-damper element that approximates the underlying soil response (step 2.1).
- The track-soil transfer function $\tilde{\mathbf{u}}_{\mathrm{ff}}$ (step 2.2) is approximated from the soil Green's function $\tilde{\mathbf{u}}_{\mathrm{g}}$ using a correction factor estimated using a neural network procedure.

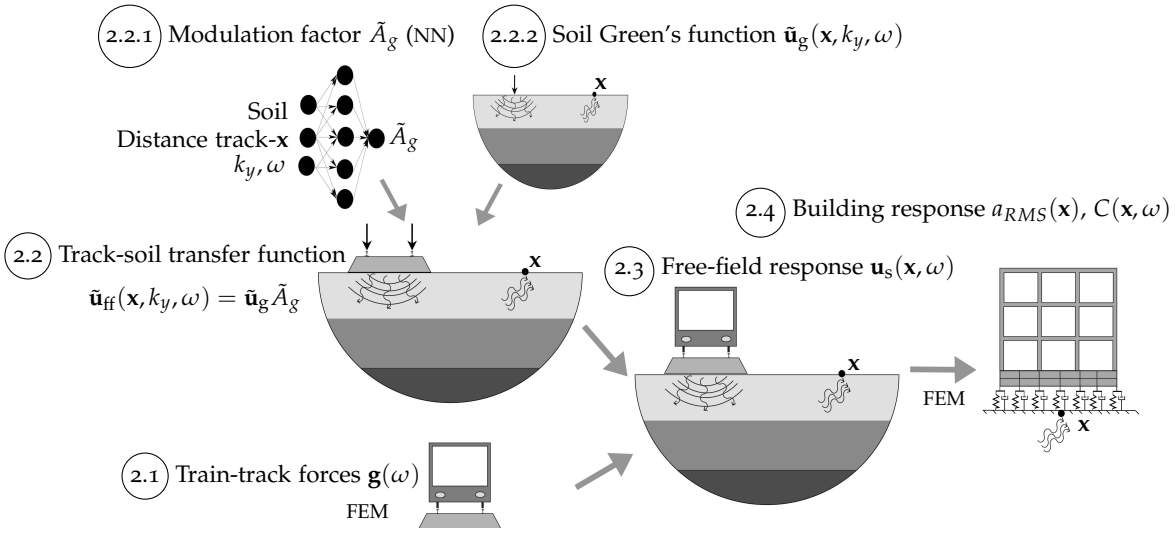

Figure D.1: Scheme of the scoping model.

- For the building response, the scoping model used a FEM approach based on a modal superposition analysis considering the SSI through a set of spring and damper elements at the foundation (step 2.4).

D.2.1 *Track-soil forces*

D.2.1.1 *Track model*

The track-soil forces (Figure D.1, step 2.1) are calculated using a simplified 2.5D FEM model (Figure D.2). The model allows both linear hysteretic or viscous damping models for the constituents in the ballasted and slab track structure.

For the ballasted track model, the rails are represented using Euler-Bernoulli beams with a bending stiffness $E_r I_r$ and a mass $\rho_r A_r$ per unit length. The rail displacements are denoted as $u_{r1}(x_1, t)$ and $u_{r2}(x_2, t)$. The position of the rails is determined by the track gauge w_r. The internal energy dissipation in the rail is modelled using a loss factor η_r.

The rail pads are modelled as continuous spring-damper connections. The rail pad stiffness k_{rp} and damping coefficient c_{rp} are used to calculate the equivalent stiffness $\overline{k}_{rp} = k_{rp}/d_{sl}$ and damping $\overline{c}_{rp} = c_{rp}/d_{sl}$, where d_{sl} is the sleeper spacing. Alternatively, a loss factor η_{rp} can be used to describe rail pad behaviour as, $\overline{k}_{rp} = \overline{k}_{rp}(1 + i\eta_{rp})$.

The concrete sleepers are assumed to be rigid, so that the vertical sleeper displacements along the track are determined by the vertical displacement $u_{sl}(x, t)$ and rotation $\theta_{sl}(x, t)$ at the centre of gravity of the sleeper. The sleepers are modelled as a uniformly distributed mass $\overline{m}_{sl} = m_{sl}/d_{sl}$, where m_{sl} is the mass of the sleeper. The rotational inertia of the sleeper is estimated as $\rho_{sl}\overline{I}_{sl} = \rho_{sl} I_{sl}/d_{sl}$, where the inertia I_{sl} is calculated as $I_{sl} = 1/6 l_{sl} h_{sl} b_{sl}(h_{sl}^2 + l_{sl}^2)$, where l_{sl}, h_{sl} and b_{sl} the sleeper length, height and width, respectively.

The ballast bed is represented by a set of distributed linear springs and dampers. The smeared ballast stiffness is computed from the vertical spring stiffness k_b per sleeper, as $\overline{k}_\mathrm{b} = k_\mathrm{b}/d_\mathrm{sl}$. The viscous damping in the ballast bed is accounted for using a complex impedance $\overline{k}_\mathrm{b} + i\omega\overline{c}_\mathrm{b}$. Alternatively, a loss factor η_b can be used to describe ballast behaviour as $\overline{k}_\mathrm{b} = \overline{k}_\mathrm{b}(1 + i\eta_\mathrm{b})$. The equivalent ballast mass $\overline{m}_\mathrm{b}$ is computed using the ballast mass m_b under each sleeper as $m_\mathrm{b}/d_\mathrm{sl}$. The ballast mass m_b is estimated from the height h_b of the ballast layer and lengths $l_\mathrm{b1} = l_\mathrm{sl}$ and l_b2 at the top and the bottom of the ballast layer, respectively, as $m_\mathrm{b} = 0.5\rho_\mathrm{b}h_\mathrm{b}(l_\mathrm{b1} + l_\mathrm{b2})b_\mathrm{sl}$.

The embankment is represented using a Euler-Bernoulli beam with a bending stiffness $E_\mathrm{e}I_\mathrm{e}$, a torsional rigidity $G_\mathrm{e}J_\mathrm{e}$, a loss factor η_e, a rotational inertia $\rho_\mathrm{e}I_{pe}$, and a mass $\rho_\mathrm{e}A_\mathrm{e}$ per unit length, where E_e, I_e, G_e, J_e, I_{pe}, ρ_e and A_e are the Young's modulus, the bending moment of inertia, the shear modulus, the torsion constant, the polar moment of inertia, the density and the area, respectively. The embankment properties are approximated to be equal to the uppermost soil layer.

A ballast mat can be simulated using spring-damper elements between the embankment and the ballast with equivalent stiffness and damping (or loss factor) $\overline{k}_\mathrm{m}$ and $\overline{c}_\mathrm{m}$ (or η_m), respectively.

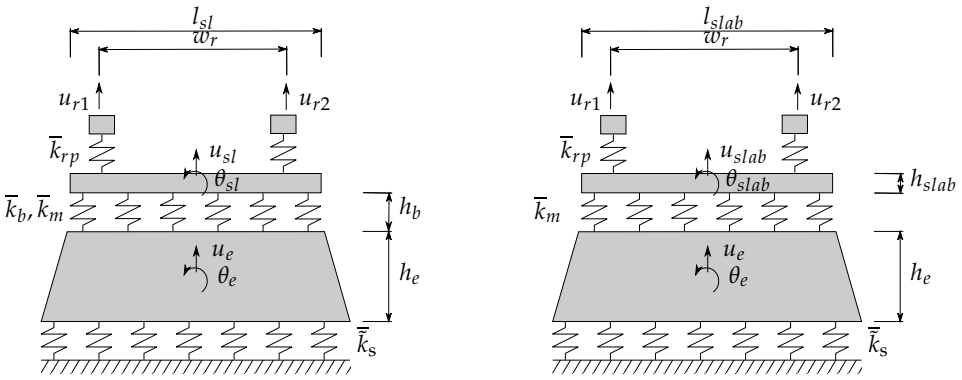

Figure D.2: Cross section of (left) ballasted and (right) slab track models.

For the slab track model, the rails, rail pads and embankment are modelled in the same manner as the ballasted track model. The slab is a Euler-Bernoulli beam with a bending stiffness $E_\mathrm{slab}I_\mathrm{slab}$, a torsional rigidity $G_\mathrm{slab}J_\mathrm{slab}$, a rotational inertia $\rho_\mathrm{slab}I_{p\mathrm{slab}}$, a loss factor η_slab and a mass per unit length $\rho_\mathrm{slab}A_\mathrm{slab}$, where E_slab, I_slab, G_slab, J_slab, $I_{p\mathrm{slab}}$, ρ_slab and A_slab are the Young's modulus, the bending moment of inertia, the shear modulus, the torsion constant, the polar moment of inertia, the density and and the area, respectively.

The underlying soil is represented using a spring-damper element with stiffness $\overline{\tilde{k}}_\mathrm{s}(k_y, \omega)$. A tilde above a variable denotes its representation in the frequency-wavenumber domain. The equivalent stiffness and damping of the soil are estimated by the vertical soil response computed from the Green's function for a homogeneous or layered half-space due to a unit vertical load applied at a distance $w_\mathrm{r}/2$ from the track axis. Note that because the

spring-damper element does not consider the effect of a moving load, the model ignores the dynamic effects that may be induced when approaching critical velocity (e.g. [47]). The continuity of displacement is fulfilled between the soil and the track.

The 2.5D FEM formulation follows that outlined by Galvín et al. [21]:

$$\left[-\omega^2\mathbf{M}_{\mathrm{bb}} + \mathbf{K}^0_{\mathrm{bb}} - ik_y\mathbf{K}^1_{\mathrm{bb}} - k_y^2\mathbf{K}^2_{\mathrm{bb}} + ik_y^3\mathbf{K}^3_{\mathrm{bb}} + k_y^4\mathbf{K}^4_{\mathrm{bb}} + \tilde{\mathbf{K}}^{\mathrm{s}}_{\mathrm{bb}}(k_y,\omega)\right]\tilde{\mathbf{u}}_{\mathrm{b}}(k_y,\omega) = \tilde{\mathbf{f}}_{\mathrm{b}}(k_y,\omega) \tag{1}$$

where $\mathbf{K}^0_{\mathrm{bb}}$, $\mathbf{K}^1_{\mathrm{bb}}$, $\mathbf{K}^2_{\mathrm{bb}}$, $\mathbf{K}^3_{\mathrm{bb}}$ and $\mathbf{K}^4_{\mathrm{bb}}$ are the stiffness matrices, $\mathbf{M}_{\mathrm{bb}}$ is the mass matrix, $\tilde{\mathbf{f}}_{\mathrm{b}}(k_y,\omega)$ is the external load vector, and $\mathbf{K}^{\mathrm{s}}_{\mathrm{bb}}(k_y,\omega)$ represents the dynamic soil stiffness matrix. For simplicity, matrices $\mathbf{K}^1_{\mathrm{bb}}$, $\mathbf{K}^2_{\mathrm{bb}}$ and $\mathbf{K}^3_{\mathrm{bb}}$ are discarded so that the proposed model does not contain any volume or shell elements. The finite element matrices $\mathbf{M}_{\mathrm{bb}}$, $\mathbf{K}^0_{\mathrm{bb}}$ and $\mathbf{K}^4_{\mathrm{bb}}$ in Equation (1) are independent of wavenumber k_y and frequency ω, and are only assembled once. Equation (1) is now further elaborated by dividing the finite element degrees of freedom $\tilde{\mathbf{u}}_{\mathrm{b}}(k_y,\omega)$ into internal degrees of freedom $\tilde{\mathbf{u}}_{\mathrm{b}_1}(k_y,\omega)$ and degrees of freedom $\tilde{\mathbf{u}}_{\mathrm{b}_2}(k_y,\omega)$ for the soil-structure interface:

$$\left(-\omega^2\begin{bmatrix}\mathbf{M}_{\mathrm{b}_1\mathrm{b}_1} & \mathbf{M}_{\mathrm{b}_1\mathrm{b}_2}\\ \mathbf{M}_{\mathrm{b}_2\mathrm{b}_1} & \mathbf{M}_{\mathrm{b}_2\mathrm{b}_2}\end{bmatrix} + \begin{bmatrix}\mathbf{K}^0_{\mathrm{b}_1\mathrm{b}_1} & \mathbf{K}^0_{\mathrm{b}_1\mathrm{b}_2}\\ \mathbf{K}^0_{\mathrm{b}_2\mathrm{b}_1} & \mathbf{K}^0_{\mathrm{b}_2\mathrm{b}_2}\end{bmatrix} + k_y^4\begin{bmatrix}\mathbf{K}^4_{\mathrm{b}_1\mathrm{b}_1} & \mathbf{K}^4_{\mathrm{b}_1\mathrm{b}_2}\\ \mathbf{K}^4_{\mathrm{b}_2\mathrm{b}_1} & \mathbf{K}^4_{\mathrm{b}_2\mathrm{b}_2}\end{bmatrix} + \begin{bmatrix}0 & 0\\ 0 & \tilde{\mathbf{K}}^{\mathrm{s}}_{\mathrm{b}_2\mathrm{b}_2}(k_y,\omega)\end{bmatrix}\right)\begin{bmatrix}\tilde{\mathbf{u}}_{\mathrm{b}_1}(k_y,\omega)\\ \tilde{\mathbf{u}}_{\mathrm{b}_2}(k_y,\omega)\end{bmatrix} = \begin{bmatrix}\tilde{\mathbf{f}}_{\mathrm{b}_1}(k_y,\omega)\\ \tilde{\mathbf{f}}_{\mathrm{b}_2}(k_y,\omega)\end{bmatrix} \tag{2}$$

The dynamic soil stiffness matrix $\tilde{\mathbf{K}}^{\mathrm{s}}_{\mathrm{b}_2\mathrm{b}_2}(k_y,\omega) = \overline{\overline{\tilde{k}}}_{\mathrm{s}}(k_y,\omega)$, which it is computed by means of the Green's function [30] (Figure D.1 step 2.2.2).

The following section describes the evaluation of train-track interaction forces (Figure D.1, step 2.1). Both quasi-static excitation and dynamic excitation due to random track unevenness are taken into account [36]. The dynamic contribution depends upon the rail displacements $\tilde{\mathrm{u}}_{\mathrm{r}}(k_y,\omega)$ which are obtained from Equation (2).

D.2.1.2 *Train forces*

The train forces $\mathbf{g}(\omega)$ (Figure D.1, step 2.1) are computed by the superposition of the dynamic $\mathbf{g}_d$ and quasi-static $\mathbf{g}_q$ excitations.

To compute the dynamic forces, a Power Spectral Density (PSD) function is assumed for the simulation of random track unevenness [35]:

$$\tilde{S}_{\mathrm{rzz}}(k_y) = \tilde{S}_{\mathrm{rzz}}(k_{y0})\left(\frac{k_y}{k_{y0}}\right)^{-w} \tag{3}$$

where $\tilde{S}_{\mathrm{rzz}}(k_{y0})$ is the reference value of the PSD at $k_{y0} = 1\,\mathrm{rad/m}$ and w is the exponent that determines how the PSD function decreases with increasing wavenumber k_y. The coefficients $\tilde{S}_{\mathrm{rzz}}(k_{y0})$ and w are obtained from standards.

The rail unevenness $\mathbf{u}_{w/r}(\omega)$ is evaluated as:

$$\mathbf{u}_{w/r}(\omega) = \mathbf{T}(\omega, v)\frac{1}{v}\tilde{u}_{rz}\left(-\frac{\omega}{v}\right) \tag{4}$$

where $\tilde{u}_{rz}(k_y)$ is the wavenumber transform of the rail unevenness $u_{rz}(y)$ and $\mathbf{T}(\omega)$ is a vector that collects the phase shift for each axle moving at a constant speed v, being:

$$u_{rz}(y) = \sum_{m=1}^{n} \sqrt{2\tilde{S}_{rzz}(k_{ym})\Delta k_y}\cos(k_{ym}y - \theta_m) \tag{5}$$

where $k_{ym} = m\Delta k_y$ is the wavenumber sampling, Δk_y the wavenumber step, n the size of the wavenumber sample and θ_m represents random phase angles uniformly distributed in the interval $[0, 2\pi]$.

The dynamic forces $\mathbf{g}_d(\omega)$ are computed from the track and vehicle compliances assuming a perfect contact between both [35]:

$$\mathbf{u}_c(\omega) = \mathbf{u}_r(\omega) + \mathbf{u}_{w/r}(\omega) \tag{6}$$

where $\mathbf{u}_c(\omega)$ contains the vehicle displacements at the train-track interface and both the rail displacements $\mathbf{u}_r(\omega)$ and the rail unevenness $\mathbf{u}_{w/r}(\omega)$ are evaluated at a fixed position in the moving frame of reference. The dynamic loads are computed as:

$$\left[\mathbf{C}^t(\omega) + \mathbf{C}^v(\omega)\right]\mathbf{g}_d(\omega) = -\mathbf{u}_{w/r}(\omega) \tag{7}$$

where $\mathbf{C}^v(\omega)$ is the vehicle compliance and $\mathbf{C}^t(\omega)$ is the track compliance.

The vehicle's unsprung mass M_u is the only train mass considered when computing the vertical dynamic loads [34]. Then, the vehicle compliance is computed as $\mathbf{C}^v(\omega) = \text{diag}(-1/(M_u\omega^2))$. The vehicle compliance C^v_{lk} represents the displacement at the contact point k due to a unit load at the contact point l.

Additionally, track compliance C^t_{lk} relates the track displacement at the position of axle k due to a unit load at axle l. The track compliance is obtained from the rail impulse response $\tilde{u}_{\mathrm{r}}(k_y, \tilde{\omega})$ (Equation (2)) using the following equation [35]:

$$C^t_{lk}(\tilde{\omega}) = \frac{1}{2\pi}\int_{-\infty}^{+\infty} \tilde{u}_{\mathrm{r}}(k_y, \tilde{\omega} + k_y v)e^{-\mathrm{i}k_y(y_l - y_k)}\mathrm{d}k_y \tag{8}$$

where y_l and y_k are the positions of l-th and k-th axles respectively. Also, the change of variables $\tilde{\omega} = \omega - k_y v$ is considered and v is the train speed.

The quasi-static load is computed as:

$$\mathbf{g}_q(\omega) = \sum_{k=1}^{n_a} w_k \exp\left(i\frac{\omega}{v}y_k\right) \tag{9}$$

where w_k and y_k are the weight and the position of the k-th axle, while n_a is the number of axles.

D.2.2 *Track-soil transfer function*

Many vibration prediction models consider track-soil interaction using comprehensive methodologies, which imply a high computational cost. In order to reduce the computational effort, the proposed model estimates the track-soil transfer function $\tilde{\mathbf{u}}_{\mathrm{ff}}(\mathbf{x}, k_y, \omega)$ (Figure D.1, step 2.2) by combining the Green's functions $\tilde{\mathbf{u}}_{\mathrm{g}}(\mathbf{x}, k_y, \omega)$ [30] (Figure D.1, step 2.2.2) for a homogeneous or layered soil with a correction factor $\tilde{A}_g$ obtained using a neural network (Figure D.1, step 2.2.1). Note that the sub-indexes ff and g indicate free-field response and Green functions, respectively. The track-soil transfer function $\tilde{\mathbf{u}}_{\mathrm{ff}}(\mathbf{x}, k_y, \omega)$ represents the response at a point $\mathbf{x} = \{d, y, 0\}$ located at the soil surface due to an impulsive vertical load at the rail. Correction factor $\tilde{A}_g$ depends on the track type and the soil properties. It is evaluated for a point $\mathbf{x}$, a frequency ω and a wavenumber k_y. The track-soil transfer function at a point $\mathbf{x}$ can be obtained as:

$$\tilde{\mathbf{u}}_{\mathrm{ff}}(\mathbf{x}, k_y, \omega) = \tilde{A}_g(d, k_y, \omega)\tilde{\mathbf{u}}_{\mathrm{g}}(\mathbf{x}, k_y, \omega) \tag{10}$$

In order to estimate the correction factor, $\tilde{A}_g$, a Multilayer Perceptron (MLP) neural network architecture with a back-propagation training algorithm [10] is used. One, two and three hidden layers are tested. A NN framework with four layers (Figure D.3: one input, two hidden and one output) is chosen to construct the proposed model.

The input layer (Figure D.3) contains six inputs parameter: soil parameters c_{s_1}, h_1, V_{s30}, the distance d between the evaluated point $\mathbf{x}$ and the track, frequency ω and wavenumber, that is represented by the non-dimensional wavenumber $k_{dy} = k_y c_{s_1}/\omega$. h_1 and c_{s_1} are the depth and the shear wave velocity of the upper layer respectively. Whereas, V_{s30} is the average shear wave velocity defined in [15]:

$$V_{s30} = \frac{30}{\sum_i^{N_s} \frac{h_i}{c_{s_i}}} \tag{11}$$

where h_i is the thickness of the $i-$th layer, N_s the total number of layers in the top 30 m and c_{s_i} the shear wave velocity of the $i-$th layer. The shear wave velocity of the upper layer matches with the V_{s30} parameter $c_{s_1} = V_{s30}$, with $h_1 = 30$ m for an homogeneous soil.

The output layer has two parameters because the correction factor $\tilde{A}_g$ is a complex number. Therefore it is defined using its modulus $|\tilde{A}_g|$ (transformed to a logarithmic scale $K_g = 20\log_{10}|\tilde{A}_g|$) and argument $arg\,(\tilde{A}_g)$ wrapped to 2π rad.

The aim of the NN procedure is to map the weighted inputs (e.g. distance) to outputs (i.e. vibration). First, weighted inputs are assumed and the resulting predicted outputs are compared against the known output targets to quantify the error. This error is fed back through the network using a back-propagation training algorithm. The input weightings are then modified and the process is repeated until convergence.

The NN approach is developed using the `Matlab Neural Network Toolbox` [39]. A tangent hyperbolic function is used as the activation function in the hidden layer due to its faster convergence compared to nonsymmetric functions [55]. The NN architecture is

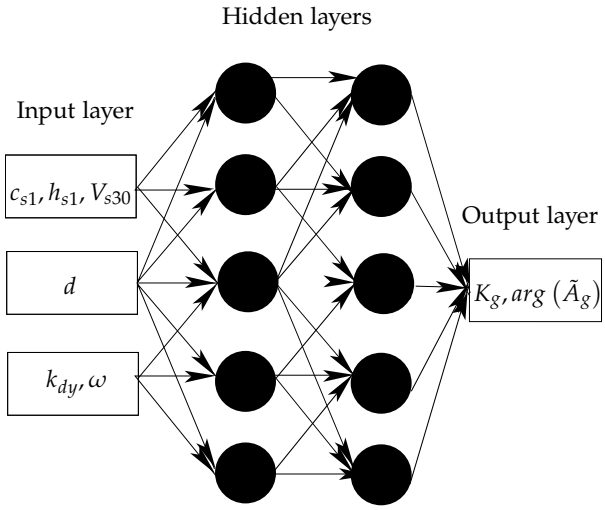

Figure D.3: Neural network model schematic.

trained using the Levenberg-Marqurdt algorithm that has been be shown to be one of the faster methods for training NN [40]. Also, to evaluate the performance of the NN model and select the best framework, mean squared error (MSE) and determination coefficient (R^2) are used [41, 42, 56]:

$$MSE = \frac{1}{N_n}\sum_{i=1}^{N_n}\left(X_i - \hat{X}_i\right)^2 \tag{12}$$

$$R^2 = 1 - \frac{\sum_{i=1}^{N_n}\left(X_i - \hat{X}_i\right)^2}{\sum_{i=1}^{N_n}\left(X_i - \text{mean}(X)\right)^2} \tag{13}$$

where X_i and $\hat{X}_i$ are the output targets and predicted outputs, respectively, and N_n is the size of the sample. Next expressions are used to build the output targets:

$$\arg\left(\tilde{A}_g\right) = \arg\left(\tilde{\mathbf{u}}^r_{\text{ff}}\right) - \arg\left(\tilde{\mathbf{u}}_{\text{g}}\right) \tag{14}$$

$$K_g = 20\log_{10}\left(\frac{\left|\tilde{\mathbf{u}}^r_{\text{ff}}\right|}{\left|\tilde{\mathbf{u}}_{\text{g}}\right|}\right) \tag{15}$$

where $\tilde{\mathbf{u}}^r_{\text{ff}}$ is the track-soil transfer function computed by using the reference model [19, 21] (super-index r) and $\tilde{\mathbf{u}}_{\text{g}}$ the Green's functions.

To train and evaluate the NN a large number of data output targets are used. Ballasted and slab tracks situated on top of an embankment are considered. Table D.1 summarises the properties of track types (Figure D.2). The material properties of the embankment are chosen equal to those of the top layer of the soil. A linear hysteretic damping model is used for all constituents of the ballasted and slab track structure.

A description of the NN database construction and performance is given in [22].

Table D.1: Ballasted and slab track properties.

RAIL	Bending stiffness $E_{\mathrm{r}} I_{\mathrm{r}}$ $\left[\mathrm{N/m^2}\right]$	6.18×10^6
	Mass per unit length $\rho_{\mathrm{r}} A_{\mathrm{r}}$ [kg/m]	60.83
	Loss factor η_{r}	0.05
RAIL PAD	Equivalent stiffness $\overline{k}_{\mathrm{rp}}$ $\left[\mathrm{N/m^2}\right]$	150×10^6
	Loss factor η_{rp}	0.25
SLEEPER	Spacing d_{sl} [m]	0.6
	Length l_{sl} [m]	2.6
	Width b_{sl} [m]	0.35
	Height h_{sl} [m]	0.22
	Mass per sleeper m_{sl} [kg]	300
	Rotational inertia $\rho_{\mathrm{sl}} \overline{I}_{\mathrm{sl}}$ $\left[\mathrm{kgm^2/m}\right]$	567
BALLAST	Length at the top l_{b1} [m]	2.6
	Length at the bottom l_{b2} [m]	2.87
	Width b_{b} [m]	0.35
	Height h_{b} [m]	0.3
	Equivalent mass $\overline{m}_{\mathrm{b}}$ [kg/m]	796
	Vertical stiffness k_{b} [N/m]	500×10^6
	Loss factor η_{b}	1.0
SLAB	Length l_{slab} [m]	2.6
	Height h_{slab} [m]	0.3
	Bending stiffness $E_{\mathrm{slab}} I_{\mathrm{slab}}$ $\left[\mathrm{Nm^2}\right]$	117×10^6
	Mass per unit length $\rho_{\mathrm{slab}} A_{\mathrm{slab}}$ [kg/m]	1950
	Loss factor η_{slab}	0.01
EMBANKMENT	Length at the top l_{e1} [m]	3.5
	Length at the soil surface l_{e2} [m]	7
	Height h_{e} [m]	1.5

D.2.3 *Free-field response*

Once the track-soil transfer function $\tilde{\mathbf{u}}_{\mathrm{ff}}$ (Equation (10)), dynamic $\mathbf{g}_d$ (Equation (7)) and quasi-static $\mathbf{g}_q$ (Equation (9)) excitations are obtained, soil response $\mathbf{u}_{\mathrm{s}}(\mathbf{x}, \omega)$ due a train passage at speed v is determined by following the 2.5D formulation in the wavenumber-frequency domain described in [35]. The free-field response $\mathbf{u}_{\mathrm{s}}(\mathbf{x}, \omega)$ is decomposed into its quasi-static $\mathbf{u}_{\mathrm{qs}}$ and dynamic $\mathbf{u}_{\mathrm{ds}}$ components as $\mathbf{u}_{\mathrm{s}}(\mathbf{x}, \omega) = \mathbf{u}_{\mathrm{qs}}(\mathbf{x}, \omega) + \mathbf{u}_{\mathrm{ds}}(\mathbf{x}, \omega)$. The quasi-static u_{qsi} and dynamic u_{dsi} contributions in the i-th direction at a point $\mathbf{x}$ is evaluated as:

$$u_{\mathrm{qsi}}(\mathbf{x}, \omega) = \sum_{k=1}^{n_a} w_k \tilde{h}_{\mathrm{ffi}}(y - y_k, \omega, 0) \tag{16}$$

$$u_{\mathrm{dsi}}(\mathbf{x},\omega) = \frac{1}{2\pi}\sum_{k=1}^{n_a}\int_{-\infty}^{+\infty}\tilde{h}_{\mathrm{ffi}}(y-y_k,\omega,\tilde{\omega})g_{\mathrm{d}_k}(\tilde{\omega})\mathrm{d}\tilde{\omega} \tag{17}$$

where n_a is the number of axles and w_k, y_k and g_{d_k} refer to weight, position and dynamic load of the k-th axle, respectively. A change of variables $\tilde{\omega} = \omega - k_y v$ is again considered and the relation used to express Equations (16) and (17) in compact forms is:

$$\tilde{h}_{\mathrm{ffi}}(y-y_k,\omega,\tilde{\omega}) = \frac{1}{v}\tilde{u}_{\mathrm{ffi}}(\mathbf{x},\frac{\omega-\tilde{\omega}}{v},\omega)\exp\left[-i\frac{\omega-\tilde{\omega}}{v}(y-y_k)\right] \tag{18}$$

D.2.4 *Building response*

Next the foundation of structure is excited by a ground motion that corresponds with the free-field response $\mathbf{u}_{\mathrm{s}}$ calculated previously (Equations (16) and (17)). Then, the dynamic analysis of the building due to railway traffic is computed from the 3D FEM methodology presented in [38]. This methodology is based on a modal superposition analysis [8], to assess an overall value of the response and the contribution of the modes to this response. However, the time domain history of the building response can not be obtained from the proposed model. Below this methodology is briefly recapitulated.

Total building response $\mathbf{u}_{\mathrm{t}}$ (Figure D.1, step 2.4) is defined as the superposition of the ground motion $\mathbf{u}_{\mathrm{s}}$ and structure deformation $\mathbf{u}_{\mathrm{b}}$:

$$\mathbf{u}_{\mathrm{t}}(t) = \mathbf{u}_{\mathrm{b}}(t) + \mathbf{r}\mathbf{u}_{\mathrm{s}}(t) \tag{19}$$

where $\mathbf{u}_{\mathrm{s}}$ is the free-field response in the time domain and the influence matrix $\mathbf{r}$ defines the wave incidence on the structure. The structure deformation $\mathbf{u}_{\mathrm{b}}$ is obtained by modal superposition as:

$$\mathbf{u}_{\mathrm{b}}(t) = \sum_{i=1}^{N}\sum_{j=1}^{3}\boldsymbol{\phi}_i\Gamma_i^j\xi_i^j(t) \tag{20}$$

where $\boldsymbol{\phi}_i$ is the i-th mode shape, N the number of modes, and Γ_i^j and ξ_i^j the modal participation factor and the amplitude for the i-th mode at direction j, respectively.

The vibration level of the structure is evaluated using the overall Root-Mean-Square (RMS) value of the acceleration [24]:

$$a_{RMS} = \sqrt{\frac{1}{T}\int_0^T \ddot{\mathbf{u}}_{\mathrm{t}}^2(t)dt} \tag{21}$$

where T is the characteristic period defined by the standard [11] where the structural response is assumed to be stationary. Substituting the building response (Equation (19)) and the structure deformation (Equation (20)) in Equation (21), and considering some assumptions in the methodology [38], leads to the next simplified expression to estimate the overall RMS:

$$a_{RMS} = \sqrt{H_s + H_b'} \tag{22}$$

where $\sqrt{H_s}$ and $\sqrt{H'_b}$ are related to the contributions to the RMS value of the ground motion and the structural response respectively. H_s is calculated as:

$$H_s = \frac{1}{M^2} \sum_{n=1}^{M} \sum_{j=1}^{3} r^{j^2} \left| \ddot{U}_s^j(f_n) \right|^2 \tag{23}$$

where $M = \frac{T}{\Delta t}$, $\ddot{U}_s^j(f_n)$ is the Discrete Fourier transform of $\ddot{u}_s^j(t_n)$, t_n is the time sampling and f_n is the frequency sampling. On the other hand, H'_b is computed from superposition of the modes as $H'_b = \sum_{i=1}^{N} H'_{bi}$, where the participation H'_{bi} of the i-th mode is evaluated by:

$$H'_{bi} = \boldsymbol{\phi}_i^2 \sum_{j=1}^{3} \left(\Gamma_i^j \Lambda_i^j \right)^2 \tag{24}$$

where Λ_i^j is the ground-borne response spectra defined for the natural frequency f_i at direction j. The ground-borne response spectra Λ_i^j is obtained as:

$$\Lambda_i^j = \frac{1}{M} \sqrt{\sum_{n=1}^{M} \left| \ddot{\Xi}_i^j(f_n) \right|^2} \tag{25}$$

where $\ddot{\Xi}_i^j(f_n)$ represents the Discrete Fourier transform of the amplitude $\ddot{\xi}_i^j(t_n)$ computed by solving the Duhamel's integral as [8]:

$$\xi_i^j(t) = \frac{1}{f_{di}} \int_0^t -\ddot{u}_s^j e^{-2\pi\zeta_i f_i (t-\tau)} \sin\left(2\pi f_{di}\,(t-\tau)\right) d\tau \tag{26}$$

where ζ_i is the damping ratio and $f_{di} = f_i \sqrt{1-\zeta_i^2}$ the damped natural frequency.

The contribution of the i-th mode to the overall RMS value of the acceleration is estimated from Equations (22) and (24) as:

$$C_i = \sqrt{H'_{bi}} \tag{27}$$

Soil-structure interaction is considered by adding spring k_f and damper c_f elements to the foundation of the building model. Next correlations for shallow foundations [2] are used:

$$k_f = 3.4 G_s \sqrt{A_f} \tag{28}$$

$$c_f = 1.6 \sqrt{G_s \rho_s A_f} \tag{29}$$

where G_s and ρ_s are the shear modulus and the mass density of the soil, respectively, and A_f is the foundation area.

Finally, Table D.2 summarises the main steps to compute track vibration generation and its propagation into buildings ((Figure D.1).

Table D.2: Scoping model implementation.

1. Compute rail displacement $\tilde{u}_r(k_y, \omega)$ using 2.5D FEM method (Equation (2)).
2. Compute dynamic $\mathbf{g}_d(\omega)$ and quasi-static $\mathbf{g}_q(\omega)$ train excitations using Equations (7) and (9).
3. Estimate correction factor $\tilde{A}_g(d, k_y, \omega)$ via NN (Figure D.3).
4. Evaluate soil Green's function $\tilde{\mathbf{u}}_g(\mathbf{x}, k_y, \omega)$.
5. Compute track-soil transfer function $\tilde{\mathbf{u}}_{ff}(\mathbf{x}, k_y, \omega)$ using Equation (10).
6. Compute soil response due to a train passage $\mathbf{u}_s(\mathbf{x}, \omega)$ (Equations (16) and (17)).
7. Solve the immission problem of waves in building (Equations (22) and (27)).

D.3 ANALYSIS

An analysis of the effect of track, soil, building type and train speed on building vibration are now investigated. Two track types are considered. Track 1 is a classical ballasted track (Section D.2.2 (Table D.1)) supported by an embankment. Track 2 is a slab track (Figure D.2) with identical rails, rail pads and embankment as Track 1 (Section D.2.2 (Table D.1)).

The structures are four, eight and twelve storey buildings with the same floor plan dimensions $12\,\text{m} \times 12\,\text{m}$ (Figure D.4.a). It consists of eight concrete columns with $0.6\,\text{m} \times 0.4\,\text{m}$ section, four edge beams with $0.6\,\text{m} \times 0.2\,\text{m}$ section and two framed concrete walls with $2.4\,\text{m} \times 0.15\,\text{m}$ section. The floors are simply supported concrete slabs with a thickness of $0.2\,\text{m}$. The floors consist of a two-dimensional frame with axial stiffness per unit length $EA = 1.433 \times 10^9\,\text{N/m}$, bending stiffness per unit length $EI = 9.935 \times 10^6\,\text{Nm}$, and a mass per unit area of $m = 172\,\text{kg/m}^2$. The structure is founded on a $1.0\,\text{m}$ thick concrete slab. The concrete material has the following properties: Young's modulus $E = 20 \times 10^9\,\text{N/m}^2$, Poisson's ratio $\nu = 0.2$, density $\rho = 2400\,\text{kg/m}^3$ and Rayleigh damping is used, with $\zeta = 0.05$ for all modes that contribute to the building response. The structure is discretised using two-node Euler-Bernoulli elements to represent columns and beams and four-node shell elements for floors and framed walls.

The midpoint of the foundation is located at distances $d = \{20, 30, 40, 50\}\,\text{m}$ from the track axis. The building response is evaluated using a Single Point Response (SPR) excitation model, where the soil vibration is transmitted simultaneously to the whole foundation of the structure. It should be noted that as the building response is based upon the free-field response calculated using the scoping methodology, any errors are propagated through to the building calculation. The building responses at points A and B (Figure D.4.(a)) located at the top floor are analysed.

Figure D.5 presents the bending mode shapes of the floors computed without considering SSI for increasing edge (Figure D.5.(a-c)) and framed wall (Figure D.5.(d-f)) deformations.

The passage of a S-100 train travelling at $\{100, 150, 200\}$ km/h is studied. Table D.3 shows the carriage length L_t, the distance between bogies L_b, the axle distance L_a, the total axle mass M_t and the unsprung axle mass M_u for all carriages.

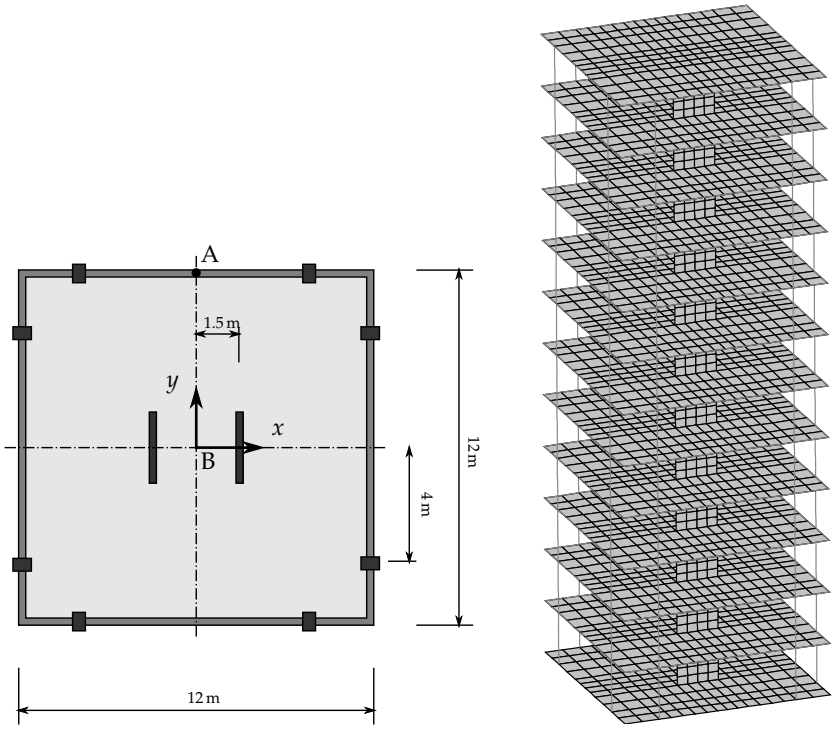

Figure D.4: (a) Four, eight and twuelve-storey buildings plan geometry and (b) discretization of the twelve-storey building.

Table D.3: Geometrical and mass characteristics of the S-100 train.

	No. of carriages	No.of axles	L_t[m]	L_b[m]	L_a[m]	M_t[kg]	M_u[kg]
Traction cars	2	4	22.15	14.00	3.00	17185	2048
End carriages	2	3	21.84	18.70	3.00	11523	2003
Central carriages	6	2	18.70	18.70	3.00	15523	2003

Quasi-static and dynamic excitations are taken into account [34] using the same track unevenness profile for all the studied cases. The dynamic contribution is expected to be dominant in the free-field response [34] because the train speeds are below the critical velocity of the track system [44].

D.3.1 *Track type*

Next, the influence of the ballasted and slab tracks on the results is studied. Embankment properties are identical to the underlying soil modelled as a homogeneous elastic half-space

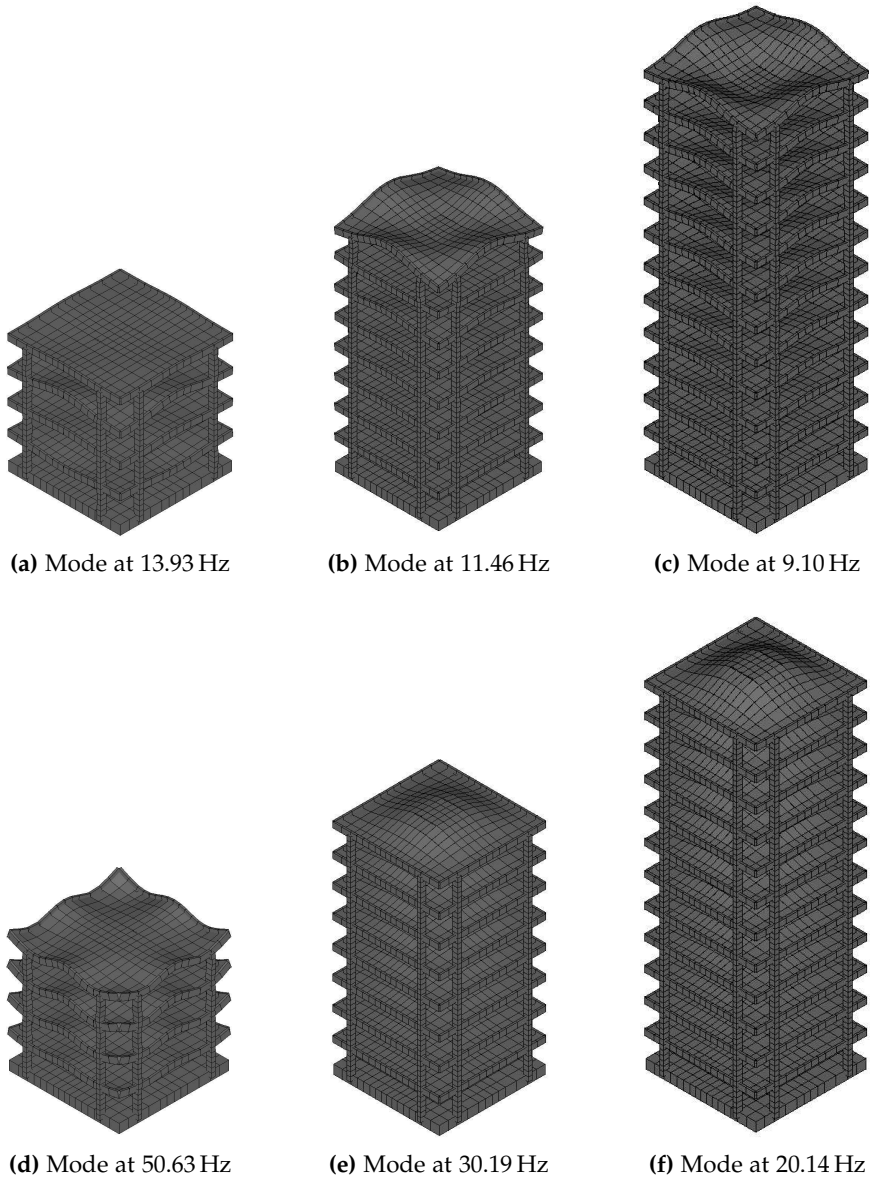

(a) Mode at 13.93 Hz **(b)** Mode at 11.46 Hz **(c)** Mode at 9.10 Hz

(d) Mode at 50.63 Hz **(e)** Mode at 30.19 Hz **(f)** Mode at 20.14 Hz

Figure D.5: Bending floor mode shapes of the (a and d) four-storey building, (b and e) eight-storey building and (c and f) twuelve-storey building.

with a shear wave velocity $c_s = 200\,\mathrm{m/s}$, a dilatational wave velocity $c_p = 400\,\mathrm{m/s}$ and density $\rho = 1800\,\mathrm{kg/m^3}$. The material damping ratio β for both deviatoric and volumetric deformation has a value of 0.05.

Figure D.6 shows the modulation of the dynamic loads and the free-field response due to the track type. The free-field response has been computed from the weighted acceleration with a time window of 1 s as prescribed by the ISO 2631 standard [24]. It can be seen

that the dynamic slab track loads are higher at frequencies above 40 Hz. This is because slab track has a higher stiffness which also causes the free field response to increase at this frequency range. However, the soil response due to the train passage at the low and medium frequency ranges is attenuated by the slab track due to the effect of the free-field mobility (Figure D.7).

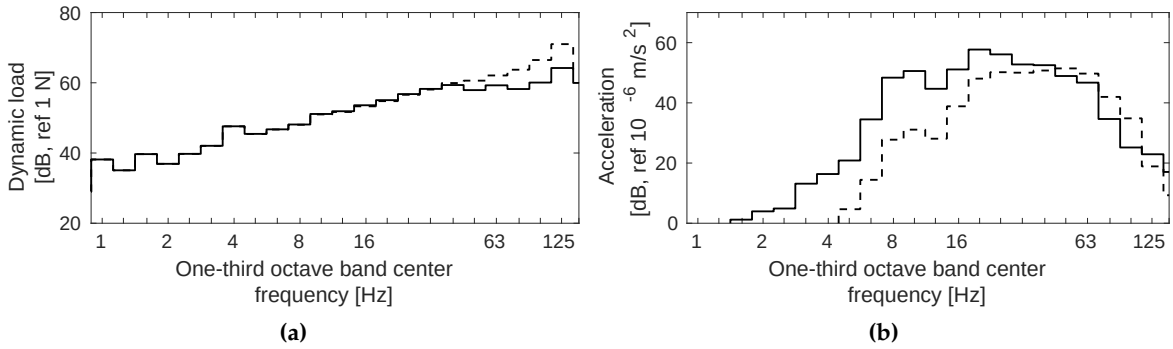

Figure D.6: One-third octave band center frequency of the (a) dynamic load of an axle with unsprung mass $m_s = 2048\,\text{kg}$ and (b) the vertical weighted acceleration in the free-field at 20 m from the track due to a S-100 train passage, at $v = 100\,\text{km/h}$: (solid line) ballasted and (dashed line) slab tracks.

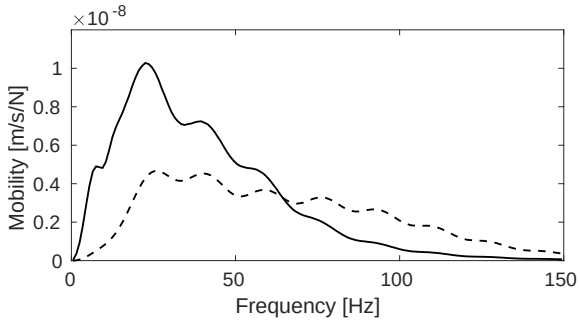

Figure D.7: Free-field vertical mobility at 20 m from the axis track: (solid line) ballasted and (dashed line) slab tracks.

Figure D.8 shows the Maximum Transient Vibration Value (MTVV) [24] of the free-field acceleration and the overall RMS value (Equation (21)) of the twelve storey building vibration level. The predicted vibration responses have been weighted according to ISO 2631 [24] to obtain these values. Note that building response is computed considering the weighted ground motion $\ddot{\mathbf{u}}_s$ (Equations (23) and (25)). Results for the ballasted track present the highest vibrations. As expected, free-field and building responses are attenuated with increasing distance from the track axis. The building vibration level is higher than the free-field response being this amplification more important for the ballasted track in this case.

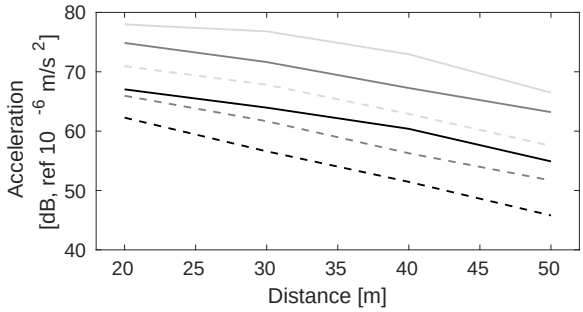

Figure D.8: (Black line) MTVV at the free-field and overall RMS value of the weighted acceleration at the top floor of the observation points (dark grey line) A and (light grey line) B, depending on the distances from the track due to a S-100 train passage at $v = 100\,\mathrm{km/h}$ considering (solid line) ballasted and (dashed line) slab tracks.

D.3.2 *Soil properties*

The influence of the soil stiffness on the scoping model predictions is studied using three homogeneous soils [15], (Table D.4): soft, medium and stiff soils. Their properties are shown in Table D.5.

Table D.4: Soil types based on Eurocode 8.

	Description	V_{s30} [m/s]
A	Rock outcrop	> 800
B	Very dense sand or gravel, or very stiff clay	$360 - 800$
C	Dense to medium-dense sand or gravel, or stiff clay	$180 - 360$
D	Loose-to-medium sand or gravel	< 180

Table D.5: Homogeneous soil properties.

	c_p [m/s]	c_s [m/s]	ξ [-]	ρ [kg/m^3]
Soft soil	345.2	172.6	0.05	1800
Medium soil	669.8	334.9	0.05	1800
Stiff soil	993.6	496.8	0.05	1800

Figure D.9 shows the influence of soil stiffness on the rail receptance. The response decreases with increasing soil stiffness. Furthermore, rail displacement is smoother and the dominant frequency increases as soil stiffness increases. This is because the differences between the stiffness of the embankment and the ballast are lower for the medium and stiff soils compared to the soft soil.

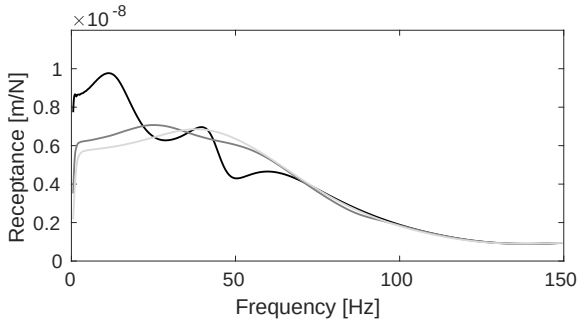

Figure D.9: The displacement of the rail for (black line) soft, (dark grey line) medium and (light grey line) stiff soils (Table D.5), considering the ballasted track.

Regarding the dependence on soil stiffness of the track-soil transfer function estimations, free-field mobility at a distance of 20 m from the axis track is presented in Figure D.10. Again, the response decreases and the dominant frequency increases with soil stiffness.

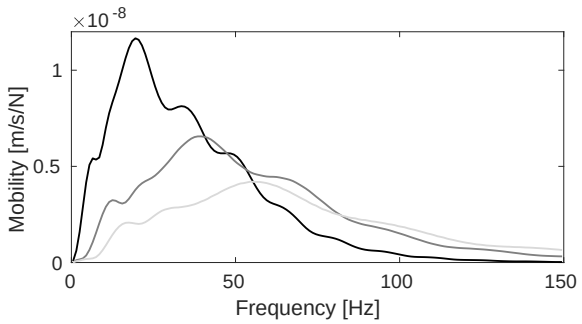

Figure D.10: Free-field vertical mobility at 20 m from the ballasted track for (black line) soft, (dark grey line) medium and (light grey line) stiff soils (Table D.5).

The effect of soil stiffness in the ground-borne response spectra and building vibrations due to the train passage is presented in Figure D.11. The ground-borne response spectra $\Lambda_i^j(f_i)$ is computed from the weighted ground motion $\ddot{\mathbf{u}}_s$ using Equation (25), considering a damping ratio $\zeta = 0.05$ for all mode shapes. The contribution to the overall RMS value of the response of the building mode shapes, within a frequency band centred at Ω_j, is computed as:

$$C_j\left(\Omega_j\right) = \sum_i \sqrt{C_i^2(f_i)} \qquad \forall\, f_i \in \left[\Omega_{j0}, \Omega_{j1}\right] \tag{30}$$

where Ω_{j0} and Ω_{j1} are the limits of the one-third octave band center frequency Ω_j, and C_i is calculated from Equation (27).

According to the previous results (Figure D.10), the frequency content of the ground-borne response spectra (Figure D.11.a) shows that dominant frequencies due to the dynamic excitation vary from 10 to 50 Hz for the soft soil, to 20 and 60 Hz for the medium

and stiff soils. Building response is most dominant distributed between frequencies from 8 Hz to 80 Hz. The observation point B presents the highest response (Figure D.11.c). This is because point B is located at the part of the slab supported by the frame walls, where the bending stiffness of the floor is higher than at the edge (point A). The response at point A is concentrated at approximately 9 Hz corresponding to the mode with highest displacements on the edge (Figure D.5.(c)), whereas maximum level of vibration at point B is found at approximately 20 Hz matching the mode associated with highest framed wall deformation. According to the differences in the ground-borne response spectra (Figure D.11.a). at the natural frequencies (9 and 20 Hz) of the building (Figure D.5.(c and f)), building response is higher for the soft soil (Figure D.11.b and c).

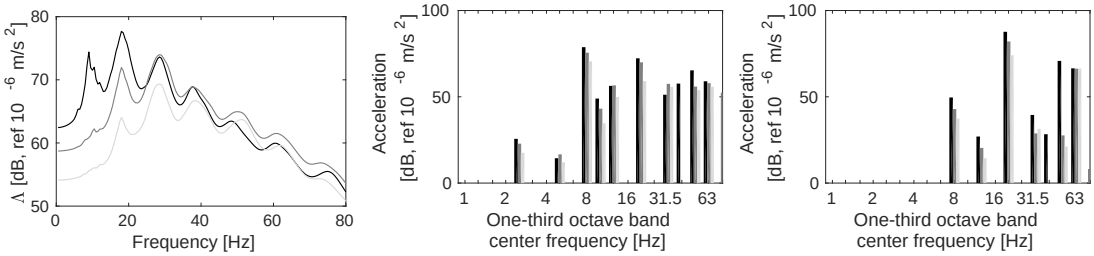

Figure D.11: (a) Ground-borne response spectra $\Lambda_i^j(f_i)$ and (b and c) contribution of the modes to the overall RMS value of the vertical weighted acceleration at the top floor of the observation points (b) A and (c) B, due to a S-100 train passage at $v = 100$ km/h at 20 m from the ballasted track for (black line) soft, (dark grey line) medium and (light grey line) stiff soils (Table D.5).

D.3.3 *Building height*

The effect of building height on building response computed from the scoping model is now studied considering the passage of a S-100 train travelling at 100 km/h on the ballasted track on an embankment (Table D.1) supported by a homogeneous soil with $c_s = 200$ m/s (Section D.3.1). Figure D.12 shows the contribution of the modes to the overall RMS value of the vertical vibration. Dominant frequencies for the four, eight and twelve-storey buildings are found at approximately 12 Hz, 10 Hz and 8 Hz for observation point A, and 50 Hz, 30 Hz and 20 Hz for observation point B respectively. Thus, the natural frequencies decrease as the building height increases. Also, there are slight differences in the response magnitude of the dominant modes.

Figure D.13 presents the influence of building height on the overall RMS value of response. The results are shown for different storey levels. The response increases with storey level, however, this correlation is not observed at observation point A for the four-storey building (Figure D.13.(a)). This can be explained from the dominant response at observation point A for the four-storey building (Figure D.12.(a)) where the natural frequency (13.93 Hz) of

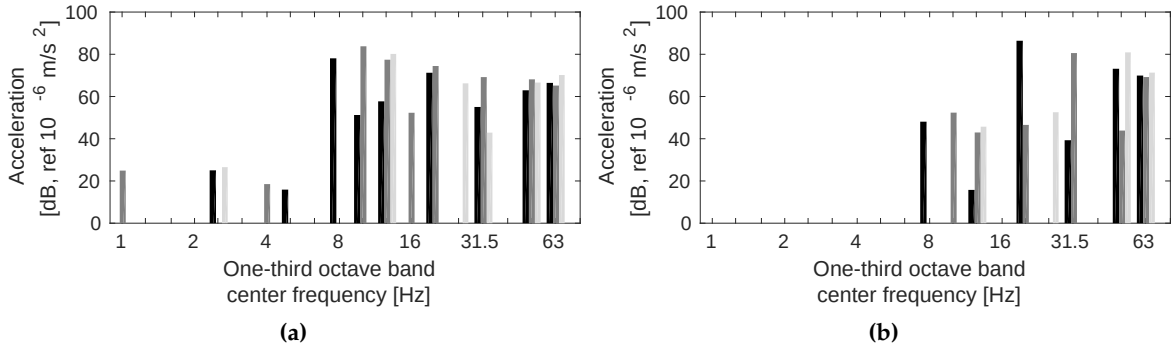

Figure D.12: Contribution of modes to the overall RMS value of the vertical weighted acceleration of observation points (a) A and (b) B at the top floor, due to a S-100 train passage at $v = 100\,\mathrm{km/h}$ at 20 m from the ballasted track for the (light grey bars) four-storey building, (dark grey bars) eight-storey building and (black bars) twelve-storey building.

a bending mode (Figure D.5.(a)) experiences larger amplitudes at the middle floors of the building than at the top floor. Differences in the vibration level on the top floor, depending on the building height, are within a narrow range of 5 dB.

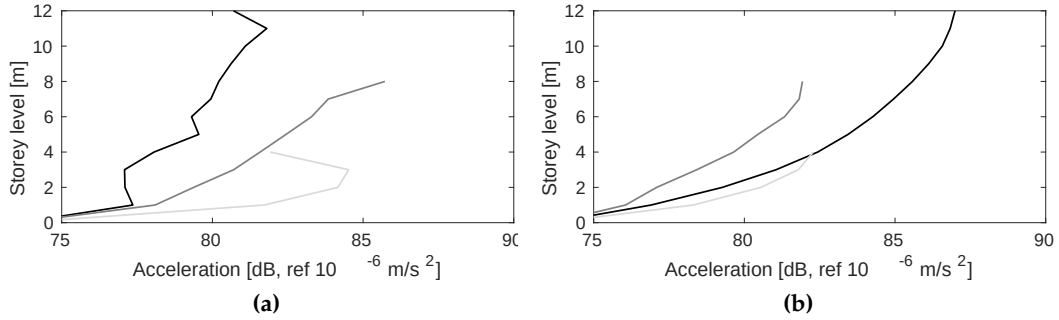

Figure D.13: Overall RMS value of the weighted acceleration at the observation points (a) A and (b) B depending on the storey level, due to a S-100 train passage at $v = 100\,\mathrm{km/h}$ at 20 m from the ballasted track for the (light grey line) four-storey building, (dark grey line) eight-storey building and (black line) twelve-storey building.

D.3.4 *Train speed*

Next, the scoping model is used to assess the effect of train speed on railway vibrations. The passage of a S-100 train travelling at $\{100, 150, 200\}$ km/h is simulated. The ballasted track on a top of an embankment (Table D.1) and a homogeneous medium with $c_s = 200\,\mathrm{m/s}$ are considered again.

Figure D.14 presents the influence of the train speed on the free-field predictions of the proposed model. The quasi-static contribution is observed in the frequency content at a-

pproximately the axle passing frequency $f_a = v/L_a = \{9.26, 13.9, 18.52\}$ Hz. The dominant frequency due to the dynamic excitation remains in the range 20 - 40 Hz for the different train speeds. Both quasi-static and dynamic contributions increase with train speed, however it is more noticeable for the quasi-static case.

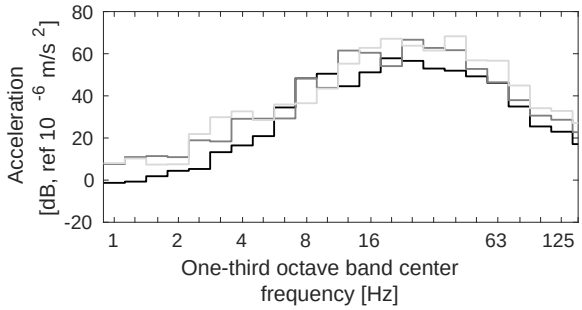

Figure D.14: One-third octave band center frequency of the vertical weighted acceleration in the free-field due to a S-100 train passage at (black line) $v = 100$ km/h, (dark grey line) $v = 150$ km/h and (light grey line) $v = 200$ km/h at 20 m.

Finally, Figure D.15 correlates train speed with both the MTVV of the free-field acceleration and the overall RMS value (Equation (21)) of the building response. A clear trend is observed, with vibration levels increasing with train speed. However, the amplification in the building response in relation to the soil response does not depend on the train speed.

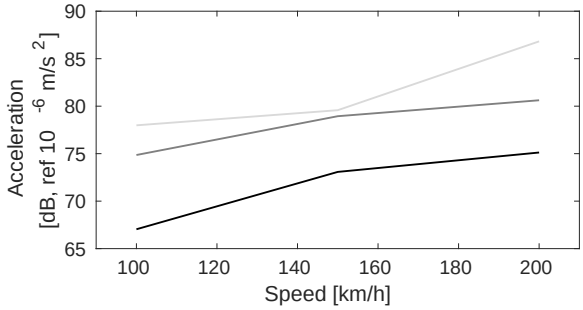

Figure D.15: (Black line) MTVV at the free-field and overall RMS value of the weighted acceleration for the observation points (dark grey line) A and (light grey line) B at the top floor, due to a S-100 train passage at 20 m depending on the speed of train.

D.4 v_{s30} PARAMETER

V_{s30} is a measure of the mean shear wave speed in the top 30 m of soil [15]. It is a property commonly used in fields such as earthquake engineering as an estimate of surface shear wave velocity. Databases of V_{s30} values exist that cover the entire earth's landmass, meaning that V_{s30} can potentially be used to increase the accuracy of desktop vibration sco-

ping studies. However, a challenge is that the mean shear wave velocity over a 30m depth is typically greater than the shear wave speed at the uppermost soil surface (i.e. where ground-borne vibration is most efficient). Therefore, although a recognised parameter in international standards [4, 15], there have been studies about its limitations [5, 33, 52, 53]. Therefore the accuracy of using V_{s30} to approximate layered soils, within a railway vibration setting is investigated.

To do so, results for layered soils are compared with those obtained for a homogeneous soil considering $c_s = V_{s30}$. Hereafter the homogeneous soil with $c_s = V_{s30}$ is called equivalent homogeneous soil. Three layered soils and the equivalent homogeneous soils are considered (Table D.6). The layered soil properties are chosen to ensure V_{s30} match the c_s properties shown in Table D.5.

Table D.6: Layered soil properties.

		h [m]	c_p [m/s]	c_s [m/s]	ξ [-]	ρ [kg/m^3]	V_{s30} [m/s]
Soft	Layer 1	24.1	318.9	159.5	0.05	1800	172.6
	Half-space	∞	518.1	259.1	0.05	1800	
Medium	Layer 1	1.7	220.9	110.5	0.05	1800	334.9
	Layer 2	7.8	479.4	239.7	0.05	1800	
	Layer 3	2.7	726	363	0.05	1800	
	Half-space	∞	1038	519	0.05	1800	
Stiff	Layer 1	2	361.5	180.7	0.05	1800	496.8
	Layer 2	3.6	660.4	330.2	0.05	1800	
	Layer 3	1.8	1113.2	556.6	0.05	1800	
	Half-space	∞	1291.6	645.8	0.05	1800	

The twelve storey building (Figure D.4) and the classical ballasted track on an embankment described previously in Section D.2 (Table D.1) are considered again.

Figure D.16 shows the rail receptances for the layered soils (Table D.6) and the equivalent homogeneous soils. It is observed that peaks in the track response for the three layered soils are found in the frequency range 12 Hz to 16 Hz. This is because the dominant frequency is strongly dependent upon the properties of the uppermost soil layer, which are similar for the three layered soils. A better agreement in terms of peak amplitudes is obtained at high frequencies. Regarding the three different soils, the homogeneous approximation performs best for the soft soil. This is because it has a smoother soil stratigraphy, characterised by a smaller discrepancy between the upper and lower layers' stiffness.

Figure D.17 shows the influence of soil stratigraphy on free-field mobility. In these results, it should be remembered that the neural network approach only utilises the upper layer properties (h_1 and c_{s_1}) and the V_{s30} parameter (Figure D.3), meaning the full soil profile is not considered. Regarding mobility results the level of error is similar to the receptance results, with the soft soil showing better agreement compared to the medium and stiff soils.

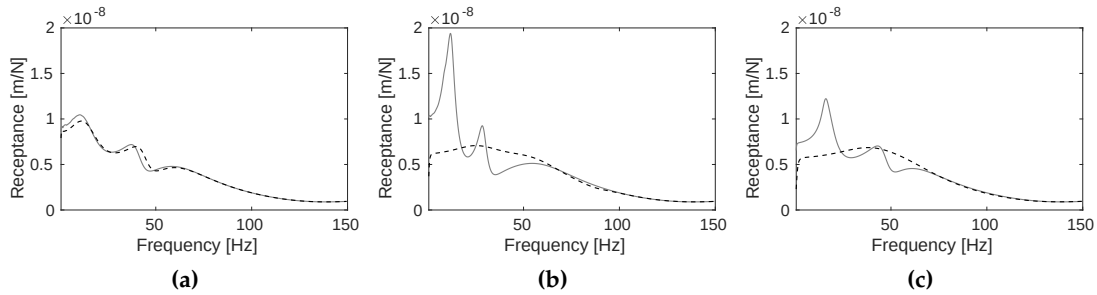

Figure D.16: (Grey line) The displacement of the rail for the layered (a) soft, (b) medium and (c) stiff soils. (Black dashed line) Superimposed is the solution for the equivalent homogeneous soil .

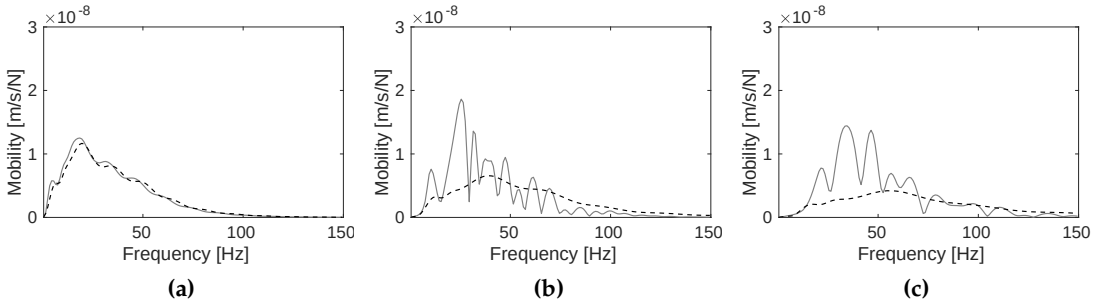

Figure D.17: (Grey line) Free-field vertical mobility at 20 m from the axis track for the layered (a) soft, (b) medium and (c) stiff soils. (Black dashed line) Superimposed is the solution for the equivalent homogeneous soil.

Figure D.18 shows frequency contents and the running RMS values [24] of the free-field response, due to a S-100 train passage at $v = 100\,\text{km/h}$. It is seen for the soft and stiff soils there are discrepancies at low frequency range, and for the medium and stiff soils at mid frequencies. Also, at some frequencies there are errors up to 13 dB in the frequency range 0 Hz to 100 Hz. Regarding the running RMS curves, the correlation is very similar, with a maximum error of 9 dB for the stiff soil.

After the track and free-field responses, the building response is studied. Figure D.19 shows that differences in ground-borne response spectra are in accordance with those observed previously in the free-field response (Figure D.18), where results for the stiff soils present the highest discrepancies.

Figure D.20 shows the contribution to the response of the building mode shapes. The small differences observed in the results for the soft soil (Figure D.20 (a and d)) are mainly due to the foundation system of springs and dampers that represents the SSI (Equations (28) and (29)) which depends on the uppermost soil layer stiffness c_{s1}. Taking into account $c_{s1} < V_{s30}$, this system has a lower energy dissipation for the equivalent homogeneous soil. Also, for the medium soil predictions, it is seen that modes of vibration are found at different frequencies (Figure D.20 (b and e)) for both the layered and the equivalent

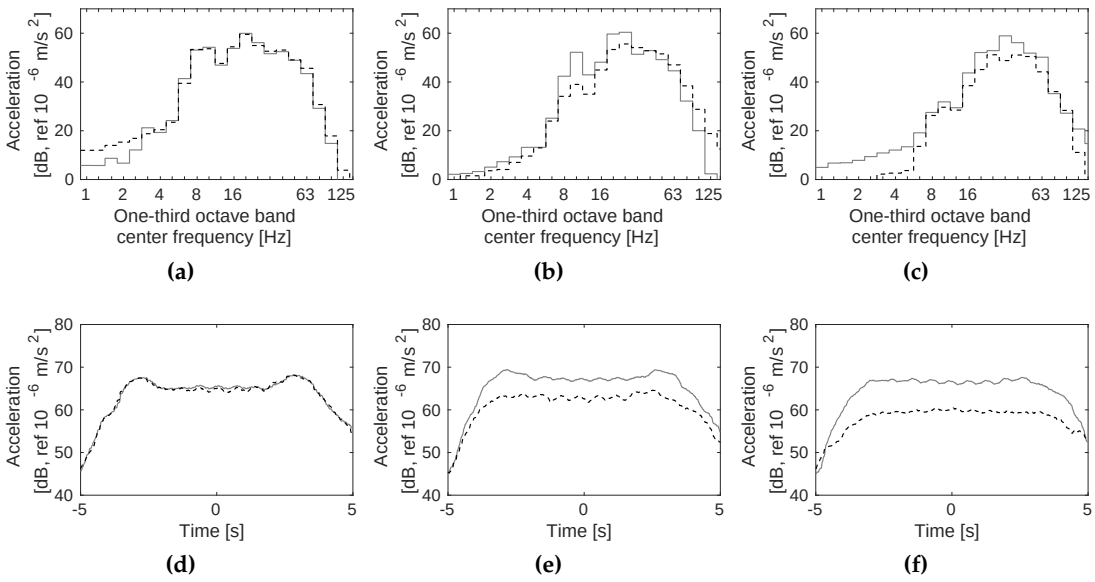

Figure D.18: (Grey line) (a-c) One-third octave band center frequency and (d-f) running RMS value of the vertical weighted acceleration in the free-field at 20 m from the axis track due to a S-100 train passage at $v = 100$ km/h for the layered (a and d) soft, (b and e) medium and (c and f) stiff soils. (Black dashed line) Superimposed is the solution for the equivalent homogeneous soil.

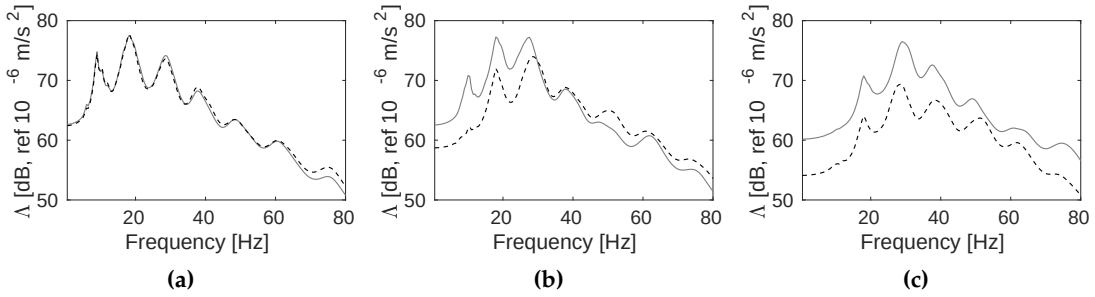

Figure D.19: (Grey line) Ground-borne response spectra $\Lambda_i^j(f_i)$ at 20 m from the axis track due to a S-100 train passage at $v = 100$ km/h for the layered (a) soft, (b) medium and (c) stiff soils. (black dashed line) Superimposed is the solution for the equivalent homogeneous soil.

homogeneous soils. Regarding the results for the stiff soil (Figure D.20 (c and f)), the response of the equivalent homogeneous soil is underestimated at the dominant frequencies.

Figure D.21 presents the overall RMS value (Equation (21)) of the free-field and twelve storey building vibration levels, considering different V_{s30} values. The soil response for homogeneous soils decreases as soil stiffness increases, however, the response of the layered soils show a contrasting behaviour. This is due to the shear wave velocity of the upper layer in each soil (Table D.6). In all cases, this shear wave velocity is lower than the V_{s30} parameter and the difference between both increases from the soft to the stiff soil. This behaviour

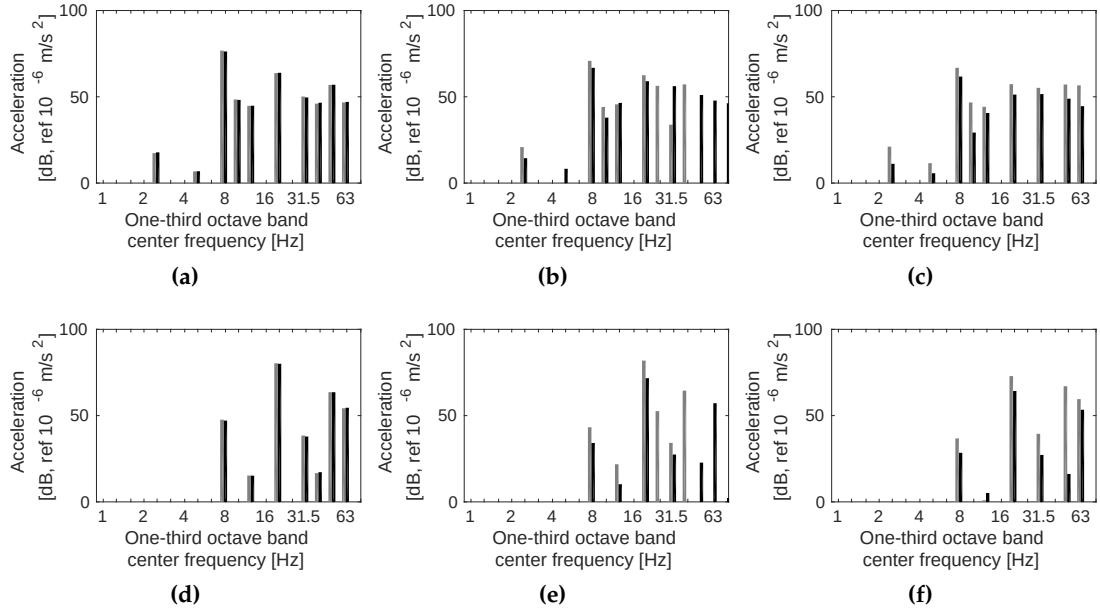

Figure D.20: (Grey bars) Contribution of the modes to the overall RMS value of the vertical weighted acceleration of the building response at the top floor of the observation points (a, b and c) A and (d, e, and f) B, for the layered (a and d) soft, (b and e) medium and (c and f) stiff soils. (Black bars) Superimposed is the solution for the equivalent homogeneous soil.

propagates to building response, where differences of approximately 10 dB are found. Predictions using the equivalent homogeneous soils underestimate the railway vibrations for the layered soils which is undesirable for the scoping model because it is designed to give conservative predictions. Therefore, it is concluded that the use of V_{s30} for ground vibration prediction should be used carefully and only for cases with straightforward stratigraphies.

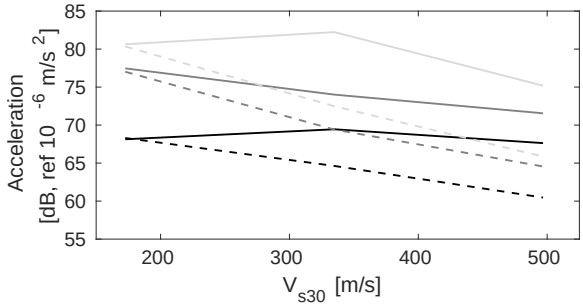

Figure D.21: (Black line) MTVV at the free-field and overall RMS value of the weighted acceleration at the top floor of the observation points (dark grey line) A and (light grey line) B, due to a S-100 train passage at $v = 100\,\mathrm{km/h}$ considering (solid lines) layered and (dashed lines) homogeneous soils charecterized by their V_{s30} parameter.

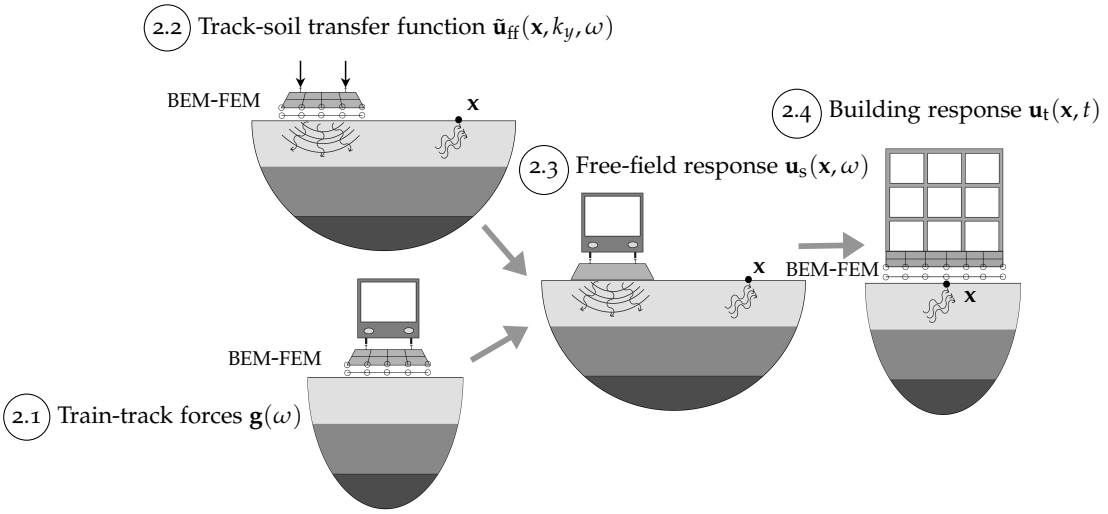

Figure D.22: Scheme of the reference model.

D.5 DISCUSSION

In an attempt to make a global uncertainty comparison, predictions from the scoping model and a more comprehensive 'reference' approach are presented. The reference model is developed using a BEM-FEM approach (Figure D.22). Source and wave propagation mechanisms (Figure D.22, step 2.3) are decoupled from the wave building immission (Figure D.22, step 2.4). The reference model combined two methodologies. The first method is used to compute the source-propagation problem of waves in the soil and the second one to study the immission problem due to waves propagation in buildings:

- The first method (Figure D.22, steps 2.1, 2.2 and 2.3) is based upon a 2.5D BEM-FEM methodology in the frequency-wavenumber domain [21, 35]. It is designed to compute the generation of railway vibrations and their propagation through the neighbouring soil. The train-track forces $\mathbf{g}(\omega)$ are calculated considering both quasi-static and dynamic contributions (Figure D.22, step 2.1). Next, the track-soil transfer function $\tilde{\mathbf{u}}_{ff}$ is calculated by modelling the track using FEM and the soil using BEM. The soil response is considered due to an impulse load applied on the rails (Figure D.22, step 2.2). Train-track interaction forces are combined with the track-soil transfer function, resulting in the free-field response due to train passage $\mathbf{u}_s$ at a point $\mathbf{x}$ (step 2.3).
- The second approach is used to obtain building vibrations due to a train passage. The foundation of the building is excited by the previously obtained free-field vibrations due to a train passage. The dynamic response of the building $\mathbf{u}_t$ (Figure D.22, step 2.4) is computed using the `SSIFiBo` toolbox based on a 3D time domain BEM-FEM methodology [19].

The discrepancies between scoping and reference model results for all the cases previously presented in this study are analysed. Only free-field responses are included because the

uncertainty of the scoping model to solve the immission problem of waves in buildings was studied enough previously by López-Mendoza et al. [38]. The authors found an uncertainty range between -3 dB and 11 dB for building vibrations computed from the scoping model.

The difference in soil vibration predictions is calculated as $\Delta a = 20\log_{10}\left(\Lambda^P/\Lambda^R\right)$, where Λ^P and Λ^R are the the ground-borne response spectra from the scoping and the reference model, respectively. Ground-borne response spectra Λ involves the building excitation in the scoping model (Equation (24)), represents a better way to determine the accuracy of the proposed model to solve the source-propagation problem of waves in the soil.

Figure D.23 shows the discrepancy between both models for all the cases. Prediction accuracy is good, with 98.5% of the samples having an uncertainty in the range -7.5 dB to 7.5 dB.

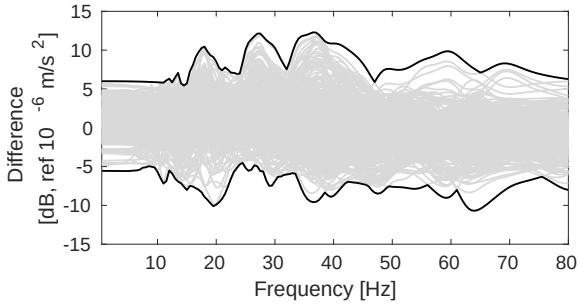

Figure D.23: (Grey lines) Frequency content of the differences Δa for all the cases. (Black lines) Superimposed is the envelope of the highest discrepancies.

The global uncertainty of the scoping model is determined using the MTVV vibration metric [24]. Figure D.24 presents the response for all the cases and a good agreement is found, with differences concentrated between -4.8 dB to 5.6 dB. Therefore the accuracy is similar to the uncertainty range between 5 dB to 20 dB as found using more comprehensive models [36, 28, 14].

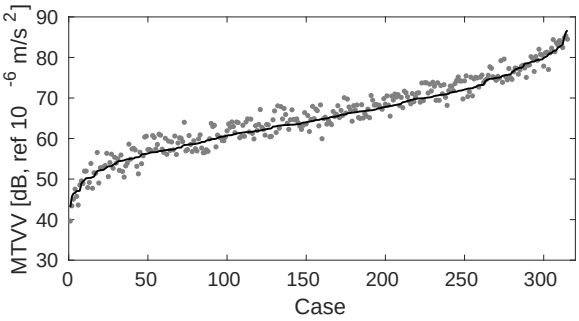

Figure D.24: MTVV in the free-field due to a S-100 train passage for all the cases, computed by (black line) the reference model and (grey points) the scoping model.

An important advantage of the new scoping model compared to comprehensive models is its computational efficiency. Table D.7 shows the computational costs to obtain the res-

ponse of the twelve storey building due to a S-100 train travelling at $v = 100\,\mathrm{km/h}$ using an `Intel One Core i7@1.87 GHz` computer. The CPU time refers to the source-propagation problem of waves in the soil and the immission problem of waves in the building. Taking into account the architecture of the scoping and reference models (Figures D.1 and D.22), Table D.7 outlines the main calculation steps and their run times. Note that the time required to obtain free-field predictions (step 2.3) is not presented because the models were identical. It should be noted that:

- The simplified track model (Figure D.2) allows the scoping model to reduce computations of the prediction of train-track excitation $\mathbf{g}$ (step 2.1). The reference model uses a BEM-FEM methodology to calculate the train-track excitation, thus requiring additional computations.
- The time required to calculate the track-soil transfer function $\tilde{\mathbf{u}}_{\mathrm{ff}}$ (step 2.2) using the scoping model is primarily due to the evaluation of the soil Green's function (step 2.2.2). The correction factor $\tilde{A}_g$ is estimated through a NN approach (step 2.2.1) and requires a minimal computational cost. The combination of these two steps results in a run time that is much lower than that for the reference model.
- The largest boost in computation efficiency come from the prediction of building response. Regarding the reference model computational cost, it should be noted that the cost required to compute the soil BEM domain under the building foundation is not included, and the CPU time is obtained from parallel computing.

The difference in run times is mainly due to the more comprehensive BEM-FEM methodology used in the reference model to consider track-soil and soil-structure interactions. Alternatively, the time required for the scoping to solve the whole vibration analysis from adding source-propagation and immission problems, is much lower than the necessary for the reference model.

Table D.7: Average running time.

Step	Reference model	Scoping model
Train-track forces	25 min	38 s
Track-soil transfer function	15 min	5 min
Building response	37 min	12 s

Considering these much reduced computational requirements, the range of uncertainty and the versatility of the proposed scoping model, it is concluded that it could be a powerful tool during the early design stages of railway lines where a large number of building vibrations assessment is required.

D.6 CONCLUSIONS

In this chapter, a simplified methodology to compute the propagation of railway vibrations into nearby buildings is presented. The model is novel because it is able to simulate the generation, propagation and immission of vibrations, for complex vehicle, track, soil and building arrangements in minimal time. The model is designed to be conservative in nature, to ensure that it is able to identify any high risk vibration sites during scoping tests, thus avoiding the application of any safety factor (e.g. 10 dB is commonly added in practise).

To do so, the source-propagation of wave energy through the ground has been decoupled from the immission of waves within buildings. Then, a simplified 2.5D FEM track model, a hybrid direct stiffness-neural network procedure and a modal superposition analysis for building response have been combined to create an overall model describing the vehicle-track-soil-building problem.

A sensitivity analysis is undertaken using the scoping model. Track type, soil stiffness, building height and train speed effects are studied and it is found that there is a strong relationship between vibration levels and these parameters.

Comparisons have been made to determine the accuracy of using a global database of V_{s30} soil properties to predict vibration levels. Track receptance, free-field mobility, soil vibration, dominant building modes and building response due to railway traffic have been analysed and it has been found that this simplification is only satisfactory for cases with smooth stratigraphies.

Finally, results from the proposed model and a reference BEM-FEM approach have been compared and the new model has presented a good prediction ability. Discrepancies are due to modelling disparities between its architecture and that of the reference model.

In conclusion, the scoping model acts as a powerful `MATLAB` toolbox that allows users to evaluate free-field and building vibrations due to train passage at the early design stage.

D.7 ACKNOWLEDGEMENTS

This research was funded by the Spanish Ministry of Economy and Competitiveness (Ministerio de Economía y Competitividad) through research project BIA2016-75042-C2. Financial support is gratefully acknowledged. The support given by the Andalusian Scientific Computing Centre, the Leverhulme Trust and the University of Leeds Cheney Award Scheme is also gratefully acknowledged.

The first author would like to thank the Spanish Ministry of Education, Culture and Sport (Ministerio de Educación, Cultura y Deporte) for the financial support of his research stay at the School of Civil Engineering of the University of Leeds through the scholarship "Salvador de Madariaga" Reference PRX18/00115.

REFERENCES

[1] L. Auersch. The excitation of ground vibration by rail traffic: theory of vehicle–track–soil interaction and measurements on high-speed lines. *Journal of Sound and Vibration*, 284:103–132, 2005. doi: https://doi.org/10.1016/j.jsv.2004.06.017.

[2] L. Auersch. Building Response due to Ground Vibration–Simple Prediction Model Based on Experience with Detailed Models and Measurements. *International Journal of Acoustics and Vibration*, 15(3):101–112, 2010.

[3] L. Auersch, A. Romero, and P. Galvín. Respuesta dinámica de edificaciones producida por campos de onda incidentes considerando la interacción suelo-estructura. *Revista Internacional de Métodos Numéricos para Cálculo y Diseño en Ingeniería*, 30(4):256–263, 2014. doi: https://doi.org/10.1016/j.rimni.2013.09.001.

[4] *NEHRP Recommended Seismic Provisions for New Buildings and Other Structures, FEMA P-1050*. Building Seismic Safety Council, 2015.

[5] S. Castellaro, F. Mulargia, and P.L. Rossi. Vs30: Proxy for seismic amplification? *Seismological Research Letters*, 79(4):540–543, 2008. doi: http://dx.doi.org/10.1785/gssrl.79.4.540.

[6] C.E. Hanson, D.A. Towers, and L.D. Meister. High-speed ground Transportation Noise and Vibration Impact Assessment, HMMH Report 293630-4. *U.S. Department of Transportation, Federal Railroad Administration, Office of Railroad Development*, 2005.

[7] C.E. Hanson, D.A. Towers, and L.D. Meister. Transit Noise and Vibration Impact Assessment, Report FTA-VA-90-1003-06. *U.S. Department of Transportation, Federal Transit Administration, Office of Planning and Environment*, 2006.

[8] R.W. Clough and J. Penzien. *Dynamic of Structures*. McGraw-Hill, New York, 1975.

[9] D.P. Connolly, G.P. Marecki, G. Kouroussis, I. Thalassinakis, and P.K. Woodward. The growth of railway ground vibration problems – A review. *Science of the Total Environment*, 568:1276–1282, 2015. doi: http://dx.doi.org/10.1016/j.scitotenv.2015.09.101.

[10] D. E. Rumelhart and J. L. McClelland. *Parallel distributed processing: Explorations in the microstructure of cognition. Vol 1*. MIT Press, Cambridge, MA, 1986.

[11] *DIN 45672 Teil 2: Schwingungsmessungen in der Umgebung von Schienenverkehrswegen: Auswerteverfahren*. Deutsches Institut für Normung, 1995.

[12] D.P. Connolly, G. Kouroussis, A. Giannopoulos, O. Verlinden, P.K. Woodward, and M.C. Forde. Assesment of railway vibrations using an efficient scoping model. *Soil Dynamics and Earthquake Engineering*, 58:37–47, 2014. doi: https://doi.org/10.1016/j.soildyn.2013.12.003.

[13] D.P. Connolly, G. Kouroussis, P.K. Woodward, A. Giannopoulos, O. Verlinden, and M.C. Forde. Scoping prediction of re-radiated ground-borne noise and vibration near high speed rails lines with variable soils. *Soil Dynamics and Earthquake Engineering*, 66: 78–88, 2014. doi: https://doi.org/10.1016/j.soildyn.2014.06.021.

[14] D.P. Connolly, P. Alves Costa, G. Kouroussis, P. Galvín, P.K. Woodward, and O. Laghrouche. Large scale international testing of railway ground vibrations across Europe. *Soil Dynamics and Earthquake Engineering*, 71:1–12, 2015. doi: https://doi.org/10.1016/j.soildyn.2015.01.001.

[15] *Eurocode 8: Design of structures for earthquake resistance–Part 1 : General rules, seismic actions and rules for buildings*. European Committee for Standardization, 1998.

[16] S. François, L. Pyl, H.R. Masoumi, and G. Degrande. The influence of dynamic soil-structure interaction on traffic induced vibrations in buildings. *Soil Dynamics and Earthquake Engineering*, 27:655–674, 2007.

[17] S. François, M. Schevenels, P. Galvín, G. Lombaert, and G. Degrande. A 2.5d coupled fe–be methodology for the dynamic interaction between longitudinally invariant structures and a layered halfspace. *Computer Methods in Applied Mechanics and Engineering*, 199(23):1536 – 1548, 2010. doi: https://doi.org/10.1016/j.cma.2010.01.001.

[18] P. Galvín and J. Domínguez. High-speed train-induced ground motion and interaction with structures. *Journal of Sound and Vibration*, 307:755–777, 2007. doi: https://doi.org/10.1016/j.jsv.2007.07.017.

[19] P. Galvín and A. Romero. A MATLAB toolbox for soil-structure interaction analysis with finite and boundary elements. *Soil Dynamics and Earthquake Engineering*, 57:10–14, 2014.

[20] P. Galvín, A. Romero, and J. Domínguez. Fully three-dimensional analysis of high-speed train–track–soil–structure dynamic interaction. *Journal of Sound and Vibration*, 329:5147–5163, 2010. doi: https://doi.org/10.1016/j.jsv.2010.06.016.

[21] P. Galvín, S. François, M. Schevenels, E. Bongini, G. Degrande, and G. Lombaert. A 2.5d coupled fe-be model for the prediction of railway induced vibrations. *Soil Dynamics and Earthquake Engineering*, 30(12):1500 – 1512, 2010. doi: https://doi.org/10.1016/j.soildyn.2010.07.001.

[22] P. Galvín, D. López-Mendoza, D.P. Connolly, G. Degrande, G. Lombaert, and A. Romero. Scoping assessment of free-field vibrations due to railway traffic. *Soil Dynamics and Earthquake Engineering*, 114:598–614, 2018. doi: https://doi.org/10.1016/j.soildyn.2018.07.046.

[23] M. Hussein, H. Hunt, K. Kuo, P. Alves Costa, and J. Barbosa. The use of sub-modelling technique to calculate vibration in buildings from underground railways. *Proceedings of the Institution of Mechanical Engineers, Part F: Journal of Rail and Rapid Transit*, 229(3): 303 – 314, 2013. doi: https://doi.org/10.1177/0954409713511449.

[24] *ISO 2631-1:2003: Mechanical vibration and shock–Evaluation of human exposure to whole-body vibration–Part 1: General requirements*. International Organization for Standardization, 2003.

[25] *ISO 2631-2:2003: Mechanical vibration and shock–Evaluation of human exposure to whole-body vibration–Part 2: Vibration in buildings (1–80 Hz)*. International Organization for Standardization, 2003.

[26] *ISO 14837-1:2005 Mechanical vibration–Ground-borne noise and vibration arising from rail systems–Part 1: General guidance*. International Organization for Standardization, 2005.

[27] P. Jean, C. Guigou, and M. Villot. A 2.5D BEM Model for Ground-Structure Interaction. *Building Acoustics*, 11(3):1–17, 2004. doi: https://doi.org/10.1260/1351010042250376.

[28] S. Jones, K. Kuo, M.F.M. Hussein, and H.E.M Hunt. Prediction uncertainties and inaccuracies resulting from common assumptions in modelling vibration from underground railways. *Proceedings of the Institution of Mechanical Engineers, Part F: Journal of Rail and Rapid Transit*, 226:501–512, 2012. doi: https://doi.org/10.1177/0954409712441744.

[29] E. Kausel. *Fundamental solutions in elastodynamics: a compendium*. Cambridge University Press, 2006.

[30] E. Kausel and J.M. Roësset. Stiffness matrices for layered soils. *Bulletin of the Seismological Society of America*, 71(6):1743, 1981.

[31] G. Kouroussis, K.E. Vogiatzis, and D.P. Connolly. A combined numerical/experimental prediction method for urban railway vibration. *Soil Dynamics and Earthquake Engineering*, 97:377 – 386, 2017. doi: http://dx.doi.org/10.1016/j.soildyn.2017.03.030.

[32] K.A. Kuo, H. Verbraken, G. Degrande, and G. Lombaert. Hybrid predictions of railway induced ground vibration using a combination of experimental measurements and numerical modelling. *Journal of Sound and Vibration*, 373:263–284, 2016. doi: https://doi.org/10.1016/j.jsv.2016.03.007.

[33] L.A. Wald and J. Mori. Evaluation of methods for estimating linear site-response amplifications in the los angeles region. *Bulletin of the Seismological Society of America*, 90(6B):S32–S42, 2000. doi: https://doi.org/10.1785/0119970170.

[34] G. Lombaert and G. Degrande. Ground-borne vibration due to static and dynamic axle loads of intercity and high-speed trains. *Journal of Sound and Vibration*, 319(3–5): 1036–1066, 2009. doi: http://dx.doi.org/10.1016/j.jsv.2008.07.003.

[35] G. Lombaert, G. Degrande, J. Kogut, and S. François. The experimental validation of a numerical model for the prediction of railway induced vibrations. *Journal of Sound and Vibration*, 297(3):512 – 535, 2006. doi: https://doi.org/10.1016/j.jsv.2006.03.048.

[36] G. Lombaert, P. Galvín, S. François, and G. Degrande. Quantification of uncertainty in the prediction of railway induced ground vibration due to the use of statistical track unevenness data. *Journal of Sound and Vibration*, 333(18):4232 – 4253, 2014. doi: https://doi.org/10.1016/j.jsv.2014.04.052.

[37] P. Lopes, P. Alves Costa, M. Ferraz, R. Calçada, and A. Silva Cardoso. Numerical modeling of vibrations induced by railway traffic in tunnels: From the source to the nearby buildings. *Soil Dynamics and Earthquake Engineering*, 61–62:269–285, 2014. doi: https://doi.org/10.1016/j.soildyn.2014.02.013.

[38] D. López-Mendoza, A. Romero, D.P. Connolly, and P. Galvín. Scoping assessment of building vibration induced by railway traffic. *Soil Dynamics and Earthquake Engineering*, 93:147–161, 2017. doi: http://dx.doi.org/10.1016/j.soildyn.2016.12.008.

[39] M. H. Beale, M. T. Hagan, and H. B. Demuth. *Neural network toolbox User's guide*. Mathworks, Inc, 2017.

[40] M. T. Hagan and M. B. Menhaj. Training feedforward networks with the marquardt algorithm. *EEE Transactions on Neural Networks*, 5(6):989–993, 1994. doi: https://doi.org/10.1109/72.329697.

[41] M. Monjezi, M. Ahmadi, M. Sheikhan, A. Bahrami, and A. R. Salimi. Predicting blast-induced ground vibration using various types of neural networks. *Soil Dynamics and Earthquake Engineering*, 30:1233–1236, 2010. doi: https://doi.org/10.1016/j.soildyn.2010.05.005.

[42] V. Nourani and M. S. Fard. Sensitivity analysis of the artificial neural network outputs in simulation of the evaporation process at different climatologic regimes. *Advances in Engineering Software*, 47:127–146, 2012. doi: https://doi.org/10.1016/j.advengsoft.2011.12.014.

[43] P. Alves Costa, R. Calçada, and A. Silva Cardoso. Track–ground vibrations induced by railway traffic: In-situ measurements and validation of a 2.5D FEM-BEM model. *Soil*

Dynamics and Earthquake Engineering, 32:111–128, 2012. doi: https://doi.org/10.1016/j.soildyn.2011.09.002.

[44] P. Alves Costa, A. Colaço, R. Calçada, and A. Silva Cardoso. Critical speed of railway tracks. Detailed and simplified approaches. *Transportation Geotechnics*, 2:30–46, 2015. doi: https://doi.org/10.1016/j.trgeo.2014.09.003.

[45] A. Romero, A. Tadeu, P. Galvín, and J. António. 2.5D coupled BEM–FEM used to model fluid and solid scattering wave. *International Journal for Numerical Methods in Engineering*, 101:148–164, 2015. doi: https://doi.org/10.1002/nme.4801.

[46] A. Romero, P. Galvín, J. António, J. Domínguez, and A. Tadeu. Modelling of acoustic and elastic wave propagation from underground structures using a 2.5d bem-fem approach. *Engineering Analysis with Boundary Elements*, 76:26 – 39, 2017. doi: http://dx.doi.org/10.1016/j.enganabound.2016.12.008.

[47] S.B. Mezher, D.P. Connolly, P.K. Woodward, O. Laghrouche, J. Pombo, and P. Alves Costa. Railway critical velocity – analytical prediction and analysis. *Transportation Geotechnics*, 6:84 – 96, 2016. doi: https://doi.org/10.1016/j.trgeo.2015.09.002.

[48] M. Schevenels, S. François, and G. Degrande. Edt: An elastodynamics toolbox for MATLAB. *Computers & Geosciences*, 35(8):1752 – 1754, 2009. doi: http://dx.doi.org/10.1016/j.cageo.2008.10.012.

[49] X. Sheng, C.J.C. Jones, and D.J. Thompson. Prediction of ground vibration from trains using the wavenumber finite and boundary element methods. *Journal of Sound and Vibration*, 293:575–586, 2006. doi: https://doi.org/10.1016/j.jsv.2005.08.040.

[50] A. Triepaischajonsak and D.J. Thompson. A hybrid modelling approach for predicting ground vibration from trains. *Journal of Sound and Vibration*, 335:147 – 173, 2015. doi: http://dx.doi.org/10.1016/j.jsv.2014.09.029.

[51] H. Verbraken, G. Lombaert, and G. Degrande. Verification of an empirical prediction method for railway induced vibrations by means of numerical simulations. *Journal of Sound and Vibration*, 330(8):1692–1703, 2011. doi: https://doi.org/10.1016/j.jsv.2010.10.026.

[52] T. Volti, D. Burbidge, C. Collins, M.W. Asten, J.K. Odum, W.J. Stephenson, C. Pascal, and J. Holzschuh. Comparisons between V_{S30} and spectral response for 30 sites in newcastle, australia, from collocated seismic cone penetrometer, active- and passive-source V_S data. *Bulletin of the Seismological Society of America*, 106(4):1690–1709, 2016. doi: https://doi.org/10.1785/0120150073.

[53] V.W. Lee and M.D. Triufnac. Should average shear-wave velocity in the top 30 m of soil be used to describe seismic amplification? *Soil Dynamics and Earthquake Engineering*, 30:1250–1258, 2010. doi: https://doi.org/10.1016/j.soildyn.2010.05.007.

[54] H. Xia, Y.M. Cao, and G. De Roeck. Theoretical modeling and characteristic analysis of moving-train induced ground vibrations. *Journal of Sound and Vibration*, 329:819–832, 2010. doi: https://doi.org/10.1016/j.jsv.2009.10.007.

[55] Y. L. Cun, I. Kanter, and S. A. Solla. Second order properties of error surfaces: Learning time and generalization. *Advances in Neural Information Processing Systems*, 3:918–924, 1991.

[56] M. Yurdakul and H. Akdas. Modeling uniaxial compressive strength of building stones using non-destructive test results as neural networks input parameters. *Construction and Building Materials*, 47:1010–1019, 2013. doi: https://doi.org/10.1016/j.conbuildmat.2013.05.109.

This research has been supported by the Spanish Ministry of Economy and Competitiveness (Ministerio de Economía y Competitividad) through research projects BIA2013-43085-P and BIA2016-75042-C2-1-R. Financial support is gratefully acknowledged.